

Monolithic Particle Detectors based on Hydrogenated Amorphous Silicon

THÈSE N° 6290 (2014)

PRÉSENTÉE LE 26 AOÛT 2014

À LA FACULTÉ DES SCIENCES ET TECHNIQUES DE L'INGÉNIEUR
LABORATOIRE DE PHOTOVOLTAÏQUE ET COUCHES MINCES ÉLECTRONIQUES
PROGRAMME DOCTORAL EN SCIENCE ET GÉNIE DES MATÉRIAUX

ÉCOLE POLYTECHNIQUE FÉDÉRALE DE LAUSANNE

POUR L'OBTENTION DU GRADE DE DOCTEUR ÈS SCIENCES

PAR

Andrea FRANCO

acceptée sur proposition du jury:

Prof. H. Hofmann, président du jury
Prof. C. Ballif, Dr N. Würsch, directeurs de thèse
Dr M. Despeisse, rapporteur
Dr J. S. Lapington, rapporteur
Prof. P. Seitz, rapporteur



ÉCOLE POLYTECHNIQUE
FÉDÉRALE DE LAUSANNE

Suisse
2014

To my wife, Vittoria.

Learn from yesterday, live for today, hope for tomorrow.

The important thing is not to stop questioning.

— Albert Einstein

Acknowledgements

My four years at the PV-Lab have been a unique opportunity for my professional and personal growth and I would like to thank all the people that contributed to make this time so exceptional.

First of all, I would like to thank my thesis director, Prof. Christophe Ballif, for welcoming me into the PV-Lab, a stimulating and dynamic laboratory. I share your passion for renewable energies and photovoltaics, striving for a greener world. I appreciated the team spirit you foster in the laboratory, your knowledge and how you convey it to different types of audience. I would like to thank you for your very useful suggestions and remarks you provided me throughout the thesis. I also would like to thank you for the opportunity you gave me to travel around the world, to present my research and to show how multidisciplinary we are at the PV-Lab. I enjoyed the extracurricular activities you organized and it was great fun to follow you in off-slope skiing races.

The second person I want to thank, with whom I had very fruitful discussions about the physical explanations behind the measurements, is my thesis co-director, Dr. Nicolas Wyrsh. I really appreciated the freedom you gave me, so as to show to myself that I could achieve good results with an autonomous and rigorous research attitude. Your broad knowledge and varied interests made for lively conversations. Finally, I am grateful for the help you gave me in improving my scientific writing skills and particularly for all your comments and corrections relevant to this manuscript.

I would like to thank Prof. Heinrich Hoffman, who was the jury president both at my PhD private defense and at my candidacy exam. I thank the experts who spent their precious time to evaluate my research and for their positive feedback: Prof. Peter Seitz, Dr. Jon Lapington and Dr. Matthieu Despeisse. In particular, I thank Jon for your remarks and corrections, which helped me to greatly improve the quality of this manuscript. I thank Matthieu for your corrections and for welcoming me into our office, together with Fanny, at my arrival at the PV-Lab. I esteem your intelligence, your positive attitude and your passion for photovoltaics. Then, to the person who provided me with valuable help at the beginning of my PhD: thanks, Yannick! I appreciated above all your unconditional kindness, availability and support. You are one of those people who make life in the lab a better place! I also enjoyed all our activities outside the lab, especially skiing and hiking.

I am very grateful to Jonas. As with Yannick, your availability to help other people is extremely valuable, as I witnessed in my research. The amorphous-silicon-based microchannel plates (AMCPs) have your signature as well, with all the clever solutions you found for the pho-

Acknowledgements

tolithography processes.

I would like to deeply thank Pierre-André Clerc, at the CSEM of Neuchâtel, who performed the deep reactive ion etching, the last delicate step in the fabrication of AMCPs. He challenged himself in realizing channels with a diameter of 5 μm and as deep as 100 μm . His scrutinizing eye was the only one to reach the bottom of these channels, apart from the multiplied electrons!

I would like to thank all the technical staff at PV-Lab: Cedric, Reto, Lionel and, in particular, Jérémie and Joël, who helped me build the system to characterize the AMCPs.

Merci beaucoup à Sylviane Pochon, du CSEM Neuchâtel. J'ai beaucoup apprécié ta disponibilité pour le plusieurs sciages des plaques AMCPs et les centaines de bondage des puces AMCPs! Je partage ta passion pour la nature et les ballades en montagne.

I would like to thank also the microscopy group at CSEM, especially Dr. Massoud Dadras and Mireille Leboeuf, for welcoming me at their facilities, for being always available to answer my questions and for supporting me with my exotic measurements with the scanning electron microscope.

Thanks to my office mates Fanny, Matthieu and Franz, with whom I shared nice moments and interesting discussions.

Thanks, Lara and Zak, for helping me to improve my English writing skills and the quality of this manuscript.

I would like to thank also some of my former university professors, whose teaching helped me during the thesis, especially Prof. Ettore Vittone and Dr. Marco Truccato.

Finally, I would like to thank all my colleagues and their partners for making the PV-Lab such a great place to work. In particular, thanks to Laura, Darya, Monica, Lara, Johannes, Linus, Mathieu, Marcelo and Zak, with whom I shared many adventures, feasts with food from all over the world and nice evenings together!

Thanks to the Italian team at PV-Lab, especially Lorenzo, Federico and Andrea. Running, climbing and skiing with you guys is always great!

Thanks also to Bénédicte, Max and Valentin for the nice time spent together while climbing.

Thanks to the Pub Quiz team: Jan-Willem, Stefaan and Kaustav among others. Those evenings were fun, instructive and a nice distraction from work.

Thank you, Fabien, for joining me in the craziest mountain race I have ever done: an amazing adventure for 61 km and 4000 metres of positive difference in altitude.

A special thank you goes to my family, starting with my father and mother, who always cheer me and encourage me to improve myself and to whom I owe most of the person I am today. Thank you, Lorenzo and Caterina: you are a fantastic brother and sister and together we are the best team ever!

My last words are for the most special person in my life, my wonderful wife Vittoria. Thank you for always listening to me and encouraging me, and for being understanding and supportive in the difficult moments of these four years. This work bears the mark of your indelible contribution, from my first days at PV-Lab to the final sprint to complete this manuscript.

Neuchâtel, July 2014

Andrea Franco

Riassunto

In questa tesi sono stati studiati due tipi di rivelatori di particelle, monolitici e in silicio amorfo. Il primo è il rivelatore a piatto di microcanali in silicio amorfo (AMCPs), ovvero un moltiplicatore di elettroni a dinodo continuo, integrato su anodi metallici. In questo rivelatore, un campo elettrico è stabilito nei canali del piatto. I canali sono lunghi da 60 a 100 μm e larghi da 5 a 9 μm . Gli elettroni che entrano nei canali, sono accelerati dal campo elettrico e collidono diverse volte contro le pareti dei canali. Ad ogni collisione, il numero di elettroni aumenta così che si genera un effetto valanga che permette la rivelazione.

Il secondo tipo è il rivelatore di particelle chiamato TFA, ovvero “thin-film-on-ASIC” (“film sottile su ASIC”). Questo rivelatore consiste in un diodo in silicio amorfo che viene integrato verticalmente su un ASIC, cioè un circuito integrato sviluppato per un’applicazione specifica. Il diodo ha uno spessore che varia tra 5 e 50 μm ed è polarizzato tramite un elettrodo superiore comune, rispetto all’elettrodo inferiore che è a massa e che corrisponde alle metallizzazioni dell’ASIC. La rivelazione delle particelle avviene tramite la creazione di un certo numero di coppie elettrone-lacuna, che sono generati dall’energia rilasciata dalla particella.

Gli AMCPs sviluppati in questa tesi sono stati fabbricati con un processo di fabbricazione completamente diverso dai piatti di microcanali (MCPs) tradizionali. I vantaggi di questo nuovo processo sono: l’integrazione verticale dei AMCPs e l’eliminazione dello strato semiconduttore sulla parete dei canali. Quest’ultimo viene utilizzato nei MCPs per ricaricare gli elettroni emessi durante la moltiplicazione. Gli AMCPs sono fabbricati con la deposizione chimica del silicio amorfo tramite dei gas precursori. Il plasma permette di ridurre la temperatura del processo a 200°C. La resistività del silicio amorfo varia da 10^{10} a $10^{12} \Omega\cdot\text{cm}$ e lo spessore depositato da 50 a 100 μm . Sebbene l’obiettivo finale sia l’integrazione degli AMCPs su ASICs, in questa tesi gli AMCPs sono stati fabbricati su anodi metallici, in modo tale da semplificare l’ottimizzazione strutturale degli AMCPs.

I primi prototipi di AMCPs, realizzati prima di questa tesi, sono stati radicalmente modificati. L’innovazione principale consiste nell’introduzione di un elettrodo intermedio, separato dall’anodo (che raccoglie gli elettroni moltiplicati) tramite 2 μm di silicio amorfo. La moltiplicazione degli elettroni avviene tra l’elettrodo superiore e questo elettrodo intermedio, che è mantenuto a massa e permette di evacuare le correnti elettriche parassite. In questo modo, la corrente parassita che raggiunge l’anodo è ridotta di cinque ordini di grandezza. La fabbricazione dei canali è ottenuta con la tecnica di attacco chimico ionico (DRIE). I canali realizzati in questa tesi hanno un rapporto massimo di lunghezza su diametro di circa 12.5:1. La conferma del funzionamento del AMCP come moltiplicatore di elettroni è stata ottenuta

con l'introduzione dell'elettrodo intermedio. Il fattore di moltiplicazione, o guadagno, è 45 per un rapporto di lunghezza su diametro di 12:1 e una tensione di polarizzazione di 500 V. L'analisi del guadagno in funzione del rapporto lunghezza-diametro ha permesso di confermare che il guadagno degli AMCPs è simile a quello dei MCPs, per rapporti lunghezza-diametro comparabili. Inoltre, il primo tentativo di migliorare il coefficiente di emissione secondaria, tramite la deposizione di uno strato di ossido di alluminio di 5 nm, ha permesso di raggiungere un guadagno di 80.

Questi risultati dimostrano il potenziale di questo nuovo processo di fabbricazione di MCPs. Grazie all'ottimizzazione della deposizione del silicio amorfo, un rapporto lunghezza-diametro dei canali di 20:1 è facilmente ottenibile nel futuro prossimo e rapporti superiori a 25:1 sono possibili. In conclusione, il processo di fabbricazione degli AMCPs ha oramai raggiunto un livello tale che le prime applicazioni saranno possibili in pochi anni.

I rivelatori TFA sono stati caratterizzati, in questa tesi, in termini di risoluzione spaziale relativa al posizionamento di un fascio elettronico, ottenuto con un microscopio a scansione elettronica. Queste misure sono state effettuate muovendo il fascio sopra alcune regioni del diodo in silicio amorfo, al di sotto del quale le metallizzazioni dell'ASIC hanno la forma di strisce micrometriche. Questa geometria produce una modulazione del segnale di rivelazione, che è dovuta a una migliore efficienza di raccolta delle cariche generate dalla radiazione ionizzante in corrispondenza di ciascuna striscia. In questo modo, ogni metallizzazione può essere individuata, anche quelle che sono larghe solo $0.6\ \mu\text{m}$ e distanziate da $1.4\ \mu\text{m}$. Questi risultati sono stati riprodotti con tre spessori del diodo in silicio amorfo, cioè 5, 10 e $20\ \mu\text{m}$, grazie a un allargamento trascurabile del volume entro il quale sono state create le cariche. L'assenza di un sostanziale allargamento è dovuto a una lunghezza di diffusione trascurabile delle coppie elettrone-lacuna nel silicio amorfo e al campo elettrico molto intenso all'interno del diodo. Di conseguenza, i rivelatori TFA si distinguono dai rivelatori microstrips in silicio cristallino, dove la diffusione laterale delle coppie elettrone-lacuna viene utilizzato per determinare la posizione del passaggio della particella.

Malgrado l'insensibilità del silicio amorfo relativa ai difetti prodotti dallo spostamento di alcuni atomi rispetto alla loro posizione originale, le proprietà elettroniche del silicio amorfo sono fortemente degradate dal fascio elettronico. Questa degradazione è dovuta alla rottura dei legami atomici, i quali a loro volta inducono la ricombinazione delle cariche prodotte durante la rivelazione. La ricombinazione, di conseguenza, riduce il segnale complessivo. Ciò nonostante, in questa tesi è stato dimostrato che questi legami atomici possono essere ricostituiti con un riscaldamento del silicio amorfo a $130\ ^\circ\text{C}$, per alcune decine di ore.

In conclusione, la resistenza alla radiazione del silicio amorfo e le ottime prestazioni di risoluzione spaziale fanno, dei rivelatori di particelle TFA, degli ottimi candidati per applicazioni di posizionamento di fasci di particelle.

Parole chiave: silicio amorfo, piatto a microcanali (MCP), integrazione monolitica, elettroni secondari, film per l'emissione secondaria, moltiplicazione elettronica, rifornimento della carica, rivelatore a vuoto, rivelatore TFA, rivelatore a stato solido, deposizione chimica gassosa assistita dal plasma.

Abstract

Two types of monolithic particle detectors based on hydrogenated amorphous silicon (a-Si:H) are studied in this thesis. The first consists of amorphous-silicon-based microchannel plates (AMCPs), vacuum detectors that are vertically integrated on metallic anodes. In these detectors, an electric field is set across a resistive stack with microchannels that are 60–100 μm long and 5–9 μm wide. Impinging electrons are accelerated inside the channels and collide against their surfaces a number of times. After each electron collision, a few secondary electrons are ejected which generates a multiplication process and enables the detection.

The second type consists of thin-film-on-ASIC (TFA) particle detectors, which features a solid-state a-Si:H sensing diode vertically integrated on an application-specific integrated circuit (ASIC). The sensing diode is typically 5–50 μm thick and is biased by a common top electrode with respect to a number of independent grounded bottom electrodes, which are the ASIC pads and determine the detector pixels. Detection occurs by means of the collection of the electron-hole pairs, which are generated by the ionizing energy of different types of impinging particles.

AMCPs address the challenge of replacing the complicated and expensive glass multifiber draw process of conventional MCPs with a completely new one based on a-Si:H. The immediate advantages, proven in this work, are the possibility of vertical integration of the AMCPs and the elimination of any additional semiconducting layer, on the channel wall, for charge replenishment. These remarkable achievements are obtained by plasma-enhanced chemical vapor deposition of a-Si:H at about 200 °C, whose resistivity can be tuned within 10^{10} – 10^{12} $\Omega\text{ cm}$ and whose thickness can be large enough (typically 50–100 μm) to realize working AMCPs. Although the ultimate aim is the vertical integration of AMCPs on an ASIC—to combine the AMCP's electron multiplication and micrometric spatial resolution with the ASIC's in-situ data processing—AMCPs are here fabricated on metallic anodes deposited on an oxidized Si wafer. This substrate provides the required flexibility for optimization of the AMCP structure.

In this thesis, the first AMCP prototypes, which had been developed before the thesis began, are first characterized and then radically revised. The breakthrough is the introduction of a third intermediate electrode decoupled from the anode by 2 μm of a-Si:H. Electron multiplication occurs between the AMCP top electrode and this intermediate electrode, which is grounded and enables evacuation of the leakage current induced by the large bias voltage through the a-Si:H bulk. Consequently, we show that the residual leakage current on the anode, where the multiplied electrons are collected, is reduced by more than five orders of magnitude with

respect to the original architecture. Channel micromachining through the AMCP layer stack is performed by deep reactive ion etching with a maximum aspect ratio (channel length over diameter) of 12.5:1.

The AMCP proof of concept is successfully achieved with this improved AMCP architecture, in terms of a multiplication gain that reaches about 45 for the aspect ratio of 12.5:1 and a bias voltage of 500 V, with significant room for improvement. Analysis of the electron multiplication versus the aspect ratio shows that a gain similar to that of conventional MCPs is achievable, if similar aspect ratios are compared. Additionally, the first attempt to enhance the secondary electron emission coefficient by depositing a 5-nm-thick alumina (Al_2O_3) layer on the channel surface almost doubles the gain, which reaches almost 80.

These results clearly demonstrate the potential of this novel fabrication process of MCPs. Thanks to the acquired knowledge in mastering the deposition of a-Si:H layers thicker than 100 μm , an aspect ratio of 20:1 is within immediate reach and more than 25:1 seems technologically possible. In conclusion, the state-of-the-art AMCP reached in this thesis paves the way to the first real application in the very near future.

The TFA detectors are characterized, in this thesis, in terms of spatial resolution when tracking the electron beam of a scanning electron microscope. This study is done by sweeping the electron beam over specific regions of the a-Si:H sensing diode, beneath which ASIC pads are patterned in micrometric strips. The more efficient charge collection when the beam is over, rather than between, the microstrips produces a modulation of the induced signal. This modulation enables the resolution of 0.6- μm -wide strips, which are spaced by 1.4 μm and beneath a-Si:H diodes of 5, 10 and 20 μm in thickness. This notable result is achieved by the negligible lateral spreading of the generated charge packet, almost 1 μm wide, due to the very low carrier diffusion lengths of a-Si:H and the large electric field across the sensing diode. Consequently, the TFA detectors differ from crystalline silicon microstrip detectors, in which the longer diffusion lengths play a role in the charge-sharing mechanism used for beam positioning.

Despite the insensitivity of a-Si:H to displacement damages, a severe degradation of the a-Si:H electronic properties is attributed to the ionizing radiation released by the electron beam. The dynamic of this degradation is shown to correspond to the creation of additional defects, which act as recombination centers and deteriorate the induced signal. Nevertheless, it is demonstrated that these radiation-induced defects are metastable and can be removed with an annealing cycle to 130 °C for a few tens of hours.

In conclusion, the high a-Si:H radiation resistance and the high spatial resolution make of the TFA detector a promising candidate for beam hodoscope applications.

Key words:

amorphous silicon, microchannel plates, monolithic integration, secondary electrons, secondary emissive layer, electron multiplication, charge replenishment, vacuum detector, thin film on ASIC, TFA detector, solid-state detector, plasma-enhanced chemical vapor deposition, microcrystalline silicon, dangling bonds.

Contents

Acknowledgements	vii
Abstract (Italiano/English)	ix
1 Introduction	1
1.1 Aim and outline of the thesis	2
1.2 Contribution of this work to the research field	4
2 Solid-state and vacuum-based particle detectors	6
2.1 Solid-state particle detectors	6
2.1.1 Solid-state photodetectors	6
2.1.2 Solid-state detectors as particle trackers in high-energy physics	7
2.1.3 TFA imagers and TFA particle detectors	10
2.2 Vacuum-based particle detectors	11
2.2.1 Microchannel plates	13
3 Hydrogenated amorphous silicon: Growth, properties and applications	15
3.1 Introduction	15
3.2 a-Si:H deposition by PE-CVD	16
3.3 The a-Si:H atomic structure	18
3.3.1 Band tails	18
3.3.2 Midgap states	19
3.4 a-Si:H metastability	21
3.5 Electronic transport in a-Si:H	22
3.5.1 Thermally-activated electrical conductivity	23
3.5.2 Drift mobility in a-Si:H	25
3.5.3 Doping of a-Si:H	26
3.5.4 Conduction at the a-Si:H surface	27
3.6 Trapping and recombination	28
3.7 Photoconductivity in a-Si:H	29
3.8 Secondary electron emission of a-Si:H	31
3.9 Summary	33

4	Detection of electron beams with TFA detectors	34
4.1	Motivation and prior art	34
4.2	The TFA particle detector	35
4.2.1	The a-Si:H sensing diode	36
4.2.2	The front-end readout ASIC	37
4.3	Description of tested TFA pixels	38
4.4	Microvoids and hillocks in a-Si:H	41
4.5	Electric field in a-Si:H diodes	42
4.5.1	Signal formation in microstrip pixels	44
4.6	Electron beam interaction in a-Si:H	46
4.7	Setup for EBIC measurements	48
4.8	Results	50
4.8.1	EBIC maps and line scans	50
4.8.2	Lateral charge collection	55
4.9	Discussion and Outlook	59
4.10	Conclusion	60
5	Electron-beam-induced degradation of hydrogenated amorphous silicon	62
5.1	Motivation and prior art	62
5.1.1	a-Si:H degradation under photon and electron beams	63
5.2	Degradation during EBIC measurements	64
5.3	Test plan of the a-Si:H degradation study	65
5.4	EBIC measurements	67
5.5	Hecht's function and evaluation of mobility-lifetime product	68
5.5.1	I-V characteristics with an illumination at 655 nm	68
5.5.2	Hecht's fitting of the I-V characteristics	69
5.5.3	Mobility-lifetime results	70
5.6	FTPS measurements to determine the absolute defect density	71
5.7	ASA and CASINO simulations of the defect generation profile	73
5.7.1	Parameters for ASA simulations of the I-V characteristics	73
5.7.2	Comparison of ASA simulations with experimental I-V characteristics	74
5.8	Conclusion	76
6	Fabrication of amorphous-silicon-based microchannel plates	78
6.1	Motivation and prior art	78
6.2	First generation of AMCPs	80
6.2.1	Fabrication process of 1 st -gen AMCPs	80
6.2.2	Fabrication problems of 1 st -gen AMCPs	85
6.3	Second generation of AMCPs	87
6.3.1	Showerhead hole traces in 2 nd -gen AMCPs	89
6.4	Third generation of AMCPs	90
6.4.1	3 rd -gen AMCP architecture	90
6.4.2	Resolution of 2 nd -gen fabrication problems	94

6.5	Outlook	99
6.6	Conclusion	99
7	Electrical characterization of AMCPs	101
7.1	Motivation	101
7.2	Overview of 3 rd -gen AMCPs	102
7.3	Dark conductivity measurements of AMCP layers	103
7.4	Current-to-voltage characteristics of the AMCP layer stacks	104
7.4.1	Electrical conduction through the multiplying stack	104
7.4.2	Electrical conduction through the decoupling stack	107
7.5	Residual leakage current on the anode for 3 rd -gen AMCPs	112
7.6	Conclusion	113
8	Electron multiplication in AMCPs: Dynamics and results	115
8.1	Introduction	115
8.2	Preliminary tests with the three AMCP generations	116
8.2.1	EBIC measurements of 1 st -gen AMCP	117
8.2.2	UV setup and preliminary measurements	120
8.2.3	Measurements of 3 rd -gen AMCPs with UV setup, without photocathode	126
8.3	Quantification of the electron multiplication with the UV setup	127
8.3.1	Gain results with photocathode: AMCP proof of concept	128
8.3.2	Eberhardt's model and comparison with conventional MCPs	130
8.3.3	Effect of the long channel surface exposure to the impinging electrons	132
8.4	Quantification of the electron multiplication with the SEM	134
8.4.1	Testing conditions with the electron beam	135
8.4.2	Electron multiplication dynamics with the SEM electron beam	136
8.4.3	AMCP gain results obtained with the SEM beam	140
8.5	Discussion and Outlook	146
8.5.1	Corrective actions for the gain variations over time	146
8.5.2	Estimation of the maximum gain with an AMCP aspect ratio of 12:1	146
8.5.3	Pulse testing mode	146
8.5.4	AMCP possible applications	147
8.6	Conclusion	148
9	Conclusions and perspectives	150
9.1	Summary of the key results	151
9.1.1	Fabrication of amorphous-silicon-based microchannel plates	151
9.1.2	AMCP electrical characterization and electron multiplication	152
9.1.3	Evaluation of the TFA spatial resolution when tracking the SEM beam	153
9.1.4	a-Si:H degradation induced by the exposure to the SEM beam	153
9.2	Perspectives	154
9.2.1	Future AMCP development	154
9.2.2	Future AMCP applications	155

Contents

9.2.3 Future TFA development and applications 155

Bibliography 157

Curriculum Vitae 180

1 Introduction

One peculiarity of mankind is our curiosity for the world surrounding us. The fact that this curiosity does not vanish when the age of majority is reached, different from any other animal, contributed to make us the most “successful” living creatures on planet Earth. The ancient Egyptians and Mesopotamians were already so advanced in mathematics, geometry and material science that they built monumental structures for their time. Let us just think about the pyramids of the Giza Necropolis, which have lasted for thousands of years and today are still the object of theories about their construction. Later, the ancient Greeks reached levels of knowledge about astronomy, mathematics, physics, medicine, philosophy, art, architecture and literature that could not be matched again for hundreds of years.

In the last century, mankind has witnessed another big thrust towards a better understanding of our world and a better quality of life. In physics, Einstein’s relativity and quantum mechanics revolutionized the theories elaborated so far. A few phenomena like the photoelectric effect, which these new theories were able to describe, are also employed in this thesis. More recently, the standard model came to unify most of the fundamental interactions, initially the electromagnetic and the weak force, in the so-called electro-weak force. Eventually, the “grand unification” unified strong and electro-weak force. Additionally, it predicted particles that were successively discovered. Some of these particles are so exotic that they can be observed only indirectly, for instance by the detection of cosmic rays produced by the most energetic sources of the universe like black holes and quasars. Alternatively, particles can be accelerated and made to collide so as to access such high energies. Today, the most advanced particle accelerator is the Large Hadron Collider (LHC) at CERN, which is another good example of the human curiosity.

The LHC is the fifth-stage 27-km-long accelerator ring, which increases a proton’s energy from 450 GeV (obtained by the fourth-stage super proton synchrotron) to 7 TeV. At this energy, the proton’s mass at rest is increased by seven thousand times. When the protons are forced to collide, the energy available for producing some of the exotic particles predicted by the standard model is 14 TeV. Only two years ago, the Higgs boson breakthrough was announced as a reward for this immense technological effort.

Such cornerstone results are achieved by big experiments, which employ many types of detec-

tors, from solid-state to vacuum and gas detectors. There are four of these big experiments at the LHC: CMS (Compact Muon Solenoid), ATLAS (A Toroidal LHC Apparatus), LHCb (LHC beauty) and ALICE (A Large Ion Collider Experiment). The usual structure of these experiments is composed of four sections that are the tracking chamber, the electromagnetic calorimeter, the hadron calorimeter and the muon chamber. The tracking chamber measures the directions, momenta and signs of any charged particle. It is normally made of a pixel, a microstrip and a large-volume detector. **The thin-film-on-ASIC (TFA) detector, which was characterized in this thesis, was originally developed as a possible pixel detector for the tracking chamber.** The electromagnetic calorimeter fully absorbs all electrons and photons and generates a signal proportional to the initial particle energy. The hadron calorimeter measures the energies of heavier particles, like protons and neutrons. The particle interaction with the calorimeters produces also a type of radiation, called Cherenkov light, which can be detected by a **microchannel plate, the other detector technology researched in this thesis.**

Finally, the muon chamber, as its name suggests, measures muon momentum. This particle loses only 1 MeV per millimeter through steel or copper, so muons of 5 GeV penetrate up to 5 meters in steel and are the only ones to reach the muon chamber.

The TFA detector was developed as a possible candidate for the future upgrade of the LHC, namely the Super LHC (SLHC), in which the luminosity will be increased tenfold, to $10^{35} \text{ cm}^{-2}\text{s}^{-1}$. The driving goal for future detector candidates is to develop technologies that can withstand a fluence of 10^{16} cm^{-2} of 1 MeV neutrons and a total absorbed dose of 50 MGy. Most crystalline-silicon-based technologies are no longer operational after this dose, due to the displacement damages that deteriorate the electronic properties. This explains the investigation of alternative radiation-hard materials [Sellin 06], such as hydrogenated amorphous silicon (a-Si:H). The TFA detector is made of an a-Si:H sensing diode, which is monolithically integrated on an application-specific integrated circuit (ASIC). Due to its compactness, it is well suited for both tracking applications in high-energy physics (HEP) experiments and in medical imaging applications. A comprehensive description of its structure as well as the characterization performed in this thesis is provided in the next chapters.

The main objective of this thesis was the development of amorphous-silicon-based microchannel plates (AMCPs). The first AMCP prototype was invented and patented by Dr. Nicolas Wyrsh and Prof. Pierre Jarron [Jarron 11]. The aim is to realize a microchannel plate (MCP) that is monolithically integrated on an ASIC, similar to the a-Si:H sensing diode in TFA detectors. The targeted application was single photon detection for fast fluorescence imaging. Although this thesis did not reach this level of performance, it successfully provides the proof of concept of the technology.

1.1 Aim and outline of the thesis

The aim of this thesis was to improve the knowledge of, quantify the properties of and propose new designs for the two types of particle detectors mentioned above. The main objectives

were:

- To solve the structural problems of the first AMCP prototypes and possibly to modify their structure to improve the performances before the vertical integration on ASICs;
- To characterize the AMCP performances as electron multipliers and assess their potential for different types of applications;
- To measure the spatial resolution of TFA detectors when tracking an electron beam. These measurements were motivated by former promising results when detecting beta particles;
- To understand and possibly quantify the a-Si:H structural and electrical degradation when exposed to the particles typically detected by AMCPs and TFA detectors.

The thesis is structured as follows:

- Chapter 2 reviews a number of solid-state and vacuum detectors that are similar to the two types of detector researched in this thesis, in terms of either structure, or detection principle and performance.
- Chapter 3 presents an overview of a-Si:H in terms of deposition technology, as well as its structural, optical and electrical properties. Several explanations of the physical phenomena observed during the characterization of AMCPs and TFA detectors are addressed in this chapter.
- Chapter 4 presents the characterization of the TFA induced signal when tracking an electron beam of medium energy, i.e. tens of keV. The attainable TFA spatial resolution is evaluated and compared to crystalline silicon (c-Si) microstrip detectors. Simulations performed with the Monte Carlo software for electron interaction in solids, called CASINO, is used to support the measurement analysis.
- Chapter 5 is devoted to the investigation of the a-Si:H degradation upon exposure to electrons of the scanning electron microscope (SEM) beam. Such degradation induces the formation of dangling bonds, which correspond to midgap states (defects) and are detrimental for the electronic properties, since they act as recombination centers. The a-Si:H metastability is confirmed with annealing cycles, which can restore the initial defect concentration. Additionally, simulations are performed to evaluate the defect evolution during degradation and the recovery after annealing.
- Chapter 6 presents the work done to improve the first AMCP prototypes in terms of device architecture and resolution of structural defects. The benefits of the most important upgrade, which consists of the implementation of an intermediate electrode for the evacuation of the leakage current, is described. Additionally, a particular focus is spent on the corrective actions for reducing the a-Si:H intrinsic stress, which was particularly problematic due to the unconventional deposited thicknesses.

- Chapter 7 focuses on the electrical characterization of the upgraded AMCPs. The reduction of the leakage current on the anodes, which collect the multiplied electrons, after the implementation of the intermediate electrode, is presented. The current-to-voltage measurements provide insights about the working principle of this electron multiplier, vertically integrated on the readout anode.
- Chapter 8 concludes the AMCP development with the measurements of electron multiplication. The results provide the proof of concept for the technology. The gain dependence on a number of AMCP geometrical parameters and testing conditions are analyzed and provide important insights about the multiplication process in AMCPs. The gain enhancement achieved with the deposition of a secondary-electron emissive layer on the channel wall is also presented.
- Finally, the overall conclusions about the thesis contributions are summarized in Chapter 9 and the perspective for future developments and applications is discussed.

Please note that the chapters are rather self-consistent, which does not require their being read in the order they are presented in this manuscript. The only exceptions are Chapter 7 and Chapter 8, which are strongly correlated.

1.2 Contribution of this work to the research field

The main contributions of this thesis are

- The understanding and the resolution of a number of structural problems that affected former AMCP prototypes. This required the mastering of the plasma-enhanced chemical vapor deposition (PE-CVD) of a-Si:H at the exceptional rate of about 20 Å/s and the management of the intrinsic stress of a-Si:H layers as thick as 100 μm .
- The upgrade of the AMCP architecture with an additional intermediate electrode, for decoupling the measurements of electron multiplication from the leakage current evacuation. This enabled the device to evolve from a simple a-Si:H layer with channels micromachined throughout it, to effective electron multipliers with performances comparable with commercial MCPs, when similar aspect ratio are compared.
- The demonstration of the AMCP proof of concept in terms of electron multiplication. This was shown to increase with the bias voltage and the channel aspect ratio (length over diameter), as expected. The SE coefficient of a-Si:H was inferred from the gain dependence on the aspect ratio. The beneficial effect in terms of gain enhancement obtained by the deposition of a SE emissive layer on the channel wall are shown to be in line with one major research trend for MCPs.
- The evaluation of the TFA spatial resolution of about 1 μm , achieved when electrons of tens of keV are detected. Whilst previous results were obtained with the relatively low

fluxes typical of radioactive beta sources, here the electron beam of a scanning electron microscope, up to 350 pA, is tracked. The mechanism that enables such high resolution, with an a-Si:H diode as sensing element and a few ASIC metallizations patterned in micrometric-sized strips, is described. Finally, the comparison between this mechanism and the charge-sharing one of c-Si microstrip detectors is made.

- The dynamics of defect generation in a-Si:H, upon exposure to the SEM electron beam, is investigated. This dynamics is compared to the well-known light-induced degradation, which reduces the efficiency of a-Si:H solar cell. A few techniques for monitoring the formation of new defects before, during and after degradation are employed. Finally, the confirmation of the additional defects removal with annealing cycles evidences the a-Si:H suitability for detection applications in which large absorbed doses are involved.

In conclusion, this thesis provides two examples of the successful monolithic integration of a sensing element on specific substrates by the PE-CVD of a-Si:H. It evidences the a-Si:H potential for particle detection applications either by exploiting the generation of many electron-hole pairs in the sensing diode of the TFA detector or by sustaining large bias voltages and replenishing electrons along the channel surface of AMCPs, in which the detection occurs by means of the electron multiplication inside a continuous-dynode structure.

The work led to three first-authored [Franco 12a, Franco 12b, Franco 14] and two co-authored [Wyrsh 11, Wyrsh 14] publications.

2 Solid-state and vacuum-based particle detectors

In this chapter, we provide a brief overview about some solid-state and vacuum-based detectors that are similar to the two types of detector researched in this thesis, in terms of either structure, or detection principle and performance.

2.1 Solid-state particle detectors

Solid-state detectors feature a semiconductor, usually crystalline silicon (c-Si), in the sensing element. The detection is achieved by exploiting the ionizing energy of the impinging high-energy particle to produce many electron-hole pairs. If the impinging particle has rest mass, like an electron or a proton, it gradually transfers its energy with inelastic collisions. Alternatively, if the particle is a photon, it transfers all its energy at the first collision (besides the inelastic Compton scattering), for instance to an electron (photoelectric effect), which, in turn, releases its energy as just explained.

An electric field across the whole sensing element, set by an external bias voltage, enables the collection of the generated electron-hole pairs. In some detectors, the electric field is enhanced beyond that required for full collection so that it induces an avalanche process by impact ionization of the generated electron-hole pairs.

A brief overview of the main detector technologies for photon detection and particle tracking in high energy physics (HEP) experiments is provided below. Many of the mentioned applications are related to the big experiments at the Large Hadron Collider (LHC) of CERN: ATLAS, CMS, Alice, LHCb.

2.1.1 Solid-state photodetectors

The solid-state photodetectors for low photon intensities (down to one photon) include the widely known photodiode, which is made of a p-n junction in its simplest configuration, whereas it has a more complex architecture when operated in avalanche and Geiger mode. Avalanche photodiodes (APD) provide an amplification factor, namely a gain, between 50

and 200, while retaining proportionality with the energy deposited by the impinging particles [Farrell 91]. The quantum efficiency is about 80%, the equivalent noise factor can be as low as a few electrons and they are faster than photodiodes (in the nanosecond range). When operated in Geiger mode, the electric field is so intense that it produces an avalanche, which is no longer proportional to the photon intensity and is only limited by a quenching resistor. These photodetectors are, for instance, the silicon photomultipliers (SiPM) [Renker 06] and have excellent photon-counting capabilities, with gains of 10^5 – 10^6 . Another Geiger-mode avalanche photodiode is the single-photon avalanche photodiode (SPAD) [Charbon 14]. The photodiode operated in Geiger mode have a temporal resolution almost comparable with the best vacuum-based detectors, although they are biased at much lower bias voltages. They are compact and robust, insensitive to magnetic field and less expensive to manufacture than photomultiplier tubes (PMT). One of their main limitations is the dark count rate, which can be reduced by working below room temperature and by improving the fabrication process so as to minimize the crystal impurities and defects. They also suffer from optical crosstalk, when a photon is emitted during an avalanche and is detected by a neighboring pixel, and afterpulse, when trapped charges trigger a second avalanche. Finally, their recovery time can go up to hundreds of nanoseconds depending on the photodiode capacity and the quenching resistor.

The solid-state photodiodes for imaging applications include also the charge-couple devices (CCDs) [De Ruijter 95]. They are based on the metal-oxide-semiconductor (MOS) technology and their key strengths are detection efficiency up to 90%, a low detection limit, wide dynamic range and broad spectral response. Filters can be adopted for providing sensitivity to colors. Their applications are very broad: from fluorescence imaging [Hoshino 07] to cameras for electron microscopes, near-infrared thermography [Teyssieux 07] and imagers with high spatial resolution for optical measurements [Seitz 95].

Imagers are also based on the complementary metal-oxide-semiconductor (CMOS) technology [Bigas 06]. They are normally made of an array of photodiodes that are addressed by the CMOS electronics so that they are often called active pixel sensors (APS). Every pixel is made of the sensing element for most of its area, whilst the rest is devoted to the readout so that the active area (fill factor) can go up to 80–90%. They outperform CCDs with a lower power consumption and on-chip functionality, because they can feature amplifiers, analog-to-digital converters (ADCs) and color processing circuits in the same pixel. They also have a random access of image data, a high-speed imaging and limit blooming and smearing effects typical of CCDs. However, they are less sensitive than CCDs and they suffer from different sources of noise. APS can compete with CCDs for infrared imaging (low light intensity) and they are used in the automotive sector, for consumer electronics as well as in medical, space and x-ray imaging applications.

2.1.2 Solid-state detectors as particle trackers in high-energy physics

Most particle trackers of HEP experiments, which measure directions, momenta, and signs of the particles, are semiconductor devices. The closest ones to the beam line, where bunch of

particles are accelerated until they collide, are microstrip [Peisert 92] and hybrid pixel detectors [Wermes 05]. The former are largely used in vertex detectors for colliding experiments [Bingefors 93]. They consist in heavily doped micrometric-wide strips that are fabricated on a n-type c-Si wafer (figure 2.1(a)). The electron-hole pairs, generated by the ionizing energy, drift towards the strips, where they are collected. Although the charges drift according to the electric field set by the bias voltage, the diffusion plays also a role by widening the charge packet, which moves towards the electrodes. This normally produces a signal that is shared by two strips. This mechanism of charge sharing enables one to determine the trajectory of the ionizing particle. The bi-dimensional positioning can be achieved by a double-side microstrip detector, where the microstrips are rotated of 90° on the rear side (figure 2.1(b)).

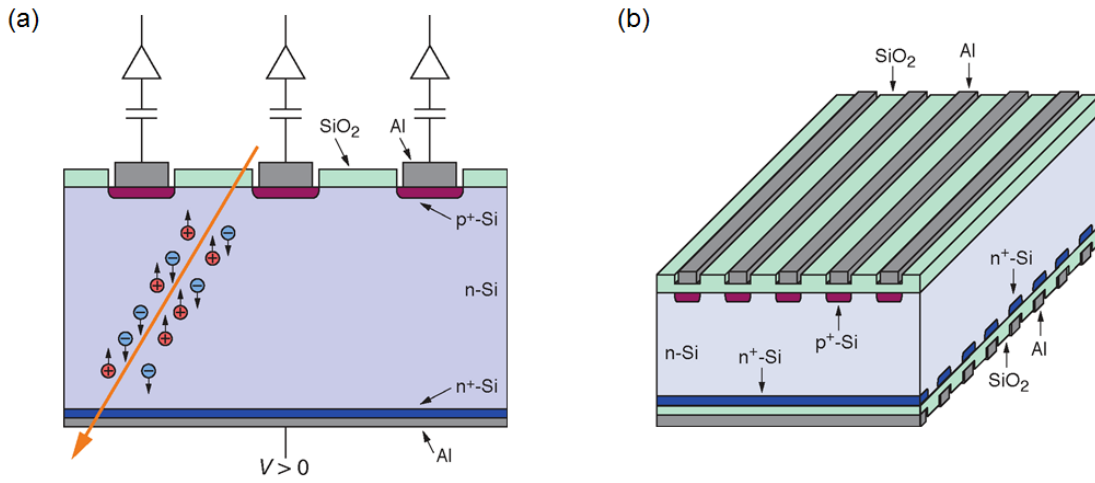


Figure 2.1: Cross-sectional artistic drawing of a single-side (a) and double-side (b) microstrip detector. The advanced architecture of (b) allows the bi-dimensional position encoding and is ac-coupled by means of the dielectric layer between the c-Si bulk and the metal strips.

The structure of a hybrid pixel detector is shown in figure 2.2(a). The pixels are normally made of a c-Si p-n junction, which is contacted on one side by one common thin metal layer and on the other side by many independent electrodes that define the pixels. These electrodes belong to the readout electronics and they have different shapes according to the application, like the $50 \times 400 \mu\text{m}$ rectangular ones employed in ATLAS [Grosse-Knetter 06]. The electrical connection between the sensing element and the readout electronics is achieved by the bump-bonding technique, as shown in figure 2.2(b). This technique has been facing more and more technological, cost and reliability issues as the requirements of future HEP experiments become more demanding.

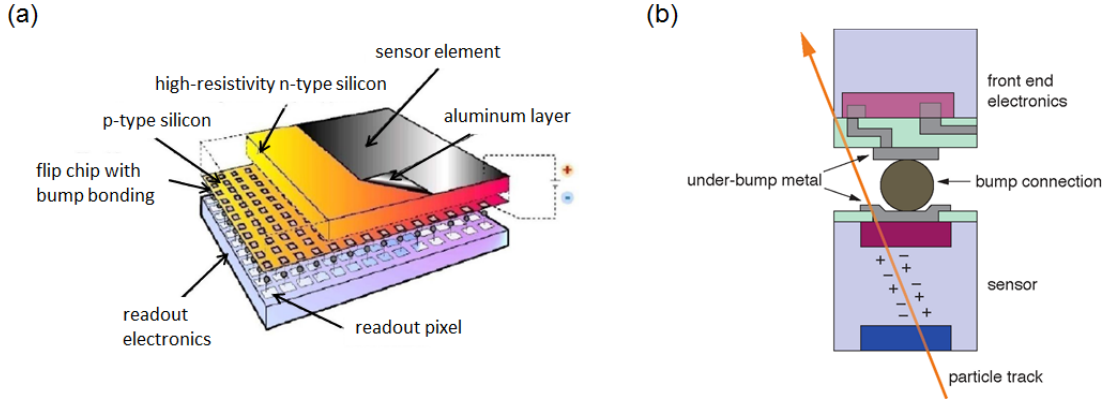


Figure 2.2: (a) artistic drawing of a c-Si hybrid pixel detector. (b) cross-sectional view of a pixel bonded to a front-end electronics by the bump-bonding technique [Rossi 03].

Recently, alternative detector technologies, which avoid the bump-bonding technique, have been proposed. One is the monolithic active pixel sensor (MAPS), shown in figure 2.3(a), which is based on the CMOS technology and has the sensing p-n junction vertically integrated on the readout electronics [Turchetta 01]. The MAPS features a lower noise than a pixel detector because the removal of the bump bonding decreases the parasitic capacitance.

Another example of advanced architecture is the 3D detector [Pellegrini 08], where heavily doped n-type and p-type columnar electrodes are fabricated throughout the more-resistive n-type c-Si (figure 2.3(b)). The electrode spacing ranges within 50–100 μm so that low depletion voltages (about 15 V for a 50 μm pitch) are required and collection times as short as 1 ns can be achieved [Kok 05]. Additionally, the 3D detectors are much more radiation hardened than conventional solid-state detectors because, due to their architecture, the charge generation is decoupled from the effects of the radiation damage.

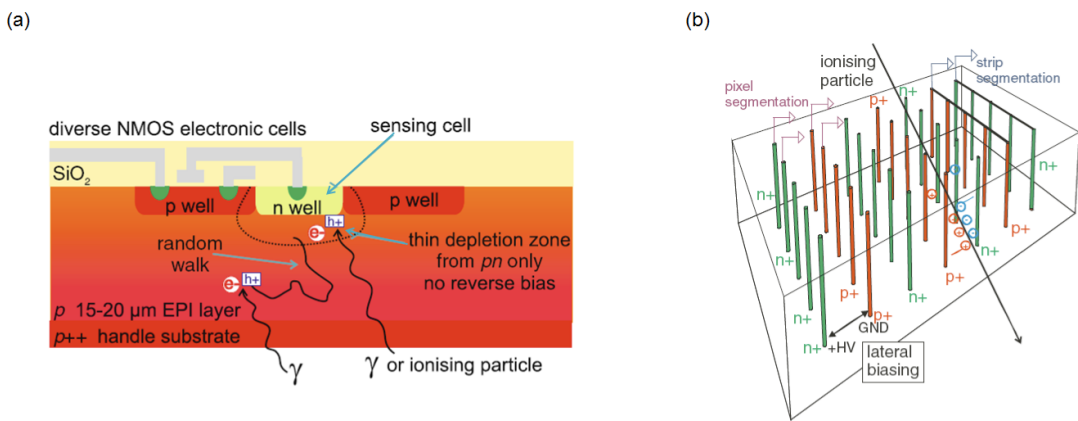


Figure 2.3: (a) artistic drawing of the MAPS, where the sensing element is vertically integrated on the CMOS readout electronics. (b) artistic drawing of a 3D detector with columnar electrodes throughout the sensing element.

2.1.3 TFA imagers and TFA particle detectors

The thin-film-on-ASIC (TFA) imagers were originally developed by Markus Böhm's group at the University of Siegen (Germany). Basically, it consists of an a-Si:H n-doped/intrinsic/p-doped (n-i-p) sensing diode, which is vertically integrated on a CMOS readout electronics, the application-specific integrated circuit (ASIC) [Lule 00]. The TFA combines the advantages of a CMOS imager, namely random access mode, individual pixel signal processing and easy implementation of extensive on-chip electronics (with the vertical integration). The latter enables a fill factor (percentage of device surface devoted to the sensing material) close to 100%. The TFA sensing diode has a high absorption coefficient in the visible range, with maximum response for green light. In addition, it can be sensitive to colors because the TFA's spectral response can be tuned with the bias voltage if three intrinsic layers (i-layers) are stacked one on another. The three i-layers have slightly different bandgap, thanks to the introduction of small quantities of either carbon or germanium, which extends the sensitivity to ultraviolet (UV) and infrared (IR) edges of the visible spectrum. As highlighted in figure 2.4, the n-layer is patterned together with the rear electrode for defining a number of independent pixels and preventing the lateral parasitic current among pixels (crosstalk). The ASIC beneath the sensing layer performs the signal processing with customized electronic architectures. At present, the TFA dynamic range is limited by the CMOS readout electronics to 70 dB, but by varying the integration time, accordingly to the brightness, the dynamic range can be enhanced to almost 120 dB.

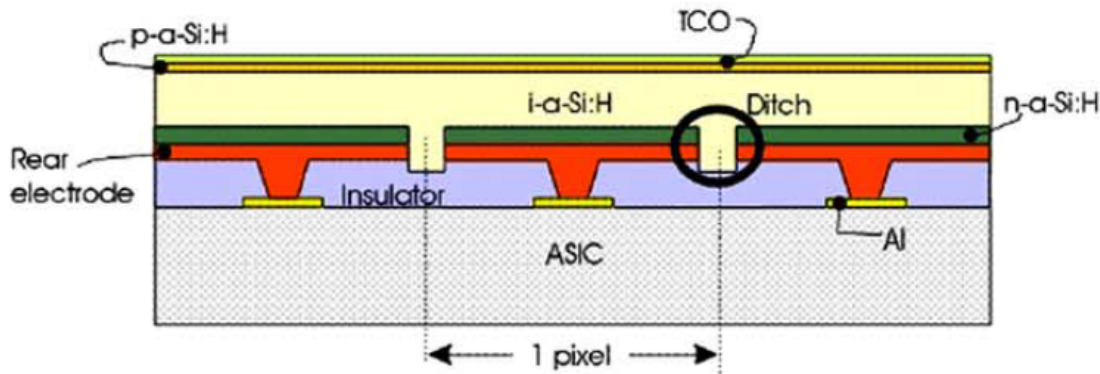


Figure 2.4: Artistic drawing of a TFA imager cross section.

The TFA for particle detectors employs a very similar architecture to TFA imagers. Many versions of the TFA detector have been realized in a former collaboration between CERN and the Photovoltaics and Thin-Film Electronics Laboratory (PV-Lab) of the Ecole Polytechnique Fédérale de Lausanne (EPFL). A remarkable contribution to this development was achieved in the framework of Dr. M. Despeisse's PhD thesis [Despeisse 06b]. A comprehensive description of the TFA detector characterized in this thesis is provided in Chapter 4.

Since the late 70's, the a-Si:H n-i-p diode was shown to be able to detect many different type of particles, like alpha and beta particles from radioactive isotopes, thermal neutrons, protons

of a few MeVs, x- and γ -rays [Perez-Mendez 86, Dubeau 91, Hong 95, Hordequin 01]. TFA detectors also succeeded in detecting different particle sources [Despeisse 08]. For instance, the signal induced by a pulsed laser at a wavelength of 660 nm was shown to be made of 15-ns-long electron plus a 1- μ s-long hole contribution. The detection of beta particles was achieved with a spatial resolution of a few micrometers. The detection of 5.9 keV x-rays, emitted from a ^{55}Fe radioactive source, pointed out the necessity of having an a-Si:H i-layer thicker than 15 μm to generate enough signal. Moreover, despite the good detection performances of 24 GeV protons and the TFA high radiation hardness for fluencies up to $2 \times 10^{16} \text{ cm}^{-2}$, the detection of single minimum ionizing particles (MIPs) could not be achieved. This was again due to the too thin a-Si:H diode because only 60 electron-hole pairs per micrometer are generated by one MIP [Perez-Mendez 88]. The problem here is that about 100 V are necessary to deplete an i-layer thicker than 10 μm . This voltage induces leakage currents that heavily affect the detector noise or exceeds the current limit acceptable by the readout electronics. Consequently, one on-going research activity of the PV-Lab is to develop more effective blocking contacts so as to reduce the leakage current [Wyrsh 05]. Despite the low sensitivity to MIPs, TFA detectors represent an attractive alternative to c-Si particle trackers [Sellin 06], due to their low sensitivity to displacement damages [Srouf 98, Kishimoto 98] and the high spatial resolution presented in this thesis.

2.2 Vacuum-based particle detectors

The vacuum-based detectors rely on the signal formation obtained by accelerating charged particles towards a series of targets, usually called dynodes, which are housed in a vacuum vessel [Iijima 11]. The most important detector of this category is the photomultiplier tube, whose first prototype was already fabricated in 1939 by Zworykin [Zworykin 39]. A schematic cross-sectional view of a typical modern photomultiplier is shown in figure 2.5(a). It consists of a vacuum vessel with an optical window on one end. The interior of the optical window is covered with a photocathode that converts the incoming photons into photoelectrons. The photoelectrons are focused by means of an electrostatic field towards the first dynode. This element is made of or coated with a material that enhances the emission of secondary electrons (SEs), when an electron of a certain energy impinges on its surface. These SEs are, in turn, electrostatically accelerated towards the second dynode, where other secondary electrons are emitted again. This process is repeated for all dynodes and generates a multiplication process, which grows exponentially to the number of discrete dynodes. Finally, the electrons are collected on the anode, which enables the photon detection. The photomultiplier tubes can also feature a segmented anode to improve the spatial resolution [Albrecht 02].

Photomultipliers are used in a large variety of domains like spectrophotometry, medical equipment, biotechnology, high-energy physics (HEP), oil well logging (exploration), environmental measurements to detect dust particles and aerosols, radiation monitors, industrial applications (like non-contact measurements of object thickness), aerospace applications and finally mass spectrometry and solid surface analysis. One fascinating application, in the HEP domain,

is the Super-Kamiokande experiment, shown in figure 2.5(b). This experiment was designed to detect both the proton decay and the neutrino, which is among the most elusive particles. The experiment was built 1 km underground, in a Kamioka mine. It consists of a tank filled with 50,000 tons of ultrapure water, which features 11200 photomultiplier tubes, 20 inches in diameter, installed on the top, the bottom and the side wall of the tank. The photomultipliers detect the Cherenkov radiation produced by the interaction of neutrinos with water. Solar neutrinos, generated by fusion reactions in the Sun, are detected at a rate of once every 9 days. Eventually, the detection of atmospheric neutrino oscillation proved that neutrinos have mass [Ashie 05].

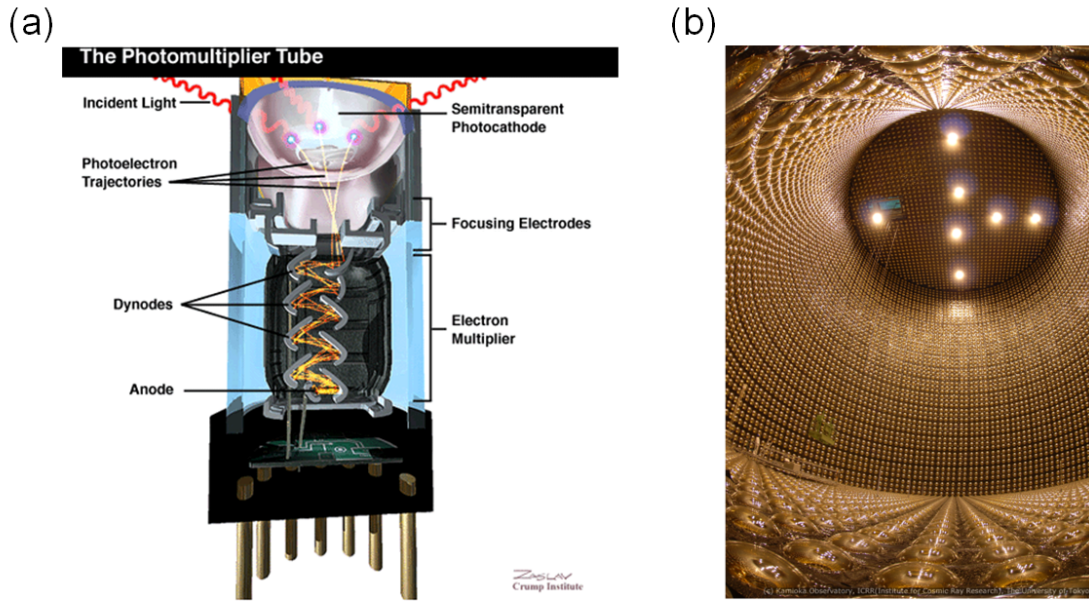


Figure 2.5: (a) artistic drawing of the cross-sectional view of a photomultiplier. (b) photograph of the Super-Kamiokande experiment with large-aperture photomultipliers.

A different type of vacuum-based detectors, which employ only one stage for the signal multiplication, includes the hybrid photon detectors (HPD) [Braem 02], shown in figure 2.6(a) and whose sensing element can be an avalanche photodiode (HAPD) [Nishida 09], the electron-bombarded charge coupled device (EBCCD) [Cianfarani 94], shown in figure 2.6(b), and the electron-bombarded CMOS (EBCMOS) [Barbier 09]. In these detectors, the photon is converted into a photoelectron with a photocathode at the detector entrance window. The photoelectron is eventually focused on the silicon detector, where the detection occurs as explained in Section 2.1.1. They combine the sensitivity of PMT with the spatial and energy resolution of solid-state detectors. The HPD has a large aperture and small number of pixels, whereas EBCCD and EBCMOS can have up to mega-pixel anodes, they are fast detectors and are employed for low-illumination imaging applications, such as night vision.

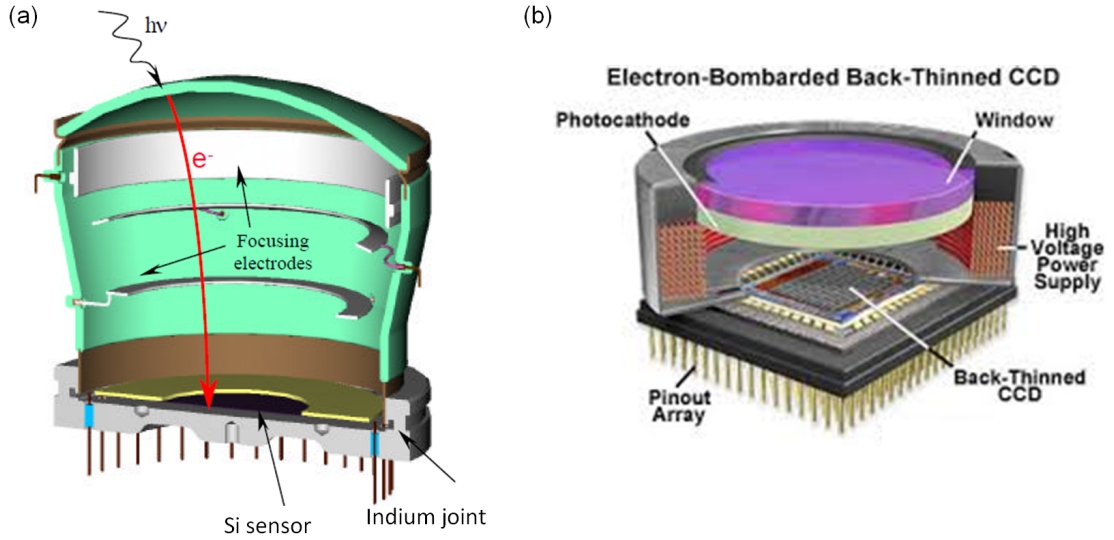


Figure 2.6: Artistic drawings of: (a) a hybrid photon detector and (b) an electron-bombarded CCD.

2.2.1 Microchannel plates

Microchannel plates (MCPs) [Wiza 79], as the name suggests, are thin discs that feature many channels that go throughout them, as shown in figure 2.7.

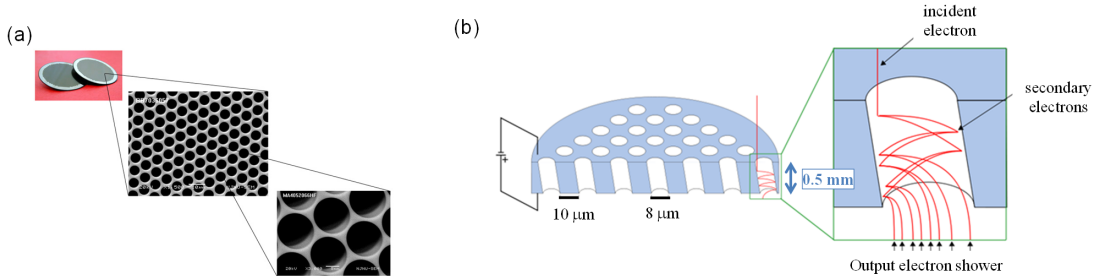


Figure 2.7: (a) photograph of a conventional lead-glass MCP with zoom on a few channels. (b) drawing of the microchannel plate with a bias voltage applied on one side of the plate with respect to the other grounded side.

The MCP working principle is similar to that of the photomultiplier tubes. The photoelectrons (or other particles) reach one side of the plate and enter in the channels. There, they drift according to an accelerating electric field towards the other channel end. During their movement, they experience multiple collisions against the channel wall. At each collision, a few secondary electrons are emitted, similarly to what happens with the discrete dynodes of the photomultiplier tubes. The advantage of the MCP is that, because of its many channels, the signal multiplication of about 10^4 is provided over areas as large as 10 cm^2 . MCPs are also intrinsically imaging devices (with suitable readout). MCPs are among the parti-

cle detectors with the highest temporal resolution in the order of a few tens of picoseconds [Fraser 90, Tremsin 06]. They are also radiation hardened so that they can be employed in high energy physics (HEP) applications, and are insensitive to magnetic fields up to a few teslas. The structure of conventional MCPs is made of lead glass. Since this material is too resistive for replenishing the secondary electrons emitted during the electron multiplication, a semi-conducting layer is grown on the channel surface by a high-temperature hydrogen reduction process (hydrogen firing). The replenishing current, usually called strip current, also sets the uniform electric field distribution inside the channels. Additionally, a SE emissive layer is implemented on the semiconducting one, normally by the channel wall oxidation with SiO_2 , to boost the electron multiplication.

Microchannel plates find applications in many different domains. They were originally developed for night vision goggles and astrophysics [Fraser 82, Siegmund 84]. In HEP, they are used, for instance, to detect Cherenkov radiation [Siegmund 11]. They are also employed in the experimental fusion reactors to diagnose the plasma properties [Kempenaars 08]. Other uses are in mass spectrometry [Barnes IV 04] and to observe rapid fluorescence phenomena of single molecule in biological processes [Michalet 07]. When they are not employed as electron multipliers, they work as x-rays collimators [Willingale 98].

There are a number of techniques to collect and encode the position of the electron cloud out from the microchannel plate. The first one is the wedge-and-trip anode [Lapington 87], which is based on the principle of charge division. The position coordinates are calculated from the ratios of the collected charges by independent anodes. The second one is the resistive anode [Lampton 08], similar to the previous one because the electron cloud position is calculated from the ratios of charges collected at the four edges of the anode. The third one is the cross delay line [Jelinsky 03], where the positioning is achieved by the difference in arrival time at either end of the line, according to the principle of the RC circuitry. The fourth one is the cross-strip (XS) anode [Siegmund 01], where a multilayer of metal and ceramic cross-strip pattern is realized on a ceramic substrate. Here, the electron cloud is divided into a number of orthogonal lines and its position is localized with a full width half maximum (FWHM) of $10\text{ }\mu\text{m}$. The arrival time can also be resolved with a FWHM of 100 ps. The gain required for the detection can be one order of magnitude smaller than the cross-delay line, which increases the counting rate capability. Another charge division readout with a FWHM of $10\text{ }\mu\text{m}$ is the Vernier anode [Lapington 02]. One of latest developments in readout technology is the capacitive division image readout [Lapington 13], where the charge is capacitively divided into the measurement anodes. Finally, Medipix2, a CMOS ASIC originally developed for x-ray imaging, has been employed to readout the charge cloud of a MCP [Vallerga 08].

3 Hydrogenated amorphous silicon: Growth, properties and applications

3.1 Introduction

This chapter provides an overview about the material used to realize the active element of both monolithic detectors studied in this thesis, namely hydrogenated amorphous silicon (a-Si:H). This material started to be successfully deposited in thin layers of acceptable electronic properties in the 70s' and ever since it experienced a tremendous growth in the range of applications. In order to give just few examples of applications, thin-film a-Si:H solar cells experienced an improvement in efficiency, for the conversion of sunlight to electricity, up to today's 10.1% as laboratory cell and to 9% as module. Thin-film transistors (TFTs) made of a-Si:H, are currently found in most flat panel displays such as liquid crystal displays (LCDs). The overall processed area of LCDs exceeded 400 km² in 2013. A third example is in the field of medical diagnosis with x-ray imagers. Such imagers usually feature an active matrix of a-Si:H photodiodes and a-Si:H TFTs. Finally, a-Si:H has been employed for the active layer of detector prototypes since the 80s'. Recently, a-Si:H has been classified as radiation-hardened material for its low sensitivity to displacement damages [Sellin 06], compared to its crystalline counterpart. However, a-Si:H has never significantly been employed in particle detectors for high-energy physics so far, mainly due to worse electronic properties compared to crystalline silicon (c-Si).

In the following sections, the main a-Si:H deposition technique is presented, followed by an overview about the material microscopic structure and the origin of localized states in the forbidden gap. Then, the metastability of a-Si:H defects is discussed, in terms of the formation and annealing of a particular type of localized states. The role of hydrogen in the material metastability is also mentioned. Successively, a comprehensive section is dedicated to the material conductivity and doping, as they constitute the background to understand the working principle of the monolithic detectors presented in this thesis. Finally, important aspects relevant to the specific applications of this thesis such as the secondary electron (SE) emission coefficient and the photoconductivity are overviewed.

3.2 a-Si:H deposition by PE-CVD

In the 50s', amorphous silicon was deposited for the first time by evaporation. The absence of hydrogen resulted in highly defective material, not usable for any electronic application, like photovoltaic devices or transistors. Eventually, a-Si:H layers started to be deposited by glow discharge [Sterling 65] of silane (SiH_4), the gas precursor used still today to produce the state-of-the-art a-Si:H devices. As explained in more details below, the role of hydrogen is to passivate a large amount of defects so that the electronic properties are largely improved. Soon afterwards, it was shown that a-Si:H could be doped [Spear 75, Spear 76] and, in 1976, the first p-i-n a-Si:H solar cells was realized with an efficiency of 2.4% [Carlson 77].

Nowadays, the most widely used method to deposit a-Si:H is plasma-enhanced chemical vapor deposition (PE-CVD), which is one expertise of the Photovoltaics and Thin-Film Electronics laboratory (PV-Lab), at EPFL. It is called chemical vapor deposition because it consists in the dissociation of gas-precursor molecules. The process is usually achieved by the application of a radio-frequency (RF) electrical field, between two capacitive-coupled parallel plates, which sustains the partial ionization of the gas precursors, i.e. a plasma. Indeed, the plasma enables to lower the process temperature so that the deposition can be achieved on different types of substrate, at approximately 200 °C. A few plasma examples for different gases are shown in figure 3.1.

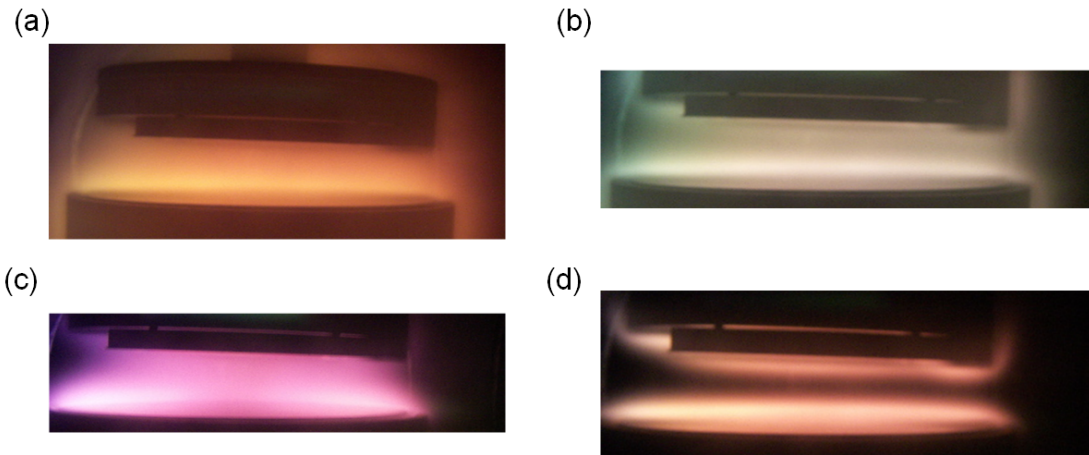


Figure 3.1: *Examples of plasmas used at PV-Lab: (a) an argon plasma, (b) a carbon-dioxide plasma, (c) a silane plasma and (d) a hydrogen plasma.*

The dissociation of SiH_4 molecules is the most important process for the a-Si:H deposition and an overview of the dissociation reactions are shown in figure 3.2. The SiH_x neutral species are very reactive and easily deposit on the substrate, where the film grows. There is also the possibility that the radicals grow—whilst suspended in the plasma—to high-order Si_mH_n species, until they form tiny particles, which can be both embedded in the growing film and deposited on the reactor wall and be pumped out [Fridman 96]. Their formation is favored at high-rate deposition regimes [Dorier 95, Watanabe 96] and, when embedded in the layer, these tiny particles are detrimental for the material electronic properties, so that they should

be avoided as much as possible.

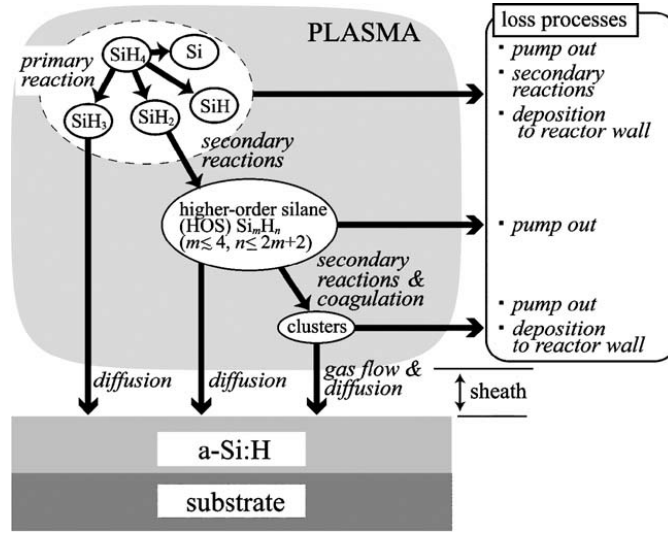


Figure 3.2: Model of silane molecules dissociation in primary-reaction as well as secondary-reaction species, which deposit on the substrate and make the film grow [Matsuda 04].

The sketch of a PE-CVD reactor as well as the photograph of the reactor used for the fabrication of both the Thin-Film-on-ASIC (TFA) detectors and amorphous-silicon-based microchannel plates (AMCPs) is shown in figure 3.3.

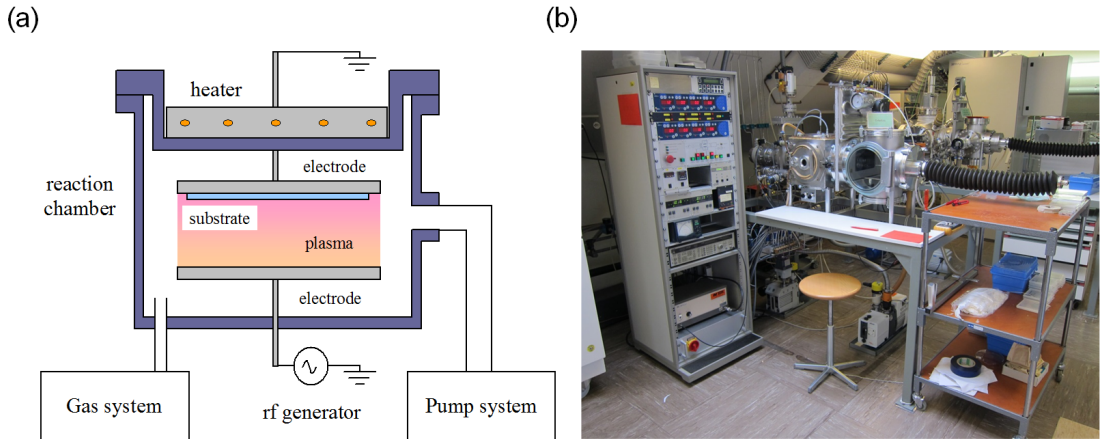


Figure 3.3: (a) sketch of a PE-CVD reactor with capacitive-coupled parallel plates, one with an applied RF electrical signal and the other grounded. (b) photograph of "System D", where "D" stands for "detector", employed for the AMCPs and TFA detectors fabrication.

The gas precursors are normally introduced into the plasma region through one plate, which features many tiny holes and is therefore called showerhead. This provides a uniform distribution of the gas precursors across the electrode area. The frequency of the RF signal can vary from 13.56 MHz (the standard one of industrial processes) to 110 MHz. For a-Si:H-based detectors, whose a-Si:H layers are as thick as 10–100 μm , the adopted frequency

of 70 MHz (known as very-high frequency, VHF PE-CVD) enables larger deposition rates [Schwarzenbach 96, Chabloz 96]. In conclusion, PE-CVD is the most frequently used technique for depositing a-Si:H for solar cells and TFTs. The process strengths are the deposition on large areas and the low costs. Today, the largest deposition surface can go up to 9 m² with the Applied Materials AKT Gen10 PE-CVD systems [Chae 07] and NEW ARISTO platform [Repmann 07].

3.3 The a-Si:H atomic structure

Hydrogenated amorphous silicon has an atomic structure that retains the organized configuration of crystalline silicon at short range (within the first-order neighboring atoms), whereas the crystallographic periodicity is gradually lost from the second-order neighboring atoms [Brodsky 70]. Generally, every atom is four-fold coordinated with other silicon atoms, although the bond length and angle is not fixed.

3.3.1 Band tails

The bond length and angle variability yields stretched and twisted Si-Si bonds, which, in turn, induce the formation of localized states in the band gap, near the extended states. These so-called band tails exponentially decrease in density towards the middle of the gap (as shown in figure 3.4). The tail characteristic energy, associated to the density drop by a factor of $1/e$, corresponds to $E_V^0 = 45\text{--}50\text{ meV}$ and $E_C^0 = 25\text{ meV}$ for valence and conduction band tails, respectively.

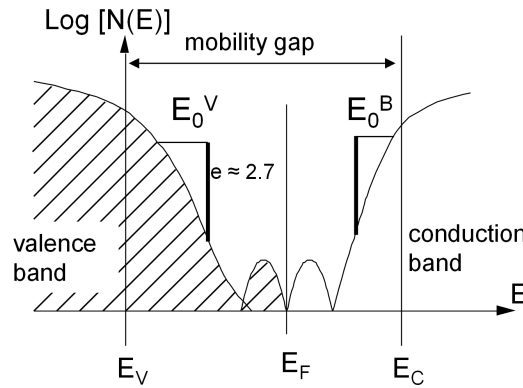


Figure 3.4: Qualitative representation of the density of states as a function of energy. The density drop above E_V and below E_C corresponds to the band tails. The two bumps near the Fermi energy (E_F) correspond to localized defects that are originated by broken Si-Si bonds, explained in Section 3.3.2.

The density of the band-tail states is about 10^{19} cm^{-3} , which is a quite considerable value if compared to the a-Si:H atomic density of $5 \times 10^{22}\text{ cm}^{-3}$. They have a large influence on the

optical and electronic properties. Concerning the optical ones, the band tails are responsible for the light absorption at energies below the band gap, in the range between 1.7 and 1.4 eV (as shown in figure 3.5). The exponential falloff of the absorption coefficient in this energy range is quantified by the Urbach's energy ($E_{0,U}$), which takes into account both band tail contributions, although the valence one is predominant. For electronic-grade a-Si:H, $E_{0,U}$ is about 50 meV. The light absorption enables the carrier transition from the valence extended states to the conduction band tail states and from the valence band tail states to the conduction extended states.

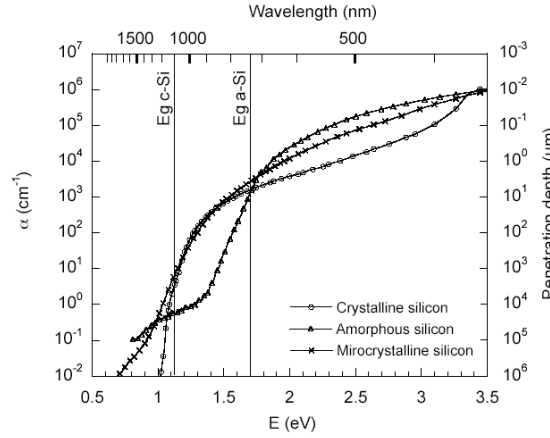


Figure 3.5: *Absorption coefficient for crystalline, microcrystalline and amorphous silicon.*

The band tails influence also the carrier mobility, especially the hole one, because of the larger density of valence band-tail states. Indeed, these states act as traps for carriers; the trapping efficiency is quantified by the factor $\theta_{p,n}$, defined as the ratio of free over trapped carriers. For holes, θ_p can be as small as 10^{-2} – 10^{-3} , whereas for electron is about 10^{-1} . This means that when carriers move through the material, they undergo multiple trapping and releasing processes, which reduces the band mobility, as further discussed in Section 3.5.

3.3.2 Midgap states

In a-Si:H, a number of Si-Si bonds are also broken, i.e. they are dangling bonds (DBs). It is important to point out that when we talk of defects in a-Si:H, we normally refer to the dangling bonds, if not stated otherwise. They generate additional localized states near midgap. The hydrogen presence during deposition (supplied by the hydrogen of SiH_4 and possibly by the addition of H_2 in the gas mixture) promotes the passivation of the DBs majority so that their density drops by 99.9% to 10^{15} cm^{-3} [Hata 92]. Hydrogen can either replace one missing silicon atom in the so-called mono-vacancy, as shown in figure 3.6(a), or two or three silicon atoms (di-vacancy and tri-vacancy), as shown in figure 3.6(b). By fitting the experimental data, the di-vacancy seems the most abundant ones [Smets 07]. The amount of hydrogen in a-Si:H can vary from 5 to 20% but the required amount to passivate most of dangling bonds is about 1%. This means that the residual hydrogen is concentrated in some regions with less

Chapter 3. Hydrogenated amorphous silicon: Growth, properties and applications

dense material, where microscopic voids are formed [Beyer 12]. These hydrogen reservoirs are deemed to actively participate in the material metastability, as presented in Section 3.4.

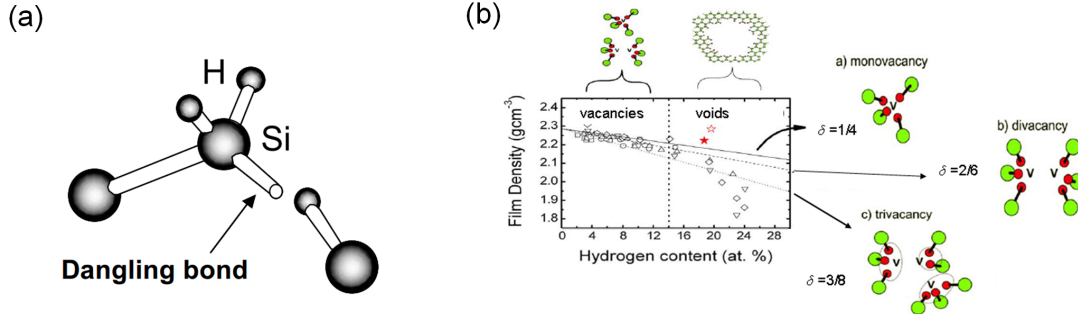


Figure 3.6: (a) drawing of a broken Si–Si bond, where one hydrogen atom eventually bonds to a silicon one [Matsuda 04]. (b) density of a-Si:H films versus hydrogen content [Smets 07]. The lines represent the regression curves for the different type of vacancies, which can be passivated by the hydrogen atoms. At a hydrogen concentration larger than 14%, microscopic voids with many hydrogen atoms start to appear.

From the optical point of view, the dangling bonds are responsible for the residual light absorption below 1.4 eV (figure 3.5). Their density can be measured by Photothermal Deflection Spectroscopy (PDS) [Jackson 82] and Constant Photocurrent Method (CPM) [Vaněček 95]. The localized states near midgap, induced by the DBs, act as recombination centers, rather than traps (like the band tail states), for the carriers. Indeed, once an electron is trapped near the middle of the band gap, the likelihood to eventually trap a hole and make the charges recombine is larger than the electron re-emission in the conduction band. Therefore, DBs are more detrimental to the electronic properties than the band tails because the charges are lost. DBs have an amphoteric behavior, meaning that they can be either neutrally charged (one trapped electron, D^0) or positively charged (no electrons, D^+) or negatively charged (two trapped electrons, D^-), as sketch in figure 3.7. The D^- state, with two trapped electrons, has an associated energy that is about 0.3 eV higher than that of the two other states, because of coulomb repulsion between the two electrons. This energy difference is called “correlation” or Hubbard energy (E_U). When the material is doped with acceptor states (e.g. boron doping), additional D^+ defects are created. Similarly, additional D^- defects are created with donor states (e.g. doping with O or P). The reason for it is explained in Section 3.5.3.

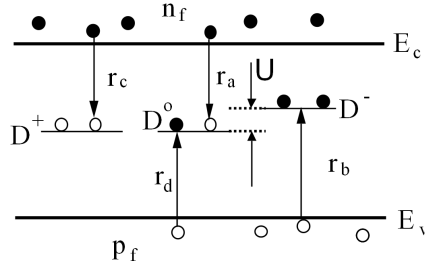


Figure 3.7: Schematic representation of the three electronic states for dangling bonds: without electrons (D^+), with one electron (D^0) and with two electrons (D^-). U is the “correlation” energy and r_a , r_b , r_c , r_d represent the four possible capture mechanisms.

3.4 a-Si:H metastability

The defect (dangling bond) density varies not only with the hydrogen concentration, but also with the material doping, the temperature and the exposure to light. At each temperature there is an optimum in the defect density, so that midgap defects can be generated and removed according to a reversible process, which corresponds to the a-Si:H metastability. The equilibrium corresponds to the minimization of the free energy of various states. The kinetics to reach the equilibrium is characterized by a relaxation time τ_R and it is associated to an energy barrier E_B , according to

$$\tau_R = \frac{1}{\omega_0} \exp\left(\frac{E_B}{kT}\right) \quad (3.1)$$

where ω_0 is a prefactor, in the order of 10^{-10} – 10^{-12} s. The energy barrier separates the ground state from another one (associated to a defect, for instance) at a higher energy U_d , which corresponds to its formation energy, as shown in figure 3.8(a). The variation of the dangling bond density versus temperature is shown in figure 3.8(b). First, the samples were rapidly quenched from 290 °C to room temperature to “freeze in” the equilibrium defect density at 290 °C (which is larger than that at lower temperatures). Eventually, the samples were annealed at different temperatures, so that energy was provided to the material for allowing the defect density to reach the new equilibrium. The larger the annealing temperature, the faster the new equilibrium is attained.

The “weak bond” model is the most accepted one to explain the a-Si:H metastability. This describes the band tail states as a pool of possible states that can be converted into dangling bonds, when the necessary energy is provided. The process is reversible because a dangling bond can be restored to a band tail state.

When a weak bond is broken, two spatially close dangling bonds should be generated, but this was never observed experimentally, with characterization techniques such as electron spin resonance (ESR) [Street 89]. The reason is that hydrogen passivates one of the two dangling bonds, which means that hydrogen plays an active role also in the defect metastability. The

energy to break or restore a weak bond can be provided by the temperature, the exposure to light and charged particles, like electrons. For instance, if the defect density is increased under light exposure, according to the well-known Staebler-Wronski effect [Staebler 77], a following annealing can restore the initial equilibrium density. In this thesis, annealing procedures were extensively employed to remove the additional defects induced by an exposure to electrons of a few keV.

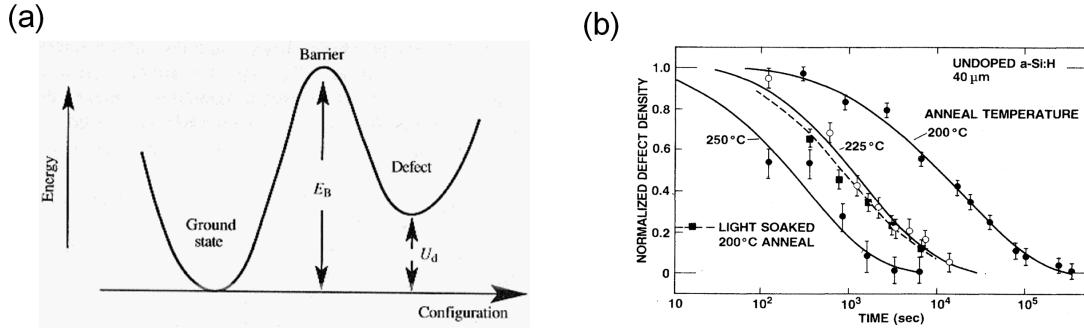


Figure 3.8: (a) schematic representation of a ground state and a state of higher energy (U_d), which can be associated to a defect, separated by an energy barrier E_B [Street 91]. (b) decay of the defect density during annealing at different temperatures [Street 89].

3.5 Electronic transport in a-Si:H

The electrical conductivity of a-Si:H was already studied in the early 70s' and a few important works revealed different behaviors at different temperature ranges [Brodsky 70, Le Comber 70, Le Comber 72]. The results of these studies are presented in Arrhenius' plot of figure 3.9, in which the logarithm of the conductivity is plotted as a function of the inverse of temperature. Eventually, it was discovered that the different behaviors corresponded to different conduction mechanisms that take place either in the extended states or within the localized states.

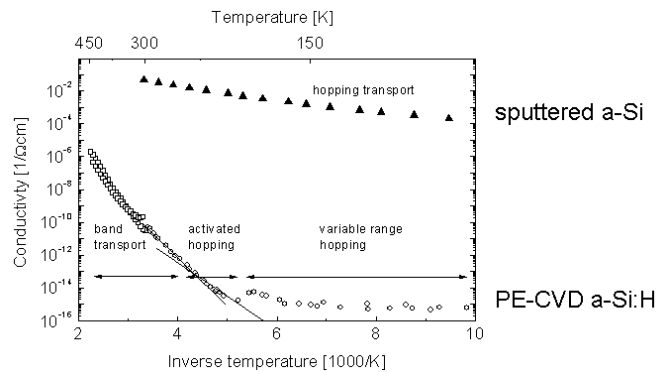


Figure 3.9: Conductivity versus the inverse of temperature, from Le Comber and Spears' [Le Comber 70]

The characteristics of each conduction mechanism, sketched in figure 3.10, are:

1. *Variable-range hopping* (figure 3.10, n.1). It occurs within midgap states. It consists in the carrier hopping between the two energetically closest states, regardless to their spatial proximity. The mechanism is dominant below 200 K for a-Si:H, whereas it occurs also at room temperature in sputtered amorphous silicon, without hydrogen, due to the large defect density of 10^{20} cm^{-3} .
2. *Nearest-neighbor hopping* (figure 3.10, n.2). This time the hopping takes place from one band-tail state to the spatially closest one, by means of tunneling. The hopping includes the emission or absorption of a phonon, which compensates for the difference in energy between initial and final state. Since the band-tail state density is as large as 10^{19} cm^{-3} , the conductivity strongly depends on temperature, as shown in figure 3.9 with the label “activated hopping”.
3. *Extended-state conduction* (figure 3.10, n.3). It corresponds to the conduction in the extended states and it is characterized by fluctuations in the carrier density due to trapping and release processes between the band-tail states and the extended ones. This is the main conduction mechanism in a-Si:H at room and higher temperatures.

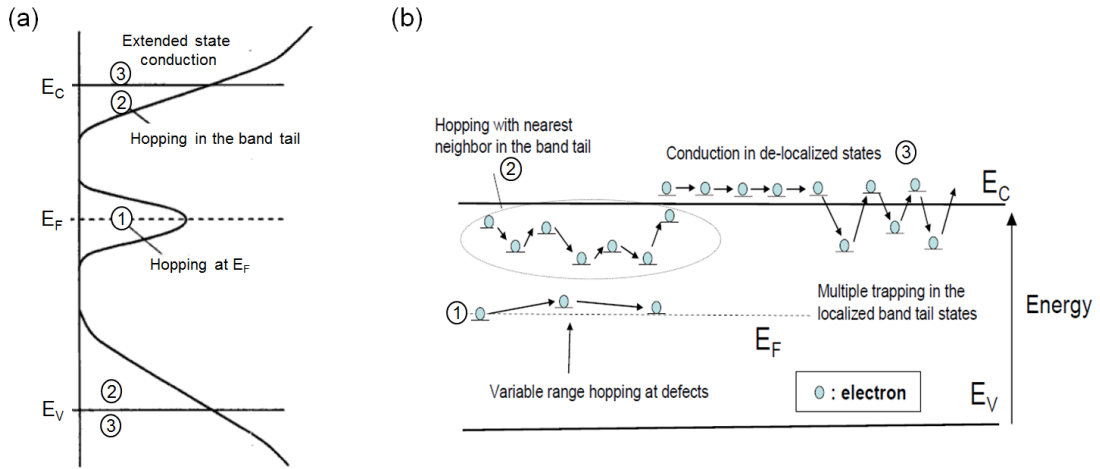


Figure 3.10: (a) energy position of the three electrical conduction mechanisms in a-Si:H, as explained in the text. (b) schematic representation of the dynamic of the conduction mechanisms: variable-range hopping (1), nearest-neighbor hopping (2) and extended-state conductivity (3). Courtesy of Dr M. Despeisse.

3.5.1 Thermally-activated electrical conductivity

Here, we describe in more details the a-Si:H electrical conduction in the extended states (figure 3.10, n.3), as this is dominant mechanism at room temperature and that concerns the working principle of the detectors presented in this thesis. As mentioned before, if the temperature

Table 3.1: Typical values of room-temperature conductivity and activation energy for intrinsic and doped a-Si:H and μ c-Si:H.

	T_{room} conductivity ($S \cdot cm^{-1}$)	Activation energy (eV)
<i> a-Si:H	$10^{-10} - 10^{-12}$	0.7 – 0.8
<i> μ c-Si:H	10^{-6}	0.5
<n> a-Si:H	$10^{-2} - 10^{-4}$	0.12 – 0.4
<n> μ c-Si:H	$1 - 10^{-2}$	0.03
<p> a-Si:H	$10^{-4} - 10^{-6}$	0.25 – 0.6
<p> μ c-Si:H	$10^{-1} - 10^{-3}$	0.05

3.5.2 Drift mobility in a-Si:H

The electrical conduction in a-Si:H, as well as the drift mobility, is influenced by a multiple charge trapping-and-release process, as mentioned before. Because of it, the conduction changes from a dispersive to a non-dispersive process, according to the temperature. For a better understanding of the difference between dispersive and non-dispersive transport, the drift mobility is defined as

$$\mu_D = \frac{\mu_0}{1 + f_{trap}} \quad (3.6)$$

where μ_0 is the band mobility, namely the theoretical mobility without any trapping and f_{trap} is the ratio of the time spent in traps over that spent in the extended states. If the temperature increases, f_{trap} decreases because the trapped carrier can be re-emitted in the extended state more easily. Time-of-flight experiments were employed to study the transition between dispersive and non-dispersive transport [Tiedje 81]: When the trapping time is much shorter than the measurement time frame, so that photocurrent signal drops sharply upon interruption of the carrier injection, the transport is defined as non-dispersive. For electrons, the transport becomes non-dispersive at 312 K, whereas for the holes it is still dispersive at room temperature and up to 500 K. The lower hole mobility can be addressed to the larger hole effective mass and the larger density of valence band-tail states.

Since the electron transport is non-dispersive at room temperature, the drift mobility is similar to the band mobility, with a value of approximately $1 \text{ cm}^2 \text{V}^{-1} \text{s}^{-1}$. On the contrary, the holes have a band mobility of $1\text{--}5 \text{ cm}^2 \text{V}^{-1} \text{s}^{-1}$, but only $3 \cdot 10^{-3}\text{--}0.1 \text{ cm}^2 \text{V}^{-1} \text{s}^{-1}$ as drift mobility [Takada 87]. It is interesting to point out that even the values of band mobility are much lower than the mobility of c-Si, because of the large amount of carrier scattering induced by the amorphous structure. The mobility band gap (E_μ), beyond which the transport is diffusive (non-dispersive), was measured to be 1.9 eV [Wronski 89], 0.16 eV larger than the Tauc (optical) gap ($\approx 1.73 \text{ eV}$). The reason for this discrepancy is that the band tails contribute to the optical absorption but make the transport dispersive, if the temperature is not high enough.

3.5.3 Doping of a-Si:H

The introduction of hydrogen in the deposition of a-Si:H allowed a drastic improvement of the material electronic properties as well as the doping efficiency [Spear 76]. The a-Si:H conductivity can be varied over several orders of magnitude by adding phosphine (PH_3) and diborane (B_2H_6) to the gas mixture of the PE-CVD process, as shown in figure 3.11(a). The activation energy is lowered from 0.7-0.8 eV for intrinsic material to 0.15 eV in case of n-doping (with phosphorous) and 0.3 eV in case of p-doping (with boron), as shown in figure 3.11(b). The reason why slightly p-doped material exhibits the lowest conductivity (rather than the undoped one) is because the non-intentionally doped a-Si:H is actually slightly n-doped due to the incorporation of impurities such as oxygen. The same behavior is observed in figure 3.11(b), where the largest activation energy is attained with a slight p-doping. Additionally, for high doping level, the activation energy does not reflect the exact position of the Fermi level (as measured from the band edge) due to the statistical shift [Wronski 77].

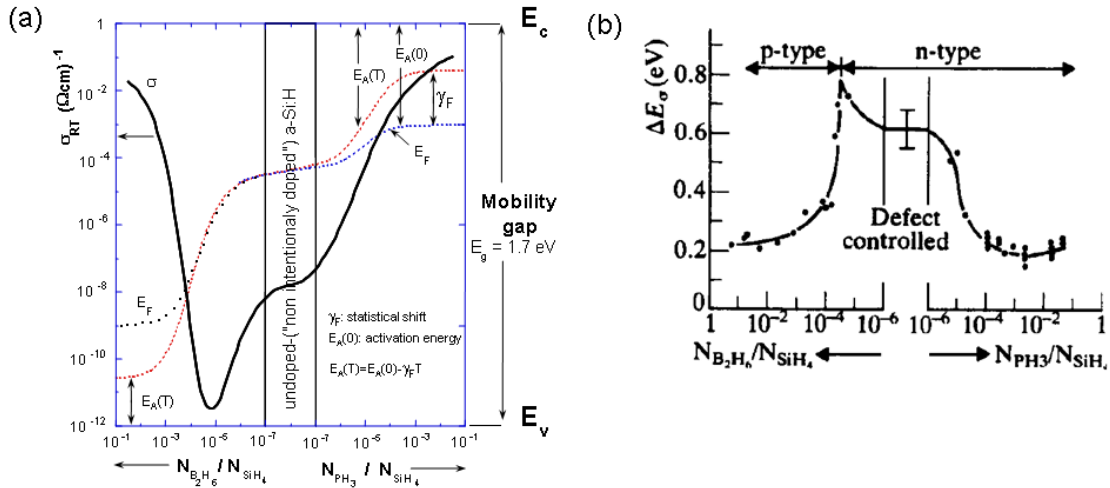


Figure 3.11: Effect of the doping on (a) the room conductivity and (b) the activation energy [Spear 76]. In (a), the effect of the statistical shift, for highly doped samples, is shown in terms of E_F variation between the blue and the red dotted lines.

Although a-Si:H conductivity can be varied by several orders of magnitude, the doping efficiency is not as good as in the c-Si. The conductivity varies sharply with a small doping but it rapidly saturates for a larger doping. The main reason is that the doping efficiency depends on the inverse square root of the doping concentration [Street 82, Stutzmann 87]. This is explained by the concept of substitutional doping, according to which also the defect density increases with the square root of the doping concentration so that all additional carriers provided by the doping are trapped in the localized states. The formation of additional dangling bonds is explained as a reversible reaction whereby a phosphorous atom in the amorphous silicon matrix can give away an electron and create a negative-charged dangling bond, according to reaction $\text{P}_5^0 + \text{Si}_4^0 \leftrightarrow \text{P}_4^+ + \text{D}^-$ and shown schematically in figure 3.12.

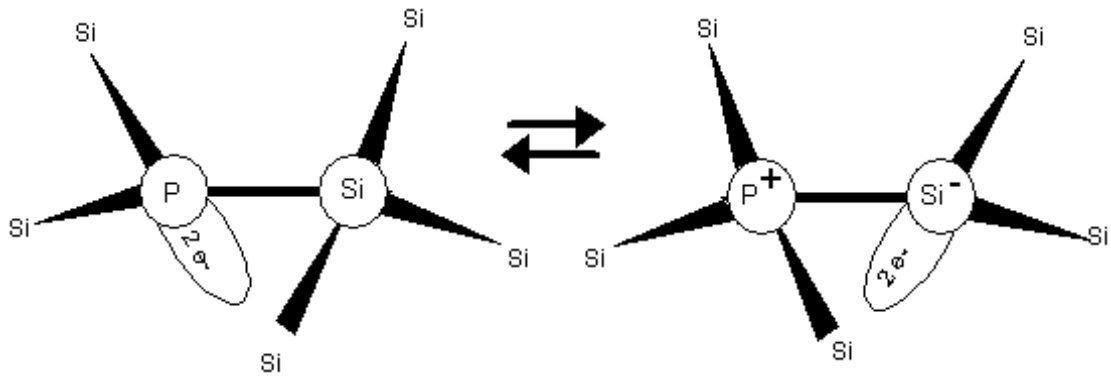


Figure 3.12: *schematic representation of the substitutional doping where a phosphor electron is transferred to make a negatively charged dangling bond.*

3.5.4 Conduction at the a-Si:H surface

Another important aspect of the a-Si:H electrical conductivity, especially for the AMCP application, concerns the surface. In general, the surface represents the disruption of the periodic atomic structure in crystalline materials, which may induce a great number of surface defects. This is also the case for a-Si:H with many additional dangling bonds and band-tail states [Winer 87]. Therefore, the surface is not only a preferential location for charge recombination, but also of carrier hopping and tunneling within the localized states. Another mechanism of enhanced conductivity on the surface can be induced by the band bending, which is caused by the absorption of atmosphere molecules like oxygen or water vapors. This promotes the electrons injection into the conduction band already at room temperature. Oxygen induces the a-Si:H surface to oxidize [Ponpon 82], down to a depth that increases with the square root of time [Pankove 84]. The oxidation was reported to increase the surface state density by about one order of magnitude [Winer 87], although the opposite effect occurs in c-Si. Additionally, the band bending is induced by the oxygen atoms that act as donors in a-Si:H and shift the Fermi level closer to the conduction band.

This phenomenon can be further amplified if the absorbed molecules are not simply oxygen but water vapors. Beside the n-type doping induced by oxygen, a positive charge accumulation by the electropositive hydrogen attracts and increases even more the electron accumulation on the surface (sketch in figure 3.13). The electrical conductivity can locally increase by a few orders of magnitude [Tanielian 82]. An annealing at temperatures above 100 °C, in vacuum, makes the trapped molecules to desorb and the conductivity is restored to that of the bulk.

In conclusion, special care has to be taken when one does an electrical characterization of a device with a large surface over volume ratio, like the AMCPs. Measurements have to be conducted with a residual pressure of at least 10^{-2} mbar and possibly after an annealing, like the one mentioned above, to desorb the water vapors from the channel wall.

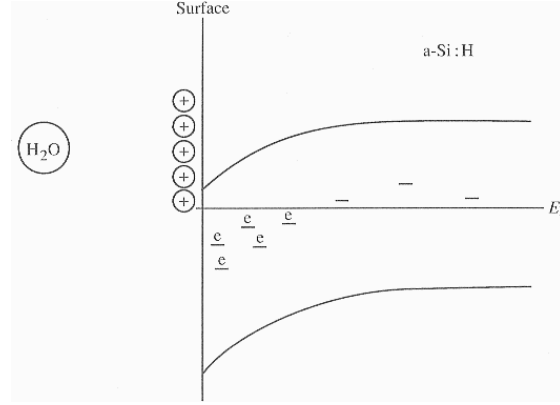


Figure 3.13: schematic representation of the band bending caused by absorption of water molecules on the a-Si:H surface. Oxygen acts as a donor in a-Si:H and the hydrogen of the water molecules induces an electron accumulation near the surface.

3.6 Trapping and recombination

Carrier recombination in a-Si:H occurs through one of three different channels, depending on the experimental conditions. These are represented in figure 3.14 and described below.

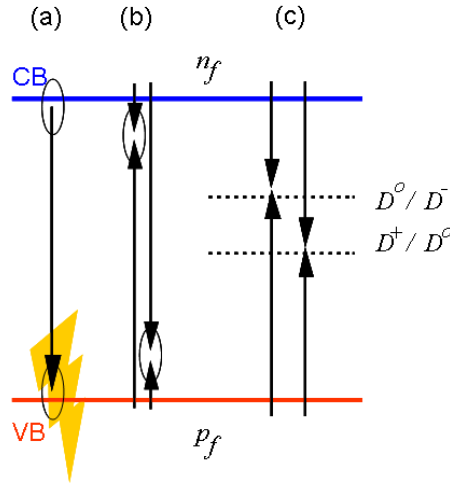


Figure 3.14: schematic view of the three possible channels for charge recombination in a-Si:H: (a) radiative recombination between band-tail states, (b) non-radiative recombination at a band-tail state and (c) recombination through midgap states.

1. Recombination with consecutive emission of a photon, i.e. a radiative recombination. It is the predominant mechanism below 200 K and the intensity of luminescence is larger at weak photo-excitation intensities and in low-defective samples ($< 10^{17} \text{ cm}^{-3}$).
2. Recombination within a band-tail state, but non-radiative even if the amount of released energy is similar to channel (a). It is not very effective because band-tail states are far

from midgap so that the process is energetically more demanding.

3. Recombination within midgap defects (dangling bonds). It is the main process at room temperature, energetically more favorable than channel (b).

The recombination can involve one, two and three carriers simultaneously depending on the doping concentration, the generation rate of photo-induced carriers and the proximity to a material discontinuity like the surface. These mechanisms are [Street 91]

1. “geminate” recombination, which occurs with a geminate pair, namely a bounded electron-hole pair. They do not contribute to a photo-induced conductivity enhancement (cf. Section 3.7) and recombine after a certain time. This recombination takes place at low temperatures (< 200 K), at which geminate pairs are created (rather than free electron-hole pairs, due to the insufficient thermal energy).
2. “Auger” recombination consists in the recombination of an electron-hole pair and the promotion of a third electron or hole in the extended state, thanks to the energy released by the recombination. It has a significant contribution only at a high injection or doping level. Although Auger recombination is limited in crystalline semiconductors by the energy and momentum conservation (which limits the density of final states to which the third particle can be excited), it can play a larger role in amorphous materials, where the conservation requirements are relaxed.
3. “mono-molecular” recombination, which occurs at midgap defects by means of the trapping of one charge and its following recombination with the complementary charge. This is the preferred recombination channel in a-Si:H when the dangling bond density is larger than 10^{16} cm^{-3} and the temperature is higher than 200 K. This process is further explained below and it is mainly non-radiative.
4. “bi-molecular” recombination, which occurs with direct recombination of charges between extended states. This makes the recombination dependent on the square of carrier density. It can be both radiative and non-radiative.

Finally, although the surface of a-Si:H entails an enhanced recombination due to a larger surface defect density, it does not influence electronic properties as much as in c-Si because the a-Si:H diffusion coefficients of 10^{-2} – $10^{-3} \text{ cm}^2 \text{ s}^{-1}$ for electrons and 10^{-3} – $10^{-4} \text{ cm}^2 \text{ s}^{-1}$ for holes [Gu 96] are much smaller than those of c-Si. Therefore, the influence of the surface on the material conduction plays a role only within 10–20 nm.

3.7 Photoconductivity in a-Si:H

Photoconductivity consists of an increase in conductivity upon illumination with photon energies large enough to produce electron-hole pairs that are free to move in the material.

Chapter 3. Hydrogenated amorphous silicon: Growth, properties and applications

This phenomenon was observed to play an important role in AMCPs, as presented in Chapter 8, so that an overview about it is provided here.

When an a-Si:H layer is evenly shined with visible light, its conductivity can increase up to five orders of magnitude [Wronski 81]. The magnitude of this phenomenon is much lower in c-Si because, while the amount of photogenerated carriers is about the same for the two materials, the c-Si dark conductivity is a few orders of magnitude larger than that of a-Si:H (at room temperature) so that the net enhancement is smaller. The overall conductivity is given by

$$\sigma_{tot} = \sigma_{dark} + \sigma_{photo} = \sigma_{dark} + e(\mu_n n_f + \mu_p p_f) = \sigma_{dark} + e(N\mu_n^d + P\mu_p^d) \quad (3.7)$$

where μ_n and μ_p are the electron and hole band mobilities, n_f and p_f are the free-electron and free-holes densities (in the extended states), N and P is the photogenerated electron and hole concentration, and μ_n^d and μ_p^d are the electron and hole drift mobilities. If the generation is homogeneous throughout the a-Si:H layer (3.7), it can be rewritten as

$$\sigma_{photo} = eG(\mu_n \tau_n^R + \mu_p \tau_p^R) \quad (3.8)$$

where G is the generation rate and τ_n^R and τ_p^R are the the electron and hole lifetimes before recombination. This is the phenomenon for steady-state photoconductivity and for the setup configuration shown in figure 3.15(a).

The carrier generation and recombination are the same and every carrier extracted at one contact is balanced with another one of the same sign (positive or negative) injected at the other side, so that charge neutrality is maintained. In such of a way, the electrical current in the layer is not limited by the slower carrier, namely the holes in a-Si:H, because for each electron collected on one side, another electron is injected from the other side so that there is not a hole accumulation. This results in a current, flowing in the external circuit, which is up to five orders of magnitude larger than the generation rate.

A different scenario occurs when there are blocking contacts (figure 3.15(b)), like in the case of a photovoltaic device. Here, the current measured in the external circuit (sometimes called “primary photoconductivity”) is, in the ideal case, equal to the generation rate times the generation volume, and, more realistically, given by

$$I_{ph} = G \cdot \eta_G \cdot \eta_C \quad (3.9)$$

where η_G is the quantum efficiency, namely the efficiency of one photon to produce an electron-hole pair and η_C is the charge collection efficiency, namely how many electron-hole pairs are collected prior to their recombination. An η_C of 1 is achieved for a maximum thickness of the a-Si:H main layer of 1 μm and with a potential difference across the diode of 1 V, for state-of-the-art a-Si:H solar cells.

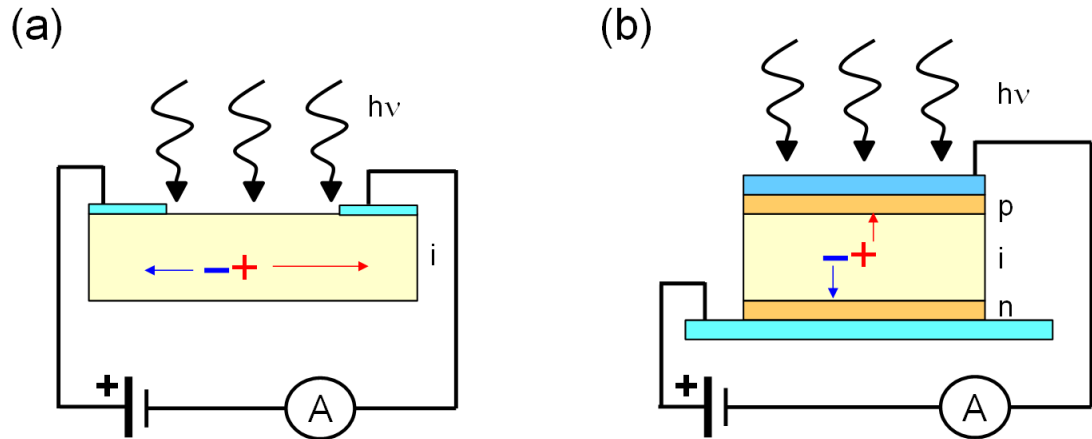


Figure 3.15: (a) configuration of a photoconductor device, which exhibits a photocurrent signal a great deal larger than the generation rate (especially for a-Si:H). (b) configuration of a photovoltaic device with blocking contacts, which exhibits a photocurrent signal never larger than the generation rate.

3.8 Secondary electron emission of a-Si:H

When an electron impinges on the surface of a material, there is a certain probability that one or more electrons are emitted from that surface. They are called secondary electrons (SEs) because they are the products of the interaction between the impinging particle and the material. The secondary electron emission (SEE) was discovered in 1902 [Austin 02] and comprehensive studies were published already in the 40s' [Wooldridge 39, Bruining 54]. The SEE coefficient—i.e. the ratio of emitted SEs per impinging particle—started to be systematically measured for different metals in the 50s' [Baroody 50]. It was shown that a higher work function corresponded to a higher SEE coefficient, ranging within 0.8–1.6. Shortly afterwards, metal compounds, among which many insulators, were measured to feature much larger SEE coefficient [Bruining 54]. The highest values of 5–7 were obtained with alkali compounds, like LiF, NaF, NaCl, CsCl, KI to mention a few. The reason for this larger SEE coefficient was clarified only few decades later [Shih 97] and consisted in the fact that the energy-loss processes are less effective in wide-bandgap materials, resulting in SEs larger escape depths and coefficients. The SEE process can be divided in three steps: the particle penetration inside of the material, the electron promotion to the conduction band, where their free movement depends on the mobility, the lifetime and the crystallinity of the material. The electrons that reach the surface can be emitted as SEs, if they are provided with an energy larger than the material electron affinity (E_A). Only the second step, namely the SEs production, is affected by the material work function, which explains the weak dependency on it and the large SEE coefficients for insulators.

The SEE depends on many parameters: the particle energy and the impinging angle, the energy loss rate into the material, the work function, the temperature and the escape depth of SEs. First, the SEE coefficient has a maximum as a function of the electron energy between

Chapter 3. Hydrogenated amorphous silicon: Growth, properties and applications

100–800 eV for individual elements [Baroody 50] (diamond SE emission maximum can be at much higher energy than 800 eV [Lapington 09]) and between 300–1800 eV for compounds [Seiler 83]. Second, it grows with decreasing grazing angle. This is explained by the fact that a grazing angle corresponds to a larger amount of energy deposited at a shallower depth so that a larger number of SEs can escape prior to being absorbed. A number of equations have been proposed for quantifying the dependency on the angle of incidence, among which the following one [Bronshtein 68]:

$$\delta(\theta) = \delta_0 (\cos\theta)^{-n} \quad (3.10)$$

where δ is the SEE coefficient, δ_0 is that for normal incidence, n is a factor of about 1.3 for light elements ($Z < 30$), it decreases to 1 for $Z=30$ and stabilizes to 0.8 for heavier elements [Kanaya 72]. The SE escape probability decreases exponentially with depth; the mean escape depth is 0.5–1.5 nm for metals and 10–20 nm for insulators [Seiler 83]. The energy distribution of SEs is peaked at about 2.5 eV for metals with a maximum at about 50 eV.

As far as a-Si:H is concerned, a few sets of data about the SEE coefficient were found in the literature [Joy 95, Schade 79, Mulhollan 10]. The data set obtained with bare a-Si:H is shown in figure 3.16. The maximum SEE coefficient does not appear for primary electron energy as low as 500 eV. This is not surprising since c-Si, which exhibits similar values to those of a-Si:H, has a maximum SEE at 250–300 eV [Seiler 83]. The SEE coefficient is slightly larger for a-Si:H than c-Si, probably because of the hydrogen bonding, which, in the case of the surface termination on diamond, was shown to increase the SEE coefficient because it produces a negative electron affinity [Shih 97, Lapington 09].

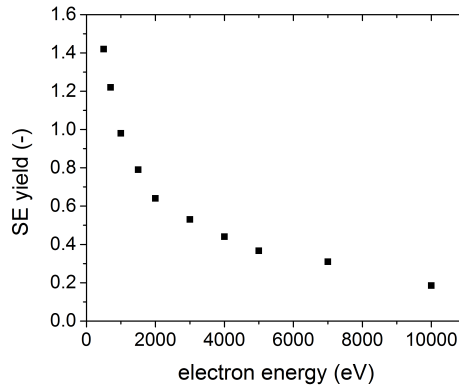


Figure 3.16: SEE coefficient as a function of primary electron energy in a-Si:H [Joy 95].

As far as the AMCP performances are concerned, the data of figure 3.16 can provide an indication for assessing the electron multiplication factor, according to the channel aspect ratio. One possible enhancement of the a-Si:H SEE coefficient could be provided by the activation (coating) of the a-Si:H surface with caesium. This was showed to be an effective method for increasing the photoelectron emission [Schade 79, Mulhollan 10] and it could

have a similar effect on the SEE coefficient.

3.9 Summary

This chapter provided an overview on the basic physical properties of a-Si:H. The focus was on the material characteristics that were more important for the specific applications presented in this thesis. The defects, i.e. the dangling bonds, will be proved to play a fundamental role for the performances of both TFA detectors and AMCPs. The material metastability will also be shown to play an important contribution for the recovery of the a-Si:H electronic properties after a given material degradation.

Different electrical conduction mechanisms will be identified to play a role in the signals measured with the two detectors studied in this thesis. Their dependence on many parameters like the temperature, the light exposure, the defect density and the different interfaces between layers will be presented in relationship with the detector performances.

To conclude, the table 3.17 summarizes the most important a-Si:H properties with respect to the results presented in this thesis, together with their values and units (as they are normally provided).

Property	Value	Unit
density	2.15	g/cm ³
atomic density	$5 \cdot 10^{22}$	cm ⁻³
band tail states	$\sim 10^{19}$	cm ⁻³
defect density	$\sim 10^{15}$	cm ⁻³
optical (Tauc) bandgap	1.6–1.7	eV
Urbach energy	0.05	eV
mobility bandgap	1.7–1.8	eV
dark conductivity (intrinsic)	10^{-10} – 10^{-12}	$\Omega^{-1} \text{ cm}^{-1}$
activation energy (intrinsic)	0.7–0.8	eV
electron drift mobility	1–10	cm ² V ⁻¹ s ⁻¹
hole drift mobility	$3 \cdot 10^{-3}$ – 10^{-1}	cm ² V ⁻¹ s ⁻¹
electron diffusion coefficient	10^{-3} – 10^{-2}	cm ² s ⁻¹
hole diffusion coefficient	10^{-4} – 10^{-3}	cm ² s ⁻¹
e-h pair creation energy	4–6	eV

Figure 3.17: *Most important a-Si:H properties for the applications presented in this thesis.*

4 Detection of electron beams with TFA detectors

Abstract. Thin-film-on-ASIC (TFA) particle detector consists of a hydrogenated amorphous silicon (a-Si:H) diode, which is vertically integrated on an application-specific integrated circuit (ASIC). In this chapter, the investigation of the TFA spatial resolution, when tracking the electron beam of a scanning electron microscope (SEM), is presented. This study is performed by sweeping the electron beam across a few TFA pixels, whose bottom metallization is patterned in micrometric-wide strips. The modulation of the electron-beam-induced current, produced by a better charge collection at each connected strip, is compared for different thicknesses and configurations of the a-Si:H diode. The signal modulation is larger than the noise for all the strip geometries, which enables one to resolve the position of each strip, even for those that are $0.6\ \mu\text{m}$ wide and spaced by $1.4\ \mu\text{m}$. This remarkable result, which evidences an attainable spatial resolution of about $1\ \mu\text{m}$, is achieved for all the tested a-Si:H diode thicknesses of 5, 10 and $20\ \mu\text{m}$ and the beam parameters of 10 keV and 200 pA. Other beam parameters are tested as well, and their influence on the signal modulation is discussed. The explanation of the obtained results is supported by means of simulations performed with the Monte Carlo software CASINO. Finally, the diode configuration without the n-doped layer is shown to cause larger charge loss, than that of the conventional n-i-p diode, for strips spaced by $33\ \mu\text{m}$.

4.1 Motivation and prior art

TFA particle detectors are pixel detectors [Anelli 04, Wyrsh 05] that were developed in a former collaboration between CERN and the Photovoltaics and Thin-Film Electronics Laboratory (PV-Lab) of the Ecole Polytechnique Fédérale de Lausanne (EPFL). The detector's name refers to its structure where the sensing element, which is made of an a-Si:H n-doped/intrinsic/p-doped (n-i-p) diode, is directly deposited on top of an application-specific integrated circuit (ASIC), namely the front-end readout electronics.

The previous characterization of the TFA detector with the electron-beam-induced current (EBIC) technique [Despeisse 06a] and the resolution of a few micrometers achieved when detecting beta-particles [Despeisse 08] motivated the study presented in this chapter. Indeed,

if this high spatial resolution had been confirmed also for larger electron fluxes (than those of the radioactive beta sources), it could have been of interest for beam hodoscope applications. Therefore, this characterization was carried out by measuring the electron-beam-induced current collected by a few specific TFA pixels, whose metallization is patterned in strips of micrometric-sized width and pitch. An additional goal was to study the lateral charge collection when the beam was between two strips and compare it with the charge sharing mechanism [Peisert 92] of crystalline silicon (c-Si) microstrip detectors.

This study was done with the TFA detectors developed by Dr. M. Despeisse in his PhD thesis [Despeisse 06b]. Y. Riesen contributed to the installation of the EBIC technique. Dr. M. Dadras, affiliated to the Centre Suisse d'Electronique et de Microtechnique (CSEM) in Neuchâtel, helped with the use of the SEM.

In the following sections, a detailed description of the TFA structure is provided with a special focus on the sensing element and the features of the measured pixels. Then, the electric field profile in the sensing element is analyzed, as well as its modification upon detection, as this determines the signal modulation in the TFA detector. Next, the results of the signal modulation, when sweeping the SEM beam across the pixel, are presented in terms of both direct measurements of the induced current and qualitative maps of the current intensity across the pixel. We conclude with the implications of our results for future applications of the TFA particle detectors.

4.2 The TFA particle detector

The TFA particle detector is the product of two well-established concepts. The first is the vertical integration of an a-Si:H diode on top of readout electronics, which has been exploited in the field of imaging sensors [Lule 99, Wyrsh 08]. The second is the use of an a-Si:H diode as the detecting element for a variety of charged particles [Perez-Mendez 86, Dubeau 91, Perez-Mendez 91, Bacci 91, Hordequin 01].

The vertical integration presents a number of advantages compared to standard c-Si-based detectors, such as a fill factor (ratio of the detector area for the sensing element over the total area) of about 100% (no guard rings needed), the possibility to optimize the detecting element and the readout electronics independently, the removal of the complicated and expensive bump-bonding technique [Wermes 05], in situ data processing and low power consumption. Finally, the vertical integration yields compact detectors, which are easier to handle and replace, and are also potentially cheaper and more reliable.

In the two following sections, we provide a detailed description of how the TFA detectors had been fabricated, in order to provide the necessary background for the explanation of the results obtained in this thesis.

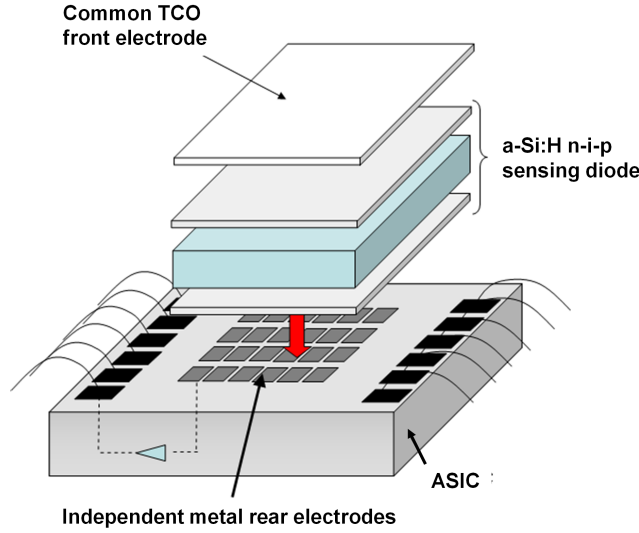


Figure 4.1: *Sketch of the TFA structure with an a-Si:H n-i-p diode electrically contacted by one common TCO front electrode and a number of independent metal rear electrodes, which correspond to the ASIC uppermost metallizations and define the TFA pixels. Courtesy of Dr M. Despeisse.*

4.2.1 The a-Si:H sensing diode

The fabrication of the a-Si:H sensing element was done, prior to this thesis, at the PV-Lab by plasma-enhanced chemical vapour deposition (PE-CVD). Three layers were deposited one after the other to realize the n-i-p diode, schematically presented in figure 4.1. The first is a 30-nm-thick n-doped a-Si:H layer (n-layer) with a resistivity of about $10^5 \Omega \text{ cm}$, which corresponds to a sheet resistance of $R_{sq} = 300 \text{ G}\Omega$. This layer is moderately resistive in order to reduce the crosstalk between the TFA pixels. The n-layer is beneath the intrinsic a-Si:H layer (i-layer), which has an average resistivity of $10^{10} - 10^{12} \Omega \text{ cm}$. The i-layer is the core of the sensing element, in which the released ionizing energy generates electron-hole pairs. These are separated by the electric field and collected at either electrodes, which enables the detection. The thickness of the i-layer basically corresponds to that of the whole diode. The realized thicknesses range from 1 to $50 \mu\text{m}$, for investigating the detection sensitivity to different type and energy of particles. The last layer is a 30-nm-thick p-doped a-Si:H layer (p-layer), with a resistivity of about $10^5 \Omega \text{ cm}$. The a-Si:H diode is biased by a common front electrode made of indium tin oxide (ITO), a transparent conductive oxide (TCO). Its thickness is between 70 and 200 nm, and its resistivity is about $10^{-3} \Omega \text{ cm}$. Inversely, the grounded rear electrode corresponds to the uppermost ASIC metallization and it is segmented into many independent metal pads, which define the TFA pixels, as sketched in figure 4.1.

In some more recent TFA detectors, the n-layer was removed to minimize the pixel crosstalk, which corresponds to the M-i-p configuration (instead of the n-i-p one), where “M” stands for metal and refers to the ASIC metallization. The effects of this configuration on the signal modulation are shown in 4.8.2.

4.2.2 The front-end readout ASIC

For the front-end readout electronics, several ASICs were developed at CERN [Despeisse 08]. The TFA detector measured in this thesis features the ASIC called *aSiHtest*. It was designed in an IBM 0.25 μm CMOS technology and has three levels of metallization, separated by insulating layers. The uppermost aluminum metallization is segmented into 35 pads (see figure 4.2), which are independently connected to a couple of different amplification circuits. The pads vary in shape and size: their area ranges from 2070 to 167747 μm^2 , and they have the shapes of squares, rectangles and octagons. The first passivation, which protects the uppermost ASIC surface by means of a layer stack of silicon nitride, silicon oxide and a polyimide, is locally removed to have direct access to the pixels. The *aSiHtest* ASIC features two types of opening in the passivation, one slightly smaller and one slightly larger than the pixel area, as sketched in figure 4.2. The opening that is larger than the pixel area was found to limit the leakage currents more effectively [Despeisse 06b]. The amplification circuits embedded in *aSiHtest* are of two types: one is an active feedback preamplifier (AFP) [Anelli 03], which is a current-sensitive preamplifier and features a transimpedance amplifier with a transistor, instead of a resistor, in the feedback line, plus a buffer stage. The other amplification circuit simply consists of three stages of current mirrors, which provide a tunable current amplification within 10^2 – 10^5 . Only this second circuit was employed in this thesis. The *aSiHtest* TFA detectors had been bonded to an interface board where the induced current, amplified by the ASIC, is terminated on a set of selectable resistances, to optimize the measurements with a high-impedance oscilloscope.

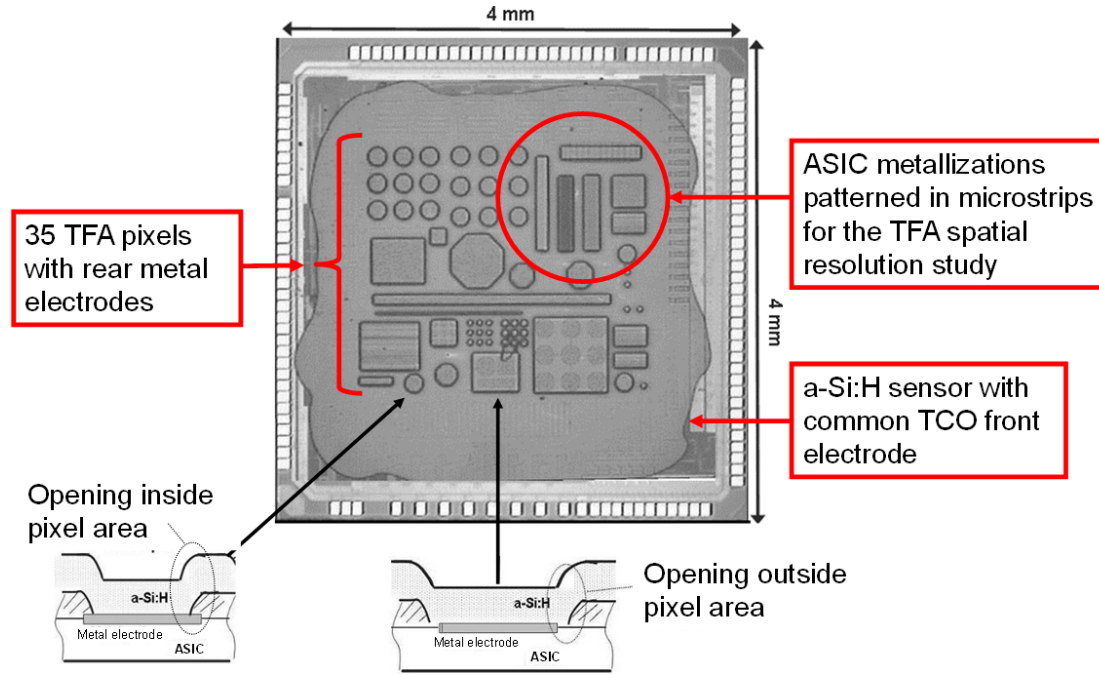


Figure 4.2: Top view of a TFA particle detector featuring 35 independent pixels, whose size and shape is defined by the ASIC uppermost metallizations. The TFA pixels are electrically connected to the peripheral bonding pads by the ASIC current amplifiers. At the bottom of the figure, schematics of TFA detector cross sections, which show the two types of opening in the first ASIC passivation, inside and outside the metal electrode. Courtesy of Dr M. Despeisse.

4.3 Description of tested TFA pixels

The TFA signal modulation, when tracking the electron beam, was characterized with particular TFA pixels, which are located near the electrical connection for the biasing of the ITO front electrode, as shown in figure 4.3. The rear electrode of these pixels is patterned in a number of micrometric-wide strips. This is shown in figure 4.4, where the bare ASIC top surface (prior to the deposition of the a-Si:H diode) was imaged with a Wyko interferometer microscope. As it can be observed in figure 4.4(a), the pixel patterning in microstrips had been performed by partially removing the metal. Additionally, for strips spaced by more than $7\ \mu\text{m}$, a number of isolated metallization pillars are still present between two strips (figure 4.4(a)).

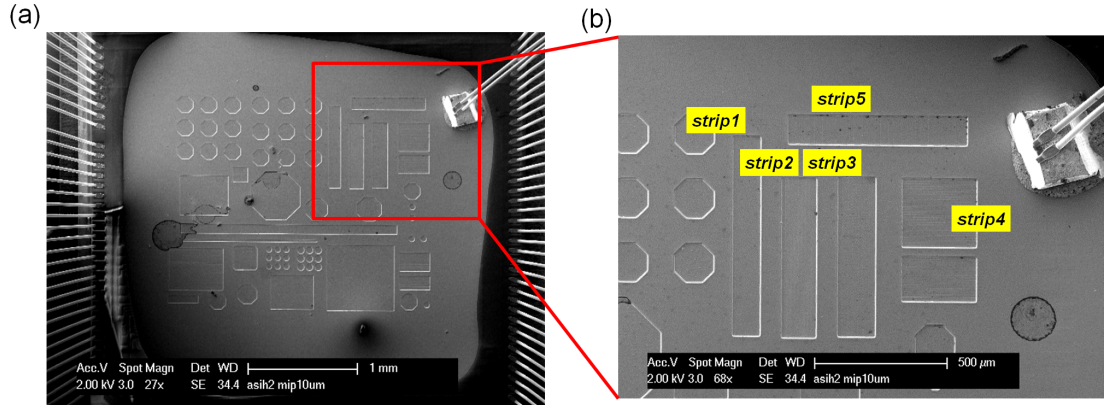


Figure 4.3: (a) SEM image of the whole TFA with a 10- μm -thick a-Si:H diode, plus the TCO front electrode, deposited on it. (b) Expanded view on the TFA pixels that were employed for the investigation of the signal modulation.

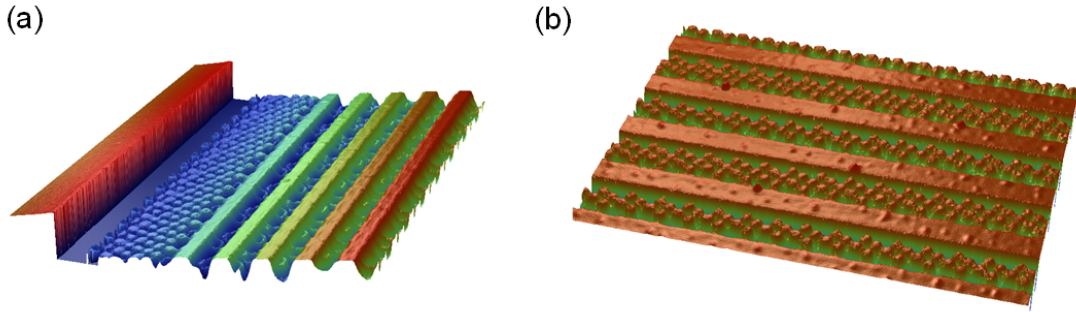


Figure 4.4: (a) Optical image (from an interferometer microscope) showing the edge of the ASIC metallization patterned with 1.5- μm -wide strips, spaced by 3.5 μm , prior to the deposition of the a-Si:H diode. (b) Optical image of another ASIC metallization patterned with 3- μm -wide strips, spaced by 7 μm .

The layout of the tested ASIC metallizations is sketched in figure 4.5 and the geometrical characteristics of their patterning are reported in table 4.1. The strips are connected altogether by two perpendicular strips on either side. The middle strip is independent from the others and is connected to an AFP, not used in the present study. Finally, the two outermost strips are independent and not connected to anything, i.e. they are floating “dummy” strips. This layout was originally realized to investigate the patterning influence on the detector leakage currents. The opening in the passivation (the pink square in figure 4.5) had been done in a way that the sensing a-Si:H n-i-p diode had been deposited on all strips except the two perpendicular strips on either side. The signal collected by any strip is amplified with a circuit featuring three stages of current mirrors. Two out of the three stages have a selectable amplification so that the overall amplification gain can be varied between 10^2 and 10^5 .

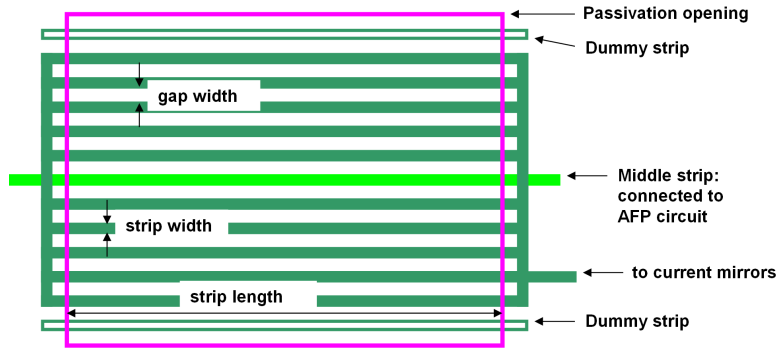


Figure 4.5: Layout of the ASIC metallizations, patterned in a number of strips. These are connected altogether by two additional perpendicular strips on either side. The signal collected by them is amplified by three stages of current mirrors. The middle strip is connected to another amplification circuit, whereas the two outermost strips are floating. Courtesy of Dr M. Despeisse.

Table 4.1: Features of the different pixel patterning in microstrips.

Pixel name (-)	Number of strips (-)	Strip length (μm)	Strip width (μm)	Strip gap (μm)	Strip pitch (μm)
strip1	43	767	0.6	1.4	2
strip2	23	621	1.5	3.5	5
strip3	13	621	3.0	7.0	10
strip4	13	282	6.6	13.4	20
strip5	13	113	16.5	33.5	50

The signal modulation was measured not only as a function of the ASIC metallization layout, but also as a function of the a-Si:H diode configuration. First, different i-layer thicknesses were tested in the n-i-p configuration. Then, the n-i-p configuration was compared to the M-i-p configuration. The overview of the tested a-Si:H diode features is reported in table 4.2.

Table 4.2: Tested a-Si:H diode configurations and thicknesses.

Configuration	Thickness of i-layer (μm)
n-i-p	20
n-i-p	10
n-i-p	5
M-i-p	10

4.4 Microvoids and hillocks in a-Si:H

The interferometer microscope images of the bare ASIC (figure 4.4(a)) showed trenches in the ASIC metallization at least as deep as the strip width. Although the PE-CVD technique has a high degree of conformal coating, with respect to other deposition techniques such as sputtering, it was not evident that a-Si:H could have been smoothly grown on this “rough” surface. Additionally, SEM images of the TFA surface evidenced the presence of micrometric-sized bubbles both over each strip and between two strips, as shown in figure 4.6(a) and figure 4.7(a). Since it was essential to understand the origin of these bubbles and whether they could influence the signal modulation, a detailed SEM investigation was performed with TFA cross sections, which were done with the focused ion beam (FIB). Figure 4.6(b) and figure 4.7(b) show the result of this investigation. The SEM image of figure 4.6(b) revealed a problem in the a-Si:H deposition near the metallization surface. Since the microstrip patterning had been realized with trenches whose depth is comparable to the spacing between two strips, in the case of *strip1* patterning (1.4 μm strip gap and trench depth of 1.2 μm), the a-Si:H growing fronts, from the lateral sides of the trenches, joined at a certain point and prevented the conformal coating between two strips. This caused the formation of microvoids in a-Si:H, shaped as thin slits, which propagated for the whole microstrip length. In Section 4.8.2, the contribution of these vertical slits on the signal modulation is mentioned.

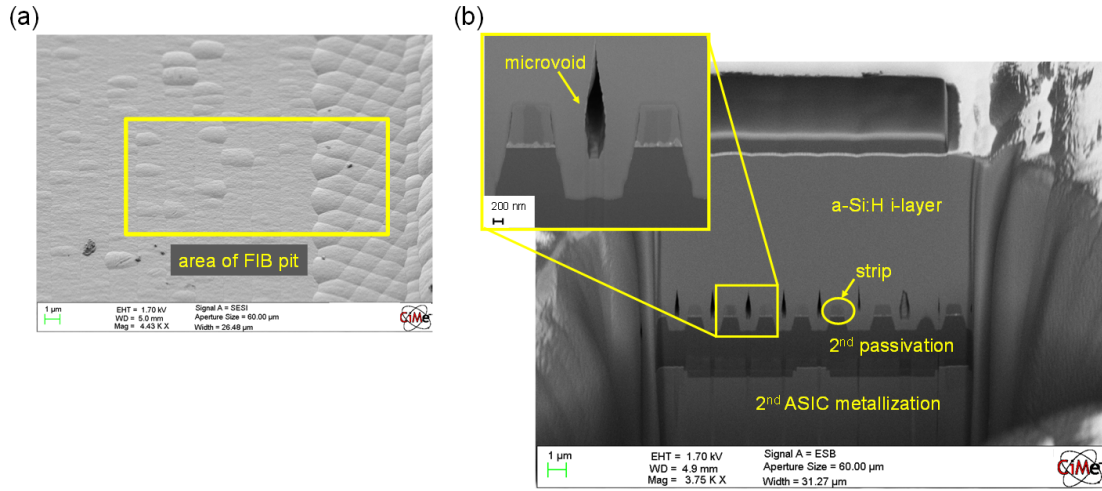


Figure 4.6: (a) SEM image of the edge of pixel “strip1”, whose rear electrode is patterned in 0.6- μm -wide strips, spaced by 1.4 μm . The yellow rectangle evidences the area where the FIB pit was realized. (b) TFA cross section, imaged with the SEM, of the a-Si:H n-i-p diode plus the upper part of the aSiHtest ASIC. Each strip can be recognized as the brighter trapezoidal shape beneath a-Si:H and above a darker layer, corresponding to the second aSiHtest passivation. Between each couple of strips, in the a-Si:H i-layer, a microvoid is identified as a vertical thin slit (in the inset).

A second FIB pit was made in the TFA pixel whose rear electrode has strips 7 μm apart (*strip3*). The aim was to verify if the microvoids were present even when there were isolated metallization residuals (pillars) between strips, in the case of *strip3*, *strip4* and *strip5*. This second FIB pit was done also to investigate the origin of micrometric-sized bumps on the a-Si:H diode surface, as the one shown in figure 4.7(a). The SEM cross section (figure 4.7(b)) pointed out again the presence of microvoids because of the pillars presence. Furthermore, beneath the bump and near the ASIC surface, a particle was spotted, which had caused a large microvoid in the a-Si:H beneath it. This particle could have been originated from a dust residual prior to the a-Si:H deposition or by a Si_xH_y particle produced in the plasma by the high deposition rates (cf. Chapter 6). These TFA defects (bumps) caused a sharp drop in the EBIC signal, identified as black spots in the EBIC maps (cf. Section 4.8.1).

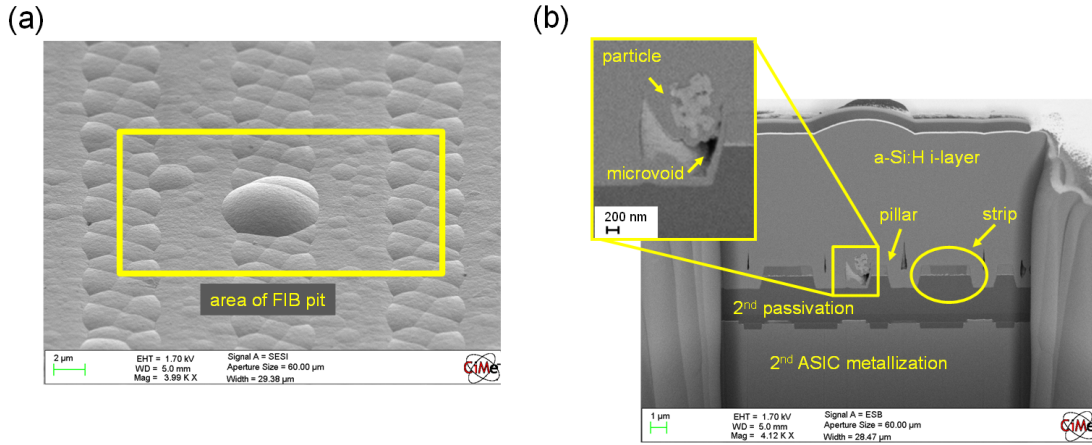


Figure 4.7: (a) SEM image of a bump, on the a-Si:H diode surface, where the FIB pit was realized. (b) TFA cross section of the FIB pit, imaged with the SEM. Each strip can be clearly recognized, as well as the metallization residuals in the form of trapezoidal pillars, which induced the formation of microvoids in the diode i-layer even for strip gaps larger than 7 μm . A dust particle is the evident cause of the bump, as shown in the inset.

4.5 Electric field in a-Si:H diodes

The n-i-p (or p-i-n) diode represents the standard configuration when a-Si:H is employed for particle detection or photovoltaics. The additional intrinsic layer (i-layer), compared to the simpler p-n junction of c-Si, is required because the a-Si:H p-doped and n-doped layers are too defective and the carrier lifetime too short for a sufficient charge collection. Therefore, the i-layer acts as an absorber, while the doped layers set the built-in potential across the diode. They also act as blocking contacts when the diode is inversely polarized. In the ideal case, the electric field is constant throughout the i-layer. However, the i-layer has also defects, albeit in a lower concentration than the doped layers, and these get positively or negatively charged, according to the position of the two quasi-Fermi levels (cf. Chapter 3). They, in turn, reduce the electric field strength so that the i-layer cannot be fully depleted by the solely

built-in potential if its thickness is larger than about $1 \mu\text{m}$. An example of the bands diagram and the electric field profile in the presence of i-layer charged states is shown in figure 4.8(a). The dotted green lines represent the ideal case without charged states in the i-layer, whereas the solid curves correspond to the real case with charged states: the electric field disappears beyond a certain depth in the i-layer. This evidences the necessity of a reverse polarization for keeping the i-layer fully depleted and maximizing the charge collection. Simulations of the electric field profiles, for different reverse polarizations, are shown in figure 4.8(b). As a result, the design of n-i-p a-Si:H diodes for particle detection is the result of a compromise. On the one hand, one wants to have the i-layer as thick as possible to maximize the signal, especially for those particles that are at the minimum ionizing potential. On the other hand, one has to limit the leakage currents through the diode, which are induced by the large bias required to deplete such thick layers. These leakage currents worsen the signal-to-noise ratio and can even become harmful for the ASIC below.

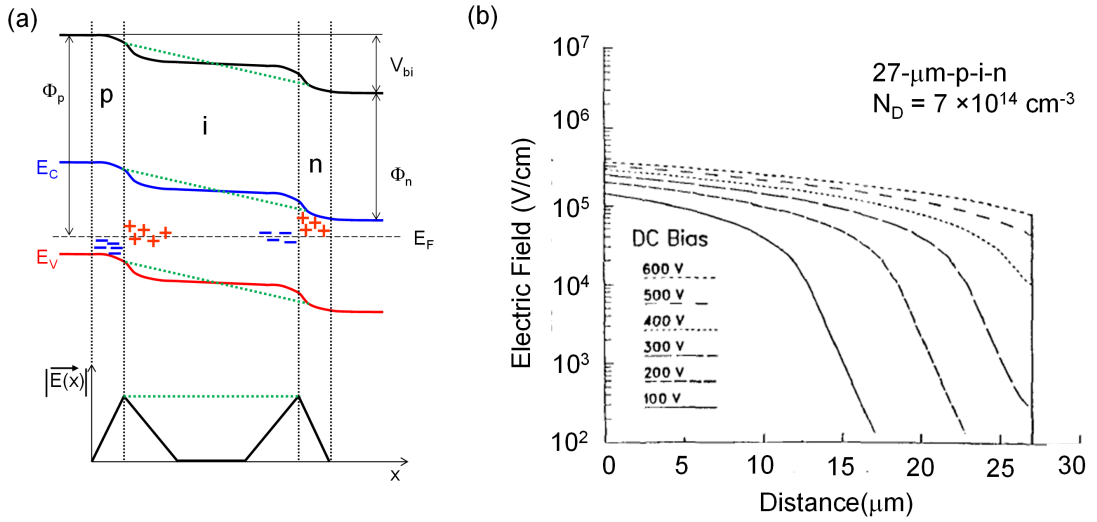


Figure 4.8: (a) band diagram and electric field profile for an unbiased a-Si:H diode. The green dotted line represents the ideal case without i-layer charged states and the solid lines represent the real case with charged states. (b) calculated electric field profiles in a 27- μm -thick p-i-n detector at various bias voltages [Qureshi 89]. N_D^* is the density of ionized i-layer defects.

To determine the required bias for depleting a given i-layer thickness, Poisson's equation in one dimension is used:

$$\frac{d^2 V}{dx^2} = -\frac{dE}{dx} = -\frac{\rho}{\epsilon} = -\frac{eN_D^*(V)}{\epsilon_0 \epsilon_{aSi}}, \quad (4.1)$$

where ρ is the space charge density, $N_D^*(V)$ is the density of ionized defects in cm^{-3} , ϵ_0 is the vacuum permittivity, ϵ_{aSi} is the permittivity of a-Si:H and e is the elementary charge. Although, $N_D^*(V)$ increases with the bias voltage, according to the positions of two quasi-Fermi levels, a usual approximation is to say that, at full depletion, 30% of the total defect density is ionized [Hong 95]. In this case, the bias voltage V_F required for the full depletion is obtained

by integrating equation 4.1 twice, which becomes

$$V_F = \frac{eN_D^*d^2}{2\epsilon_0\epsilon_{aSi}}, \quad (4.2)$$

where d is the i-layer thickness.

From equation 4.2, it results that an i-layer thickness of 20 μm is depleted with a bias of -180 V. This value had been also confirmed by means of measurements with a pulsed laser [Despeisse 08]. The corresponding average electric field of 9×10^4 V/cm was adopted also for the thinner 5- and 10- μm -thick i-layers, which were, in this way, over-depleted.

Everything presented so far is valid before the TFA exposure to the electron beam. Indeed, as soon as an electron beam of a few tens of keV interacts with a-Si:H, additional defects are produced in the i-layer. Consequently, the electric field profile decreases more rapidly, according to equation 4.1, and the condition of full depletion is no longer retained. This made the induced signal drop from one sweep to the following one. Therefore, for preventing the signal underestimation, we always performed each beam sweep in a different place across the pixel.

Moreover, the leakage current produced by the thermal emission of trapped charges [Street 90], given by equation 4.3, also increased during the exposure to the electron beam. Indeed, more and more charges were trapped in the newly created defects, which were eventually thermally released, with a consequent noise enhancement. The thermal leakage current is defined as

$$J_{th} = q \cdot d \cdot N_D \cdot \frac{1}{\tau_{gen}} \cdot \exp \left[\frac{-(E_c - E_t)}{kT} \right], \quad (4.3)$$

where q is the elementary charge, d is the i-layer thickness, N_D is the defect density, τ_{gen} is the time constant for the thermal emission of charges, and E_c and E_t are the bottom of the conduction band and the trap energy level, respectively.

In conclusion, the signal-to-noise degradation during exposure to the electron beam, which will be presented in more detail in Chapter 5, was produced by the weaker electric field (towards the i-n interface) and the larger thermal leakage current.

4.5.1 Signal formation in microstrip pixels

The electric field across the a-Si:H diode is set by the bias voltage applied to the TFA's front electrode with respect to the grounded ASIC metallization. However, the potential at the bottom of the a-Si:H diode, between two strips, might be higher than the nominal ground. This is actually the case for the M-i-p configuration, where the lack of the n-doped a-Si:H layer prevents a uniform distribution of the ground potential between strips. Although this is not the case for the n-i-p configuration before the exposure to the electron beam, during the charge generation, the potential at the bottom of the a-Si:H diode changes according to the scheme presented in figure 4.9(a). The generated charges according to the electric field, holes upward to the front electrode and electrons downward to the ASIC metallization. The lateral charge

diffusion is negligible due to the very low a-Si:H diffusion coefficients of about $10^{-2} \text{ cm}^2 \text{ s}^{-1}$ for electrons and $10^{-3} \text{ cm}^2 \text{ s}^{-1}$ for holes [Gu 96]. When the electrons reach the n-layer between two strips, collection takes place with their lateral movement through the n-doped layer to the nearby strips. However, since the n-layer has a resistivity of $10^5 \Omega \text{ cm}$, a non-negligible voltage drop occurs between the point where electrons reach the n-doped electrode and the nearby strips. This weakens the electric field because of the smaller potential difference across the diode. As a result, the charge collection is less efficient and the induced current is smaller between two strips than that when the beam is over a strip. The corresponding modulation of the induced current enabled us to resolve the position of each strip.

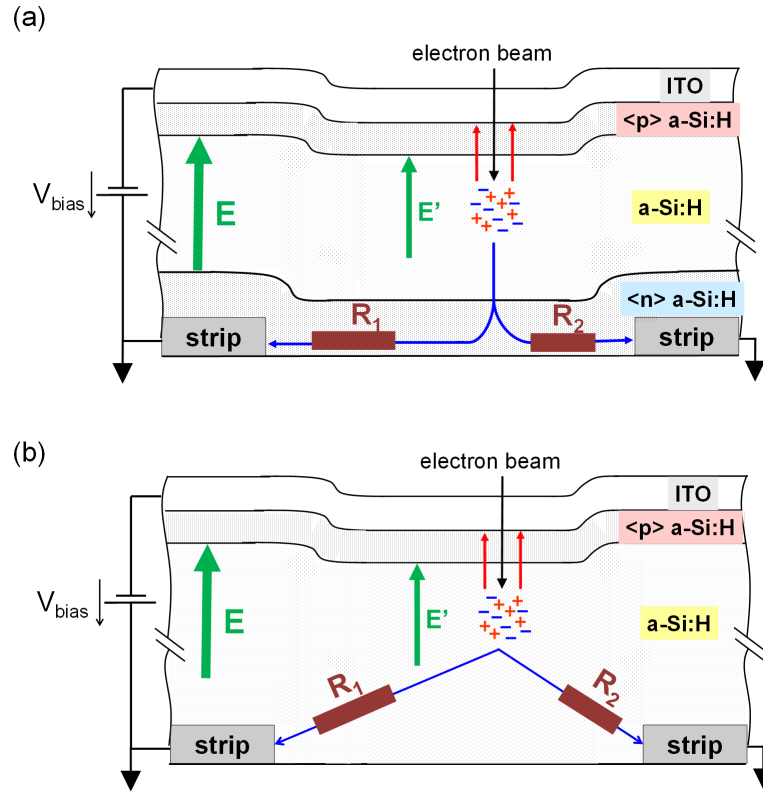


Figure 4.9: (a) schematic representation of electric field weakening induced by the electron flow in the n-layer, which raises the potential from the nominal ground of the connected strips and reduces the potential difference across the diode. (b) electric field weakening between two strips in the M-i-p configuration, which lacks of the n-layer.

Probably, this effect only partly explains the current modulation, which exhibits a current drop up to 85% between two strips (see Section 4.8.2). Additionally, a number of electrons are likely trapped along the perimeter of the microvoids, presented in Section 4.4, where the atomic structure discontinuity is richer of localized states. They, in turn, reduce even further the potential difference across the diode as well as the induced current.

For the M-i-p configuration, the smaller induced current when the beam is between two strips is originated by the lateral electron movement in the i-layer, for reaching the nearest strips.

This is shown in figure 4.9(b) and it can produce a larger voltage drop than that of the n-i-p configuration, as discussed in Section 4.8.2.

The modulation of the induced current from one strip to another, due to the partial recombination and charges loss between them, is completely different from the mechanism of charge sharing, which is exploited in c-Si microstrip detectors for tracking purposes. This difference originates from the very low a-Si:H diffusion coefficients, which prevents any lateral widening of the charge cloud during its drift towards either electrode. Although the mechanism for particle tracking, in TFA detectors, relies on the partial loss of generated charges—with the risk of losing too much in sensitivity between two strips—the drift of the charges by the electric field avoids any lateral widening and yields remarkable results in terms of signal modulation and attainable spatial resolution, as presented in Section 4.8.2.

4.6 Electron beam interaction in a-Si:H

As mentioned before, the interaction between impinging electrons of a few tens of keV and a-Si:H consists in the release of ionizing energy, which is mostly used to generate electron-hole pairs. This process does not occur all at once because first the energy is partly or fully transferred, through inelastic collisions, to other electrons that are promoted to the conduction band and above, so that they freely move in the material. Their movement does not follow the direction of the electric field because their large kinetic energy and the collisions make them change the direction many times. This random electron movement, due to both elastic and inelastic collisions mostly with other electrons, induces a droplet-like interaction volume, especially when the impinging electrons are fully absorbed in the material, as is the case for the energies employed in this study. When the initial energy has been shared among many more electrons than the impinging ones, the generation of electron-hole pairs becomes the predominant mechanism. Electrons and holes move freely in the extended states and drift under according to the electric field, until they are collected at the electrodes. The electron-hole generation volume is droplet shaped, with the largest generation density along the beam axis. Its shape, as well as the mapping of deposited energy, was simulated with a Monte Carlo software called CASINO [Drouin 07], version 2.42. The software simulates the electron interaction on user-defined 1D samples, in the range of energies typically employed in SEM microscopes, and outputs a 3D matrix of the deposited energy in the material. The simulation result for an electron beam of 15 keV is shown in figure 4.10. There, the different colors show how much energy is deposited in the a-Si:H i-layer as a function of depth and lateral width. One can reconstruct the droplet-like volume by rotating the map of deposited energy of 180° around a vertical axis passing by the x-axis origin. The origin of the vertical axis is set at the TCO upper surface. The energy difference between 15 keV and the sum of deposited energies listed on the right-hand side of figure 4.10 originates from the energy losses due to backscattered electrons plus the energy released in the first inactive layers, namely the TCO electrode and the p-layer.

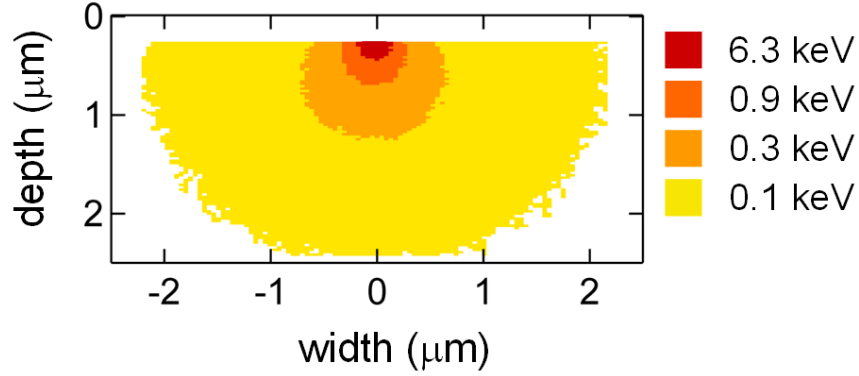


Figure 4.10: Simulated electron-hole generation volume inside the a-Si:H i-layer of the sensing diode. Different colors show how much ionizing energy is deposited, on average per impinging electron, as a function of depth and width. The origin of the vertical axis is the TCO upper surface and the energy deposited in the TCO electrode and the p-layer is not shown.

The most important inputs and outputs of the simulations are reported in table 4.3. The simulated energies range from 10 to 20 keV. Energies lower than 10 keV produced too little charge in the i-layer for the electron detection, as assessed by the simulations and confirmed by the measurements. Contrarily, energies larger than 20 keV were not adopted because they resulted in a too large lateral spread of the interaction volume, compared to the strip spacing. Here, the lateral spread is defined as the diameter of the disk containing 95% of the deposited energy (even though most of the electron-hole pairs are generated much closer to the axis of the beam direction). The average generation rate decreases with larger beam energy, as shown in table 4.3, because the interaction volume—which contributes to determine the generation rate—grows more rapidly (versus the electron energy) than the number of generated electron-hole pairs. The simulations also showed that all impinging electrons are stopped in the active layer (whose minimum thickness is 5 μm for the tested TFA detectors), with a maximum penetration depth of 3 μm for the 20 keV beam. These simulation results are further discussed in Section 4.8.1 and 4.8.2, to support the experimental results and assess the TFA spatial resolution.

Table 4.3: Simulation parameters and results about the interaction between the electron beam and the a-Si:H active layer.

Beam energy (keV)	Beam current (pA)	Energy in i-layer (keV)	Total e/h pairs (-)	Interaction volume (μm^3)	Lateral spread (μm)	Generation rate ($\text{cm}^{-3}\text{s}^{-1}$)
10	40	1.9	9×10^{10}	1	0.4	8.5×10^{22}
10	200	1.9	4.7×10^{11}	1	0.4	44×10^{22}
15	350	7.6	3.4×10^{12}	22	1	13×10^{22}
20	350	13.1	5.7×10^{12}	121	1.6	4×10^{22}

4.7 Setup for EBIC measurements

EBIC is a well-established technique [Leamy 82], which has been employed for the past 30 years to investigate semiconductor devices with respect to localized defects—like recombination centers in solar cells [Perreault 93, Yacobi 84]—spatial distribution of p-n junctions [Maher 83] and doping profiles [Chi 77]. There are two types of EBIC: qualitative, which is mostly used to determine the presence and location of electric fields, and quantitative, which is used to extract fundamental material parameters like diffusion lengths and minority carrier lifetimes [Ioannou 80, Puhlmann 91, Rau 01]. In both cases, the technique consists in sweeping an electron beam across the device under test with a consequent generation of charges by means of the energy transferred to the material. The electron beam is usually provided by a SEM with an energy in the range of tens of keV. Therefore, the only significant electron-to-matter interaction is the generation of electron-hole pairs by the released ionizing energy, whereas Bremsstrahlung and displacement damage can be neglected. This generated charges are promoted to the extended states and are free to move in the material until they are trapped or recombine. The electric field, which is induced by a p-n or a n-i-p junction and possibly strengthened by an external bias voltage, makes the free carriers drift until they are collected at the electrodes. The corresponding EBIC signal is normally a few orders of magnitude larger than the electron beam current because the energy of impinging electrons can create many electron-hole pairs. It is normally defined as

$$I_{EBIC} = I_B \cdot \frac{E_B}{E_{e-h}} \cdot \eta, \quad (4.4)$$

where I_B is the beam current, E_B is the energy of beam electrons in the range of a few tens of keV, E_{e-h} is the energy to create one electron-hole pair and η is the collection efficiency. E_{e-h} depends on the material bandgap and is about 3.6 eV and between 3.4 and 6 eV [Perez-Mendez 88, Perez-Mendez 91, Dubeau 91, Despeisse 06b] for c-Si and a-Si:H, respectively. The reason why E_{e-h} is higher than the bandgap is because just a portion of the ionizing energy is used to create free electron-hole pairs, whereas another portion is spent to excite phonons, i.e. lattice vibrations.

The standard EBIC setup consists of a current-to-voltage amplifier, which feeds a SEM video board to build a map of the device. The map shows, on greyscale tonalities, the spatial distribution of the induced current intensity as a function of beam position, which provides a qualitative overview of the electrically active areas of the device, according to the electric field distribution.

The EBIC technique employed for the testing of TFA detectors was installed and tested in an earlier phase of this thesis. A photograph of the EBIC setup is shown in figure 4.11. The electron beam is provided by an environmental scanning electron microscope (ESEM) at the CSEM in Neuchâtel. The induced current is measured and amplified with a KE Developments (KED) Limited type-31 current-to-voltage amplifier. The output signal is provided to the SEM video board to build the EBIC map. Alternatively, the direct measurement of the induced current, for a single line sweep, is done by a Keithley 6487 picoammeter. This instrument has also a

4.7. Setup for EBIC measurements

voltage source option, which was employed to bias the a-Si:H diode. The measurements were transferred to a personal computer and logged to file by means of an executable written in LabVIEW 8.6. For the fastest beam sweeps, the Keithley sampling time was not fast enough, even when its internal buffer, for data logging, was employed. Therefore, the picoammeter was replaced by a Tektronix TDS2012 oscilloscope. All the measurements of single line sweeps presented in Section 4.8.1 were carried out with this oscilloscope, to minimize the a-Si:H exposure time to the electron beam and the consequent degradation (cf. Chapter 5).

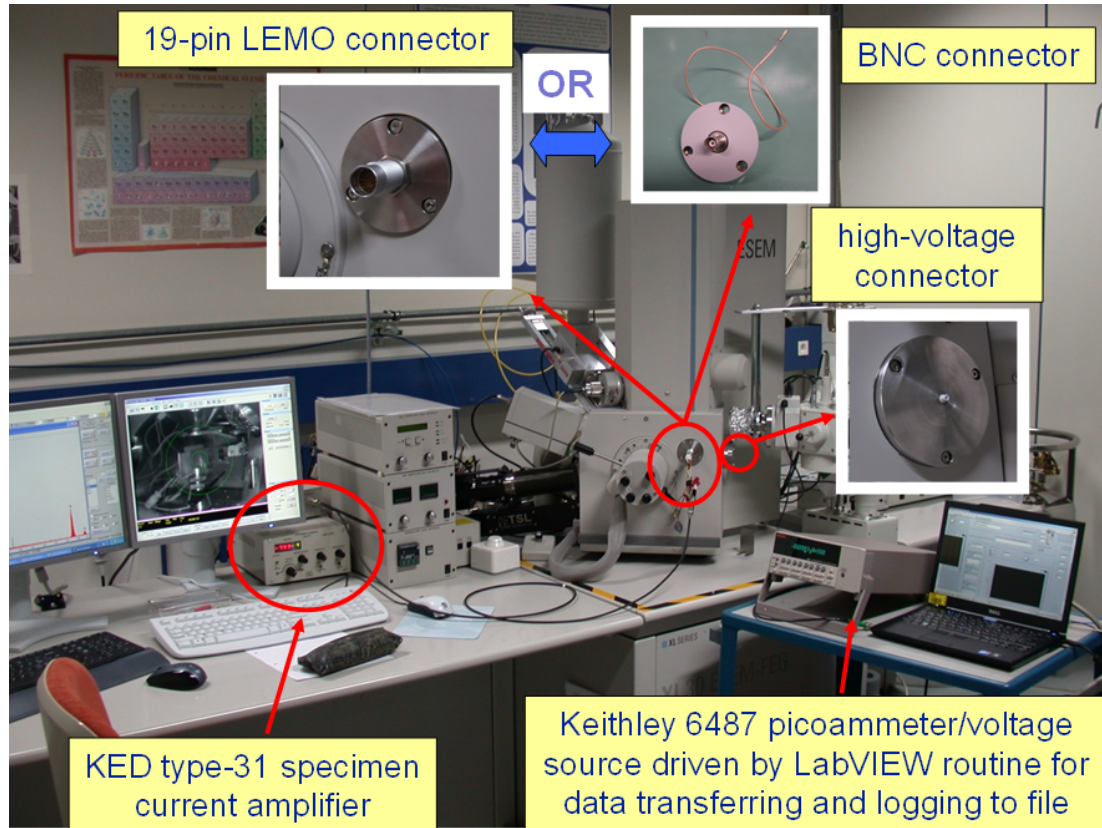


Figure 4.11: EBIC setup at CSEM, Neuchâtel. This was installed and initially tested with thin-film a-Si:H and $\mu\text{c-Si:H}$ solar cells, as a first task of this thesis.

4.8 Results

The results of EBIC measurements on the microstrip-patterned TFA pixels, also reported in [Franco 12a], are presented in two ways. First, a qualitative overview of the signal intensity induced when the beam sweeps over a certain pixel area is provided by the EBIC maps. According to the charge collection mechanism presented in Section 4.5.1, every strip appears brighter than anywhere else because the charge collection is more efficient. Second, a quantitative measurement of the induced current for beam sweeps perpendicular to a number of strips is presented. A specific parameter that quantifies the signal modulation between one strip and the next one was established to compare the lateral charge collection efficiency for different patterning layouts and assess the spatial resolution. This is presented in Section 4.8.2.

4.8.1 EBIC maps and line scans

EBIC maps of all pixels together

The SEM image of all tested pixels, plus the bonding pad for biasing the 5- μm -thick a-Si:H diode, is shown in figure 4.12(a). The corresponding EBIC map, in figure 4.12(b), reveals what was almost invisible in the SEM image, namely the position of the connected strips beneath the a-Si:H diode. As mentioned before, the EBIC map gives a straightforward overview of the TFA regions where the electric field is stronger and the charge collection more efficient. At this magnification, the EBIC signal enables us to distinguish only the connected strips, whereas all other details about the metallization patterning and not-connected strips disappear in the black background.

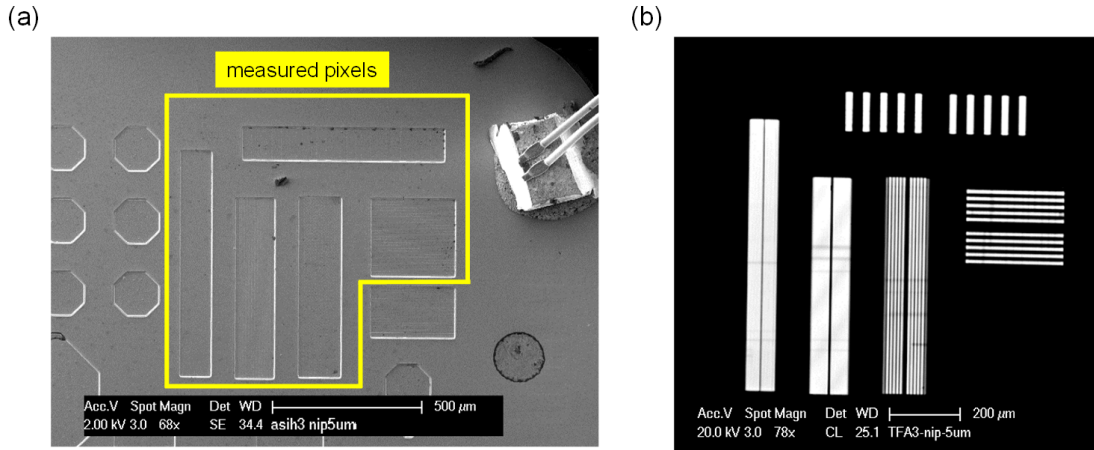


Figure 4.12: (a) SEM image and (b) corresponding EBIC map of all tested TFA pixels and an a-Si:H sensing diode, which is 5 μm thick. Each strip can be individually recognized for the patterning layouts with wider strip spacing.

Figure 4.13 shows SEM and EBIC images of the same TFA pixels, but with an a-Si:H diode thickness of 20 μm , rather than 5 μm of that of figure 4.12. The thicker diode induces the

blurring of the EBIC image. As mentioned in Section 4.5, the thicker the active layer, the harder is to reach full depletion because of the required larger voltage. This, in turn, enhances the leakage current through the diode and worsen the signal-to-noise ratio. The combination of a possible weaker electric field and an enhanced leakage current entails the sharpness loss in EBIC map.

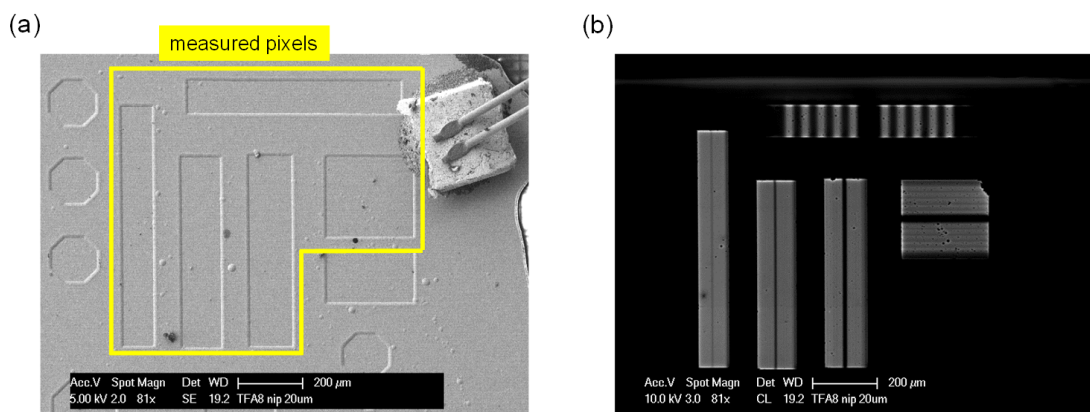


Figure 4.13: (a) SEM image and (b) EBIC map for all measured pixels with a TFA detector featuring a 20- μm -thick a-Si:H diode. The EBIC signal is blurrier than that of figure 4.12 because of the thicker diode, which entails lower collection efficiency due to the difficulty to deplete the i-layer.

EBIC map and line scan on pixel *strip4*

When the electron beam is focused on one of these pixels and the beam parameters are set to 15 keV and 350 pA, the EBIC map reveals many more details, as shown in figure 4.14(b). The tested pixel is *strip4*, with 6.6- μm -wide strips, spaced by 13.4 μm . The i-layer thickness is 5 μm . Every connected microstrip is equally brighter than anywhere else. This is confirmed by the direct measurement of EBIC current, shown in figure 4.14(c), obtained when the electron beam is swept perpendicular to the strips, along the red line drawn in both the SEM and EBIC image. Each current maximum of figure 4.14(c) corresponds to a connected strip.

In figure 4.14, the strip signal at the pixel edge is slightly brighter because, there, the first ASIC passivation partially overlaps the metallization. The passivation edge locally reduces the i-layer thickness, with a consequent stronger electric field across it and an enhanced collection efficiency, as thoroughly presented in previous works [Miazza 06, Wyrsh 08]. The tiny darker dots correspond to hillocks formed during the a-Si:H deposition and caused by embedded particles, as discussed in Section 4.4. When the beam is upon one hillock, the generated electrons are drifted downwards until they reach the dust particle. Once there, a number of electrons get trapped in the a-Si:H localized states, which are present in a larger density next to the dust particle, due to the abrupt discontinuity in the atomic structure. The accumulation of trapped electrons reduces the potential difference across the diode and the charge collection efficiency, which makes the EBIC signal drop.

In the EBIC map, the regions between two strips are as dark as the area outside the pixel, even though the measurement of induced current (figure 4.14(c)) exhibits a slightly larger signal between the microstrips (the minima in the current modulation) than off the pixel (the current after the first sharp increase, produced when the beam is focused on the TFA detector and labeled “beam ON”). The reason for this apparent mismatch is simply due to the adjustment of the gray scale lower bound in the EBIC map.

The two floating strips exhibit a lower signal, in both the EBIC map and the single line scan, than that of connected strips, but a larger one than that between two connected strips. The explanation lies in the resistance associated to the lateral electron movement through the n-layer, from the generation position to the connected strips. Indeed, when the beam is between two strips, the charges are generated within an interaction volume whose lateral spread is less than $1\text{ }\mu\text{m}$ (depending on the impinging electron energy, as presented in Section 4.6). This lateral spread does not widen any further, before moving to the connected strip, due to the n-layer moderate resistivity of $10^5\text{ }\Omega\text{ cm}$. On the contrary, when the charges are generated over the floating strip, the electrons reach the metallization and spread over its whole length before moving to the connected strip. In this way, the relevant resistance, through the n-layer, to the connected strip is smaller because the transversal area is larger. Therefore, the voltage drop is smaller, the electric field is less weakened, according to the model of Section 4.5.1, and the charge collection is more efficient.

Finally, the middle strip exhibits a faint signal in the EBIC map, which disappears completely in the line scan. This apparent contradiction between the two measurements is actually attributed to a different beam sweeping speed for EBIC maps and line scans. Furthermore, the unbiased AFP, to which the middle strip is connected, also plays a role. In fact, this AFP can be approximated as a resistor going to ground, whose resistance is deemed to depend on the amount of current flowing through it. In EBIC maps, the beam sweeps much faster than in the single line scans, whose sweep speed is limited by the oscilloscope sampling rate. Therefore, the number of charges generated at each sweep is smaller for the EBIC map than that of the line scan. When these charges reach the middle strip, they flow both to the adjacent connected strip and through the AFP, with a ratio that corresponds to that of n-layer over the AFP equivalent resistance. Since the AFP equivalent resistance is deemed to be inversely proportional to the amount of current flowing through it, it is more resistive for the measurement condition of the EBIC maps than that of the single line scan. This induces a larger amount of electrons to flow to the adjacent connected strips and explains the faint signal of the middle strip in EBIC maps, which disappears in the single line scan.

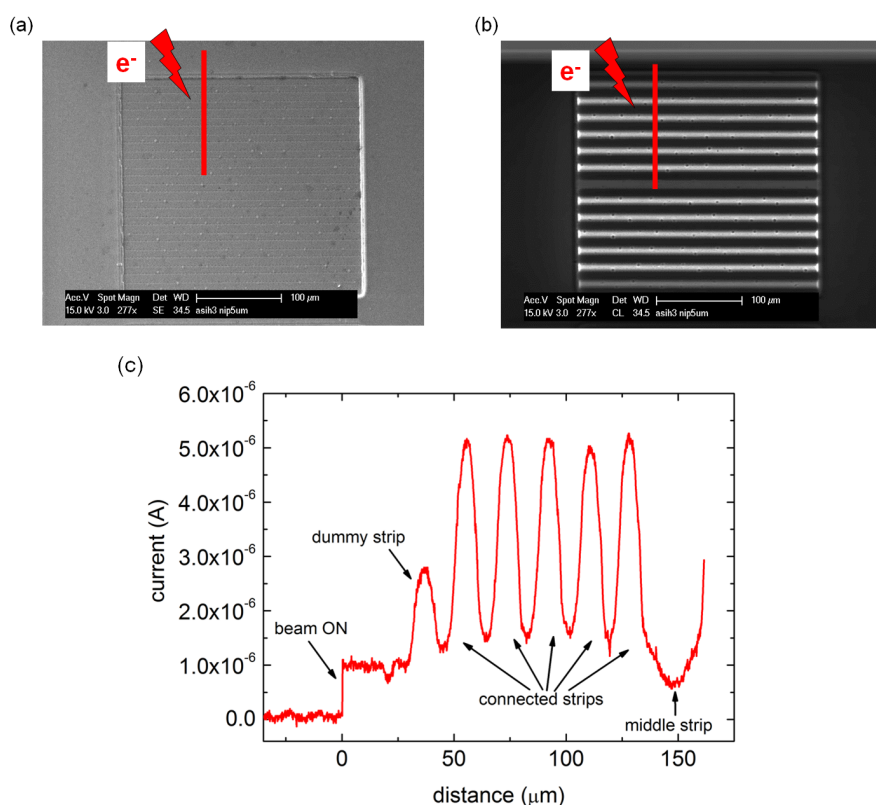


Figure 4.14: (a) SEM image of *strip4* with 13 strips, which are $6.6\ \mu\text{m}$ wide and spaced by $13.4\ \mu\text{m}$. The *i*-layer is $5\ \mu\text{m}$ thick. The beam energy is 15 keV and the beam current 350 pA. (b) EBIC map where each connected strip exhibits a brighter signal. The floating strips as well as the middle strip can also be identified with a corresponding weaker signal. (c) induced current for the beam sweep along the red line shown in (a) and (b) [Franco 12a].

EBIC map and line scan on pixel *strip2*

When the strips are thinner and closer one to another, the current modulation is less pronounced, as shown in figure 4.15(c) for an *i*-layer thickness of $10\ \mu\text{m}$. The EBIC map of figure 4.15(b) clearly shows the brighter signal collected at each strip. In this map, floating strips as well as the middle strip appear to have the same signal strength as all other strips. This is explained in terms of the charge parasitic collection by the nearby connected strips. Indeed, the strip spacing in *strip2* is reduced to $3.5\ \mu\text{m}$ so that the current modulation is less pronounced. The reason why the middle strip signal, in the line scan, is lower than anywhere else (within the pixel) is again due to the different sweeping speed, as explained above.

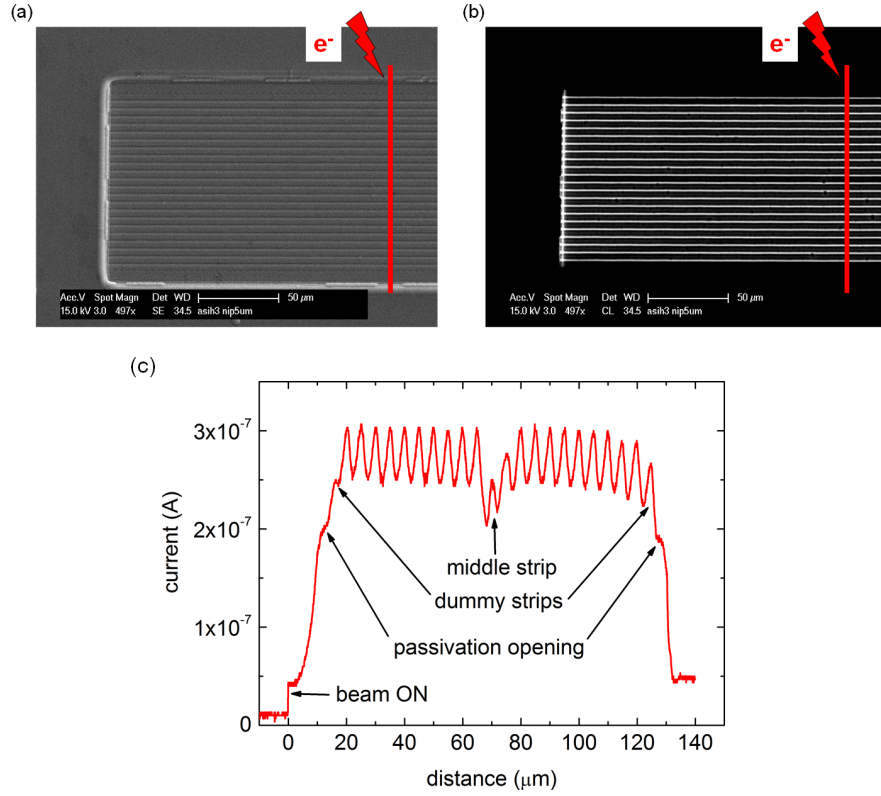


Figure 4.15: (a) SEM image of a portion of strip2, featuring 23 strips, 1.5 μm wide and spaced by 3.5 μm . The *i*-layer is 10 μm thick. (b) EBIC map acquired with a 15 keV and 340 pA electron beam. (c) induced current for a line sweep along the red line of figures (a) and (b) and perpendicular to the strips [Franco 12a]. To enhance the signal modulation, the electron beam parameters are reduced from 15 to 10 keV and from 340 to 200 pA.

EBIC map and line scan on pixel *strip1*

Finally, if the strip width and gap is reduced even further to 0.6 and 1.4 μm (*strip1*), respectively, the current modulation becomes very small but still distinguishable, as shown in the EBIC map of figure 4.16(b) and in the line scan of figure 4.16(c). Indeed, for this particular patterning, the width of the generation volume becomes comparable to the strip gap. This effect could not be avoided, even for the optimal beam parameters of 10 keV, for minimum lateral spread, and 200 pA, for sufficient signal-to-noise ratio. The weaker signal for the strips in the bottom part of *strip1*, observed in the EBIC map, is attributed to a locally defective ASIC metallization.

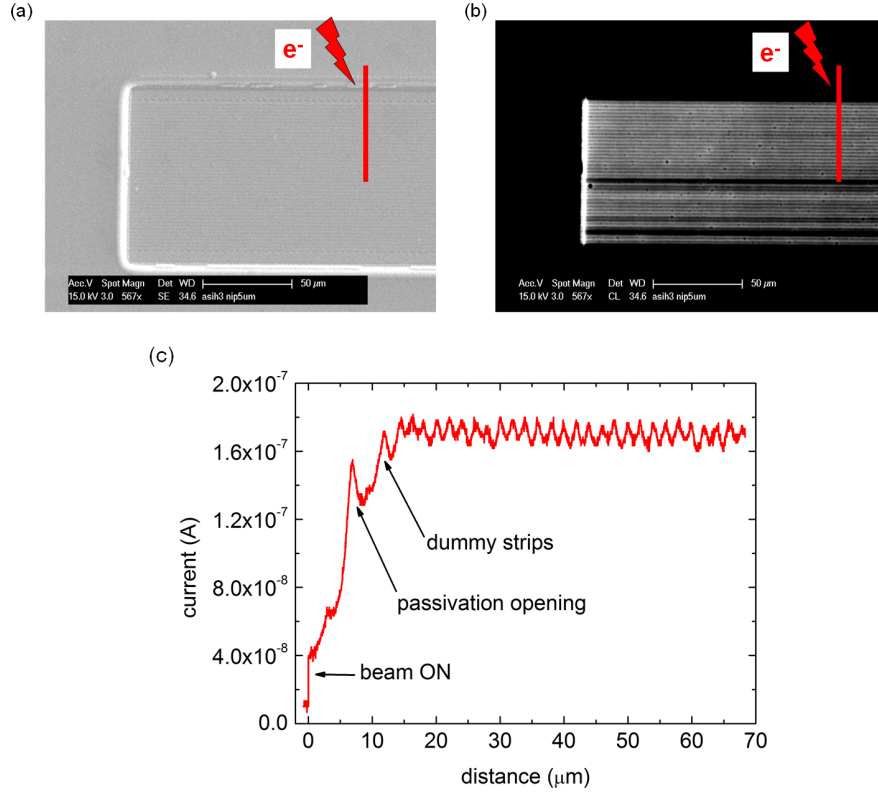


Figure 4.16: (a) SEM image of a portion of strip1, which features 43 strips, 0.6 μm wide and spaced by 1.4 μm . The i-layer is 10 μm thick. The beam parameters are 10 keV and 200 pA. (b) EBIC map showing a small but resolved signal of each strip. (c) induced current of a beam sweep across half of the pixel [Franco 12a]. The signal of middle strip, at the right end of the line sweep, is no longer distinguished from the other strips due to a charge lateral spread that is comparable to the strip spacing.

4.8.2 Lateral charge collection

The current modulation was quantified with a customized parameter for comparing the results obtained with different patterning layouts. This parameter is linked to the lateral charge collection (LCC) and is defined as

$$LCC(\%) = \frac{I_{betstrips} - I_{leak}}{I_{strip} - I_{leak}} \times 100, \quad (4.5)$$

where I_{strip} is the average current when the beam is over a strip, $I_{betstrips}$ is the average current when the beam is exactly between any two strips, and I_{leak} is the leakage current without the beam (the dark leakage current).

An LCC value of 50% between strips corresponds to the best compromise for the maximization of the current modulation, on the one hand, and the limitation of the charge loss between two strips, on the other hand. The noise below which the strips are no longer resolved corresponds to the current fluctuation at the beginning of the measurements. This condition was largely

satisfied for most of the strip gaps and an electron beam of 10 keV (which entails the lowest lateral spread achievable).

In the following analysis, *LCC* is used to compare the current modulation as a function of the strip gaps for a number of electron beam parameters and a-Si:H diode configurations.

***LCC* dependency on the beam parameters**

In the first data series, shown in figure 4.17, *LCC* is plotted versus the strip spacing for three sets of beam parameters. The strips are always resolved with a variable *LCC* between roughly 40 and 90%. The largest value of $90 \pm 1\%$, obtained with strips $1.4 \mu\text{m}$ apart (*strip1*), is still larger than the noise so that the strips are resolved. The resolution of each strip, $0.6 \mu\text{m}$ wide and $1.4 \mu\text{m}$ apart, is a noticeable result when considering that generated electrons go through $10 \mu\text{m}$ of i-layer, after an initial lateral widening of $0.4 \mu\text{m}$ (cf. table 4.3). It confirms that the lateral widening during the electron drift in the i-layer is very low because of the negligible diffusion coefficient. Note that the microvoids in the a-Si:H, described in Section 4.4, probably contributed to enhance the current modulation with a partial reduction of the potential difference across the diode and consequent signal drop between two strips.

The data for the beam parameter sets of 10 keV–40 pA and 15 keV–350 pA could not be collected for *strip1*. They would probably have yielded a negligible signal modulation because the beam current of 40 pA is too small to produce enough current modulation and the beam energy of 15 keV generates a too wide lateral spread of the interaction volume compared to the strip spacing.

For wider strip gaps, the *LCC* values gradually move towards the optimum value of 50% because the current between two strips decreases according to the charge collection mechanism presented in Section 4.6. An *LCC* of 50% value is almost reached for a strip gap of $13.4 \mu\text{m}$ and a beam of 10 keV and 200 pA. This set of beam parameters is the optimal one because, as mentioned before, the 10 keV limits the lateral spreading to $0.4 \mu\text{m}$ and the 200 pA current provides large enough signal-to-noise ratio.

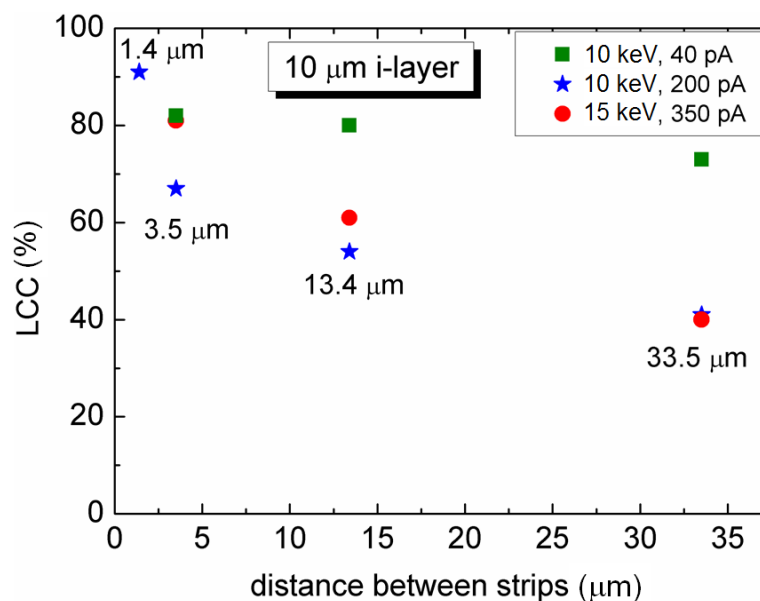


Figure 4.17: *LCC as a function of the strip gap, for different electron beam parameters. The a-Si:H n-i-p diode is 10 μm thick. For the strips spaced by 1.4 μm, results are available only for the 10 keV and 200 pA beam. Note that the error bars are smaller than the symbol size [Franco 12a].*

LCC dependency on the a-Si:H diode thickness

Another series of *LCC* values are presented for a number of a-Si:H diode thicknesses in figure 4.18. The beam parameters were 10 keV and 200 pA. The important outcome of this series is that the *LCC* values do not differ considerably for the tested i-layer thicknesses. This means that the condition of full depletion was approximately reached for all samples, so that most of the generated charges were collected. This experimental outcome confirms what was already observed in previous measurements [Despeisse 08], i.e. that the adopted mean electric field of 9×10^4 V/cm corresponds to the full depletion of i-layer thicknesses up to 20 μm. An *LCC* of $92 \pm 1\%$ was obtained for the 20-μm-thick a-Si:H diode and the patterning featuring 0.6-μm-wide strips, spaced by 1.4 μm. **This is a remarkable result, which was obtained because of the negligible charge diffusion and lateral spread in a-Si:H.**

Finally, the rather high *LCC* value for strips 13.4 μm apart, with the 20-μm-thick i-layer, is explained by a pixel with a concentration of hillocks larger than usual, which increased the measurement noise and blurred the current modulation between strips.

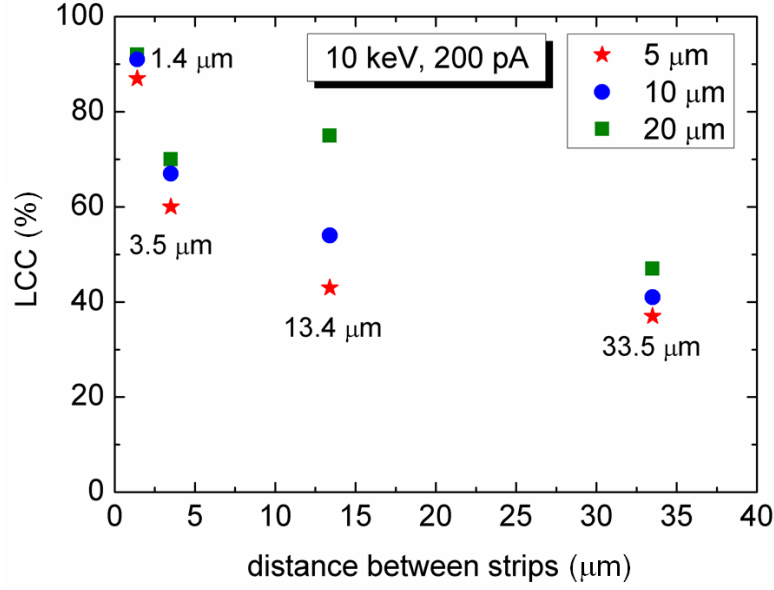


Figure 4.18: *LCC as a function of the gap width, for different a-Si:H diode thicknesses. The beam parameters are 10 keV and 200 pA. Note that the error bars are smaller than the symbol size [Franco 12a].*

LCC dependency on the a-Si:H diode configuration

Finally, we compared the n-i-p diode configuration to the M-i-p one, using a beam of 20 keV and 350 pA. The results, reported in Table 4.4, evidence that the n-i-p configuration yields a slightly better *LCC* of 14% than that of 7% of the M-i-p one, for a gap width of 33.5 μm. The *LCC* of 14% is better because both values are lower than the optimum one of 50%. According to the mechanism of the lateral charge collection in TFA detectors (cf. Section 4.6) and the larger resistivity of the intrinsic a-Si:H than that of the n-doped one, the signal drop is larger when the electrons have to move both vertically and laterally in the i-layer, as is the case for the M-i-p configuration, rather than vertically in the i-layer and laterally in the n-layer (for the n-i-p configuration). Additionally, the adopted beam parameters of 20 keV and 350 pA caused a larger a-Si:H degradation so that both *LCC* values are considerably lower than the ones presented before, for the same gap width and diode thickness. This degradation, presented in more details in Chapter 5, not only reduces the current both on the strips and between them, but also worsens the signal-to-noise ratio and the *LCC*.

With respect to the patterning layout with the strip spacing of 3.5 μm, the two diode configurations exhibit similar *LCC* values because the difference in the electron path to reach the nearby strip, is not large enough to produce significant changes in the lateral charge collection. Finally, the wider lateral spread induced by the beam energy of 20 keV explains the larger *LCC* values than those presented in the previous data series. Unfortunately, no additional tests with the M-i-p configuration were carried out with less energetic beams because this TFA detector was permanently damaged after a few bias cycles.

Table 4.4: *LCC values for the M-i-p and the n-i-p diode with a 10- μm -thick i-layer. The electron beam parameters are 20 keV and 350 pA.*

a-Si:H diode configuration	Strip width (μm)	Strip gap (μm)	LCC (%)
M-i-p	16.5	33.5	7.4 ± 0.4
n-i-p	16.5	33.5	14.2 ± 0.8
M-i-p	1.5	3.5	80.6 ± 1.2
n-i-p	1.5	3.5	80 ± 1

4.9 Discussion and Outlook

The EBIC measurements demonstrated the remarkable potential for high spatial resolution of TFA detectors, due to the low charge diffusion in a-Si:H, when tracking an electron beam of a few tens of keV and an intensity of a few hundreds of pA. The best result is the resolution, by means of the signal modulation, of the 0.6- μm -wide strips, which are interconnected and spaced by 1.4 μm , for a-Si:H diode thicknesses up to 20 μm . It is likely that the microvoids at the bottom of the i-layer contributed to this result. In any case, the potential high spatial resolution makes the TFA detector a good candidate as a particle tracker. Of course, in real tracking applications, the signal will be collected by independently amplified strips, rather than the tested ones, connected altogether. This will halve the induced current measured by each strip, when the beam is between two of them, because the electrons will be shared in even amounts by either one. However, the possibility to lose too much charge between two strips will have to be assessed according to the type of beam to be tracked (and the expected deposited energy in the i-layer of the a-Si:H diode) and possibly tackled with closer strips when needed.

As evinced from the series of measurements with different pixel geometries and beam parameters, a 10 keV beam is better located with thinner and closer strips, whereas more energetic beams produce a slightly wider generation volume and are better located with strips further apart. The lower bound for the beam energy is 10 keV, below which the charges generated in the active layer are too few for a sufficient signal-to-noise ratio. This is set by the actual TFA detector configuration with a TCO of about 150 nm and a p-layer of 30 nm. The upper bound for the beam energy could range within 50–500 keV, according to the diode thickness. This bound is not set by the degradation produced by the displacement damages, which starts to occur at about 100 keV and to which the a-Si:H is basically insensitive, but by the increasingly smaller amount of ionizing energy released in the active layer. Indeed, the electron stopping power, namely the amount of released ionizing energy per unit of length, decreases as a function of the initial electron energy. For instance, in c-Si (and similarly in a-Si:H due to the similar material density), the electron stopping power decreases exponentially from 10 to 100 keV so that it is almost tenfold smaller and even smaller at the lowest stopping power, which is attained at 1 MeV (cf. the website of the National Institute of Standards and Technology-NIST).

Although the TFA sensitivity is increased with a thicker a-Si:H diode, the bias voltages required to deplete it could induce harmful leakage currents for the readout ASIC. A solution could consist in the implementation of more effective blocking contacts so as to reduce the leaking conduction paths, especially at the p-i interface where the electric field is at maximum.

The TFA signal modulation enables one to resolve features that are comparable in size with the spatial resolution of state-of-the-art c-Si microstrip detectors, which is as high as 2–4 μm [Turala 05, Hartmann 12]. Additionally, at larger energies than those employed in the present study, as those employed in high energy physics (HEP), the TFA detector is expected to exhibit even better spatial resolution, because of high-energy particles are deviated only at small angles with respect to their initial direction (and the lateral widening of the interaction volume is smaller). All this provided that the generated signal is large enough to be above the detector noise.

Possible improvements to the TFA architecture could include a first ASIC passivation opening larger than the pixel perimeter so as to reduce the leakage current at the pixel edges. Additionally, the n-i-p configuration should be preferred to the M-i-p configuration for strips further apart. Although the M-i-p configuration reduces the pixel crosstalk, it was observed that the signal drop between strips is larger without the n-layer.

Most of the material degradation, which entails a certain amount of signal loss as discussed in more details in the next chapter, could be avoided by periodical annealing cycles at about 150 °C for few hours.

In conclusion, the tracking of an electron beam, in the energy range of 10–30 keV, could be optimized with a TFA detector featuring a number of individually amplified microstrips. Otherwise, electron beams of higher energy could be tracked by the two TFA detectors, one in front of the other and mounted with a tilt of 90° (one with respect to the other) for retrieving the coordinates on both axes perpendicular to the beam direction. In this case, the electron energy should be large enough to enable the electrons to go through the first TFA detector and still release enough ionizing energy in the active layer of the second. Most likely, this energy would approach the one corresponding to the minimum ionization, so that detection could be achieved only with very large fluxes, to compensate for the fewer electron-hole pairs produced by each impinging electron. In this case, the a-Si:H degradation (presented in the next chapter) would be less of a problem because it would be more evenly distributed throughout the active layer and the relevant absorbed dose would be smaller. Additionally, the radiation hardness of the TFA ASIC could be improved by using a CMOS technology with an as thin gate oxide as possible, such as the one of 5 nm that was shown to withstand an absorbed doses of 30 Mrad without any significant loss in performance [Anelli 99].

4.10 Conclusion

In this chapter, we presented an extensive characterization of the TFA signal modulation when detecting the electron beam of a SEM. The beam parameters were varied between 10 and

20 keV and between 40 and 350 pA. A number of TFA pixels, whose rear metallization was patterned in a number of micrometric-wide strips, was swept by the electron beam.

The signal modulation, which was measured when a beam of 10 keV and 200 pA was over a strip or between two of them, enabled the resolution of 0.6- μm -wide strips, spaced by 1.4 μm . This result was confirmed for all the tested diode thickness of 5, 10 and 20 μm , provided that the bias voltage was large enough to guarantee the full depletion of the i-layer.

Two a-Si:H diode configurations were also compared. The usual n-i-p configuration was compared to that without the n-layer. Although the signal modulation was similar for strips spaced by 3.5 μm , the M-i-p (where “M” stands for metal and refers to the rear metallization) showed worse performances with a spacing of 33.5 μm , due to the larger charge loss between two strips.

These remarkable results, which were obtained thanks to the negligible a-Si:H charge diffusion lengths and the intense electric fields across the i-layer, endorse the employment of the TFA detectors for particle beam hodoscope applications.

5 Electron-beam-induced degradation of hydrogenated amorphous silicon

Abstract. This chapter is devoted to the investigation of the a-Si:H degradation when exposed to an electron beam of tens of keVs. This degradation consists in the generation of additional defects (dangling bonds), which increase the density of midgap states. They act as recombination centers and deteriorate the a-Si:H electronic properties, such as the carrier lifetime. We confirm the increase of the defect density, after an absorbed dose of 225–450 kGy, by means of Fourier transform photocurrent spectroscopy (FTPS) measurements. We also prove that the defect density goes back to the pre-irradiation level after an annealing at 130 °C for 17 hours. We simulate the a-Si:H diode I-V characteristics with the ASA program. We also simulate the radiation-induced defect density profile with the Monte Carlo program CASINO. By combining the results of both types of simulations, we are able to calculate that an absorbed dose of 225–450 kGy produces a defect density of about $3 \times 10^{17} \text{ cm}^{-3}$.

5.1 Motivation and prior art

This chapter focuses on a-Si:H degradation under an electron beam, which was observed during the study of the spatial resolution of the TFA detectors (cf. Chapter 4). This degradation was so pronounced that the induced signal disappeared after a few consecutive beam sweeps over the same region. The explanation is that impinging electrons with energies of a few tens of keVs strongly interact with a-Si:H, by releasing all their energy within a thickness of a few micrometers. This energy increases by a few orders of magnitude the density of midgap states, i.e. dangling bonds that are normally referred to as defects. These additional defects act as recombination centers and reduce the lifetime of the electron-hole pairs that are generated by the ionizing radiation, so that the detection signal drops over time. This study aims to widen the present knowledge about the dynamics of defect formation in a-Si:H—which is induced by the beam of a scanning electron microscope (SEM)—and to compare this dynamics with that of the light-induced degradation.

This work was done on the TFA detectors developed by Dr. M. Despeisse in his PhD thesis [Despeisse 06b].

The chapter is structured as follows. Before presenting the results, a short literature review about the radiation hardness of a-Si:H, when exposed to different particles and of different energies, is provided. Then, the severe degradation of the a-Si:H electronic properties, experienced with the loss of the EBIC signal in the TFA detectors, is reviewed. The degradation dynamics is eventually studied with a specific degradation sequence, in which the material electronic properties are monitored by means of the EBIC signal evolution over time and the current-to-voltage (I-V) measurements of the a-Si:H sensing diode. The analysis of the I-V measurements permitted us to extract the $\mu\tau$ product, related to the electronic properties, and monitor its evolution with the accumulated exposure time. Successively, the FTPS measurements, for assessing the evolution of the defect density, are presented. Finally, the simulations performed with two programs, the Monte Carlo one called CASINO and ASA (Advanced Semiconductor Analysis), complemented the FTPS measurements. In the conclusion, the strengths and the weaknesses of this procedure for monitoring the a-Si:H degradation under the SEM beam are discussed.

5.1.1 a-Si:H degradation under photon and electron beams

The choice of a-Si:H for the TFA sensing layer was motivated, among other advantages such as the possibility of a monolithic integration, by its remarkable radiation hardness with respect to displacement damages [Srour 98, Kishimoto 98]. Indeed, the lack of an atomic periodic structure makes the electronic properties of a-Si:H far less sensitive than c-Si to the displacement of atoms. As an example, TFA detectors were demonstrated to suffer a drop in the proton-induced current of only 50% after irradiation with a 24 GeV proton beam and a cumulative fluence of 10^{16} cm^{-2} [Wyrsh 06]. No c-Si detector would have survived such harsh testing conditions, which corresponded to five years of operation of the future Super Large Hadron Collider (SLHC). This explains the presence of a-Si:H among the candidate materials for next-generation particle detectors [Sellin 06].

Inversely, the ionizing energy released by electrons of low and medium energy (up to tens of keV) causes the formation of additional dangling bonds. These act as recombination centers and influence the a-Si:H electronic properties much more than the displacement damages, as reported in the literature [Schneider 87] and as observed during the study of the spatial resolution of the TFA detectors.

In a-Si:H-based solar cells, degradation due to the light soaking also corresponds to the formation of dangling bonds with the energy released upon the recombination of photogenerated electron-hole pairs [Stutzmann 84].

Although many studies have been performed about a-Si:H degradation under an electron beam [Navkhandewala 81, Schneider 87, Diehl 96, Danesh 02], only a few address in detail the dynamics of defect formation and compare it with that of light soaking. In particular, one study [van Swaaij 08] about the irradiation of a-Si:H solar cells with a 1 MeV electron beam concluded that the formation of dangling bonds was caused mostly by the ionizing energy of the impinging electrons, rather than the energy released from recombination events.

We, therefore, decided to investigate in detail the a-Si:H degradation under electron beam in order to provide further insights about the defect creation kinetics. We decided to use the TFA detectors because they offered an optimal testing platform in terms of a relatively small pixel surface—easily swept by the beam—and the possibility to set much larger electric fields than those attained in solar cells. If the degradation, produced by the breaking of weak Si–Si bonds and the consequent formation of dangling bonds, was driven by the energy directly provided by impinging electrons, almost no dependency on the diode polarization should have been observed. On the contrary, if the degradation was dependent mostly on the energy released upon charge recombination, a strong electric field, capable of separating the charges prior to their recombination, would have prevented most of the degradation, as is the case for light soaking experiments [van Swaaij 08].

5.2 Degradation during EBIC measurements

The study of the TFA spatial resolution revealed a severe degradation of the a-Si:H electronic properties by the electron beam after only a few sweeps. An example is shown in figure 5.1, in which the EBIC maps exhibit large drops in the induced signal. The reason for this drop is the breaking of a large number of weak Si–Si bonds. These defects act as recombination centers, as discussed in Chapter 3, so that a larger and larger number of generated charges recombine during exposure to the electron beam. Additionally, the collection of the residual charges becomes less efficient due to an electric field profile that is less uniform because of the additional charged defects (cf. Chapter 4).

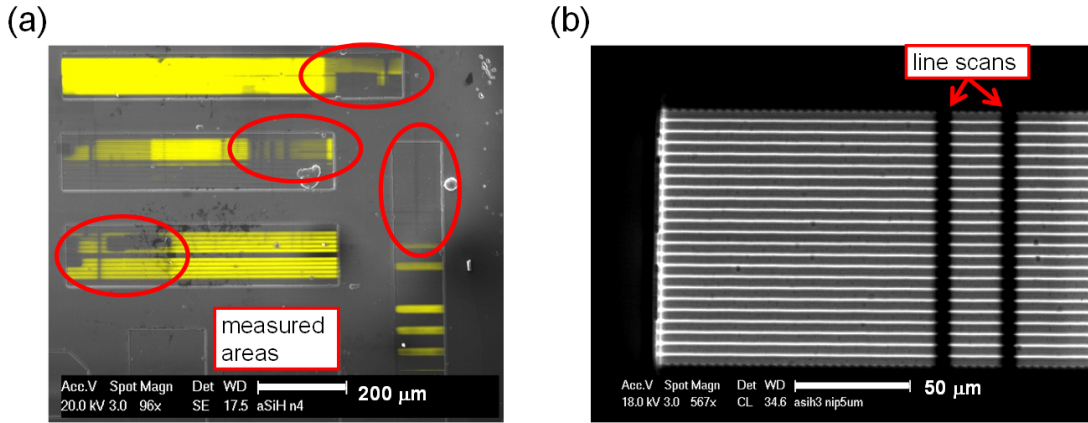


Figure 5.1: (a) EBIC map of tested pixels after a number of measurements. The areas previously swept by the beam show a drop in EBIC signal due to the a-Si:H degradation. (b) EBIC map of a portion of strip2, with 1.5-μm-wide strips spaced by 3.5 μm, which shows the loss of the EBIC signal along the two vertical lines where the beam previously swept.

The observed degradation was so severe that a sweep with a beam of 15 keV and 350 pA, with a speed of 8 μm/s along 150 μm, induced the signal to be barely measurable in a consecutive scan. The absorbed dose was 31 MGy, within a volume of 735 μm³. Therefore, for the charac-

terization of the TFA spatial resolution, we decided to limit the absorbed dose by increasing the sweeping speed to $680 \mu\text{m/s}$, which was the fastest one compatible with the oscilloscope's sampling rate. Although the dose was reduced to 360 kGy, the degradation still caused the induced signal to drop by 18% at each consecutive sweep. An additional reduction of the dose to 104 kGy, within a volume of $75 \mu\text{m}^3$, was achieved with a softer beam of 10 keV and 40 pA. Despite this sensitivity to the electron beam, the a-Si:H metastability (Chapter 3) enabled us to bring the material back to the pre-irradiation state by means of annealing cycles. Ideally, the annealing should have almost reached the deposition temperatures ($\leq 200^\circ\text{C}$) [Schneider 87]. This was not possible because the TFA interface board was incompatible to such high temperatures, so the annealing was performed at 130°C instead. A TFA detector with a $10\text{-}\mu\text{m}$ -thick i-layer was annealed at this temperature for 70 hours, after having absorbed a dose of about 17.6 MGy (in $2250 \mu\text{m}^3$) and it recovered 70% of its initial signal-to-noise ratio. After the confirmation of the degradation reversibility, the TFA was submitted to an annealing cycle after every set of measurements. Future applications of this detector, for instance as a beam tracker, could envisage periodic annealing cycles. A simple way to perform them could be to install a small heating resistor on the rear side of the TFA detector and to power it whenever needed.

5.3 Test plan of the a-Si:H degradation study

The study of the a-Si:H degradation upon exposure to an electron beam was performed with a rectangular (called *rect8*) and an octagonal (called *oct9*) pixel. They have a surface area of $167747 \mu\text{m}^2$ and a passivation opening inside the metallization. They are shown in figure 5.2. The i-layer of the a-Si:H diode, in the M-i-p configuration, was $10 \mu\text{m}$ thick.

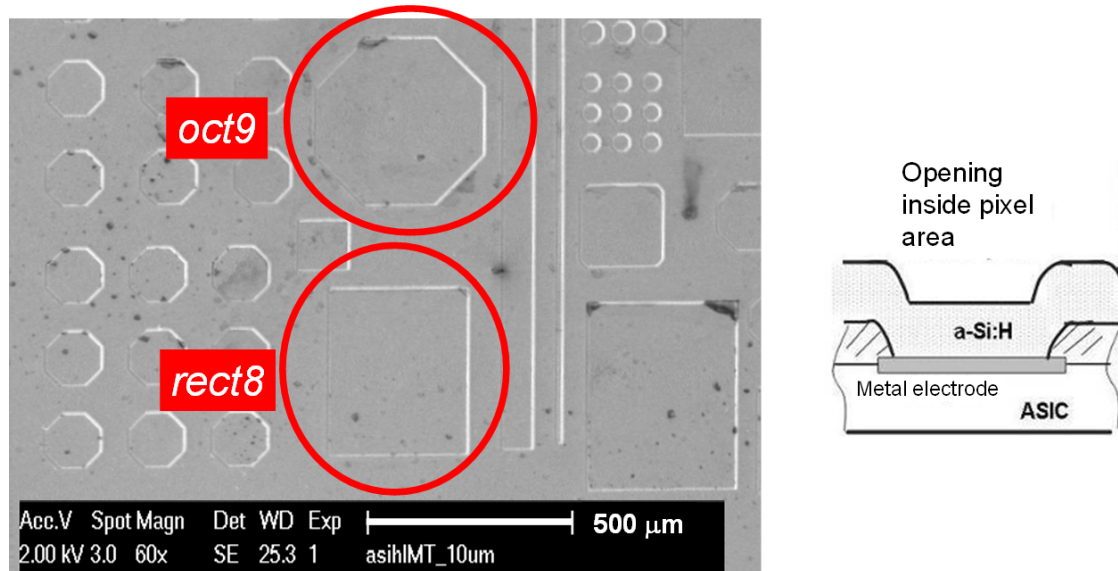


Figure 5.2: Pixels “rect8” and “oct9” used for the study of a-Si:H degradation induced by an electron beam of a few tens of keV. The passivation opening is inside the metallization.

The degradation study was performed according to the following sequence:

1. Determination of pre-irradiation a-Si:H status with a calibration of the absolute defect density.
2. First degradation step with the TFA detector biased with a large voltage.
3. First intermediate evaluation of the degraded status.
4. Second degradation step with the TFA detector biased with a small voltage.
5. Second intermediate evaluation of the degraded status.
6. Third degradation step with the TFA detector unbiased.
7. Determination of the final degraded status, in terms of absolute defect density.

The whole degradation sequence was repeated twice with an intermediate annealing step to remove the electron-beam-induced defects. In the first sequence, *oct9* pixel was irradiated with 30 keV electrons and *rect8* with 15 keV ones. These two energies were chosen for investigating the a-Si:H degradation as a function of the electron penetration and the rate of deposited energy per unit of length. The energy of 15 keV was the minimum value needed to produce considerable degradation in TFA detectors, whereas 30 keV was the maximum energy provided by the SEM.

In the second sequence, the beam energy was inverted for the two pixels. The annealing was carried out at 130 °C for 17 hours.

During the degradation step, the a-Si:H electronic properties were monitored by measuring the EBIC signal drop over time.

The variation in defect density was measured with FTPS only before and after each degradation sequences because these measurements were rather time consuming.

Alternatively, between two degradation steps, the relative increase in the defect density was assessed as follows. Without taking the TFA detector out from the SEM chamber, the I-V characteristic of the a-Si:H sensing diode was measured while this was illuminated with red light at 655 nm. The illumination source was a light-emitting diode (LED), which was affixed to the TFA evaluation board. This wavelength was chosen because its penetration depth was approximately comparable to that of the degraded zone (according to the selected beam energies). In this way, the photogenerated signal was as sensitive to the a-Si:H degradation as possible. Eventually, the I-V characteristic was fitted with the Hecht's function, which predicts the diode response as a function of the internal electric field and the light flux. This function also depends on the $\mu\tau$ product, which contains the information about the material degradation. The drop in the $\mu\tau$ product is mainly attributed to that of the lifetime (τ), due to the larger recombination [Srouf 98]. The lifetime [Wyrsh 95], in turn, is inversely proportional to the defect density, which can be monitored before and after the degradation step.

The measured I-V characteristics were successively compared to those obtained from simulations with the ASA program. The strength of this program is that the I-V characteristics

can be simulated for a customized defect density profile in each layer of the a-Si:H diode. Consequently, the aim of these simulations was to extract the real defect density profile by simulating the I-V characteristics that best matched the measured ones while shining the a-Si:H diode with light at 655 nm. In this way, we aimed at evaluating the absolute defect density produced after each degradation step and verify if the degradation was dependent on the bias voltage (defect density generation driven by the energy released upon charge recombination) or not (defect density generation driven by the ionizing energy of impinging electrons).

5.4 EBIC measurements

Every degradation step consisted of scanning the whole pixel surface of about $2 \times 10^5 \mu\text{m}^2$ with an electron beam current of 300 pA and an energy of either 15 keV or 30 keV. The irradiation time was reduced to the minimum necessary to observe a drop in the EBIC signal because we did not want to reach the saturation of the material degradation prior to the completion of the test sequence at different bias voltages. After a couple of preliminary measurements, we set the irradiation time, for each degradation step, to one minute. This produced an absorbed dose of 225 kGy for the beam energy of 15 keV and 450 kGy for the beam energy of 30 keV.

The EBIC signal during each degradation step is shown in figure 5.3. The signal was recorded with a Tektronix TDS2012 oscilloscope for the two degradation steps with a bias of -100 V (figure 5.3(b)) and -50 V (figure 5.3(c)). In these measurements, the EBIC signal corresponding to a full scan of the pixel can be easily identified by the lower current at the beginning and the end of each scan. However, the measuring time covered only to the first 500 ms of the one-minute degradation step because of the limited oscilloscope storing capacity. In this short time scale, the signal drop over time is only distinguishable in the smoothed curve of the degradation step at -100 V. The EBIC signal drop is 7% within 500 ms.

On the contrary, when the TFA detector was unbiased (figure 5.3(d)), the EBIC signal was recorded for the whole degradation step with a Keithley 6487 picoammeter because it was too small to be triggered with the oscilloscope. This measurement shows a clearer signal drop of 7% within one minute. As this drop is the same as that obtained with the degradation at -100 V within 500 ms, we observed that the degradation was independent on the electric field strength in the diode. This observation was confirmed with the analysis of the I-V characteristics, as presented in Section 5.5.

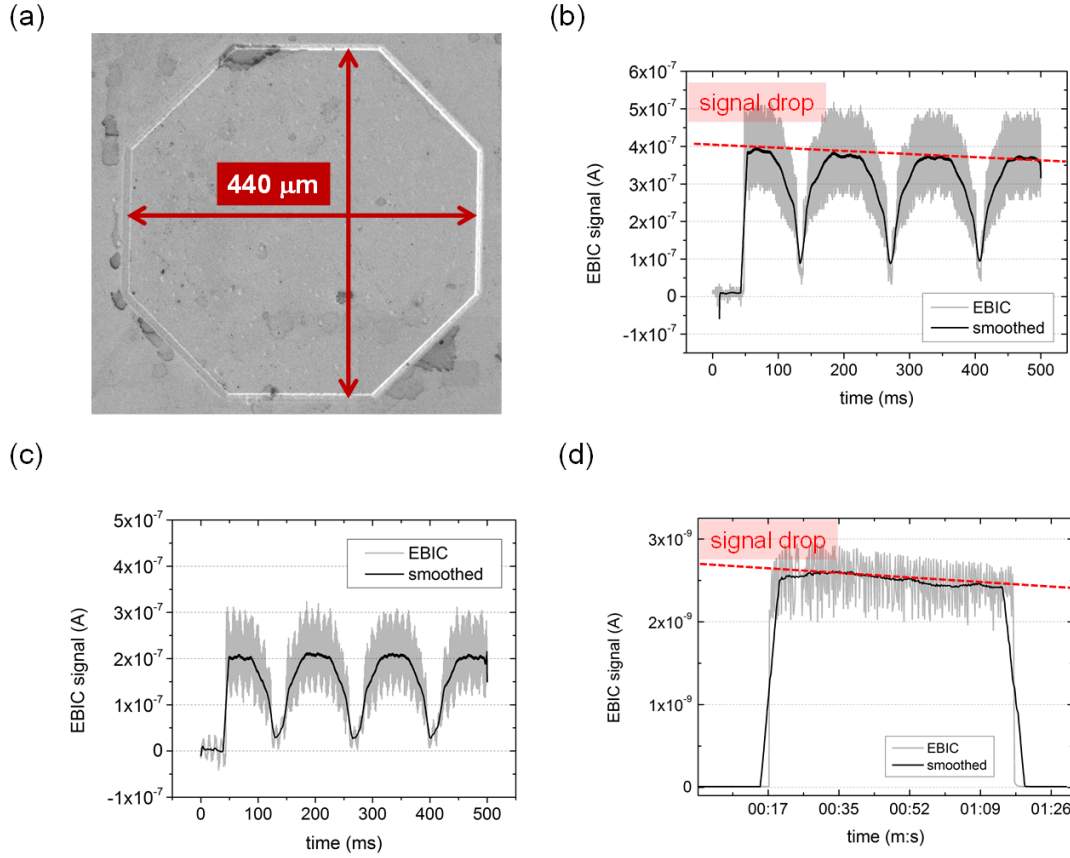


Figure 5.3: (a) SEM image of pixel oct9. (b) EBIC signal evolution within the first 500 ms of exposure to the electron beam, with the TFA pixel biased at -100 V. The smoothed curve shows a slightly decreasing trend over time. (c) same as (b) with the TFA biased at -50 V. This time the signal drop is too small to be observed within the measurement timeframe of 500 ms. (d) EBIC signal evolution for the whole degradation step of one minute, with the pixel unbiased. This time the signal drop is more easily observed.

5.5 Hecht's function and evaluation of mobility-lifetime product

5.5.1 I-V characteristics with an illumination at 655 nm

Besides the measurements of the EBIC drop while the beam was sweeping the pixel, the degradation of the a-Si:H electronic properties were monitored by means of I-V measurements while the diode was illuminated with light at 655 nm. Hecht's fitting of these measurements permitted to extract the $\mu\tau$ product and to monitor its variation after each degradation step.

5.5.2 Hecht's fitting of the I-V characteristics

Different formulations of Hecht's function [Hecht 32] can be found in the literature [Vaněček 91, Misiakos 88, Hegedus 97] and Vanecek's one fitted best our results. It defines Hecht's function as

$$I_{ph} = \frac{e\Phi A_{ill} \eta (\mu\tau)}{d} \left[E \left(1 - e^{\frac{-d}{(\mu\tau)E}} \right) \right], \quad (5.1)$$

where e is the elementary charge, Φ is the photon flux, A_{ill} is the illuminated area, η is the quantum efficiency for the free carriers photogeneration, d is the i-layer thickness and E is the electric field provided by the bias voltage. The photon flux was about $4 \times 10^{14} \text{ cm}^{-2} \text{ s}^{-1}$. The illuminated area was approximated to the pixel area (by neglecting any lateral collection from outside of the pixel). This approximation was deemed to be reasonable for the tested M-i-p configuration, since the absence of an n-doped layer [Miazza 06] or its removal between two pixels [Bigas 06] is known to limit the lateral collection. The quantum efficiency could be realistically approximated to one, as the energy of 1.9 eV for the 655 nm light is larger than the a-Si:H optical bandgap of about 1.7 eV.

The I-V characteristics and the relevant Hecht's fits are shown in figure 5.4 for most steps of the degradation study. The fits were optimized at the “knee” of the I-V characteristics, at voltages within 10–30 V. At biases lower than 10 V, the fit is no longer satisfactory because of the approximations contained in Hecht's formula, in which neither the diode leakage current nor the profile of the internal electric field (it is assumed to be uniform throughout the i-layer) is taken into account. At biases larger than 30 V, the fit becomes again less representative of the I-V characteristics due to the enhancement of the leakage current, especially after the degradation steps. Indeed, the exposure to the electron beam induces the deterioration of the p-i interface, in terms of formation of additional defects. They, in turn, enhance the leakage through the interface by means of mechanisms like Pool-Frenkel's field-enhanced thermal generation of charges trapped in the localized states [Ilie 96].

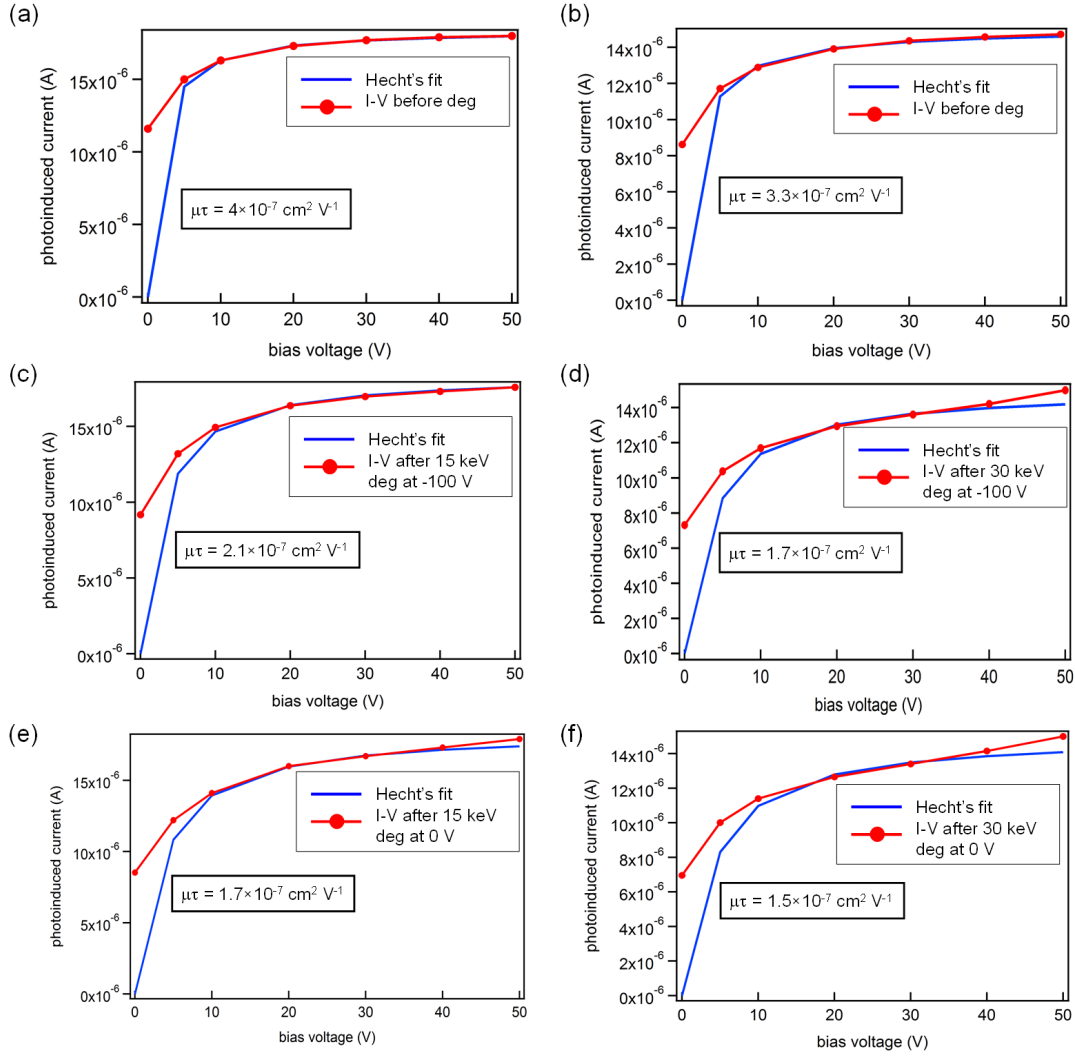


Figure 5.4: *I-V* characteristics of “oct9” and “rect8” and relevant Hecht’s fittings. (a) and (b) correspond to the pre-irradiation state and exhibit the highest mobility-lifetime product. (c) and (d) are measured after the degradation produced by the sweeping of a 15 keV (c) and 30 keV (d) electron beam over the 100 V-biased “oct9” and “rect8” pixel, respectively. (e) and (f) are measured after the last degradation, with unbiased pixels and a beam of 15 keV (e) and 30 keV (f).

5.5.3 Mobility-lifetime results

The fits show a $\mu\tau$ product that decrease after each degradation step. The largest variation, of about 50%, is observed after the first degradation step with the a-Si:H diode polarized at -100 V. This confirms what observed for the EBIC measurements, i.e. the degradation is independent on the electric field strength in the diode. However, there are not enough evidences to conclude that the weak Si-Si bonds are broken by the ionizing energy, rather than the energy released upon charge recombination. Both mechanisms could actually take place

simultaneously and these measurements do not allow to rule out one mechanism with respect to the other.

The $\mu\tau$ product, extracted from the fitting with Hecht's function, is the smaller one between that of the electron and that of the hole. In intrinsic a-Si:H, the hole $\mu\tau$ product is smaller because the hole mobility is much lower than that of the electron [Hong 95]. The reason why the hole $\mu\tau$ product has a larger influence in the photocurrent signal is because the n-i-p diode is a device with blocking contacts so that the slower carrier determines the diode collection performance. The $\mu\tau$ values obtained from our measurements, $1.5\text{--}4 \times 10^{-7} \text{ cm}^2 \text{ V}^{-1}$ are indeed those relevant to the holes [Kočka 91, Wyrsh 95].

5.6 FTPS measurements to determine the absolute defect density

The measurements of the absolute defect density, before and after the degradation sequence, were performed by FTPS [Vanecek 02, Melskens 08, Holovský 12]. This measurement was also repeated after the annealing at 130 °C for 17h and after the second degradation sequence. The FTPS is a spectroscopic characterization technique that is sensitive to the weak a-Si:H absorption of photon energies below 1.4 eV. The absorption is mostly enabled by the charge transitions to and from midgap states, i.e. the defects. When the a-Si:H diode is biased at a voltage large enough to provide an electric field throughout the i-layer, this absorption generates a photocurrent that is proportional to the defect density. Then, its absolute value is obtained by multiplying the measured photocurrent at a given photon energy by a calibration factor [Wyrsh 91]. The defect density evolution during the degradation study is shown in figure 5.5.

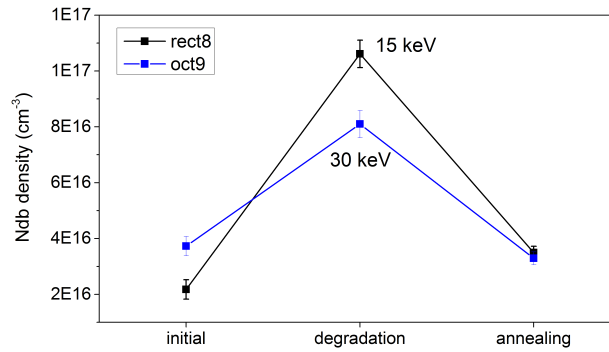


Figure 5.5: Evolution of the defect density, monitored by the FTPS technique, during the degradation study for two TFA pixels, i.e. “rect8” and “oct9”. The beam energy is 15 keV for “rect8” and 30 keV for “oct9”.

The FTPS measurements confirmed that the defect density increased after the first degradation. Interestingly, the degradation induced on pixel *rect8* by the 15-keV electron

beam, which corresponded to an absorbed dose of 225 kGy, produced an illusory defect density larger than that of 30 keV (swept across *oct9*), for which the absorbed dose was 450 kGy. This result is due to an intrinsic limitation of the FTPS technique when a non-uniform defect density is measured. Indeed, as verified with simulations of the electron interaction in a-Si:H, performed with CASINO and shown in figure 5.6, 15-keV electrons deposit all their energy within a thickness of 2 μm , whereas the electrons of 30 keV release their energy at a slower rate and penetrate for almost 8 μm . This is in agreement with the Bethe-Block formula for electrons [Owens 12]. The larger defect density near the p-i interface, generated by the 15-keV electrons, induces the electric field profile to decrease more rapidly in the i-layer, due to the larger density of charged defects near the interface (cf. Chapter 4). Additionally, the FTPS probing light is absorbed at a shallower depth by this larger defect density. Therefore, the larger FTPS signal, for the degradation at 15 keV, can be explained in terms of a larger absorption near the p-i interface and a consequent larger hole collection, which controls the photocurrent signal.

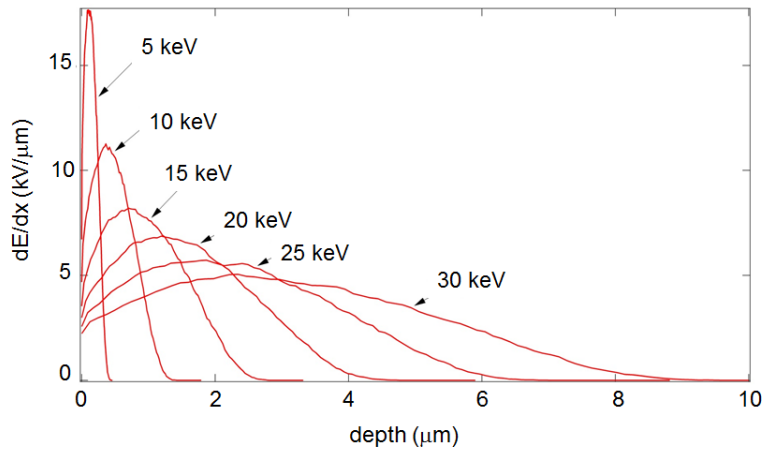


Figure 5.6: *Electron stopping power as a function of depth in a-Si:H, obtained from CASINO simulations.*

After the annealing step at 130 °C for 17 hours, the FTPS measurements confirmed the recovery of the initial a-Si:H status, as shown by the last data set of figure 5.5.

On the contrary, the FTPS measurements after the second degradation sequence showed only a slight variation of the defect density. These results were discarded because we successively realized that the ASIC had been damaged by the many measurements performed at large polarization.

To summarize, we confirmed that the FTPS technique is sensitive enough to detect the a-Si:H degradation induced by the exposure to a keV's electron beam for a few minutes. However, we also showed that its sensitivity is not high enough to extract the absolute defect density when the degradation is not uniform throughout the intrinsic layer.

5.7 ASA and CASINO simulations of the defect generation profile

Despite the limitations of the FTPS technique, we succeeded to estimate the absolute defect density by means of combined simulations, which were performed with CASINO [Drouin 07] and ASA program [Dagamseh 10]. These simulations were aimed at reproducing as good as possible the experimental I-V characteristics measured between the degradation steps and while shining red light of 655 nm on the a-Si:H diode.

The ASA program was developed by the Laboratory of Photovoltaic Materials and Devices, at Delft University of Technology (TUDelft), as an opto-electronic simulator for amorphous and crystalline semiconductor devices. It simulates both dark and illuminated behavior of a complete diode structure with intrinsic and doped layers plus front and rear electrodes. Many a-Si:H material parameters and conduction mechanisms are available for the simulations. In particular, the program accepts a customized defect density profiles as well as an external bias voltage.

5.7.1 Parameters for ASA simulations of the I-V characteristics

The problem we encountered, when defining the parameters of the ASA simulations, was that we could not select a bias voltage larger than 10 V, whereas we had to simulate voltages up to at least 50 V. We solved this problem by downscaling tenfold the thickness of all diode layers, so that we could simulate the experimental average electric field with tenfold lower bias voltage. This meant that we had to downscale also the wavelength of the light shone on the diode, in order to simulate the correct absorption depth in the a-Si:H diode. To do this, we calculated which wavelength corresponded to a tenfold increase in the a-Si:H absorption coefficient. The relevant wavelength shift was from 655 to 525 nm.

The wavelength shift corresponded to an increased parasitic absorption of the two upper layers, i.e. the Indium Tin Oxide (ITO) top electrode and the p-doped a-Si:H layer. To quantify the parasitic absorption at 525 nm, their absorbance curve was calculated between 250 and 1400 nm, with a model developed at PV-Lab [Holman 12]. Since we had no record about the ITO layer deposition parameters, four absorption curves were simulated with two thicknesses of 100 and 150 nm (which are the probable lower and upper limits of the real thickness) and two free-carrier densities of $5 \times 10^{19} \text{ cm}^{-3}$ ("low" in figure 5.7) and $6 \times 10^{20} \text{ cm}^{-3}$ ("high" in figure 5.7). Regarding the p-layer, this has roughly the same absorption as intrinsic a-Si:H, and its thickness was 30 nm. The model results, shown in figure 5.7, evidenced that the downshift from 655 to 525 nm caused an increase in parasitic absorption of about 15%. We decided that a systematic error of 15%, introduced by neglecting this parasitic absorption, was small enough for an approximate comparison between the experimental and simulated I-V characteristics.

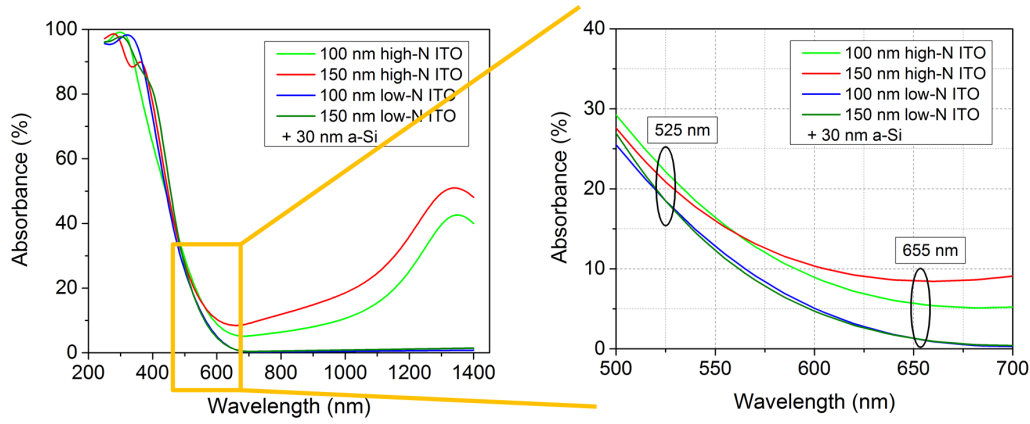


Figure 5.7: Calculation of the parasitic absorption of the ITO and *p*-doped *a*-Si:H layers. For the ITO layer, two free-carrier densities ($5 \times 10^{19} \text{ cm}^{-3}$ for “low” and $6 \times 10^{20} \text{ cm}^{-3}$ for “high”) and two layer thicknesses are investigated.

5.7.2 Comparison of ASA simulations with experimental I-V characteristics

Initially, we simulated the I-V characteristics of the pre-irradiation state. In this case, the defect density was uniform across the *i*-layer and we used the ASA default value of 10^{15} cm^{-3} . The match between ASA simulations and experimental values, shown in figure 5.8, is quite good in terms of current density values. The 15% upward shift of the simulated curve, for taking into account the parasitic absorption of the first two inactive layers, is also shown.

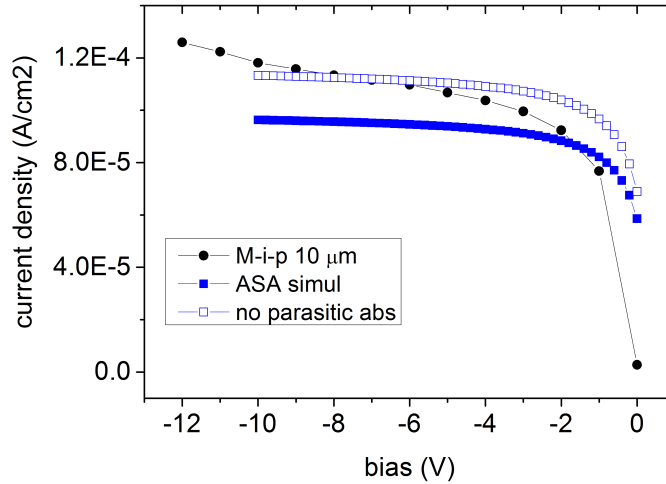


Figure 5.8: Comparison of experimental and simulated I-V characteristics. The curve “no parasitic abs” corresponds to the simulated one, which is shifted upward of 15%. The match in terms of current density is relatively good.

5.7. ASA and CASINO simulations of the defect generation profile

Once we had confirmed the good match for the initial state, we simulated the I-V characteristics of the degraded state. In this case, the defect density profile was calculated as follows. Simulations with CASINO provided the amount of deposited energy versus depth in the i-layer. The relative profile of the defect density scales proportionally to the deposited energy. Consequently, this relative profile was given as an input in ASA and its calibration was performed by means of an iterative process until the optimum match, between the simulated I-V characteristic and the measured one, was attained.

The results are shown in figure 5.9. As can be observed, the simulated curves are not good enough to reproduce the experimental ones for the different degradation steps. Therefore, it was not possible to determine the absolute defect density after the degradation step at -100 V and after that at 0 V. Nevertheless, the match is again quite satisfactory in terms of current densities. **The corresponding absolute defect density (after the whole degradation sequence) was $(2 \pm 1) \times 10^{17} \text{ cm}^{-3}$ for the 15 keV and $(5 \pm 1) \times 10^{17} \text{ cm}^{-3}$ for the 30 keV.** These values are a bit larger than those measured with the FTPS technique, which had a limited sensitivity due to the non-uniform degradation versus depth. Additionally, a larger defect density for the larger beam energy was obtained, as expected.

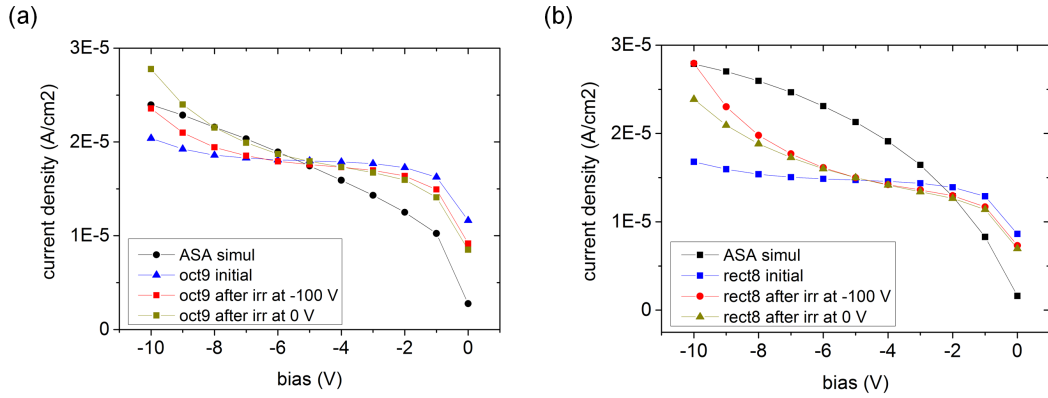


Figure 5.9: Comparison of ASA results, obtained with a simulated exposure time of three minutes to electron beams of 15 keV (a) and 30 keV (b), with the experimental I-V characteristics after each degradation step.

The calibrated defect generation rate is shown in figure 5.10, in terms of the defect density generation rate ($\text{m}^{-3}\text{s}^{-1}$). The generation rate along the y-axis is similar to that of the x-axis (for the symmetry of the generation volume). Therefore, the values along the y-axis were summed altogether in order to plot the generation rate in the bi-dimensional (2D) graphs of figure 5.10. The larger generation rate for 15 keV is simply explained by the much smaller interaction volume, even though the total amount of defects is approximately half that produced by the 30-keV electron beam.

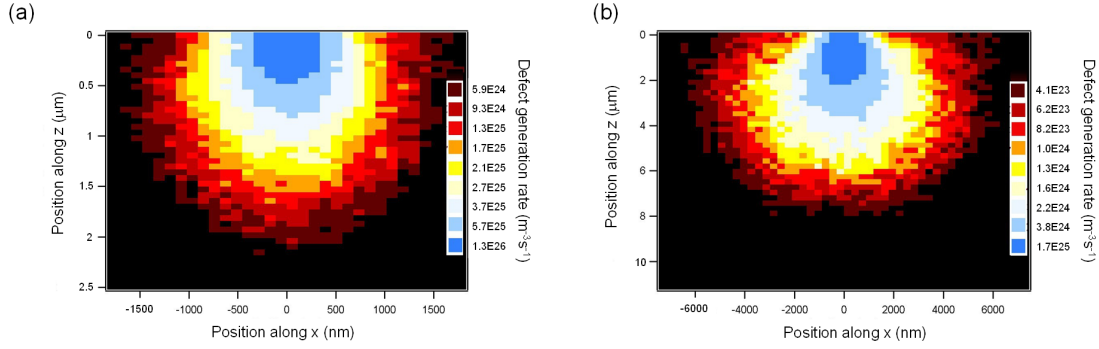


Figure 5.10: Profile of the defect generation rate shown on the x - z plane for an electron beam of 15 keV (a) and 30 keV (b).

5.8 Conclusion

We studied the a-Si:H degradation produced by the SEM beam and the a-Si:H recovery by means of annealing cycles. This degradation is mostly attributed to the generation of additional dangling bonds, i.e. midgap states that act as recombination centers and degrade the material electronic properties.

We confirmed that the degradation under an electron beam of tens of keV produces a remarkable drop of the material electronic properties, in agreement to the literature. In particular, with a series of preliminary measurements, we reported that the EBIC signal, generated by an electron beam of 15 keV and 350 pA, almost disappears after a single beam sweep of 150 μm , which caused an absorbed dose of 31 MGy. We also verified the reversibility of this degradation by annealing the TFA detector at 130 $^{\circ}\text{C}$ for 70 hours and measuring a 70% recovery of the initial induced signal after an absorbed dose of 17 MGy.

Due to this fast degradation dynamics, we defined a specific degradation sequence, which reduced the drop of the EBIC signal as much as possible. In this way, we were able to perform intermediate I-V measurements of the a-Si:H diode when illuminated with light at 655 nm. The fitting of these I-V characteristics with Hecht's function evidenced a $\mu\tau$ product that decreased more after the first degradation step, performed with the diode biased at the large voltage of -100 V, than the steps performed at a smaller bias voltage and with the diode unbiased. The larger degradation after the first step was also confirmed by the EBIC measurements. The observation that the degradation is independent of the diode electric field is an indication that some Si-Si bonds were broken by the direct ionizing energy of the impinging electrons. However, we cannot rule out the possibility that other bonds were also broken by the energy released upon carrier recombination. In order to demonstrate that the Si-Si bonds are broken only by the ionizing energy, future measurements will have to prove that the defect density saturates to a larger level, within the same timeframe, regardless the electric field intensity in the diode.

We also performed FTPS measurements to quantify the variation in absolute defect density, before and after degradation. **We succeeded to verify the defect density increases after an absorbed dose of 225 and 450 kGy, and goes back to the initial value after an annealing at 130 °C for 17 hours.** Nevertheless, the FTPS technique was not sensitive enough to provide the radiation-induced increase in defect states due to their non-uniform generation through the i-layer.

Finally, we carried out combined simulations with ASA and CASINO to extract the defect density generation profile. Although we were not able to extract the absolute defect increase after each degradation step at a different diode polarization, **we obtained an overall (after three minutes of degradation) defect density increase of $(2 \pm 1) \times 10^{17} \text{ cm}^{-3}$ for the 15-keV and $(5 \pm 1) \times 10^{17} \text{ cm}^{-3}$ for the 30-keV electron beam.**

6 Fabrication of amorphous-silicon-based microchannel plates

Abstract. In this chapter, we present the fabrication process of amorphous-silicon-based microchannel plates (AMCPs) and their vertical integration on metallic anodes. Three generations of AMCPs are described, in which structural problems and functional limitations are gradually investigated and solved. The main upgrade of former AMCP prototypes consists in the implementation of a third electrode, besides the top electrode, which is used to bias the AMCP, and the anode, which collects the multiplied electrons. This third grounded electrode is realized near the anode and evacuates the leakage current, which flows through the AMCP bulk because of the large bias voltage.

The mastering of the plasma-enhanced chemical vapor deposition technique, for realizing a-Si:H layers as thick as 100 μm , is presented. The management of the a-Si:H large intrinsic stress, due to this exceptional thickness, is coped by the optimization of the deposition parameters and the implementation of techniques for improving the layer adhesion. The channel micromachining is performed by deep reactive ion etching, which enabled a maximum aspect ratio of 13.5:1 to date, but cannot provide a channel bias angle.

6.1 Motivation and prior art

Conventional microchannel plates (MCPs) are made of an insulating lead-glass structure [Wiza 79]. A semiconducting layer on the channel surface is realized by the hydrogen firing process, to provide the replenishment of the electrons that are dispensed in the multiplication process. Although this fabrication process has reached the maturity after decades of development, it remains rather complex and expensive. It also has some drawbacks such as the hydrogen desorption, which produces ion feedback. The secondary electron coefficient of this semiconducting layer also degrades as a function of the cumulative extracted charge [Lapington 05]. Therefore, alternative fabrication methods were recently proposed.

One consisted in the channel micromachining of a thinned crystalline silicon (c-Si) wafer

[Beetz 00, Tremsin 03]. The main advantage was that the channel geometry could be easily customized by employing the photolithography of the microelectronics industry. Aspect ratios (channel length over diameter ratio) as high as 40:1 were realized by processing the wafer in an electrochemical etching solution. However, c-Si MCPs had the opposite problem of lead-glass MCPs: their structure was too conductive. Therefore, they had to be coated with an oxide layer in order to sustain the large bias voltage needed for the electron multiplication. Successively, an additional semiconducting layer was still needed for the charge replenishment. Despite the good results of electron multiplication, this fabrication process is now discontinued due to engineering problems.

Another alternative fabrication method was the microsphere plate [Tremsin 96b].

A number of recent works [Beaulieu 11, Siegmund 13, Gorelikov 14] presented the possibility to coat different borosilicate glass and plastic MCP structures with conductive and secondary-electron emissive layers. The nano-engineering of these layers is achieved by atomic layer deposition (ALD), which provides secondary electron (SE) coefficients of 1–10. The MCPs processed with ALD exhibited excellent performances as electron multipliers and they outperform lead-glass MCPs in terms of dark count, gain variation after scrubbing and lifetime [Conneely 13, Siegmund 13].

Another recent trend is the development of a bulk conductive glass [Sinor 00, Yi 08, Jingsheng 11], for removing the semiconducting charge-replenishment layer. These MCPs also feature lower outgassing than lead-glass MCP, extended lifetime and less ion feedback, mainly due to a different electrostatic field line geometry [Lapington 05].

We approached to the AMCP development with the same goal of a bulk conducting structure, but we propose to achieve it with a completely different material: hydrogenated amorphous silicon (a-Si:H). The a-Si:H resistivity, within 10^{10} – 10^{12} Ω cm (according to the deposition parameters), is, on the one hand, large enough to sustain large bias voltages without the insulating layer employed in c-Si-based MCPs, and, on the other hand, low enough to provide the charge replenishment without the semiconducting layer employed in lead-glass MCPs.

In this chapter we provide the detailed description of the AMCP development, putting in evidence the fabrication problem we had to face as well as the advantages and the constraints of the vertical integration.

At the beginning of this chapter, the architecture of first-generation (1st-gen) AMCPs, which were available at the beginning of this thesis, and the AMCP fabrication baseline is described. Then, the initial work of this thesis, which was focused on resolving the fabrication problems of 1st-gen AMCPs, is presented. The implemented corrective actions led to the second generation (2nd-gen) of AMCPs. Successively, the most advanced third-generation (3rd-gen) AMCPs are presented, which feature an additional electrode to evacuate the leakage current flowing through the a-Si:H bulk.

Concerning the AMCP fabrication, all the photolithographic processes were performed and optimized by J. Geissbühler. Additionally, all the deep reactive ion etching (DRIE) processes

were done by P.-A. Clerc, affiliated to the Centre Suisse d'Electronique et de Microtechnique (CSEM), in Neuchâtel.

6.2 First generation of AMCPs

At the beginning of this thesis, first AMCP prototypes (1st-gen AMCPs) had been already fabricated and their sensitivity to an electron beam was demonstrated [Wyrsh 05]. Their fabrication process flow, presented below, constituted the baseline on which the following more advanced AMCPs were built. However, these prototypes were affected by structural defects, presented in Section 6.2.2, which had resulted in a low yield of working devices.

6.2.1 Fabrication process of 1st-gen AMCPs

The most important feature of the MCPs, which constitutes the main difference with respect to conventional MCPs, is that AMCPs are not stand-alone structures, but are fabricated on a substrate. This is necessary because a-Si:H, which is the main material employed for their fabrication, is produced by plasma-enhanced chemical vapor deposition (PE-CVD) on a substrate. The need for a substrate represents a limitation, as it eliminates the possibility of stacking two or three AMCPs on top of one another, but it is a key strength as well. Indeed, we here aim at the fabrication of AMCPs that are vertically integrated on specific substrates, such as application-specific integrated circuits (ASICs). In this way, the performances of the AMCP can be combined with the in-situ data processing of the ASIC.

The fabrication process flow of the 1st-gen AMCPs is shown in figure 6.1. It can be divided in three main phases. The deposition of the AMCP layer stack. The reactive ion etching (RIE) of the AMCP layer stack, where this is not needed. The channel micromachining by deep reactive ion etching (DRIE). A detailed description of each step is discussed below.



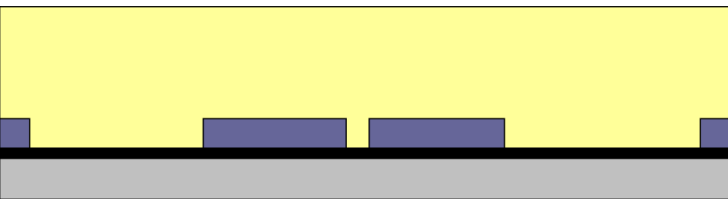
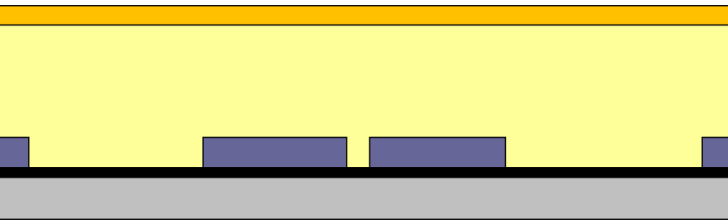
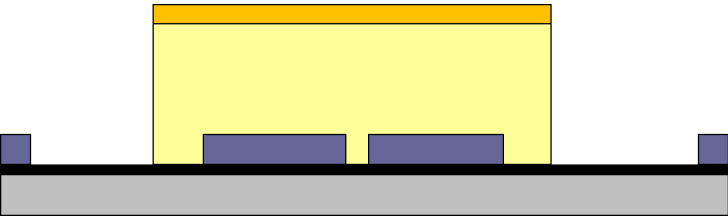
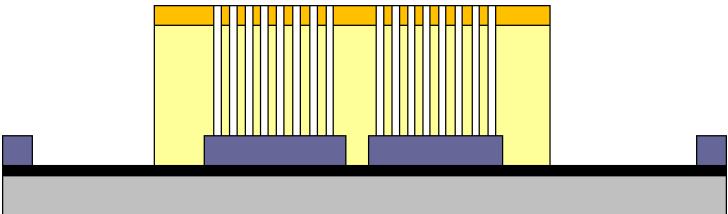
Wafer cleaning and passivation with 1.5 μm of SiO_2	
Evaporation of an aluminum layer, 100 nm thick, and patterning into independent anodes and bonding pads (at the two extremities)	
PE-CVD of a-Si:H, 60–100 μm thick	
PE-CVD of <n> $\mu\text{c-Si:H}$ electrode, 1 μm thick	
Mesa patterning by RIE for stress release and release of pads for wire bonding	
DRIE for channel micromachining	

Figure 6.1: *Process flow for 1st-gen AMCPs, which constituted the baseline also for the following generations.*

AMCP layer stack deposition

The substrates, unchanged throughout all AMCP generations, are four-inch polished c-Si wafers. Their doping and purity is not of particular concern for the AMCP fabrication, as they provide only the mechanical support. Their thickness was selected to be 0.5 mm to guarantee a certain degree of mechanical stiffness and to contain the large intrinsic stress of the a-Si:H thick layer.

The wafers are oxidized to provide an isolating surface, on which many electrodes are fabricated and kept electrically independent from one another. The oxidation, done in a wet

furnace at 800 °C, is set to grow a silicon dioxide (SiO_2), layer 1.5 μm thick. Although a thinner layer could have also guaranteed good electrical isolation, this thickness was chosen in order to provide an effective etching-stop layer for the mesa patterning (described in Section 6.2.1).

On the oxidized c-Si wafer, an aluminum layer with a thickness of about 100 nm is evaporated onto the whole wafer. Eventually, this layer is patterned with a photolithography step and wet etching. The photolithography mask is designed to produce many independent electrodes (the AMCP anodes), each of which is connected, through a 100- μm -wide line, to a pad for wire bonding. The aluminum is etched everywhere else by a selective acid.

Upon aluminum patterning, the wafer is loaded into the PE-CVD reactor for the deposition of the a-Si:H thick layer, which will constitute the structure of the future AMCP. The PE-CVD principles are described in Chapter 3. The deposition of a-Si:H layers with thicknesses of up to 100 μm is a complex process in terms of stress management, which was mastered at PV-Lab [Chabloz 96] and tailored, in this thesis, for the development of AMCPs. The PE-CVD parameters were optimized for high deposition rates, up to 20 $\text{\AA}/\text{s}$, so as to limit the deposition time to about 14 hours. The gas precursors are silane (SiH_4) and hydrogen (H_2) with a SiH_4 to H_2 ratio between 3 and 4. These parameters yield an a-Si:H of a slightly lower quality with respect to that employed in state-of-the-art a-Si:H solar cells. The reason is that a high deposition rate normally results in a less-dense material, due to a large concentration of hydrates, like SiH_2 and SiH_3 , as well as microvoids [Shimizu 05, Stuckelberger 13]. They, in turn, induce larger concentrations of localized states, which act as traps and recombination centers for the carriers and, therefore, are detrimental for the a-Si:H electronic properties. Photothermal deflection spectroscopy (PDS) [Boccaro 80, Wyrsh 91] measurements confirmed a dangling bond (recombination centers) concentration of $2\text{--}5 \times 10^{16} \text{ cm}^{-3}$, larger than that of the state-of-the-art a-Si:H of 10^{15} cm^{-3} [Hata 92].

Nevertheless, the requirements for material quality can be relaxed when a-Si:H is employed in AMCPs. Indeed, for this application, a-Si:H has to sustain large bias voltages and maintaining leakage currents at a reasonable level, which means that we care mainly about the material resistivity, which is not so affected by a larger defect density. The typical resistivity of undoped a-Si:H is about $10^{10}\text{--}10^{12} \Omega \text{ cm}$, which is the case also for the a-Si:H employed in this application, as presented in Chapter 7.

The AMCP layer stack is terminated with an n-doped microcrystalline silicon ($\langle n \rangle \mu\text{c-Si:H}$) layer, deposited in the same reactor. This layer acts as the AMCP top electrode, which could not be made of a metal as this is not allowed in the DRIE system. Since the role of the top electrode is the uniform spreading of the bias voltage (a few hundreds of volts) across the AMCP surface, its thickness was determined by the largest conductivity attainable while keeping the deposition time at a reasonable level (two hours). The resulting thickness of 1 μm corresponds to a sheet resistance of about 500 Ω_{sq} .

Mesa patterning

Once the PE-CVD process is completed, the wafer has a remarkable bowing (clearly visible at naked eye), due to the large tensile stress induced by the thick a-Si:H layer. This prevents the direct micromachining of the channels by DRIE due to problems with spinning the resist of the photolithography and for clamping the wafer in the DRIE system. Therefore, the unneeded portions of the AMCP layer stack are removed before micromachining.

This step, called mesa patterning, is performed with a second photolithography step, followed by the removal of both the $\langle n \rangle$ μ c-Si:H and the a-Si:H layer by RIE. This consists of a chemical dry etching at about 6 nm/s, inside of a plasma reactor, where sulfur hexafluoride (SF_6) and oxygen (O_2) etching gas precursors are introduced. The a-Si:H is etched by the fluorine radicals obtained by the excitation of SF_6 molecules with the free electrons of the plasma. The oxygen helps to limit the etching on the lateral walls, making the attack more directional. The mesa patterning enables also the release of the pads for wire bonding.

Channel micromachining

Once the wafer is flattened, it can be processed with the final photolithography for the channel micromachining. The photolithographic mask has different combinations of hole diameters and gaps for fabricating AMCPs with different geometrical parameters on the same wafer. The one used for the 1st-gen AMCPs featured hole diameters between 3 and 5 μm and gaps between 1.5 and 5 μm . As mentioned before, the channel micromachining is realized by DRIE, using the Bosch process [Marty 05] available at the CSEM in Neuchâtel. This process enables one to realize structures with high aspect ratios, which can reach 100:1 in the case of trenches. The DRIE is similar to the RIE used for the mesa patterning, but here many etching and passivation steps are alternated. In the passivation step, teflon-like material is deposited using octafluorocyclobutane (C_4F_8) as a gas precursor. In the following etching step, the ions drift inside the channels according to the electric field direction and remove the passivation layer at the bottom of the channels much faster than at the lateral channel surface. Once the passivation layer is removed, the fluorine radicals start etching the a-Si:H again, whereas the channel lateral surface is still protected by the teflon-like layer. This enables one to achieve the high aspect ratio mentioned before. When long and narrow channels have to be etched, the DRIE parameters have to be finely tuned in order to avoid channels with a slightly funnel shape, as those obtained at the beginning of the AMCP development and shown in figure 6.2(a). The main limitation of this channel micromachining technique is the impossibility to provide the channels with a bias angle. The relevant consequences on the electron multiplication are presented in Chapter 8. It is worth mentioning that a similar dry etching technique [Horton 90] and streaming electron cyclotron resonance etching (SECRE) [Shank 95] were already employed to micromachine channels in a c-Si wafer at the beginning of the 90s'. Nevertheless, these developments were eventually no longer pursued.

In conclusion, 1st-gen AMCPs had a relatively simple architecture, as shown in figure 6.2(b), with channels micromachined through the AMCP layer stack until to the anode. The electron

multiplication is provided by the electric field, which is set by the biased $\langle n \rangle$ $\mu\text{c-Si:H}$ electrode with respect to the grounded anode. The leakage current that flows through the a-Si:H bulk, due to the large bias voltage, is collected at the anode as well, which complicates the characterization, as discussed in Chapter 8.

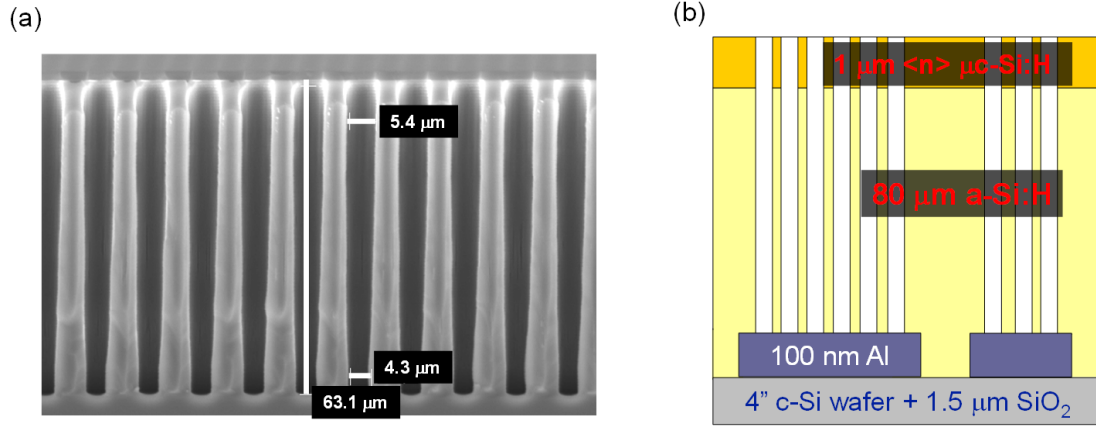


Figure 6.2: (a) SEM micrograph of one AMCP with channels micromachined by DRIE, which was not optimized yet and yielded a slightly funnel structure. (b) schematic of 1st-gen AMCP architecture. The AMCP layer stack is deposited on many independent aluminum anodes of different sizes. The electron multiplication takes place between the biased $\langle n \rangle$ $\mu\text{c-Si:H}$ electrode and the grounded anode.

AMCP test structures

On one four-inch wafer, 20 AMCP test structures and 7 sacrificial structures are realized, as sketched in figure 6.3(a). The sacrificial structures are eventually cleaved and imaged in cross-sectional view with a scanning electron microscope (SEM), to analyze the quality of the channel micromachining (e.g. in figure 6.2). Every test structure, sketched in figure 6.3(b), features 24 independent AMCPs with three active areas of 0.25, 1 and 4 mm^2 . The mesa patterning removes the AMCP layer stack outside of the area highlighted in orange, labeled “AMCP island”. In this way, the aluminum pads for wire binding are freed on either side.

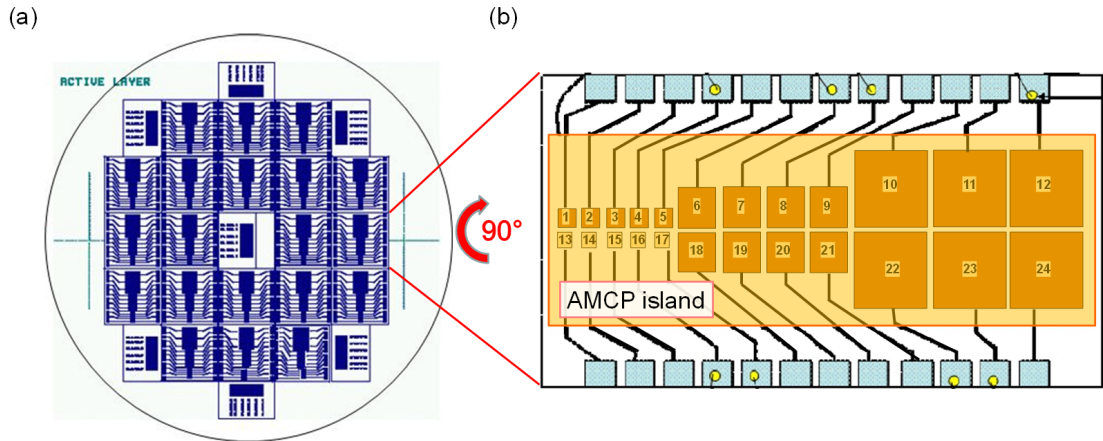


Figure 6.3: (a) Sketch of a four-inch wafer with 20 AMCP test structures plus sacrificial structures (on the edges and in the middle) for SEM micrographs. (b) Sketch of a test structure with 24 independent AMCPs in three sizes: 0.25, 1 and 4 mm². The rectangular area highlighted in orange (labelled “AMCP island”) corresponds to the zone where the AMCP layer stack is preserved, whereas it is etched everywhere else to free the pads for wire bonding.

6.2.2 Fabrication problems of 1st-gen AMCPs

The fabrication of 1st-gen AMCPs suffered a low yield of functional AMCPs due to structural defects. The three major causes of these defects were

1. An uneven thickness of the AMCP layer stack across the wafer, which made problematic the channel etching down to the anode for all test structures;
2. Columnar defects, which reduced the AMCP sensing area and occasionally led to enhanced leakage currents; and
3. The collapse of the entire AMCP layer stack for a few channel diameter–gap combinations.

The first problem was caused by a different a-Si:H deposition rate across the wafer, which produced a thicker a-Si:H layer at the wafer edge. This was very problematic because the residual, non-etched a-Si:H layer charged during electron multiplication and hindered the measurement of the electron multiplication, as discussed in Chapter 8. SEM micrographs confirmed that not-fully-etched channels were often the case, as shown in figure 6.4, in which the red line highlights the thickness of the residual a-Si:H on the anode.

With respect to the second problem, examples of the columnar defects are shown in figure 6.5. Their occurrence was attributed to the presence of bubbles in the AMCP layer stack, which locally hindered the uniform spinning of the resist for the channel photolithography. In correspondence of these bubbles, the resist was likely thinner so that it was fully etched during the DRIE process. This, in turn, caused the unwanted etching of circular areas of up to

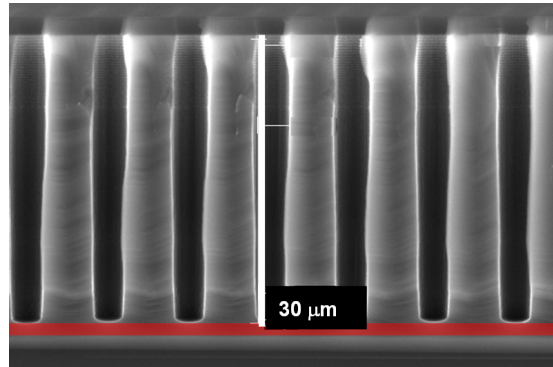


Figure 6.4: SEM micrograph showing channels that do not reach the anode for an $a\text{-Si:H}$ thickness given by the width of the red line.

100 μm in diameter. The result was the holes shown in figure 6.5, which have some residual $a\text{-Si:H}$ in the middle, shaped as a pillar, where the residual resist was probably thicker.

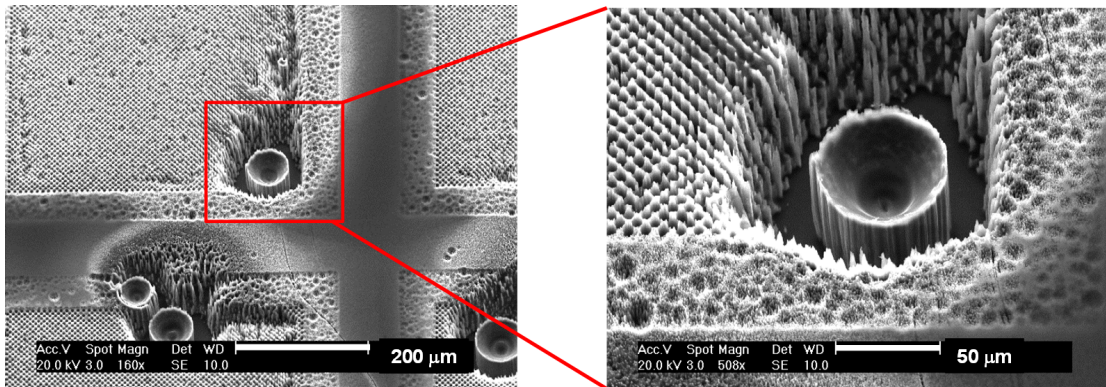


Figure 6.5: SEM images of 1st-gen AMCP columnar defects.

Finally, the partial or total collapse of the AMCP layer stack, due to the bad diameter-gap combinations, is shown in figure 6.6. This problem was generated by the slight channel widening during the DRIE process, which caused the $a\text{-Si:H}$ bulk to be almost completely etched, leaving behind just tiny whiskers. These diameter-gap combinations were simply removed from the following mask design for the channel photolithography.

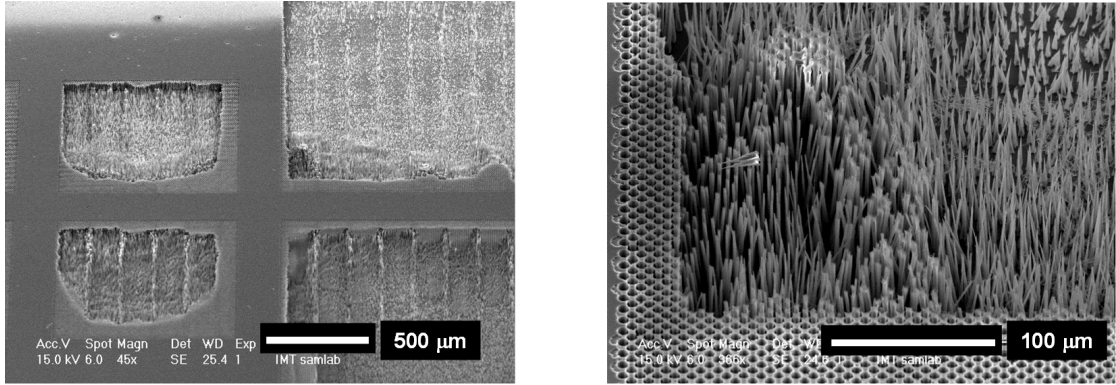


Figure 6.6: SEM images of the collapse of the AMCP layer stack due to channels that were too close to one another.

6.3 Second generation of AMCPs

In this thesis, the research on AMCPs started with a double aim: to solve the structural problems discussed above, and to enhance the channel aspect ratio, i.e. the length-over-diameter ratio, as the gain grows exponentially with it. The first round of corrective actions we implemented yielded the 2nd-gen AMCPs.

The problem of an uneven thickness of the AMCP layer stack across the wafer was not trivial to solve. A simple increase of the DRIE process time (for etching all channels down to the anode) could not be adopted for two reasons. First, this could have resulted in partially merged channels (due to the channel lateral widening) and, second, the aluminum anodes in the wafer center (where the AMCP layer stack was thinner) would have been exposed for a certain time to the DRIE ions. Consequently, the aluminum would have been slightly etched, causing the contamination of the DRIE chamber.

To solve this problem, we first finely tuned the PE-CVD parameters, mostly the partial pressure and the radiofrequency (RF) power. We succeeded in improving the a-Si:H thickness uniformity from 90 to 95%. Additionally, we upgraded the AMCP architecture with an additional “etching-stop” buffer layer, as shown in figure 6.7. This buffer layer had to be etched at a slower rate than a-Si:H so that the aluminum exposure time to the DRIE process, if any, was minimized. Additionally, the buffer layer had to be more conductive than a-Si:H, to limit possible surface charging at the channel bottom end.

The chosen buffer layer was a particular type of silicon oxide (SiO_x), developed at PV-Lab [Cuony 12], which featured an anisotropic resistivity with an out-of-plane component about five orders of magnitude smaller than in-plane one. This is achieved by a specific deposition regime that promotes the growth of thin conductive nanostructures of quasi-continuous silicon filaments, doped with phosphorous and embedded in a highly resistive SiO_x matrix. Therefore, it was called n-doped microcrystalline silicon oxide ($\langle n \rangle \mu\text{c-SiO}_x$). In addition to its electrical properties, this material exhibited a tenfold slower etching rate than that of

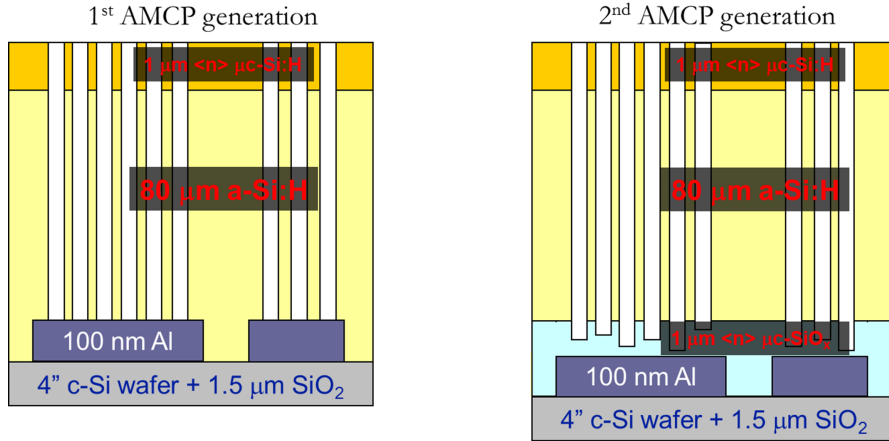


Figure 6.7: Comparison of the 1st - and 2nd -gen AMCP architecture. In 2nd -gen AMCPs, channels terminate within an $\langle n \rangle \mu\text{c-SiO}_x$ buffer layer (colored in light blue in the figure).

a-Si:H, as tested in the RIE reactor for the mesa patterning and shown in figure 6.8. The buffer layer thickness was selected to be $1 \mu\text{m}$, which meant a maximum allowable a-Si:H thickness variation of $10 \mu\text{m}$, if one wanted to prevent the exposure of the aluminum anodes to the DRIE ions. This requirement was easily met by an a-Si:H thickness variation of $5.5 \mu\text{m}$, according to the the maximum a-Si:H thickness of $110\text{-}\mu\text{m}$ and the reduced variability of 5%.

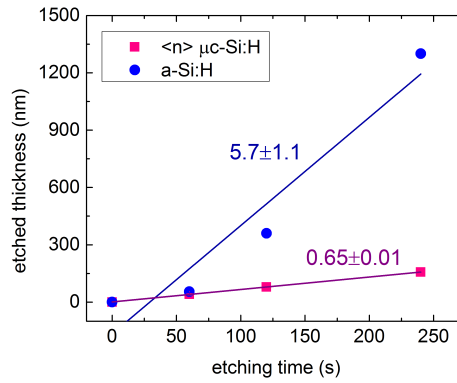


Figure 6.8: Comparison of etching rates for a-Si:H and $\langle n \rangle \mu\text{c-SiO}_x$: The latter is etched almost ten times more slowly.

The electrical characterization of the $\langle n \rangle \mu\text{c-SiO}_x$ buffer layer was limited to the measurement of its out-of-plane conductivity, which was the most important parameter for this application. For this measurement, the following stack was realized: Al/ $\langle n \rangle \mu\text{c-Si:H}$ / $\langle n \rangle \mu\text{c-SiO}_x$ / $\langle n \rangle \mu\text{c-Si:H}$ /Al. The $\langle n \rangle \mu\text{c-Si:H}$ layer provided a better ohmic contact between the $\langle n \rangle \mu\text{c-SiO}_x$ and the aluminum. Additionally, the RIE of the $\langle n \rangle \mu\text{c-SiO}_x$, to free the Al bottom electrode, was performed in two phases to avoid a sharp step between the top and the bottom Al electrode. Instead, about half the thickness of the $\langle n \rangle \mu\text{c-SiO}_x$ was left around the top electrode. This

effectively prevented enhanced leakage paths across the stack, which were suspected to be caused by the undesired deposition of zinc oxide (ZnO), which usually contaminates the RIE chamber. The resistivity measurement, performed in the dark with a residual nitrogen atmosphere of 10^{-1} mbar and a bias of a few volts, resulted in a value of about $10^8 \Omega \text{cm}$. Although this value was about three orders of magnitude lower than that of a-Si:H, it was still rather high to prevent any charging of the channel bottom end. Nevertheless, the recipe was optimized no further because after a few months of fabrication and characterization, it became clear that a more radical upgrade in the AMCP architecture was required.

6.3.1 Showerhead hole traces in 2nd-gen AMCPs

The 2nd-gen AMCPs had channels that always ended within the buffer layer. Additionally, they were almost not affected by the columnar defects anymore, due to the implementation of the $\langle n \rangle \mu\text{c-SiO}_x$ buffer layer. The reason for this improvement was that the $\langle n \rangle \mu\text{c-SiO}_x$ buffer layer improved the a-Si:H adhesion, which, in turn, limited the bubbles formation. A deeper understanding of the a-Si:H adhesion was achieved during the fabrication of 3rd-gen AMCPs and is presented in Section 6.4.2.

The remaining fabrication problem for 2nd-gen AMCPs was induced by the large deposition rate of 20 \AA/s . Indeed, the high rate causes the formation of Si_xH_y clusters [Fridman 96], which react and bond with neutral silane (SiH_4) molecules until they become crystallites of about 2 nm in size. Eventually, these crystallites coagulate and become dust particles, 50 nm in diameter. At that point, particles can no longer be electrostatically trapped in the plasma and move radially towards the electrode periphery. They exit the plasma region and deposit on the reactor wall. The problem was that a number of these dust particles were also embedded in the growing a-Si:H layer. This caused the traces shown in figure 6.9. These traces were found in correspondence to the showerhead inlet holes because the gas precursors pushed the dust particles towards the growing layer. The traces had to be avoided because they hindered the quality of the channel micromachining.

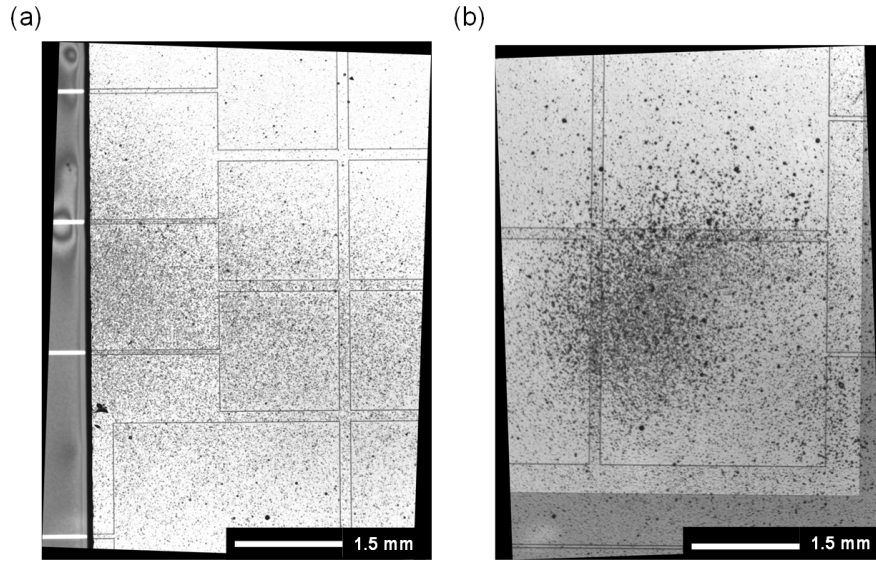


Figure 6.9: *Two images, taken with the optical microscope, of showerhead hole traces originated by the embedment of powder particles in the growing a-Si:H layer.*

6.4 Third generation of AMCPs

The structural improvements of 2nd-gen AMCPs produced devices that could sustain very large bias voltages, up to 800 V, corresponding to electric fields of 10^5 V/cm. However, the resulting leakage current on the anode were on the order of tens of microamperes. This produced to a too large background that hindered any measurement of electron multiplication (cf. Chapter 8). Therefore, it became clear that the AMCP architecture needed a more radical upgrade for decoupling the leakage current from the electron multiplication. This second upgrade yielded the AMCPs of third generation. These represent the state of the art of the AMCP development to date. They enabled us to quantify, for the first time, the electron multiplication and to provide the technology proof of concept. The next two chapters are focused on their electrical characterization and their performances as electron multipliers.

6.4.1 3rd-gen AMCP architecture

The upgrade of 3rd-gen AMCPs mainly consisted of the introduction of a third electrode, as sketched in figure 6.10. The additional electrode is just over the anode and it evacuates the leakage current, whereas the anode retains its function of collecting the multiplied electrons. This upgraded architecture closely resembles the typical assembly of conventional MCPs on readout anodes: The electrode on one side of the plate is biased with respect to the electrode on the either side, which is grounded and evacuates the strip current. The anode, which is physically separated from the plate, collects the multiplied electrons.

Since any vacuum gap is excluded by the AMCP vertical integration on the anode, a dielectric stack is implemented instead. The thorough description of each layer implemented in 3rd-gen

AMCPs is provided below.

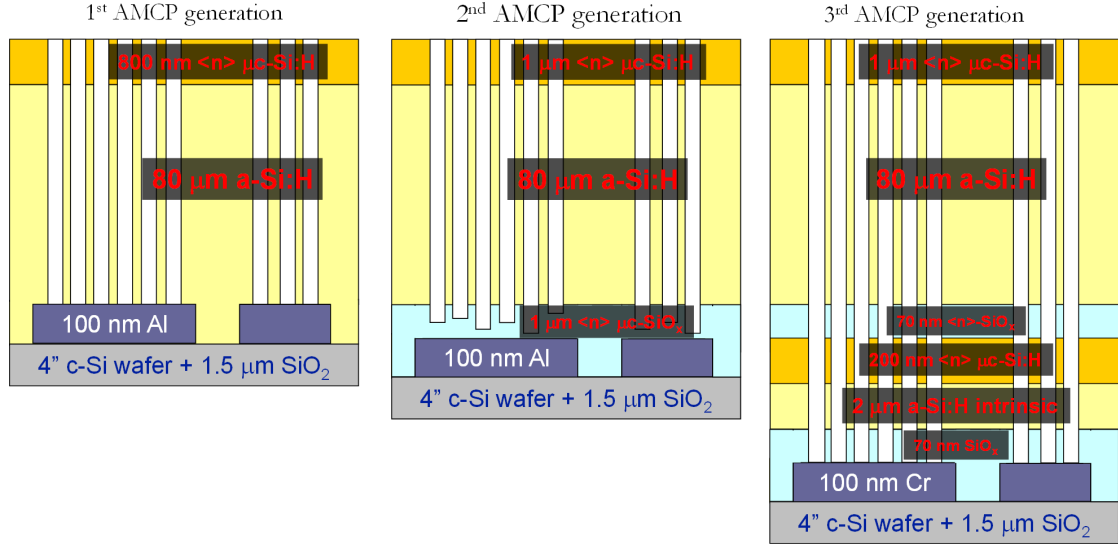


Figure 6.10: Evolution, from left to right, of the AMCP architecture. The upgrade of the third generation mainly consisted of the introduction of a third independent electrode, to decouple the signal of electron multiplication from the leakage current.

Chromium bottom electrode: the anode

In the 3rd-gen AMCPs, the aluminum anode was replaced with a chromium one. The change was motivated by a number of reasons: sputtered chromium has better adhesion than evaporated aluminum, it does not diffuse into a-Si:H at temperatures of about 200 °C and it is more resistant to a number of acids. These were occasionally used upon fabrication completion, for a final cleaning. The fact that the chromium diffuses less into a-Si:H contributed the most for the change. Indeed, a-Si:H was observed to suffer micrometric-sized bumps and bubbles, which were induced by the aluminum spiking in the a-Si:H [Haque 94, Haque 96, Al-Dhafiri 02, Jaeger 10]. This well-known effect is due to the diffusion of aluminum into a-Si:H, which catalyzes its partial crystallization and induces the formation of hillocks. Different metals have been observed to catalyze the reaction [Hultman 87, Bian 93], but aluminum is particularly effective to induce it already at the PE-CVD temperatures of about 200 °C.

Before the chromium sputtering and patterning, the wafer oxidation (SiO₂) was etched in the RIE reactor for two minutes. This increased the substrate roughness by a few nanometers (root mean square) and improved the adhesion of both the chromium and the first PE-CVD layer. Indeed, the intrinsic stress of the a-Si:H thick layer was, at times, so large as to cause the peeling of the AMCP layer stack down to this interface.

SiO_x adhesion layer

The first PE-CVD layer was a SiO_x layer with a thickness of tens of nanometers. Contrary to the second generation, this layer was used uniquely as an adhesion layer. The role of “etching-stop” layer was no longer needed because the channel micromachining was tuned to always reach the anode. Indeed, due to the improved a-Si:H thickness uniformity, the chromium anode was minimally exposed to the DRIE ion bombardment and the chamber contamination minimized. The constraints regarding the out-of-plane SiO_x resistivity were also lifted, so that a standard deposition recipe for a highly resistive SiO_x layer was adopted.

The layer thickness was reduced from the initial value of 150 nm to 10 nm. Indeed, its adhesion properties were retained with a thickness of only 10 nm when the anode thickness was reduced from 150 to 80 nm and the intrinsic stress of the thick a-Si:H layer was minimized, as explained in Section 6.4.2.

a-Si:H decoupling layer

The decoupling layer, between the anode and the intermediate electrode, consisted of a-Si:H, 2 μm thick. The choice of using a-Si:H was driven by its relatively large resistivity (about 10¹¹ Ωcm) and the possibility to tune it, as a function of the deposition parameters. The choice of its thickness was the result of a trade-off. On the one hand, its resistance and the electrical decoupling increases with thickness. On the other hand, this layer reduces the effective channel length that contributes to the electron multiplication. Indeed, both the intermediate electrode and the anode are grounded, so that there is no residual accelerating field between them. The trade-off was sorted out by targeting a drop of the leakage current on the anode by about four orders of magnitude. Taking into account the resistivity difference between a-Si:H and the intermediate electrode, made of ⟨n⟩ μc-Si:H (presented below), a few hundreds of nanometers would have been enough. However, we chose a thickness of 2 μm to be conservative and prevent possible pin-hole defects. These are generated when an object, like a dust particle, falls on the substrate prior to the PE-CVD process. Eventually, this can cause a localized shunt and, in the case of AMCPs, increase the leakage current on the anode. SEM micrographs of the decoupling layer are shown in figure 6.11.

⟨n⟩ μc-Si:H intermediate electrode

The intermediate electrode, shown in figure 6.11, has to be as conductive as possible to effectively evacuate the leakage current and reduce the residual leaking to the anode. It also has to be compatible with the DRIE process. The choice was a phosphorous-doped (n-doped) microcrystalline silicon layer (⟨n⟩ μc-Si:H) with a thickness of 200 nm and a relevant sheet resistance of about 1 kΩ.

In order to access and connect the intermediate electrode (after the AMCP layer stack deposition and the mesa patterning), a 30-nm-thick chromium layer was sputtered after the deposition of the ⟨n⟩ μc-Si:H layer. Eventually, the chromium was patterned in pads that

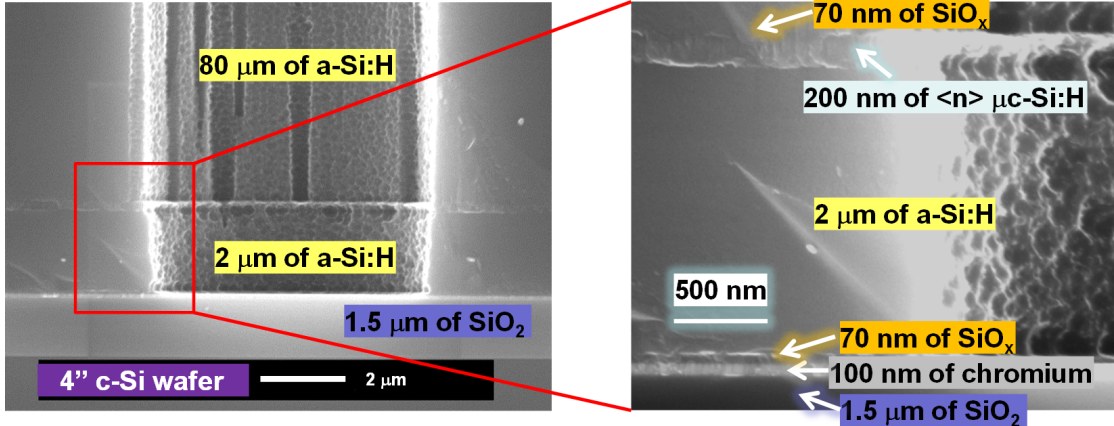


Figure 6.11: SEM micrograph showing the bottom portion of a channel of the 3rd-gen AMCP. In the magnified view on the right, every layer can be clearly identified, apart from the adhesion layers, which are too thin.

were partially inside the “a-Si:H island” of the mesa patterning, over the anode number 12 (figure 6.3(b)). Consequently, channels were no longer micromachined in correspondence of this anode. The pad portion that was outside the “a-Si:H island” enabled us to bond the intermediate electrode.

<n> SiO_x adhesion layer

After the chromium deposition and patterning, the wafer was loaded again in the PE-CVD reactor and the deposition continued with a <n> SiO_x adhesion layer, 80 nm thick. Contrary to the previous adhesion layer, this one was doped with phosphorous to increase its conductivity and make it more similar to that of a-Si:H. The aim was to avoid an uneven distribution of the accelerating field, set by the voltage drop along the channel surface, but this precaution revealed to be unnecessary due to the limited layer thickness (cf. Chapter 7).

a-Si:H thick layer for electron multiplication

The main a-Si:H layer was deposited with a thickness that ranged between 50 and 100 μm. Its deposition was more complicated than the previous generations’ because its large intrinsic stress initially caused localized peeling at the interface between the intermediate electrode and the adhesion layer. By finely tuning the deposition parameters, we succeeded to reduce the a-Si:H intrinsic stress. According to the literature [Chabloz 96], a balance between tensile and compressive stress can be achieved for a set of plasma excitation frequencies and deposition temperatures. As in our case the excitation frequency was always kept at 70 MHz, to provide a high deposition rate, the tuning was focused on the optimum process temperature. This optimization is detailed in Section 6.4.2.

$\langle n \rangle$ $\mu\text{c-Si:H}$ top electrode

The deposition sequence terminated with the $\langle n \rangle$ $\mu\text{c-Si:H}$ top electrode with a thickness ranging from 0.7 to 1.5 μm . Its sheet resistance is about 500 Ω_{sq} .

In figure 6.12, the cross sectional view of the AMCP upper part, already processed by the DRIE, shows a portion of the thick a-Si:H layer and the top electrode.

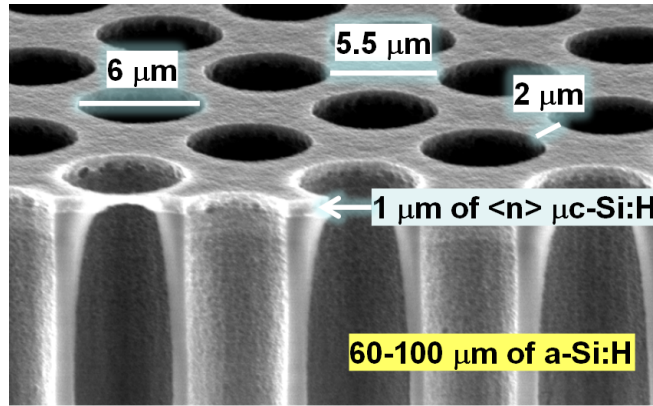


Figure 6.12: SEM cross section of the uppermost portion of a 3rd-gen AMCP. The $\langle n \rangle$ $\mu\text{c-Si:H}$ top electrode can be clearly distinguished from the main a-Si:H layer.

6.4.2 Resolution of 2nd-gen fabrication problems

The showerhead hole traces shown in figure 6.9 were prevented in the third generation with a more uniform gas injection across the electrode area. Indeed, the traces were found to be concentrated in the wafer center, an indication that gas precursors were mostly injected near the electrode center. Simulations of gas flow through the showerhead, performed by Dr. L. Sansonnens, confirmed the experimental observations and provided useful indications for the design of the optimal showerhead geometry. Once realized, we succeeded to deposit trace-free a-Si:H layers.

A new photolithographic mask with more spaced channels was realized to take into account the channel widening, also for future a-Si:H layers thicker than 100 μm . Additionally, holes were removed for a large AMCP (for the intermediate electrode electrical connection), as well as for a medium and a small one. In this way, we could measure the electrical characteristics of the AMCP layer stack with and without holes, in the same test structure (cf. Chapter 7).

The last two photolithographic masks and the different a-Si:H layer thicknesses enabled us to realize 3rd-gen AMCPs with aspect ratios between 6:1 and 13.5:1. A few examples of channel diameters and gaps, relevant to 3rd-gen AMCPs, are shown in figure 6.13.

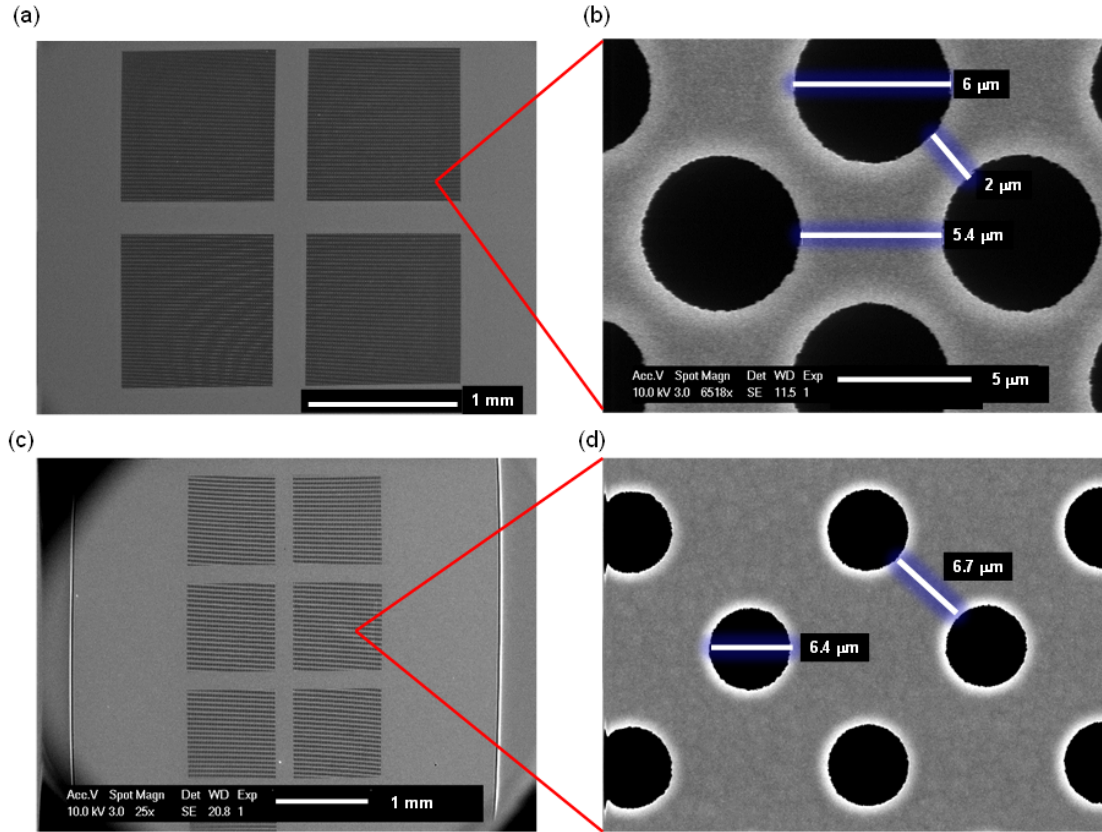


Figure 6.13: (a) and (b) are images of an AMCP whose photolithographic design featured 5- μm holes and 3- μm gaps. (c) and (d) show another AMCP whose photolithographic design featured 4- μm holes and 9.5- μm gaps. The channel widening, compared to the nominal value, is an unavoidable effect of the channel micromachining.

a-Si:H bubbling and tensile stress

As mentioned before, 3rd-gen AMCPs demanded a lot of effort to manage the large intrinsic stress of the thick a-Si:H layer, which caused an overall tensile stress on the wafer and affected the adhesion of the layers beneath it. The stress was managed mostly by modifying the PE-CVD deposition temperature. It is important to point out that the real wafer temperature was most likely higher than the chosen set point, because high deposition rates are known to increase the substrate temperature [Van den Donker 06]. Therefore, all the temperature values (set-point values) mentioned below were probably lower than that of the wafer. We observed that for temperatures below 205 °C, the a-Si:H stress was tensile, which caused, after a deposited thickness of only 10 μm , a wafer bowing that was visible to the naked eye. This hindered the resist spinning for the following mesa patterning step. However, when the temperature was increased to 215 °C, the AMCP layer stack started to exhibit bubbles. These exploded after a certain deposition time, leaving behind craters. Examples of this localized peeling are shown in figure 6.14.

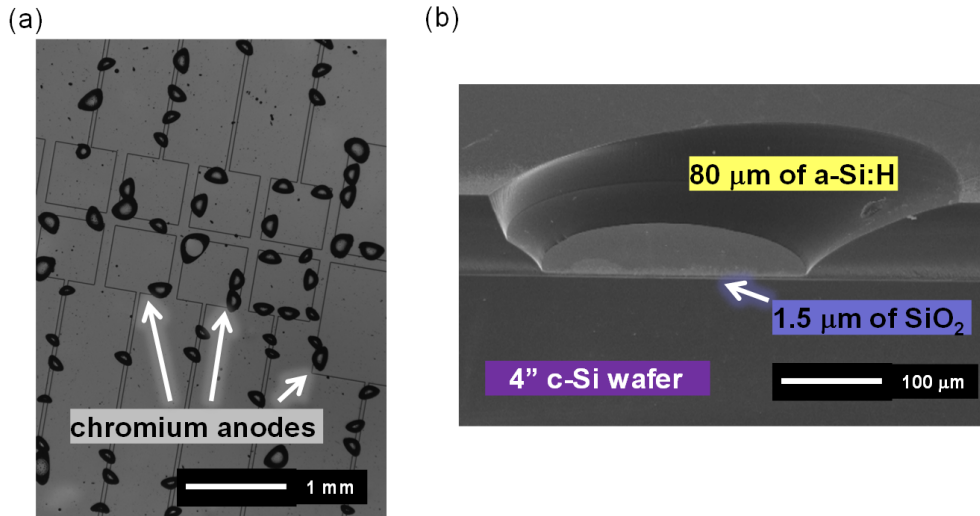


Figure 6.14: (a) *localized peeling, which can be concentrated at the anode edges, if the chromium thickness is more than 150 nm. Otherwise, they are less numerous and randomly distributed.* (b) *cross-sectional view of one of these craters.*

This type of peeling was probably the cause of columnar defects affecting the 1st-gen AMCPs (shown in figure 6.5). In the second generation, this peeling was limited by the introduction of the $\langle n \rangle \mu\text{c-SiO}_x$ buffer layer, even though the reason for the $\langle n \rangle \mu\text{c-SiO}_x$ beneficial effect was not fully understood at that time. However, in the third generation, it became clear that the localized peeling was inversely proportional to the SiO_x thickness. This and other experimental evidences could finally be explained by a model of hydrogen diffusion reported in the literature at the beginning of the 80's [Shanks 81]. Basically, **the localized peeling originated from the diffusion of atomic hydrogen to the boundary of the a-Si:H layer. Whilst the hydrogen atoms that reach the upper surface simply leave the layer, those gathering at the bottom interface gradually form molecular hydrogen. When the amount of the hydrogen molecules attains a critical value, the pressure exerted on the layer causes the localized peeling, with the bubbles formation.** Occasionally, the bubbles explode leaving behind craters like those shown in figure 6.14.

More recent papers [Mishima 88, Bustarret 91, Acco 96, Xu 09] provide an exhaustive description of this phenomenon, pointing out that it can be suppressed by minimizing the hydrogen content and that its probability to occur increases with the a-Si:H thickness. Also, it was reported that the a-Si:H deposition on a metal or a buffer layer like SiO_x could prevent such peeling and that the peeling was favored under a vacuum of 10^{-6} mbar. We confirmed most of these observations throughout the AMCP development. For instance, the localized peeling increased with the thinning of SiO_x adhesion layer and it was, otherwise, fully prevented with a thickness above 100 nm. Moreover, no localized peeling was observed above the chromium islands, used for contacting the intermediate electrode.

The hydrogen diffusion is a temperature-activated process. In the literature, localized peeling is observed to start at 300 °C. We reproduced the localized peeling with post-deposition

thermal cycles on a hot plate in air and we confirmed its occurrence at 300 °C. The surprising fact was that the peeling occurred at temperatures as low as 215 °C during the PE-CVD process. This could partly be explained by a residual pressure of about 1 mbar (peeling is enhanced in vacuum) and a real substrate temperature higher than the set point.

We reduced the localized peeling with a couple of expedients. The first consisted in the implementation of a particular temperature profile during deposition, which was 205 °C for the first 45 minutes and 215 °C for the remaining several hours. The former deposition phase, at a lower temperature, provided an a-Si:H layer with more tensile stress but without the problem of localized peeling. The latter phase did not increase the tensile stress any further and the localized peeling was limited a great deal. A possible explanation for this improvement is the absence of a hydrogen concentration gradient throughout the a-Si:H layer, which limited the hydrogen diffusion towards the bottom interface. Indeed, hydrogen diffusion tends to accumulate in areas of larger concentration and to form clusters [Acco 96]. When these are missing, the diffusion may preferentially occur towards the growing surface and effuse from the layer.

The other corrective action for reducing the localized peeling consisted of reducing the hydrogen content in a-Si:H. The last deposition of this thesis confirmed that increasing the SiH₄ concentration—which corresponds to an overall smaller hydrogen content since the H₂ gas flow was kept constant—from 66 to 80% successfully prevented the peeling. However, the lower hydrogen content yielded a denser material, which increased again the tensile stress [Kroll 96]. Therefore, future depositions with this larger SiH₄ concentration will have to be carried out at higher temperatures.

Advanced AMCP test structures

Once the deposition of the AMCP layer stack was completed, two fabrication steps were added in the third generation with respect to the baseline of figure 6.1.

The first was implemented during the mesa patterning to shield the chromium lines between the anodes and the bonding pads from the parasitic collection of incoming photoelectrons. Indeed, in the measurements with the UV setup, presented in Chapter 8, photoelectrons emitted from a photocathode are accelerated towards the test structures and attracted by any point at ground potential, not only by the bottom of the channels. The parasitic collection makes one underestimate the gain because not all the calibrated photoelectrons are multiplied in the channels. Although the parasitic collection of the bonding pads is screened by other means (cf. Chapter 8), the chromium lines were shielded with a not fully etched AMCP layer stack. This was achieved by performing the mesa patterning in two steps, as shown in figure 6.15: After a first partial etching, most of the test structure surface (except in correspondence of the bonding pads) was covered with a lacquer, which protected the stack during the second phase of the mesa patterning.

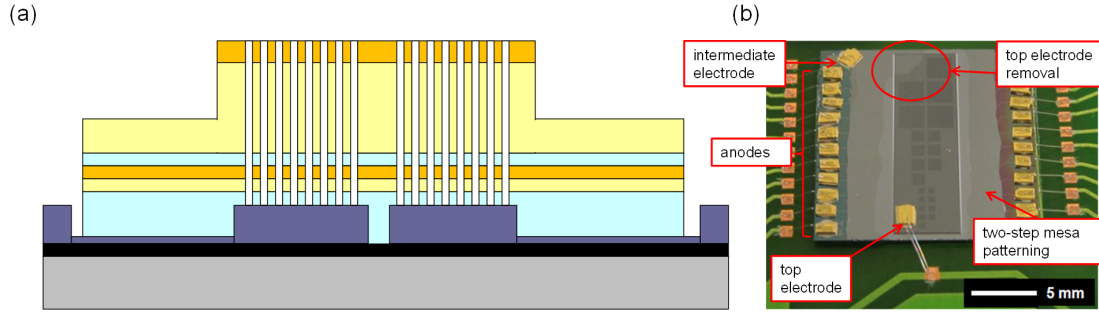


Figure 6.15: (a) drawing of the cross-sectional view of the test structure with a mesa patterning that was performed in two steps so that some residual layer stack shielded the chromium lines, between the anodes and the bonding pads, from parasitic photoelectron collection. (b) photograph of test structure of 3rd-gen AMCPs with 21 independent AMCPs of three different sizes. The grey regions on either side of the “AMCP island” corresponds to the partially etched layer stack. The AMCP bias voltage was evenly spread over the central rectangular area, except in the top left corner, where the top electrode was etched.

The other additional fabrication step consisted in the partial removal of the $\langle n \rangle$ $\mu\text{c-Si:H}$ top electrode in the top left corner of the “AMCP island”, in correspondence of the anode number 12 (figure 6.3(b)). This removal can be identified by the slightly brighter grey color in figure 6.15(b). This area of the removed electrode is slightly larger than that of the chromium pad for the intermediate electrode connection. Without this additional step, the leakage current, induced by the large bias voltage, concentrated in that area and once even caused a thermal runaway, which partially melted the a-Si:H, as shown in figure 6.16.

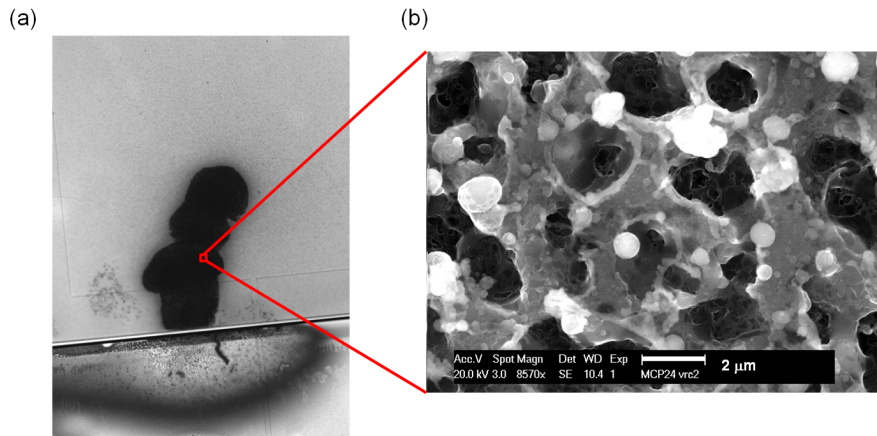


Figure 6.16: (a) optical microscope and (b) SEM images of the damaged a-Si:H layer due to a thermal runaway, induced by a bias voltage of -420 V and located in the region where the a-Si:H thick layer is sandwiched between the top electrode and chromium pad for intermediate electrode bonding.

6.5 Outlook

There are a number of possible improvements for the fabrication of future AMCPs.

1. To increase the thickness of the main a-Si:H layer to enhance the aspect ratio, upon definition of a new temperature profile for the latest a-Si:H deposition recipe, with a larger silane concentration.
2. To implement a thinner and more resistive a-Si:H decoupling layer to minimize the inactive channel portion (regarding the electron multiplication), whilst retaining the same anode isolation. A larger a-Si:H resistivity can be achieved by adding a gas precursor containing carbon [Janz 06], such as methane (CH_4), which widens the a-Si:H bandgap.
3. To engineer the channel aperture with a funnel structure by means of a tailored RIE process. This should facilitate the electrons entrance into the channels, with a consequent enhancement of the AMCP active area.
4. To deposit a secondary-electron emissive (SEE) layer by atomic layer deposition to enhance the AMCP gain. A first attempt was already done at the end of this thesis and provided first promising results (cf. Chapter 8). Possible SEE materials are alumina (Al_2O_3) and magnesium oxide (MgO).
5. To deposit a photocathode material directly on top of the AMCP surface. This may increase the number of photoelectrons that have the first collisions near the channel entrance and boost the electron multiplication. Possible photocathodes range from simple metals (wavelength sensitivity until 200–266 nm), like gold (until 266 nm), to alkali halides (until 240–300 nm) for larger quantum efficiency, like caesium iodide (CsI , 266 nm) [Fraser 84] and bi- (600–800 nm) [Nakamura 10] and multi-alkali (600–1000 nm) [Siegmond 06]. Finally, there are the materials with negative electron affinity (530–930 nm) [Martinelli 74].

Besides the proposed improvements, AMCPs will be vertically integrated on application-specific integrated circuits (ASICs), targeting a first real application.

6.6 Conclusion

In this chapter, we presented the development of a novel fabrication technique for MCPs, based on a-Si:H. Three AMCP generations were the result of a continuous effort to improve the device performances. The most important upgrade was the introduction of an intermediate electrode, near the anode, to evacuate the leakage current flowing through the AMCP bulk. This configuration closely resembles the assembly of a conventional MCP above the readout anode: Two electrodes, on either side of the plate, are employed to set the accelerating electric field in the channels, whereas the anode collects the multiplied electrons. The vacuum gap

between MCP and anode is replaced, in vertically integrated AMCPs, by an insulating layer that decouples the anode from the AMCP grounded electrode.

We detailed how we mastered the deposition of a-Si:H layers as thick as 100 μm , with a relative thickness uniformity of 95% across the four-inch wafer. We optimized the PE-CVD for deposition rates as high as 20 $\text{\AA}/\text{s}$, which contained the deposition time to about 14 hours (for 100 μm of a-Si:H). We realized a new showerhead for limiting the embedment of the silicon-based powder in the growing film. We developed effective corrective actions to limit the a-Si:H intrinsic stress, mainly by tuning the process temperature. We understood the mechanism of localized peeling, caused by the hydrogen diffusion in the film, and we prevented it by decreasing the total hydrogen concentration in the gas precursors. We improved the layer adhesion by performing a wafer surface treatment by reactive ion etching and by implementing SiO_x adhesions layers.

Concerning the channel micromachining, we increased the spacing between channels, to tackle the lateral widening during the DRIE.

In conclusion, we demonstrated the feasibility of the AMCP vertical integration on metallic anodes, which simulate the metallization pads of a future ASIC. This paves the road to new monolithic detectors, whose active layer is a vacuum-based detector, an amorphous-silicon-based microchannel plate.

7 Electrical characterization of AMCPs

Abstract. In this chapter, the electrical characterization of third-generation amorphous-silicon-based microchannel plates (AMCPs) is presented. The AMCPs are shown to withstand an electric field of 7×10^4 V/cm, which is larger than the maximum value usually employed in conventional MCPs. This proves the excellent a-Si:H capability in sustaining large bias voltages, without electrical breakdown.

The main upgrade of the third generation, namely the implementation of the intermediate electrode, enables us to reduce the leakage current on the anode by more than five orders of magnitude.

The current-to-voltage (I-V) characteristics of the multiplying stack, between the top and the intermediate electrode, and the decoupling stack, between the intermediate electrode and the anode, are measured. They both show that the channel surface is a preferential conduction path at large bias voltages, which is expected to be beneficial for the charge replenishment during the electron multiplication. Additionally, the decoupling stack shows a rectifying behavior at low biases, with a negative voltage applied to the intermediate electrode for the direct polarization. This explains the residual leakage current on the anode of a few picoamperes, when the AMCP is biased to -500 V, as this is induced by the voltage rise—with respect to the reference ground, which polarizes directly the decoupling stack—of the intermediate electrode during the leakage current evacuation.

7.1 Motivation

Before presenting the results of the electron multiplication in AMCPs (in the next chapter), it is important to evaluate the electrical behavior of the AMCP in dark. In this way, the origin of the dark currents across the structure and their possible benefits and detriments can be clarified. Ideally, one wants a large leakage current across the multiplying stack, for enhancing the charge replenishment, and no leakage current across the decoupling stack (on the anode), for increasing the sensitivity to the electron multiplication. The electrical characterization of the third-generation (3rd-gen) AMCPs, presented in this chapter, shows a scenario not far from this ideal case.

The chapter is structured as follows. Initially, an overview of the 3rd-gen AMCP architecture is provided, which serves as a reference for the rest of the chapter as well as for the interpretation of the electron multiplication dynamics presented in Chapter 8. Then, the measurements of dark conductivity for most of the resistive layer adopted in the AMCP structure are presented. This is followed by the I-V measurements of the multiplying stack, which aims at evaluating the hydrogenated amorphous silicon (a-Si:H) capability to sustain large bias voltages and at assessing the relative amount of leakage current that can be exploited for the charge replenishment. Then, the I-V measurements of the decoupling stack are analyzed, with particular focus on the comprehension of the origin and the quantification of the residual leakage current on the anode. Finally, the reduction of the leakage current on the anode, by the implementation of the intermediate electrode, is presented.

7.2 Overview of 3rd-gen AMCPs

In this section, we briefly summarize the main features of the 3rd-gen AMCP architecture, which was thoroughly described in Chapter 6 and corresponds to the most advanced device configuration developed in this thesis. This architecture enabled us to provide the device proof of concept, in terms of electron multiplication, presented in the next chapter.

The 3rd-gen AMCP architecture is shown in figure 7.1, together with SEM cross section images of the upper and lower part of the AMCP. Analyzing the structure layer by layer, starting from the top, there is

1. A top electrode, which is made of an n-doped microcrystalline silicon layer ($\langle n \rangle \mu\text{c-Si:H}$), 1 μm thick. It is used to apply the bias voltage and set the accelerating electric field in the channels for the electron multiplication.
2. An a-Si:H layer, whose thickness ranges between 60–100 μm . This is the core of the AMCP, in correspondence of which the electron multiplication takes place. The thick a-Si:H does not only work as the AMCP structural support, but also replenishes the electrons dispensed in the multiplication process.
3. A 70-nm-thick n-doped silicon oxide ($\langle n \rangle \text{SiO}_x$) layer for improving the adhesion of the thick a-Si:H layer, which can have a large intrinsic stress and peel in correspondence of a weak interface. It is doped to have a resistivity more similar to that of a-Si:H and assure a uniform accelerating electric field in the channels (set by the voltage drop along the channel).
4. An intermediate $\langle n \rangle \mu\text{c-Si:H}$ electrode, in correspondence of which the AMCP, in terms of an electron multiplier, ends. This grounded electrode is a 200-nm-thick layer, which evacuates the leakage current flowing through the multiplying stack.
5. A 2- μm -thick a-Si:H layer, which isolates the anode from the leakage current of the multiplying stack.

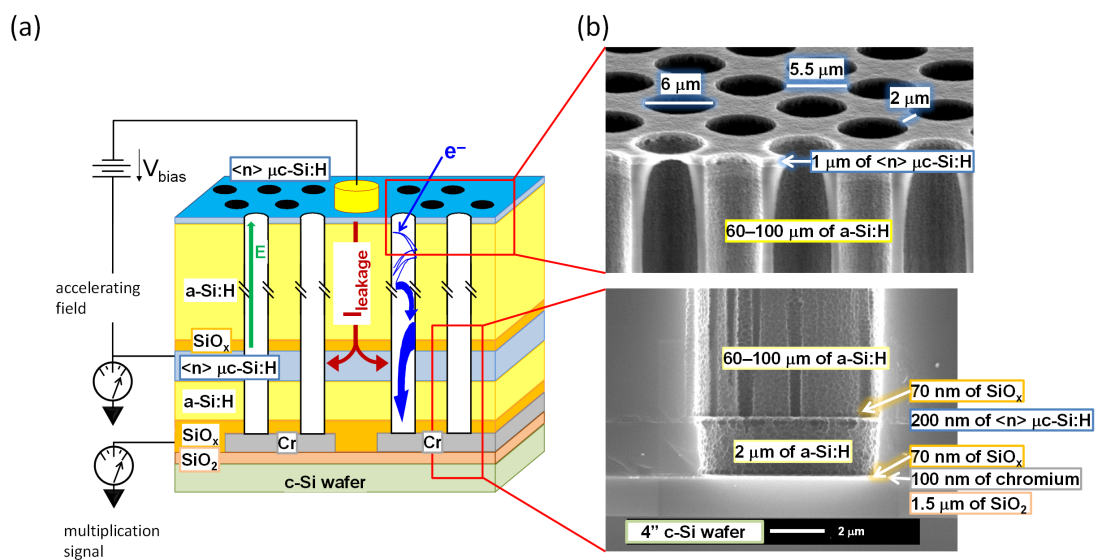


Figure 7.1: (a) schematic cross-sectional view of 3rd-gen AMCP architecture with three independent electrodes for: setting the electric field in channels, evacuating the leakage current and measuring the electron multiplication. (b) SEM cross-sectional images provide a close view on the AMCP morphology.

7.3 Dark conductivity measurements of AMCP layers

measurement was plotted in Arrhenius' plot to extrapolate, from the slow-cooling part of the curve, the room-temperature conductivity and the activation energy. Figure 7.2 shows the measurements and the results of dark conductivity and activation energy for a-Si:H and $\langle n \rangle$ SiO_x. The noisy behavior of the latter, near room temperature, was caused by measurement instabilities due to the large material resistivity.

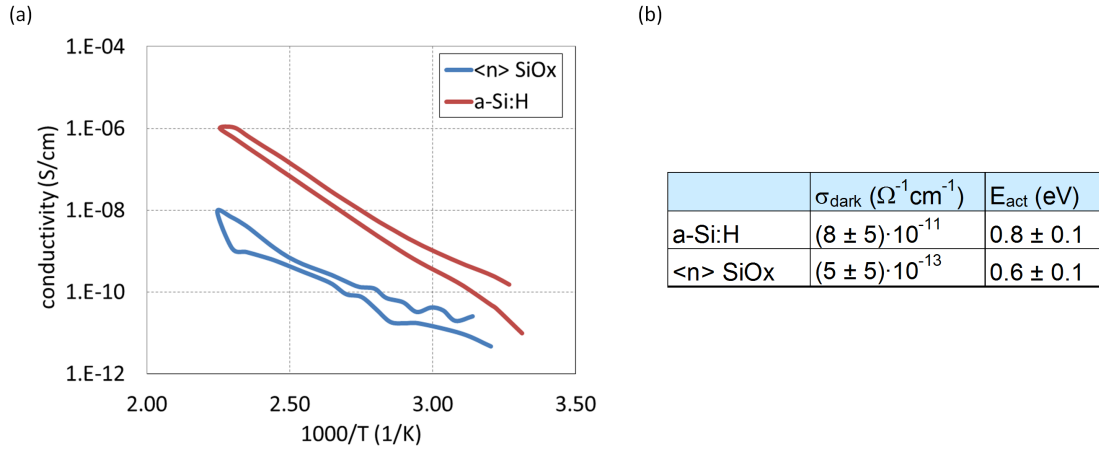


Figure 7.2: (a) dark conductivity as a function of the inverse of temperature for a-Si:H and $\langle n \rangle$ SiO_x, as measured during an annealing cycle. (b) table with the extrapolated conductivity and activation energy, calculated from the measurement cooling ramp.

The non-intentionally doped SiO_x material, employed as adhesion layer above the anode, could not be measured because it was too resistive, i.e. with dark room-temperature conductivity smaller than $10^{-14} \Omega^{-1} \text{cm}^{-1}$.

Conversely, the $\langle n \rangle$ $\mu\text{c-Si:H}$ layer of both top and intermediate electrode, was conductive enough to be directly measured by the four-point technique (the two outer contacts inject the probing current and the two inner contacts measure the voltage drop in order to extract the resistance) in air. Its sheet resistance (R_{sq}) is between 500 Ω (for 1- μm -thick layer) and 1000 Ω (for 200-nm-thick layer).

7.4 Current-to-voltage characteristics of the AMCP layer stacks

7.4.1 Electrical conduction through the multiplying stack

The AMCP's resistive layers, between each couple of electrodes, can be modeled as resistances connected in series. Since these resistances are quite large (both a-Si:H and $\langle n \rangle$ SiO_x resistivity exceeds $10^{11} \Omega \text{cm}$), we performed current-to-voltage (I-V) measurements, rather than direct resistance measurements, for the electrical characterization of the layer stack. Additionally, we adopted a waiting time to let the current stabilize between two consecutive voltage steps. This is particularly important for materials with a large density of localized bandgap states, like a-Si:H (cf. Chapter 3), since they induce stabilization times up to several

7.4. Current-to-voltage characteristics of the AMCP layer stacks

minutes [Street 90, Arch 92]. Indeed, upon a bias change, the two quasi-Fermi levels move and modify the population of trapped charges in the localized states. Several minutes can be required to attain the new equilibrium. In our case, we noticed that the current was largely stabilized after a waiting time of about 10 minutes, in case of voltage steps of 20 V and tens-of-micrometers-thick a-Si:H layers.

As shown in figure 7.3, the I-V characteristics of the multiplying stack is ohmic for voltages until -200 V. We compared the extrapolated value of $128 \pm 2 \text{ M}\Omega$, for the channel aspect ratio (channel length over diameter) of 10.3:1, with that calculated from the dark conductivity measurements. For the latter, the a-Si:H and $\langle n \rangle \text{ SiO}_x$ dark conductivities are multiplied by the thickness of $76 \text{ }\mu\text{m}$ and 70 nm , respectively. Then, they are divided by the net area (without channels) between the two electrodes of 42 mm^2 , obtained as the “AMCP island” surface of 50 mm^2 minus the total channel open area of 8 mm^2 (1.8×10^5 channels of $7.5 \text{ }\mu\text{m}$ in diameter). Therefore, the calculated stack resistance is about $220 \pm 50 \text{ M}\Omega$. This is considerably larger than the measured value of $128 \pm 2 \text{ M}\Omega$. The mismatch could be explained by an additional contribution to the conduction given by the channels presence. If this is the case, it means that there is a preferential conduction path along the channel surface. This is an important piece of information, because if confirmed, it can be beneficial for the charge replenishment during the electron multiplication.

To investigate this hypothesis, we compared the electrical behavior of two multiplying stacks with a channel aspect ratio of 10.3:1 and 12.5:1 (figure 7.3(a)), respectively. As reported in figure 7.3(b), the aspect ratio of 12.5:1 has narrower and fewer channels, albeit of the same length of $76 \text{ }\mu\text{m}$. Therefore, the multiplying stack with AMCPs of 12.5:1 has a total channel surface lower than that of the 10.3:1 aspect ratio. Now, if a significant portion of the leakage current flows on channel surface, the resistance should scale with the total channel surface. This was confirmed with a larger resistance of $205 \pm 5 \text{ M}\Omega$, for the aspect ratio of 12.5:1. Furthermore, if the resistance of $205 \pm 5 \text{ M}\Omega$ is divided by the ratio of the two total channel surfaces, one obtains a resistance of $123 \pm 3 \text{ M}\Omega$, which is compatible to the other extrapolated resistance of $128 \pm 2 \text{ M}\Omega$.

Despite this experimental indication of a preferential conduction path near the channel surface, we could not definitively prove this hypothesis because the variations in the extrapolated resistance was as high as 50% for the same channel geometries. Finally, the hypothesis was confirmed with the I-V characteristics of the decoupling stack, presented in Section 7.4.2.

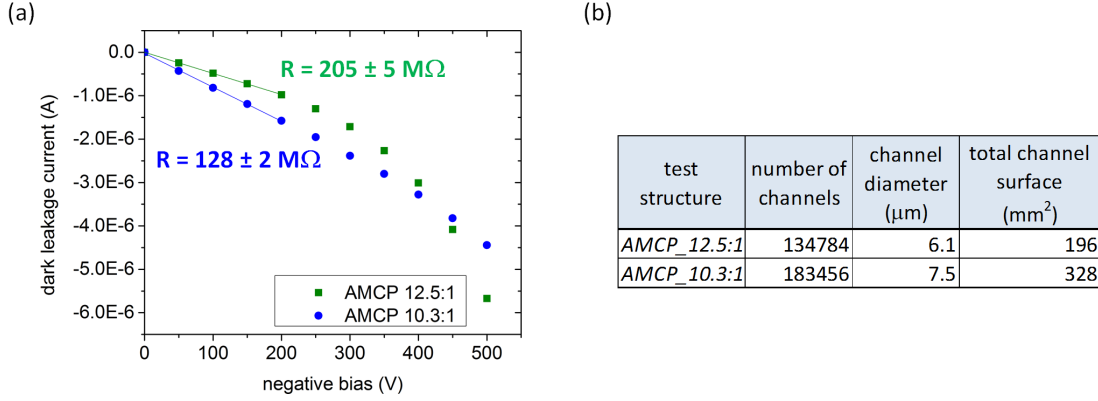


Figure 7.3: (a) Resistances of the multiplying stack, extrapolated from the I-V measurements, for two aspect ratios of 12.5:1 and 10.3:1. (b) Table with the AMCP geometrical parameters, which evidence a total channel surface that is larger for the 10.3:1 aspect ratio, due to more channels and wider diameter.

Another interesting aspect about the I-V characteristics of the multiplying stack is the more-than-linear behavior at voltages larger than -200 V (figure 7.3(a)). Although the onset of this behavior is not always the same for different test structures, it is systematically observed above a certain voltage. We attribute it to additional conduction mechanisms, activated by the large electric field [Franclova 05]. One is the Fowler-Nordheim [Simmons 71] tunneling, which takes place in a resistive element, contacted on either side by metal electrodes. Another is the Poole-Frenkel [Frenkel 38, Chévrier 94] field-enhanced thermal emission of trapped carriers in a resistive element. The former predicts a linear trend when the logarithm of the current is plotted versus the inverse of the voltage. The latter predicts a linear trend when the logarithm of the current is plotted versus the root square of the voltage, according to the formula

$$I = I_0 \exp \left[-\frac{\Phi_0 - \gamma \sqrt{E}}{kT} \right] \quad \text{with} \quad \gamma = \sqrt{\frac{q}{\pi \epsilon_0 \epsilon_{aSi}}} \quad (7.1)$$

and I_0 is the low-field current, Φ_0 is the initial barrier height between the trap state and the conduction band, E is the applied electric field and γ is the Poole-Frenkel constant with a theoretical value of $2.2 \times 10^{-4} \text{ eV cm}^{1/2} \text{ V}^{-1/2}$. Our experimental data, at voltages between 100 and 400 V (and corresponding electric fields between 1.4×10^4 and $5 \times 10^4 \text{ V/cm}$), are observed to agree more with this second mechanism, as shown in figure 7.4 for the aspect ratio of 12.5:1 and 6.1:1.

At fields lower than $2.8 \times 10^4 \text{ V/cm}$, which corresponds to the data at voltages lower than 200 V, the Poole-Frenkel mechanism is negligible, whereas at electric fields above $5 \times 10^4 \text{ V/cm}$, trends are no longer linear in figure 7.4, sign that a third mechanism prevails. This could be attributed to the space-charge-limited current (SCLC), another well-known mechanism in a-Si:H [Mackenzie 82, Weisfield 83, Solomon 84]. However, this hypothesis was not further investigated because the SCLC quantification in a-Si:H is complex and the analytical approaches do not always agree with one another.

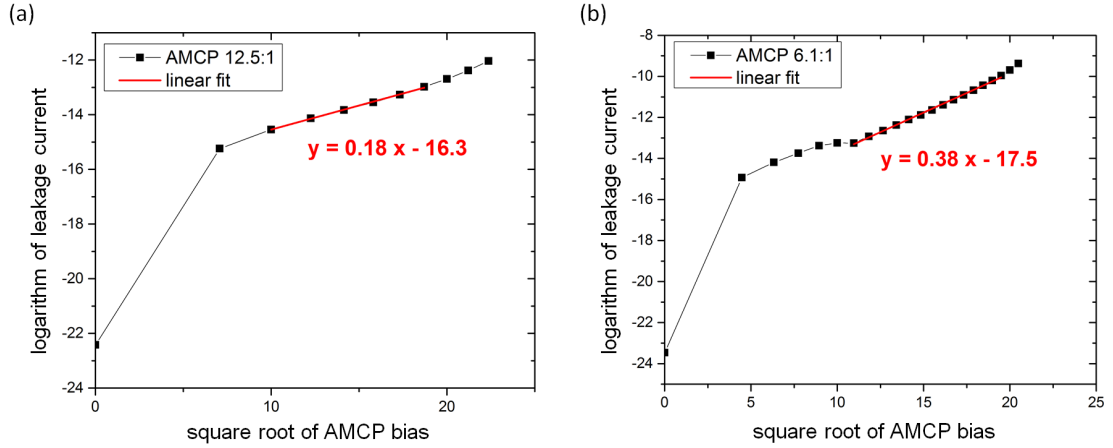


Figure 7.4: Logarithm of the leakage current plotted versus the square root of the bias voltage for the AMCP with aspect ratio of 12.5:1 (a) and 6.1:1 (b). Both trends become linear above 200 V, the signature of the Poole-Frenkel activated conduction mechanism.

7.4.2 Electrical conduction through the decoupling stack

In this section, we present the electrical characterization of the decoupling stack. The aim is to determine the residual leakage current on the anode as a function of the characteristics of the resistive layers and the features of the channels. Referring to figure 7.1, the decoupling stack includes an a-Si:H layer and an SiO_x adhesion layer. The a-Si:H thickness of 2 μm was the result of a trade-off between the anode isolation and the inactive portion of the channels, with respect to the electron multiplication (cf. Chapter 6).

The I-V characteristic of the decoupling stack exhibits a rectifying behavior, with an approximated exponential increase for negative voltages applied to the intermediate electrode and a much smaller saturated current for positive voltages (figure 7.5). This is attributed to the interface between the $\langle n \rangle$ $\mu\text{c-Si:H}$ intermediate electrode and the a-Si:H decoupling layer (n-i interface), which features a depletion region and a built-in potential. Indeed, the $\langle n \rangle$ $\mu\text{c-Si:H}$ positive fixed charges, originated by the doping, are balanced by the fixed negative charges of the a-Si:H. Indeed, although almost no doping species (besides a possible small oxygen contamination, cf. Chapter 3) are present in intrinsic a-Si:H, the Fermi level shift, near the interface, induces a number of localized states to be negatively charged. This makes the depletion region extend for a certain thickness in the i-layer (cf. Chapter 4).

This interface is the same of that between the top electrode and the thick a-Si:H layer, but, in the latter, the rectifying behavior was shadowed by the large bias steps of 20 V. These were large enough to activate additional conduction mechanisms [Ilie 96] through the n-i interface so as to produce the ohmic behavior observed within ± 200 V. These mechanisms are—according to the electric field strength at the interface—tunneling through the electrode localized states, field-enhanced thermal generation at the n-i interface and charge injection from the electrode to the a-Si:H bulk.

The electrical conduction through the SiO_x layer is deemed to occur by the electron hopping from one localized state to another. This conduction mechanism is relatively efficient because the SiO_x deposition by PE-CVD produces a material with variable oxygen content, lower than the stoichiometric one of SiO_2 [Cuony 12]. The missing oxygen, in turn, is known to produce shallow localized states in the bandgap [Nicklaw 02] and these ease the electron movement by hopping through the layer.

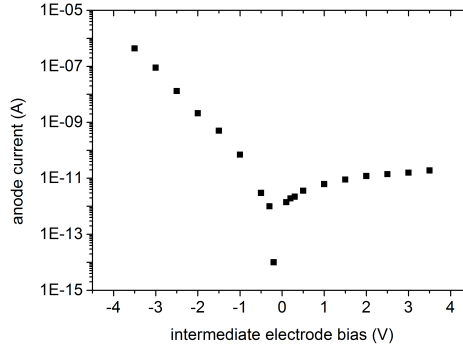


Figure 7.5: *I-V characteristics of the decoupling stack. The behavior is rectifying due to the interface between the $\langle n \rangle$ $\mu\text{c-Si:H}$ intermediate electrode and the $a\text{-Si:H}$ decoupling layer.*

Decoupling stack resistance versus SiO_x thickness

Figure 7.6(a) shows the I-V characteristics for small negative voltages (lower than -4 V) and for three thicknesses of the SiO_x adhesion layer. The fast current increase is due to the rectifying behavior and is inversely proportional to the SiO_x thickness, as expected. At larger negative voltages (larger than -4 V), the I-V characteristics become gradually ohmic, as shown in figure 7.6(b). We also observe that

- The extrapolated resistances are much lower than that of about 10 G Ω , which is calculated from the $a\text{-Si:H}$ conductivity of $8 \times 10^{-11} \Omega^{-1} \text{cm}^{-1}$, a thickness of 2 μm and an anode surface of 0.25 mm^2 . We explain this mismatch in terms of electron accumulation in the $a\text{-Si:H}$ decoupling layer. Indeed, a few volts of negative bias induce the injection of a large number of electrons in the 2- μm -thick $a\text{-Si:H}$ layer. The electrons are drifted by an electric field larger than $5 \times 10^4 \text{ V/cm}$ so that the extrapolated resistance is no longer representative of the $a\text{-Si:H}$ resistivity.
- There is a large resistance variation between test structures, which does not depend on the SiO_x thickness anymore. The explanation is attributed to the different number of channels for the three test structures. Indeed, the decoupling stack with the 150-nm-thick SiO_x layer has a number of channels that is more than threefold that with the 80-nm-thick SiO_x layer and more than twice that with 10-nm-thick SiO_x layer. A larger number of channels corresponds to a lower residual amount of the $\langle n \rangle$ $\mu\text{c-Si:H}$ electrode

between channels. Consequently, the electrode resistance is larger, which produces a larger voltage drop between the intermediate electrode bias point and the measured AMCP. In conclusion, the voltage drop lowers the nominal bias voltage and induces an apparent larger stack resistance.

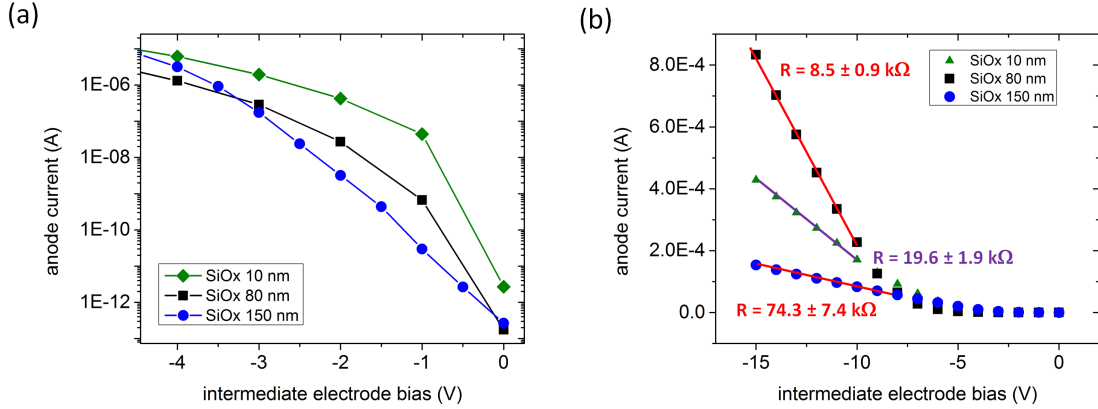


Figure 7.6: Comparison of the I-V characteristics obtained for three decoupling stacks, which feature the same α -Si:H layer, but an SiO_x layer of 10, 80 and 150 nm, respectively. Graph (a) shows the comparison at small bias voltages, where the current is inversely proportional to the SiO_x thickness. Graph (b) shows the comparison at large bias voltages, in which the current is no longer dependent on the SiO_x thickness.

Dependency of the decoupling stack resistance on the channels

The latest 3rd-gen AMCP test structures feature three anodes without channels. The aim was to investigate the channel influence on the decoupling stack resistance, within the same test structure, so as to confirm the preferential leakage path along the channel surface hypothesized in Section 7.4.1.

As shown in figure 7.7(a), this could not be confirmed at small biases, for which the more resistive decoupling stack is that with channels. However, at large bias voltages, the electrical behavior of the two stacks changes and the more conductive stack becomes that with channels, as shown in figure 7.7(b). It is worth mentioning that the uncertainties in the extrapolated resistances take already into account the variations among test structures with the same channel design. Therefore, **we proved that, at large bias voltages, there is a preferential conduction path along the channel surface**. The explanation for this enhanced conduction could be attributed to the Poole-Frenkel field-enhanced thermal generation of charges trapped in the localized states. These states are expected to be more numerous near the surface because of the abrupt interruption of the atomic structure (cf. Chapter 3). The deep reactive ion etching (DRIE) process might also have contributed to enhance their density, as it was observed in the case of the reactive ion etching (RIE) of c-Si [Kumaravelu 04, Deenapanray 06].

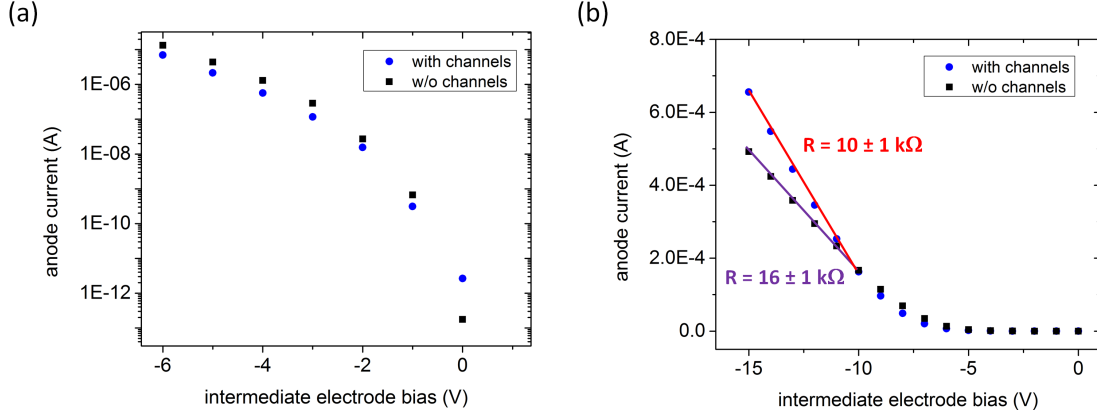


Figure 7.7: Comparison of the anode current versus the intermediate electrode bias, for two decoupling stacks, one with and one without channels. Graph (a) is for small biases and graph (b) is for large biases.

After the confirmation of a preferential leakage path on the surface, we also calculated which percentage of the total leakage current flows near the channel surface. To do so, we electrically modelled the decoupling stack as two resistances connected in parallel. One is relevant to the conduction in the bulk and one is relevant to the conduction near the surface. The bulk one is calculated from the decoupling stack resistance without channels of $16 \pm 1 \text{ k}\Omega$ multiplied by a factor that takes into account the missing bulk in case of channels. This scaling factor (ϵ) for the measured anode is calculated as

$$\epsilon = 1 - \frac{A_{ch}n_{ch}}{A_{pix}} = 0.73, \quad (7.2)$$

where A_{pix} is the anode area of 1 mm^2 , A_{ch} is the channel area of about $4.3 \times 10^{-5} \text{ mm}^2$ and n_{ch} is the number of channels, which is 6272. The corresponding bulk resistance is $22 \pm 1 \text{ k}\Omega$. Consequently, the resistance for the conduction near the channel surface is $19 \pm 2 \text{ k}\Omega$. From these calculations, **it follows that the percentage of leakage current flowing near the channel is $54 \pm 8 \%$.**

This result can also be transferred to the multiplying stack, at least in the upper part of the channel where the influence of the bias voltage is more intense. However, the charge replenishment is expected to be more demanding in the lower part of the channels, according to the electron multiplication dynamics, so that no precise estimation about the AMCP performances, at large input electron fluxes, can be made.

Variation in the voltage potential across the intermediate electrode

The residual leakage current on the anode, in normal operating conditions, is explained by the same mechanism of voltage drop in the intermediate electrode, described when we presented the leakage current dependency of the SiO_x thickness. Indeed, this residual current is generated by the voltage rise (with respect to the ground reference)—which polarizes the decoupling stack—of the intermediate electrode during the leakage current evacuation. This is schematically represented in figure 7.8. The voltage rise depends on the distance between the measured AMCP and the electrical connection at ground potential (*pad-12*).

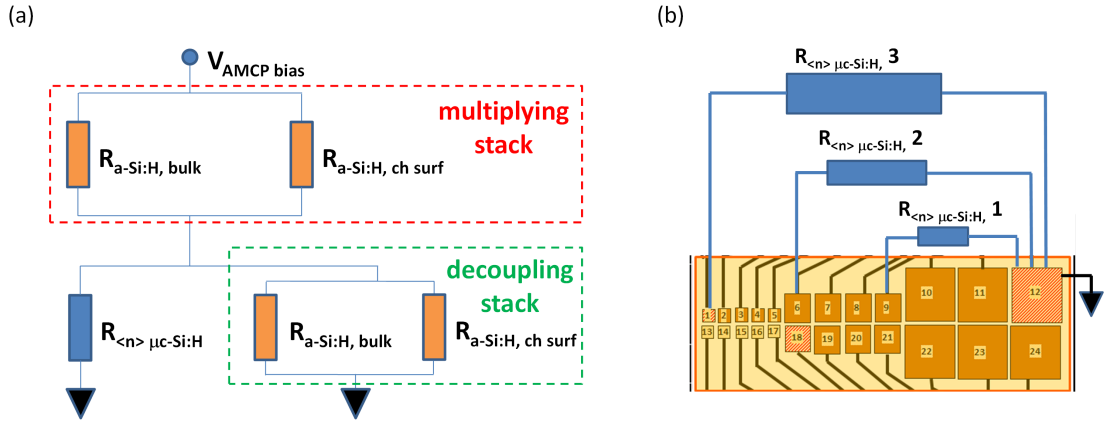


Figure 7.8: (a) AMCP electrical representation of both the multiplying stack and the decoupling stack. (b) Electrical representation of the equivalent $\langle n \rangle \mu c\text{-Si:H}$ resistance from the measured AMCP to the extraction point at ground potential (*pad-12*).

Evidence of this effect is shown in figure 7.9. Graph (a) shows the I-V characteristics of the decoupling stack for two AMCPs, corresponding to AMCP number 9 (*AMCP-9*) and AMCP number 6 (*AMCP-6*) of the test structure. They are at different distances from the bias point (*pad-12*), so that the corresponding $\langle n \rangle \mu c\text{-Si:H}$ resistance is different ($R_{<n> \mu c-Si:H, 2} > R_{<n> \mu c-Si:H, 1}$). This entails a larger voltage drop for *AMCP-6* than for *AMCP-9*, as shown in figure 7.8(b), which induces the apparent larger stack resistance.

The graph of figure 7.9(b) shows the leakage current on the anode in real operating conditions, namely with the AMCP top electrode negatively biased to a few hundreds of volts, with respect to the grounded intermediate electrode. The two curves refer to *AMCP-10*, with an area of 4 mm^2 , and to *AMCP-1,2,13,14*, connected all together for an overall area of 1 mm^2 . Even though the decoupling stack for *AMCP-10* has a lower resistance than that of the four small AMCPs together, due to its larger area, the leakage current on the anode is smaller. This result is again explained in terms of distance from the intermediate electrode connection point, which is further for *AMCP-1,2,13,14* than for *AMCP-10*. Consequently, the voltage rise with respect to the ground reference is larger for the four small AMCPs than for the big AMCP. This, in turn, polarizes the decoupling stack and increases the leakage current on the anode. By comparing this current to the I-V characteristics of figure 7.9(a), we find out that the inter-

mediate electrode polarization, in real operating conditions, is less than 1 V. As presented in Chapter 8, this leakage current is small compared to the signal of electron multiplication so that it does not constitute a problem in most cases.

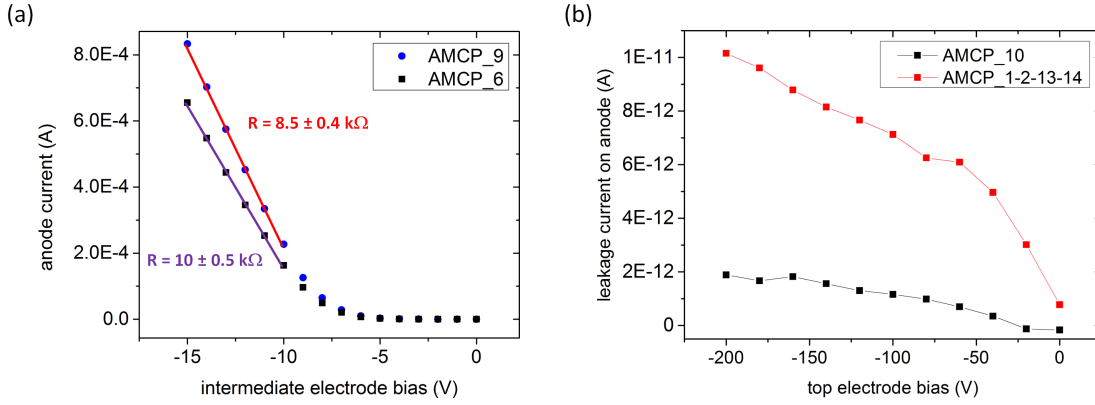


Figure 7.9: (a) *I-V* characteristics of the decoupling stack obtained with a negative bias voltage applied to the intermediate electrode. The extrapolated resistances, for two AMCPs at different distances from the intermediate electrode biasing point, (pad-12) are reported. (b) Leakage current on the anode as a function of the AMCP bias voltage for AMCP-10 and four AMCPs measured altogether: AMCP-1,2,13,14.

7.5 Residual leakage current on the anode for 3rd-gen AMCPs

The reduction of the leakage current on the anode, obtained by the implementation of the intermediate electrode, is shown in figure 7.10. **The net drop for the usual maximum bias of -500 V and the corresponding electric field of $5.6 \times 10^4 \text{ V/cm}$, is about four orders of magnitude.** The maximum current on the anode is about 100 pA for many AMCPs measured altogether, corresponding to a total AMCP area of 24 mm^2 . **If only the closest AMCP (either AMCP-11 or AMCP-24, both of 4 mm^2) to the leakage current extraction point is measured, the leakage current on the anode is less than 10 pA, five orders of magnitude smaller than the leakage current on the intermediate electrode.**

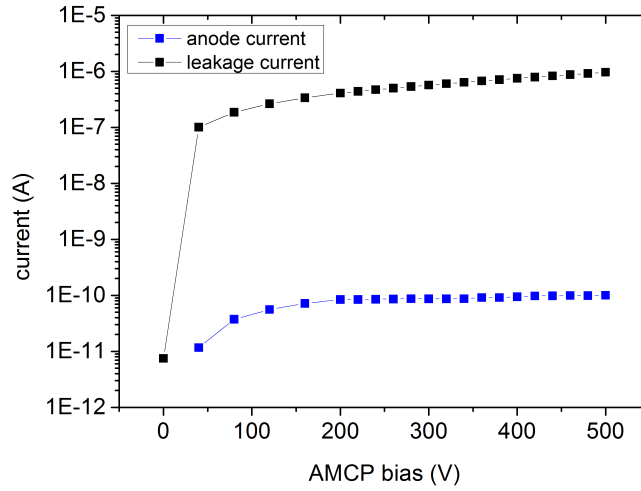


Figure 7.10: Comparison of the leakage current on the intermediate electrode and on the anode, as a function of the negative AMCP bias voltage. Many AMCPs are measured altogether for an overall area of 24 mm^2 .

7.6 Conclusion

This chapter presented the electrical characterization of 3rd-gen AMCPs, in which the evacuation of the leakage current is achieved by an additional intermediate electrode. Thanks to this upgrade, the residual leakage current on the anode was reduced by more than five orders of magnitude, from 10^{-6} – 10^{-5} to less than 10^{-11} A, at an AMCP bias voltage of -500 V and a corresponding electric field of $5\text{--}8 \times 10^4$ V/cm. This residual leakage current on the anode is induced by the voltage rise, across the grounded intermediate $\langle n \rangle \mu\text{c-Si:H}$ electrode, produced by the evacuation of the leakage current.

The I-V characteristics of the multiplying stack exhibited an ohmic behavior between ± 200 V. The extrapolated resistances are comparable to those of conventional MCPs. The maximum achieved electric fields of about 10^5 V/cm are about ten times larger than those usually adopted in conventional MCPs so that future AMCP improvements could encompass the deposition of a more-conductive a-Si:H, so as to enhance the charge replenishment at large input currents and high repetition rates, without a major risk of electrical breakdown. The a-Si:H resistivity could be varied by a fine tuning of the material bandgap, by means of the introduction of small quantities of either germanium or carbon.

The extrapolated resistances, for two AMCPs with different number of channels, suggested an enhanced conduction path near the channel surface. We confirmed this hypothesis with the I-V characteristics of the decoupling stack at large bias voltages, which seems to suggest the presence of a field-enhanced conduction mechanism. We also calculated that the percentage of the total leakage current flowing near the surface is about 50%. This result is applicable also to the multiplying stack, but mostly in the channel upper part, where the influence of the

bias voltage is more intense. However, the electron replenishment during the multiplication is expected to be more demanding in the channel lower part so that no definitive estimation about the AMCP performances at high input electron intensities can be drawn.

Finally, we verified that the SiO_x adhesion layer, above the anode, contributes to the decoupling stack resistance for a negative bias of the intermediate electrode lower than a few volts. A voltage rise smaller than 1 V (with respect to the ground) was observed to occur across the intermediate electrode for the usual AMCP operating conditions, due to the leakage current evacuation across the intermediate electrode. Therefore, a SiO_x layer slightly thicker than those implemented so far could be envisaged for effectively reducing the anode leakage current in case of future AMCPs of larger areas.

8 Electron multiplication in AMCPs: Dynamics and results

Abstract. In this chapter we present the results of the AMCP electron multiplication factor, i.e. the gain. The measurements are performed with two different test setups. The maximum gain is greater than 45, for a channel aspect ratio of 12:1 and an accelerating electric field of 7×10^4 V/cm.

The electron multiplication is confirmed to increase as a function of the aspect ratio, i.e. the channel length over diameter. A simple analytical formulation of the gain is used to compare the gain dependency on the aspect ratio for AMCPs and conventional MCPs. We observe a similar behavior for the two. The a-Si:H secondary electron coefficient of 1.7 is inferred from this analysis, for an impinging electron energy of about 100 eV. The gain is also measured versus an input electron current that ranges over almost three orders of magnitude. If the electrons flux in the channel is greater than $10^{10} \text{ cm}^{-2} \text{ s}^{-1}$, the gain is no longer constant but drops over time due to the supposed charging of the decoupling stack surface. The percentage drop, with respect to the maximum gain, ranges within 30–75% and it could be related to the channel diameter.

The gain is also observed to vary with the energy and the impinging angle of the beam electrons on the channel surface. This is explained in terms of number of secondary electrons emitted upon the first collision. In particular, the gain increases three times if the energy is increased from 1 to 7 keV, due to a larger number of secondary electrons. Finally, the gain is shown to double with the atomic layer deposition, on the channel surface, of 5 nm of Al_2O_3 as this material has larger secondary emission coefficient than a-Si:H.

8.1 Introduction

This chapter presents the characterization of amorphous-silicon-based microchannel plates (AMCPs) of different generations. This characterization was focused on the quantification of electron multiplication and its dependence on the AMCP geometrical features and the characteristics of the impinging electron. The results provide the proof of concept for this novel fabrication process of microchannel plates.

The measurements were carried out with two different electron sources. The former consisted in an ultraviolet light (UV) and a photocathode, whereas the latter was the electron beam of a scanning electron microscope (SEM). The input electron fluxes were quite large to compensate the moderate gain, according to the realized aspect ratios. The output signal was directly measured with either a picoammeter or a lock-in amplifier, so that the signal was averaged on a minimum timeframe of a few tens of milliseconds. The gain was calculated as the ratio of the output current over the calibrated input one.

The chapter is structured as follows. First, we describe our first trials in quantifying the electron multiplication before the setup optimization, with all the three AMCP generations. Although we gathered first signs of electron multiplication, we could not quantify it, due to the presence of spurious contributions to the signal. These were produced by the a-Si:H electrical conductivity sensitivity to photons and electrons.

Secondly, we present the results of electron multiplication obtained with the third-generation (3rd-gen) AMCPs, with the UV light and the photocathode. Gain is presented as a function of the AMCP bias voltage for different input photoelectron currents and aspect ratios. The comparison of the AMCP performances with those of conventional MCPs is discussed. The a-Si:H secondary electron emission (SEE) coefficient is also inferred from this comparison. Finally, the gain is presented for the measurements with the SEM beam. We discuss in detail the multiplication dynamic as a function of the electron current into channels. We show the gain dependency as a function of the beam parameters. The gain enhancement, when a SEE layer is deposited on the channel surface, is also presented.

At the end of the chapter, we review all the results and we estimate the maximum gain that can be achieved for a given aspect ratio. In the outlook, we discuss possible structural improvements according to what we have learnt so far and the measurements that still need to be done to fully characterize the dynamics of electron multiplication. We also provide a few examples of possible future applications.

8.2 Preliminary tests with the three AMCP generations

This section provides an overview of the preliminary measurements performed with the three AMCP generations. We explain why the gain quantification was hindered by the structural limitations of first-generation (1st-gen) and second-generation (2nd-gen) AMCPs. Inversely, we present the large signals that were induced by the enhancement of the a-Si:H conductivity during exposure to photons and electrons. The understanding of these effects enabled us to take the corrective actions required for finally quantifying the electron multiplication, with the 3rd-gen AMCPs.

In the next subsection, we show the 1st-gen AMCP sensitivity to the SEM beam. The analysis of the results evidenced also some limitations of this testing technique, which were successively overcome in the last measurements of this thesis. Then, we present the system called “UV setup”, which we built to characterize the AMCPs with a UV light source. The effects of the UV

illumination on 2nd-gen AMCPs and 3rd-gen AMCPs are discussed. These results evidenced the necessity to implement a photocathode for providing photoelectrons already at the channel entrance, instead of generating them inside of the channels by relying on the low a-Si:H quantum efficiency.

8.2.1 EBIC measurements of 1st-gen AMCP

The 1st-gen AMCPs were already available at the beginning of this thesis and preliminary results about their sensitivity to an electron beam were already reported [Wyrsh 05]. They showed an increase in the AMCP anode current when electrons of about 10 keV entered into the channels. This signal was also observed to increase linearly with the AMCP bias voltage. The first goal of this thesis was to reproduce these results with the SEM and the EBIC technique (cf. Chapter 4) available at the Centre Suisse d'Electronique et de Microtechnique (CSEM) of Neuchâtel. We collected a number of results that showed a large signal on the anode every time the beam electrons impinged on the channel surface [Franco 12b]. We also succeeded to confirm the results mentioned earlier. Nevertheless, our initial interpretations were successively found to be partly wrong. The reason of this mistake was that we had assumed that the channels were throughout the a-Si:H layer. However, when we started the fabrication of 2nd-gen AMCPs, we realized that the tuning of the DRIE process for the channel micromachining was a critical point, which occasionally caused the channels not to reach the anode. Therefore, we decided to perform a destructive analysis on one 1st-gen AMCP. Once cleaved, the AMCP cross section was investigated with the SEM and the result is shown in figure 8.1: The etching of the channels did not reach the AMCP anode by more than 10 μm and the channels were partially merged in the upper part. With this hindsight, we partially changed the explanation of our results, which are presented below.

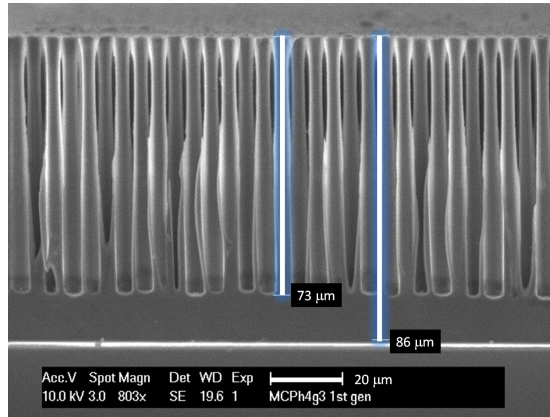


Figure 8.1: SEM image of the cross section of a 1st-gen AMCP, which shows a residual non-machined a-Si:H thickness of about 10 μm . Additionally, the channels are partially merged in the upper part.

First, EBIC maps were acquired to identify the active areas of the AMCP. The AMCP was biased to -340 V with a Stanford Research Systems PS310 high-voltage supply. As shown in

figure 8.2, all channels could be clearly identified, which proved that the bias voltage was evenly spread across the whole AMCP surface and that the electrons were multiplied in the channels. Additionally, when the AMCP was not tilted with respect to the impinging electron direction, the stronger (brighter) signal was measured to be located in a tiny annular area, around every channel (figure 8.2(a)). This suggested that the electrons had to impinge on the channel surface to generate a signal, whereas the electrons that went through them without any collision did not contribute to it. Indeed, it is worth reminding that AMCP channels do not feature a bias angle, i.e. their axis is perpendicular to the plate surface. We confirmed this hypothesis by tilting the AMCP by 10° (with respect to the direction of the incoming electron) so that all electrons that entered into the channels, experienced a number of collisions. This produced a larger signal than that between the channels, as shown in figure 8.2(b). These observations clearly supported the presence of an electron multiplication.

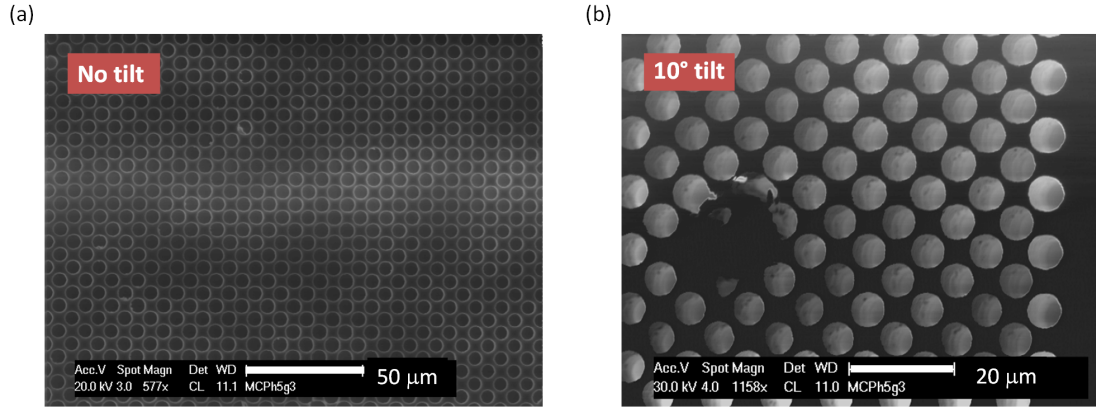


Figure 8.2: (a) EBIC map with a brighter signal where the induced current is larger. This is confined in a tiny annular area around each channel, if the AMCP is not tilted. Alternatively, when the AMCP is tilted by 10° (b), the EBIC map shows a brighter signal inside every channel [Franco 12b].

The following measurements consisted in the direct measurement of the anode current with a Keithley 6487 picoammeter. Different beam energies and currents were tested with the AMCP tilted of 15° . The measurement procedure consisted of three phases. We first focused the electron beam in a spot between two channels, then we moved it inside of a channel and finally back again to the initial position. As shown in figure 8.3, the induced current rapidly reaches a maximum and then decreases (rather than staying constant) during the phase of beam inside the channel (highlighted in green). The decrease is faster for a larger beam current, as shown by the red curve of figure 8.3(a). Initially, we interpreted this drop in terms of insufficient charge replenishment on the channel surface. However, after having verified that the channels did not reach the anode, the explanation is that the measured current was mainly produced by the collection of the electron-hole pairs, holes at the top electrode and electrons at the anode, generated in a-Si:H by the ionizing energy (released by the beam electrons). Due to their high energy, every impinging electron produced many electron-hole pairs, which were drifted by the electric field, until they reached their respective electrodes.

8.2. Preliminary tests with the three AMCP generations

At the same time, the secondary electrons that were emitted upon this first collision, were multiplied and accumulated on the residual non-etched a-Si:H layer at the bottom of the channel. This negative charge gradually reduced the potential difference across the a-Si:H layer. Consequently, the collection of electron-hole pairs became progressively less efficient, and the signal decreased over time. This explains why with larger beam currents, the signal dropped more rapidly (the a-Si:H charging at the bottom of the channel was faster).

The reason why the electron beam of 20 keV and 340 pA produced a much larger signal, which was also more stable over time than that induced by the 5 keV–150pA beam, as shown in figure 8.3(b), can be explained as follows. The larger electron energy generated an interaction volume that propagated much deeper in a-Si:H. Therefore, fewer secondary electrons reached the surface and were multiplied. Since the electron multiplication strongly depends on the amount of secondary electron emitted in the first collision, as verified in the last measurements of this thesis and presented in Section 8.4.3, the negative charging of the channel bottom end was slower and the signal less affected.

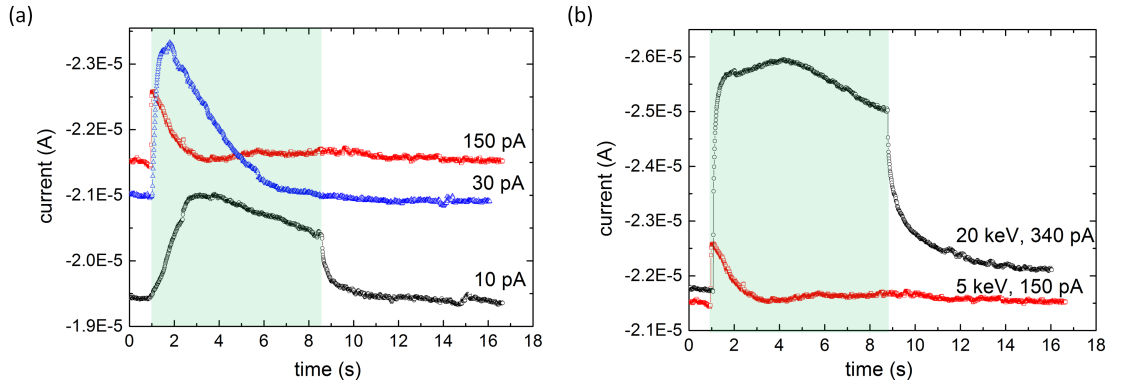


Figure 8.3: Anode current measured during the sequence where the electron beam was alternatively focused between two channels, inside of a channel (highlighted in green) and finally moved back in its initial position. The AMCP was tilted at 15° and biased at -300 V. (a) Signals obtained with a beam of 5 keV and three currents. (b) Signals obtained with two combinations of beam energy and current: 20 keV–340pA and 5 keV–150pA [Franco 12b].

Once established that the beam energy of 20 keV resulted in a more stable signal while the beam was focused inside of a channel, we investigated the signal dependence on the AMCP bias voltage. The results are shown in figure 8.4(a). Finally, we calculated the ratio of the net current increase over the beam current to obtain the gain, which is plotted in figure 8.4(b). These very large values are not compatible with an electron multiplication mechanism because a channel aspect ratio of 40:1, rather than the 12:1 measured here, is normally required for a gain of 10^4 [Wiza 79]. This gain can only be explained by the collection of the electron-hole pairs generated by the impinging electrons in a-Si:H. Indeed, considering that the electron-hole pair creation energy is about 5 ± 1 eV in a-Si:H [Perez-Mendez 88, Dubeau 91, Despeisse 06b], each electron of 20 keV can create 10^3 of them. The reason why the gain is even larger than this figure is because the generated electron-hole pairs also induce a conductivity enhancement. This effect is called betaconductivity [Kosteski 98] and it is similar to the photoconductivity

presented in Chapter 3 . As the photoconductivity can produce a gain (ratio of charges circulating in the external circuit over the generated ones) of 10^5 , the betaconductivity can easily justify gain values of 10^5 . This effect is also observed in lead-glass MCPs, whose strip current (in the semiconducting layer on the channel surface) increases when the output current approaches the strip one [Guest 71].

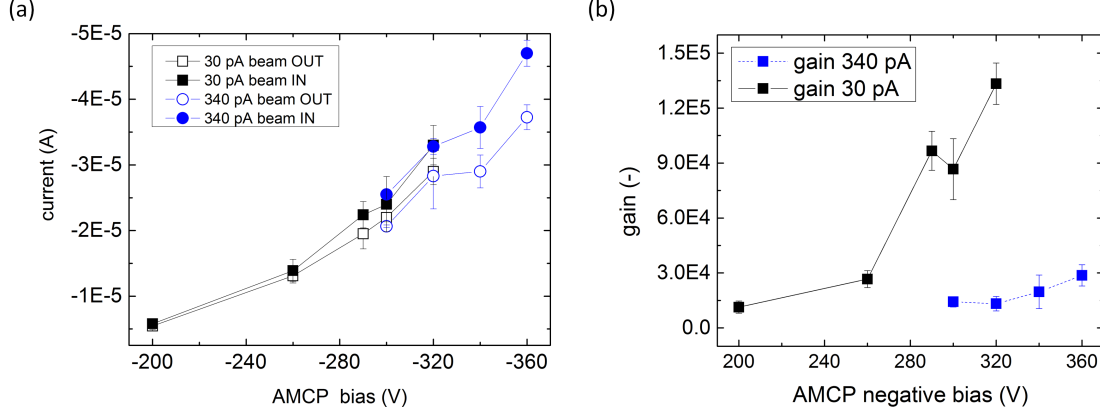


Figure 8.4: (a) Induced current when the electron beam is focused inside one channel ("beam IN") and between two channels ("beam OUT"), for two beam currents. (b) Gain calculated as the ratio of net anode current ("beam IN" - "beam OUT") divided by the calibrated beam current [Franco 12b].

To conclude, even though these measurements did not succeeded in quantifying the electron multiplication gain of 1st-gen AMCPs, they indirectly confirmed its presence in terms of a-Si:H charging at the channel end. These measurements also pointed out the presence of a betaconductivity contribution, which could be even exploited in the future for the charge replenishment.

8.2.2 UV setup and preliminary measurements

The 2nd-gen AMCPs had fewer structural defects than the 1st-gen ones and consequently smaller leakage currents. Additionally, after the optimization of the DRIE process, all channels reached the target depth, which was in correspondence of the "etching-stop" $\langle n \rangle$ SiO_x layer. This layer had an out-of-plane conductivity of about $10^{-8} \Omega^{-1} \text{cm}^{-1}$, which was a few orders of magnitude larger than that of a-Si:H ($10^{-11} \Omega^{-1} \text{cm}^{-1}$). This reduced the layer charging and eased the electron transfer to the anode, thank also to its residual thickness lower than 1 μm .

The 2nd-gen AMCPs were tested with the system built during this thesis, called "UV setup", which features a vacuum vessel and an ultraviolet (UV) source at 256 nm. Indeed, we decided that we needed a test setup more representative of most MCP applications where all channels are equally exposed to a lower flux of less energetic electrons than those of the SEM beam. The aim of the measurements was to verify if the following conditions, for measuring the electron multiplication, were met:

8.2. Preliminary tests with the three AMCP generations

1. The quantum efficiency of bare a-Si:H, which was reported to be lower than 0.04% at 220 nm [Malamud 94], was large enough to produce a certain number of photoelectrons in the first collision.
2. The secondary electron emission of a-Si:H, probably oxidized on the surface [Ponpon 82], was large enough to produce a few secondary electrons at every collision.
3. The “etching-stop” $\langle n \rangle$ SiO_x layer was conductive enough to minimize the voltage drop across the residual non-etched layer thickness and interfere the least on the potential difference across the a-Si:H thick layer.

AMCP evaluation board

The AMCP test structures were bonded to a double-side interface board for electrical connections (figure 8.5). The interface board has a hole in the middle, which enables the AMCP to be heated or cooled. The AMCP can be heated up to 100 °C by means of a heating resistor glued on a copper element (figure 8.5(b)). The thermal contact between copper and the AMCP wafer substrate is provided by the Apeizon high-temperature vacuum grease. The temperature is monitored with a Pt100 temperature probe and a Keithley 2000 multimeter. The cooling system consists in a Peltier thermoelectric element, which has the cooling side in thermal contact with the AMCP by means of an aluminum element and the Apeizon cryogenic vacuum grease. The hot side of the Peltier is cooled by a close circuit with circulating water.

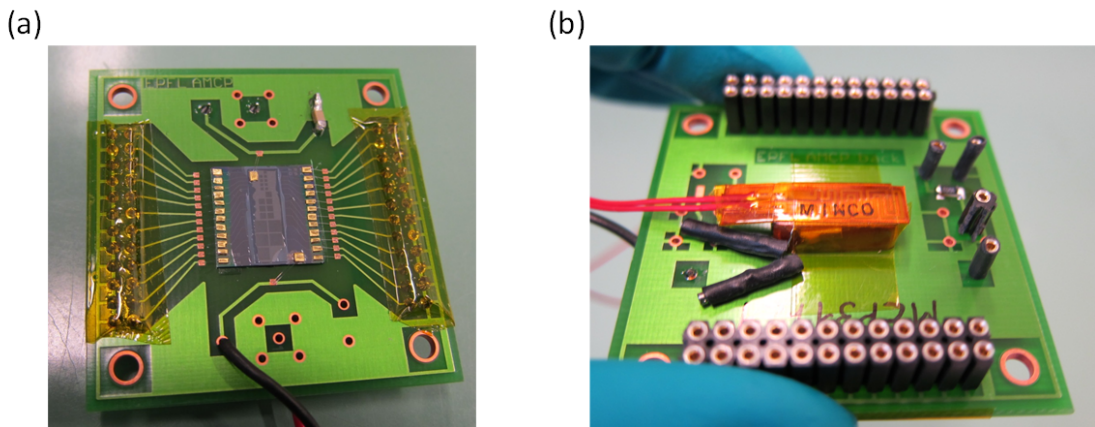


Figure 8.5: (a) AMCP interface board front side. (b) AMCP interface board rear side with the heating resistor glued to the copper element for increasing the AMCP temperature to 100 °C. Temperature is monitored with a Pt100 probe.

UV setup

The UV setup was conceived with the idea of reproducing the typical housing of commercial MCPs integrated in a sealed tube. As shown in figure 8.6, it consists of a vacuum vessel, an

Chapter 8. Electron multiplication in AMCPs: Dynamics and results

optical window made of fused silica and a tilting support for varying the angle between the AMCP channel axis and the incoming UV illumination. A residual partial pressure of 5×10^{-7} mbar is achieved by an Alcatel turbomolecular pump and a rotary dry pump, to avoid any oil contamination. The electrical connections through the vacuum vessel are provided by two feed-through connectors: a 19-pin LEMO connector, which transfers the signals collected by the anode of each AMCP to the measuring instrument, and a high-voltage 1-pin CeramTEC connector, which can accept up to 10 kV and 3 A. On the outside of the vacuum vessel, the UV light is provided by a Pen-Ray mercury-vapor lamp that has its main emission peak at 254 nm. It is equipped with a shielding cap that lets the light go out from an aperture of 8×16 mm. The light flux is decreased by means of a diaphragm that can reduce the entrance aperture by up to 100 times. Additionally, attenuation grids, placed above the diaphragm, further reduce the light intensity from 50 to 1.6%, when needed. The inside of the vacuum vessel, with the AMCP evaluation board installed on the tilting support, is shown in figure 8.7(a).

The AMCP bias voltage is provided by a Keithley 487 picoammeter with voltage source option. The same instrument measures the leakage current at the AMCP intermediate electrode of the 3rd-gen AMCPs. The anode signal is measured either by a Keithley 617 picoammeter or by a Stanford Research SR830 lock-in amplifier. The latter drives a mechanical chopper placed between the UV light and the diaphragm. It chops the light at the desired frequency so that the dc component of the induced signal can be removed, according to the lock-in principle.

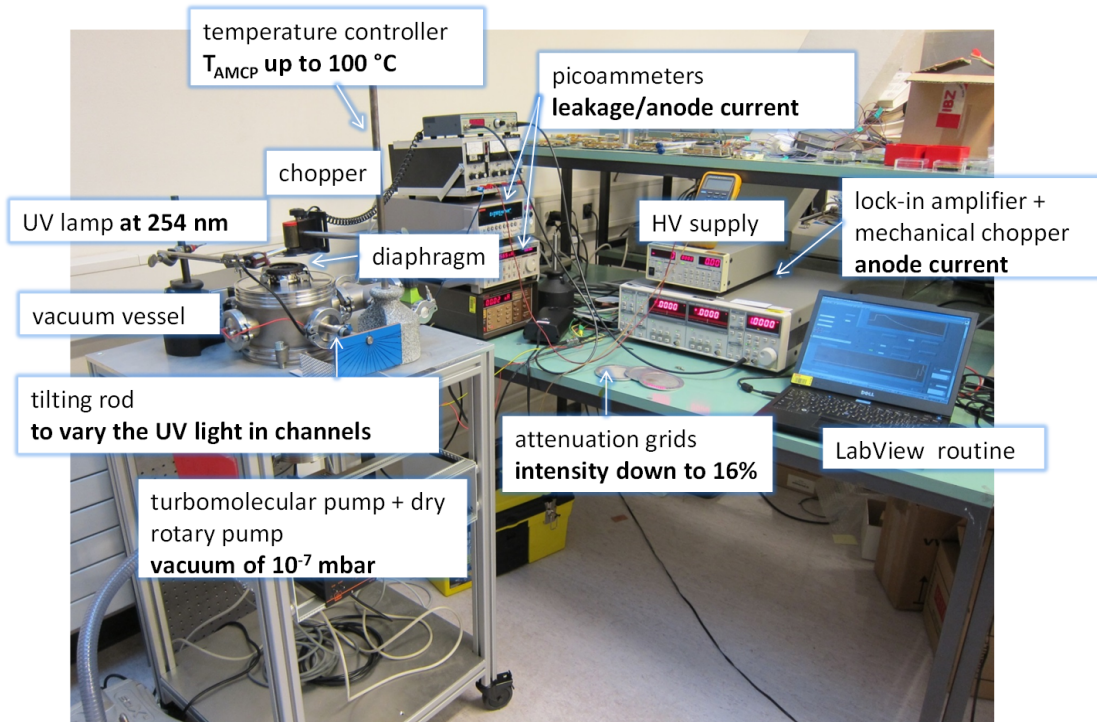


Figure 8.6: Photograph of the UV setup.

When the 3rd-gen AMCPs were tested, the UV setup was upgraded by the introduction of a photocathode (figure 8.7(b)), for converting photons into electrons before the channels

8.2. Preliminary tests with the three AMCP generations

entrance and, consequently, for increasing the sensitivity to the electron multiplication. The photocathode was fabricated by depositing a 16 nm-thick gold layer on a quartz substrate, which is substantially transparent to photons at 254 nm. The choice of the gold thickness resulted from a compromise between the photon-to-electron conversion efficiency, which increases with the gold thickness, and the escape depth of photoelectrons, which decreases with it. A thickness of 16 nm corresponds to a transmittance of 26%, according to the gold absorption coefficient of $8.4 \times 10^5 \text{ cm}^{-1}$ at 254 nm. Therefore, one fourth of UV photons are not converted. The work function of gold ranges between 4.9–5.1 eV [Rangarajan 80, de Boer 05], which means that photons at 254 nm have just the minimal energy to produce photoelectrons and their kinetic energy is less than 1 eV. Therefore, only the photoelectrons produced very close to the layer surface can actually escape from the material and being accelerated towards the AMCP.

In order to avoid the parasitic collection of photoelectrons by the anode bonding pads and wires, an aluminum foil, with a rectangular hole slightly smaller than the “AMCP island” (where there are the AMCPs, cf. Chapter 6), was placed between the photocathode and the AMCP. This aluminum foil is labeled “photoelectron screen” and it is biased to a lower voltage than that of the photocathode to guarantee an accelerating electric field between the photocathode and the AMCP. The bias voltage to the photocathode and to the “photoelectron screen” is provided by the PS310 high-voltage supply and a voltage divider.

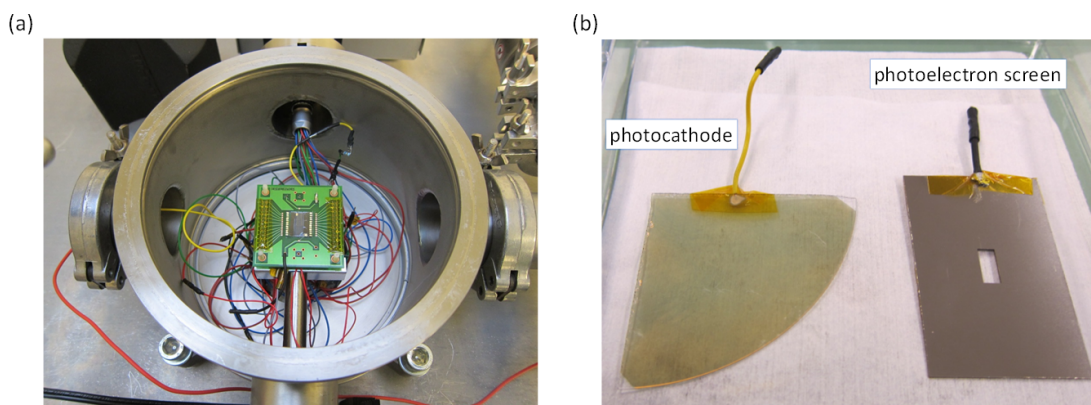


Figure 8.7: (a) Photograph of the vacuum vessel inside with the AMCP interface board mounted on the tilting support. (b) On the left, the 16-nm-thick gold layer on quartz substrate, used as photocathode and, on the right, the “photoelectron screen”.

Measurements of 2nd-gen AMCPs with the UV setup

The anode current of 2nd-gen AMCPs was measured as a function of negative bias voltage (applied on the top electrode), when UV light at 254 nm was shone on them. Figure 8.8(a) shows the measurements performed with the Keithley 617 picoammeter when the AMCP was alternatively in dark and exposed to UV light. The net contribution of the illumination (after the subtraction of the dark curve) is also reported. Figure 8.8(b) shows the measurements

carried out with the lock-in amplifier at a frequency of 225 Hz. The current values are smaller than those measured with the picoammeter simply because the light intensity was reduced by a narrower aperture of the diaphragm and the chopper partial shadowing. The three curves correspond to a non-tilted AMCP, an AMCP tilted by 54° and an AMCP tilted by 54° plus a light attenuation of 50% with one grid. The AMCP tilting was adopted to reduce the channel portion exposed to the UV light.

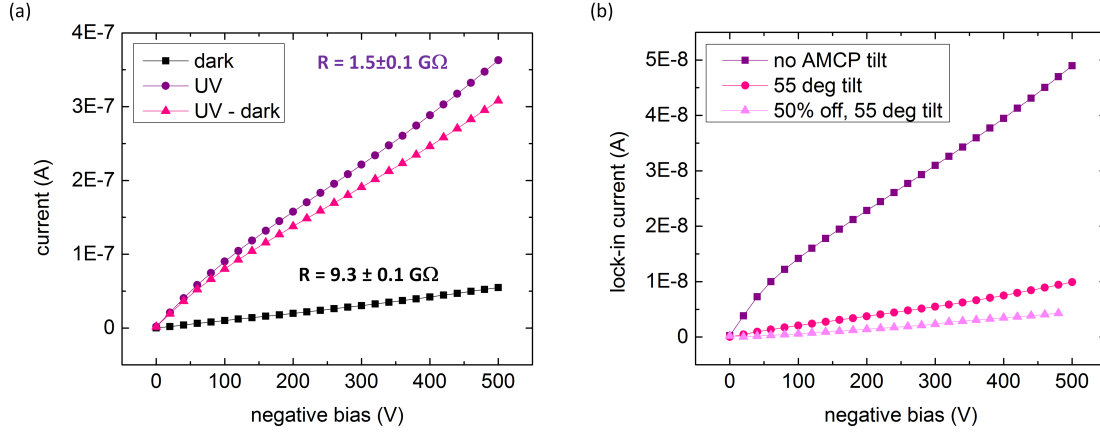


Figure 8.8: (a) Anode current as a function of the AMCP bias voltage both in dark and with illumination at 254 nm. The “UV-dark” curve was obtained by subtracting the “dark” current from the “UV” curve. (b) Anode current as a function of the AMCP bias voltage measured with the lock-in amplifier.

The conclusions of these measurements, in particular with respect to the electron multiplication, are

1. No clear trace of the electron multiplication is observed. Indeed, the multiplication is expected to produce a more-than-linear increase at low bias, before reaching the saturation. The saturation onset is approximately expected to occur for the bias voltage at which the theoretical gain curve reaches its maximum value. This curve is obtained from the well-known equation of the electron multiplication [Wiza 79], which is

$$G = \left(\frac{AV}{2\alpha V_0^{1/2}} \right)^\gamma \quad \text{with} \quad \gamma = 4\alpha^2 \left(\frac{V_0}{V} \right) \quad (8.1)$$

where V is the AMCP bias voltage, α is the channel aspect ratio, A is a factor that depends on the SEE coefficient and is about 0.2 and V_0 is the initial energy of emitted SEs, which ranges between 1-3 eV. A couple of examples of the theoretical curve for different aspect ratios and values of the initial SE energy are shown in figure 8.9.

The reason why the experimental curves of conventional MCPs do not exhibit a maximum, but saturate at a value lower than the predicted one is due to some theoretical

8.2. Preliminary tests with the three AMCP generations

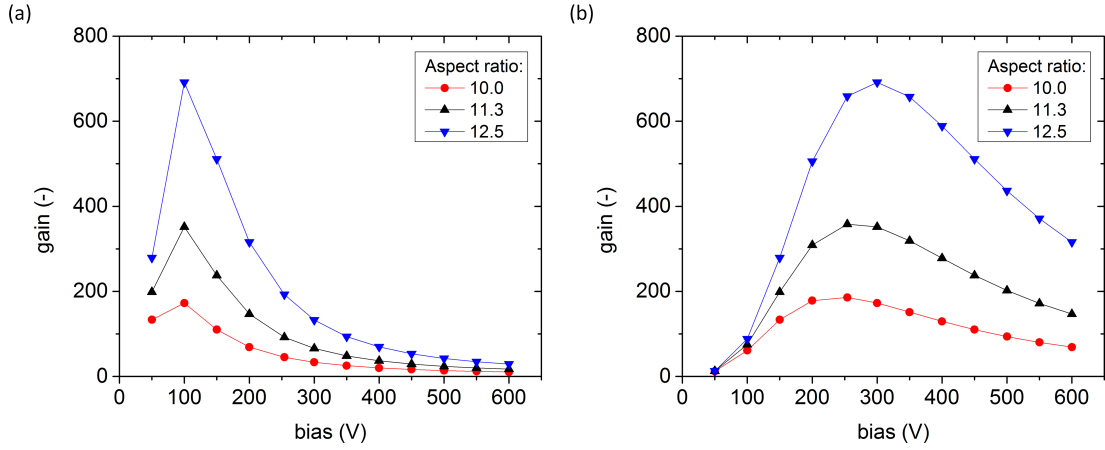


Figure 8.9: *Theoretical MCP gain curves for a few aspect ratios, which are representative of the realized AMCPs, and for an energy of emitted secondary electrons of 1 eV (a) and 3 eV (b).*

approximations such as the SE emission orthogonal to the channel surface [Wiza 79] and the evaluation of only diametric trajectories [Adams 66] (SEs moving along the channel diameter).

The onset of saturation in conventional MCPs, shown in figure 8.10, occurs at electric fields above 2×10^4 V/cm (channel length of $500 \mu\text{m}$ and bias voltage of 1000 V), whereas our measurements show a linearly increasing trend up to 8×10^4 V/cm.

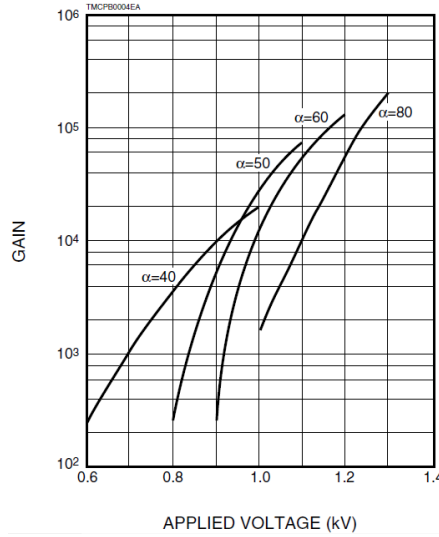


Figure 8.10: *Gain curves for Hamamatsu commercial MCPs, with channel length of $500 \mu\text{m}$.*

2. If the larger current, measured during UV illumination, cannot be attributed to the electron multiplication, it means that photoconductivity [Wronski 81] takes place instead. This makes the AMCP resistance drop by almost one order of magnitude (in the approximation that the electron multiplication has a negligible contribution), as extrapolated.

olated from the UV and the dark curve of figure 8.8(a). The conductivity enhancement is expected to be localized near the channel surface, where the UV photons interact with a-Si:H.

3. In figure 8.8(b), the photoconductivity was confirmed in terms of a smaller current increase versus bias voltage, when the illuminated channel portion and the light intensity are reduced.

In conclusion, the typical signature of the electron multiplication could not be clearly identified in the measured I-V curves. This was mostly caused by both the small a-Si:H quantum efficiency (to produce photoelectrons) and the large photoconductivity contribution on the anode current.

These results evidenced that, as long as the leakage current reached the anode, the sensitivity to the electron multiplication was too low, even when measuring the signal with the lock-in amplifier (which removes the dc contribution of the signal). We tackled this problem by upgrading the AMCP structure with an additional electrode, specifically devoted to the evacuation of the leakage current. This was separated from the anode by 2 μm of a-Si:H to minimize the residual leakage current on the anode (cf. Chapter 6). Additionally, both the intermediate electrode and the anode were grounded, in order to maximize the anode isolation. As presented in Chapter 7, this enabled us to decrease the dark leakage current on the anode by more than five orders of magnitude, i.e. to less than 10 pA. This brought us one step closer to the quantification of the AMCP gain.

8.2.3 Measurements of 3rd-gen AMCPs with UV setup, without photocathode

First measurements with the 3rd-gen AMCPs, but without the photocathode, still exhibited a signal dependency on the channel portion illuminated with UV light and therefore a non-negligible photoconductivity contribution. This is shown in figure 8.11(a), where the anode current depends on the AMCP tilt. This means that a portion of the leakage current still reaches the anode, despite the introduction of the intermediate electrode. The explanation is that the photoconductivity increases the leakage current through the multiplying stack (between top and intermediate electrode) by almost one order of magnitude, as shown in figure 8.11(b). The leakage current evacuation through the intermediate electrode induces a voltage rise, with respect to the reference ground, between the measured AMCPs and the current extraction point (the bonding point of the intermediate electrode, cf. Chapter 7). The voltage rise biases the decoupling stack and reduces the anode isolation.

This effect is particularly enhanced in these measurements, where the anode current is about the same order of magnitude as the leakage current at large bias voltages (figure 8.11(b)), because this test structure has a large number of channels. Consequently, there is a small residual amount of the $\langle n \rangle \mu\text{c-Si:H}$ electrode between channels so that the relevant resistance, as well as the voltage rise, are enhanced.

8.3. Quantification of the electron multiplication with the UV setup

In conclusion, the detection of the electron multiplication was still hindered, for the measured 3rd-gen AMCPs, by the low a-Si:H quantum efficiency and the large channel density. The first problem was solved by the introduction of the gold photocathode. Its quantum efficiency was measured to be about 0.1% at 254 nm, larger than the 0.04% of a-Si:H. Additionally, the photocathode reduced the number of photons that reached the channels (the transmittance at 254 nm is 26%), as well as the photoconductivity phenomenon. Finally, it provided photoelectrons already at the channel entrance.

The second problem was solved by measuring only the latest batches of 3rd-gen AMCPs. They have a number of channels that is about one third that of the former 3rd-gen AMCPs. As presented in Chapter 6, more spaced channels were adopted for preventing that the channel lateral widening, during the DRIE process, could etch the a-Si:H bulk between them.

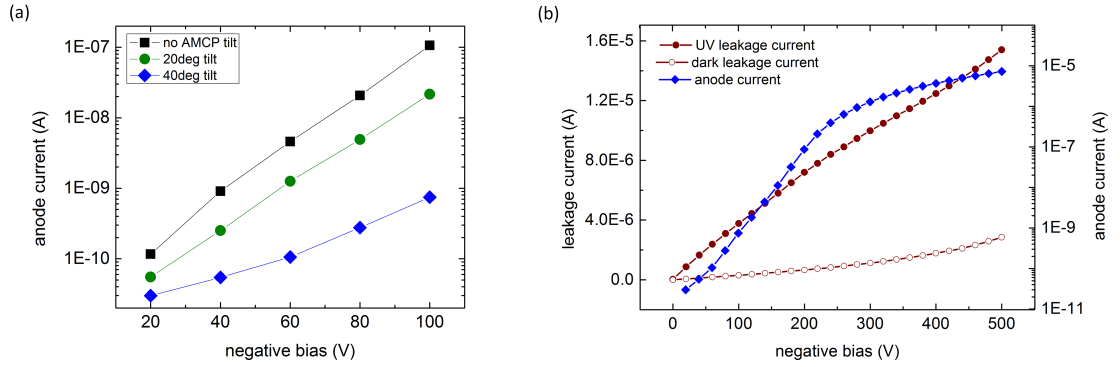


Figure 8.11: (a) Anode current as a function of AMCP negative bias, in case of no tilt and two tilting angles. (b) Leakage current measured on the intermediate electrode, in dark and under UV illumination. The anode current is also shown and it is in the same order of magnitude of the leakage current, for large bias voltages (note the different axis scale for the leakage and anode current). The AMCP is tilted at 40° with respect to the direction of the incoming light.

8.3 Quantification of the electron multiplication with the UV setup

The testing of the 3rd-gen AMCPs with the UV setup, after the photocathode implementation, enabled the achievement of the AMCP proof of concept, with an anode signal that was clearly produced by the electron multiplication. We measured an electron multiplication factor, i.e. a gain, which steadily increased as a function of the AMCP aspect ratio, according to the MCP working principle. Indeed, longer and narrower channels entail more collisions, boosting the gain according to the simplified formula [Wiza 79]: $G = \delta^n$, where δ is the SEE coefficient and n is the number of collisions. The gain was also measured as a function of the AMCP bias voltage and the photoelectron current. The reason why the gain values are quite modest compared to those of conventional MCPs is simply due to the smaller AMCP channel aspect ratios fabricated so far. A simple approach for comparing the AMCP gain with that of conventional MCPs is presented in Section 8.3.2.

8.3.1 Gain results with photocathode: AMCP proof of concept

Measurement configuration

The first evidence of electron multiplication (reported in [Franco 14]) was measured after the implementation of the gold photocathode, which is described in Section 8.2.2. The potential difference between photocathode and AMCPs was 500 V, which corresponded to an electric field of 1250 V/cm, and to a photoelectron energy of 500 eV at the channel entrance. The AMCPs were always tilted at 40° (with respect to the incoming UV light) for minimizing the photoconductivity induced by the residual non-converted photons. Indeed, the photoconductivity enhanced the leakage current on the intermediate electrode and consequently the residual leakage current reaching the anode (according to the results presented in the Section 8.2.3). By doing so, the leakage current on the anode was reduced to less than 10 pA for the maximum AMCP bias voltage of 500 V (always a negative one but presented as a positive one for simplicity). This bias, for a channel length of 80 μm , corresponded to an electric field of about 6×10^4 V/cm. The reason why the leakage current on the anode is actually larger than 10 pA (in the measurements presented below) is because many AMCPs were measured at the same time, for a total AMCP area of 24 mm². In this way, the sensitivity to the electron multiplication was maximized, but the total leakage current was about 100 pA. The anode current was alternatively measured with the Keithley 617 picoammeter and SR830 lock-in amplifier. Although the latter was eventually preferred because of the lower measurement noise, it contributed to further increase the leakage current on the anode due to the capacitive coupling between intermediate electrode and anode. An experimental evidence of this effect was the current dependency on the lock-in frequency. Nevertheless, we verified that this did not introduce any artifact in the measurements by confirming the same gain value across the whole lock-in frequency range of 25–425 Hz. The majority of the gain measurements were performed with at a frequency of 125 Hz, which corresponds to an illumination time of 8 ms. As this timeframe is much longer than both the multiplication dynamic and the charge replenishment on the channel surface, the gain is always measured in a quasi-continuous illumination regime. Finally, it is worth mentioning that the anode current growth at the beginning of the electron multiplication occurs in a timeframe of about 500 ms due to the lock-in RC time constant.

Gain curves for different input currents

Three examples of the typical electron multiplication measurement are shown in figure 8.12(a). The anode current is recorded as the photocathode is sequentially grounded, biased and grounded. When the photocathode is biased, the photoelectrons are accelerated towards the AMCP and then multiplied in the channels (the multiplication phase, highlighted in green in figure 8.12(a)). This produces the larger current in the central part of figure 8.12(a). As highlighted by the arrows, the larger the AMCP bias voltage, the larger is the electron multiplication. The gain is calculated as the current variation (with biased and grounded photocathode) di-

8.3. Quantification of the electron multiplication with the UV setup

vided by the calibrated photoelectron current inside channels (I_0). The latter is obtained as the current produced by the photoelectrons that are collected at the AMCP top, intermediate and anode electrodes, when they are all grounded, divided by the AMCP open area ratio (the total channel area of all connected AMCPs divided by that of the electron screen).

As seen in figure 8.12(b), **the gain values reaches about 30 for an AMCP aspect ratio of 12.5:1, biased at 500 V**. The gain was also measured for four photoelectron input currents (I_0). The current values lower than the maximum one of 93 pA were obtained by employing the attenuation grids. The input current of 93 pA corresponds to an input flux of $9 \times 10^9 \text{ cm}^{-2} \text{ s}^{-1}$, according to the total area of all exposed channels. This flux will be eventually used for comparing the gain results obtained with the UV setup and with the SEM beam. The fact that the gain values are similar for different I_0 proves that the charge replenishment is large enough to sustain the electron multiplication. However, input currents larger than 93 pA could not be tested because this value was the maximum achievable with the UV lamp and the gold photocathode.

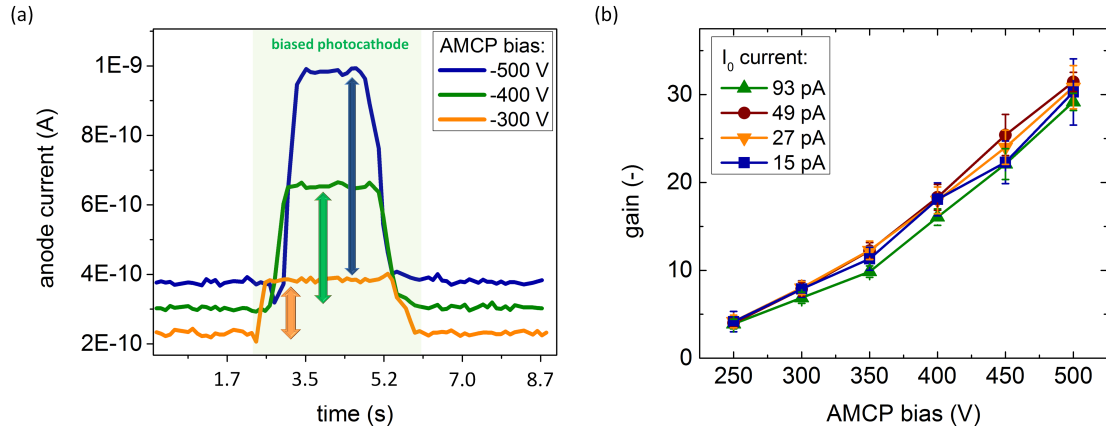


Figure 8.12: (a) Anode current when the photocathode is sequentially grounded-biased-grounded. The three curves refer to three AMCP bias voltages. The arrows evidence the increasing gain versus bias voltage. (b) Gain as a function of AMCP bias voltage for four photoelectron input currents.

Gain curves for different aspect ratios

The gain as a function of three aspect ratios are shown in figure 8.13, for an input flux of $9 \times 10^9 \text{ cm}^{-2} \text{ s}^{-1}$ ($I_0 = 93 \text{ pA}$). These results provide the definitive proof that the output signal is produced by the electron multiplication, because a larger gain for longer and/or narrower channels can only be explained by a larger number of collisions (see drawings in the top left corner of both graphs). In figure 8.13(a), the gain is compared for two AMCPs with same channel length of $76 \mu\text{m}$, but different channel diameters of 6.1 and $7.4 \mu\text{m}$. In figure 8.13(b), the gain of two AMCPs with same channel diameter of $6.1 \mu\text{m}$, but different lengths of 51 and $76 \mu\text{m}$, is plotted versus the electric field, rather than the bias voltage, for comparing with the same accelerating field strength.

These results also demonstrate the a-Si:H good performances in sustaining large bias voltages, corresponding to electric fields up to 7.5×10^4 V/cm. These values are larger than the usual ones of about 2×10^4 V/cm adopted in commercial lead-glass MCPs.

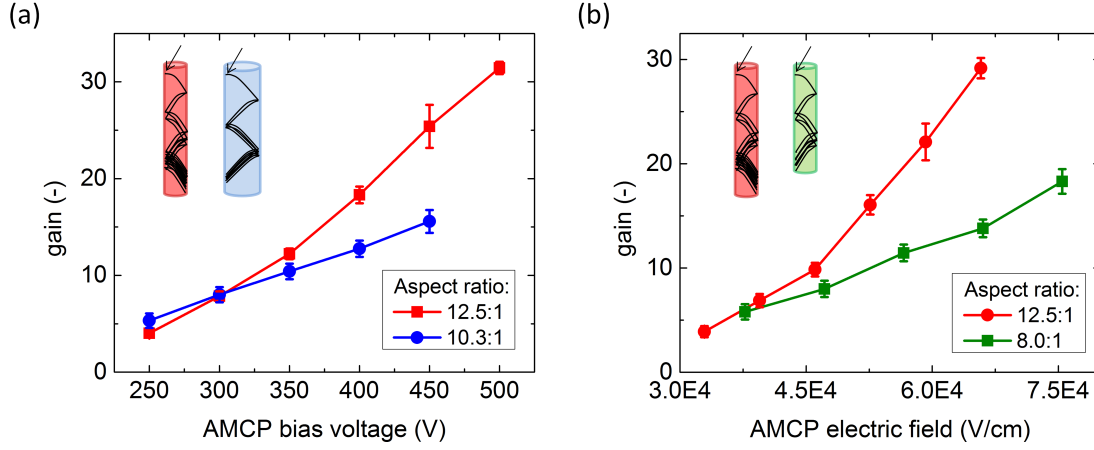


Figure 8.13: (a) Gain versus bias voltage for two aspect ratios of 12.5:1 and 10.3:1 obtained with the same channel length of $76 \mu\text{m}$, but channel diameters of 7.6 and $6.1 \mu\text{m}$, respectively. (b) Gain versus electric field for two aspect ratios of 12.5:1 and 8.0:1 obtained with the same channel diameter of $6.1 \mu\text{m}$, but different channel lengths of 76 and $53 \mu\text{m}$.

8.3.2 Eberhardt's model and comparison with conventional MCPs

The present AMCP gain is considerably lower than that of conventional MCPs due to the much smaller aspect ratio. Indeed, the MCP aspect ratio ranges within 40:1–60:1. However, we can use a simple model of the electron multiplication, developed by Eberhardt [Eberhardt 79, Eberhardt 81], for comparing the AMCP performances to those of MCPs, and taking into account the different aspect ratios. According to this model, the MCP can be “dynodized”, i.e. represented with a certain number of discrete dynodes (n) that do not depend on the bias voltage. This is quite an approximation since it is well-known that the number of collisions is inversely proportional to the accelerating field [Adams 66, Guest 71], which leads to a saturation of the gains at large bias voltages. Despite this approximation, the model is applicable to our results as it requires only the gain-versus-bias curves of a few aspect ratios for calculating the relevant number of collisions. Indeed, the model is based on the following definition of the gain

$$G = \delta_1 \cdot \delta^{n-1} = \delta_1 \cdot \left(\frac{V}{n \cdot V_c} \right)^{k(n-1)}, \quad (8.2)$$

where δ_1 is the SEE coefficient at the first collision (which takes into account that the electron energy at the first collision can be different from that of the following collisions), δ is the SEE

8.3. Quantification of the electron multiplication with the UV setup

coefficient for the following collisions and n is the number of collisions. The SEE coefficient is defined as

$$\delta = \left(\frac{V_z}{V_c} \right)^k \quad (8.3)$$

where V_c is the first crossover potential, i.e. the minimum value at which δ is equal to unity, and k is a constant coefficient that relates to the curvature of the secondary emission function $\delta(V_z)$, with V_z as the potential acquired by the electrons between two collisions. If the logarithm is applied to either side of eq. (8.2), this becomes

$$\log G = k(n-1)\log(V) - k(n-1)\log(nV_c) + \log \delta_1. \quad (8.4)$$

According to (8.4), one expects a linear dependency of the logarithm of the gain versus the logarithm of the bias voltage. By attributing a value of 0.5 to k , as it was done by Eberhardt, one can extract the number of collisions from the linear regression curves. This was done for four AMCP aspect ratios, as shown in figure 8.14(a). The relevant number of collisions is plotted as a function of the aspect ratio in figure 8.14(b). These data are also fitted and the obtained AMCP slope is compared to that of conventional MCPs [Eberhardt 81]. Despite the model approximations, the two slopes are almost compatible within the experimental errors (obtained from the least square method).

a-Si:H secondary electron emission coefficient

From the extracted number of collisions, we can also calculate the a-Si:H SEE coefficient, according to the approximated equation of the electron multiplication, i.e. $G = \delta^n$. The SEE coefficient is about 1.7 for an electron impinging energy of about 100 eV, which is obtained from the bias voltage of 500 V divided by about 5 collisions relevant to the AMCP with aspect ratio of 10.3:1. This SEE coefficient is almost compatible with those available in the literature for a-Si:H [Joy 95], whose largest one is 1.42 at 500 eV. Since the maximum in SEE coefficient for c-Si is attained for electron energies within 200–300 eV [Seiler 83], it is likely that the a-Si:H one is also larger than 1.42 for a collision energy of about 100 eV, in agreement with our results.

In conclusion, we provided a first evidence that **the AMCP gain can match that of conventional MCPs for similar aspect ratios and that the calculated a-Si:H SEE coefficient is compatible to the values reported in the literature.**

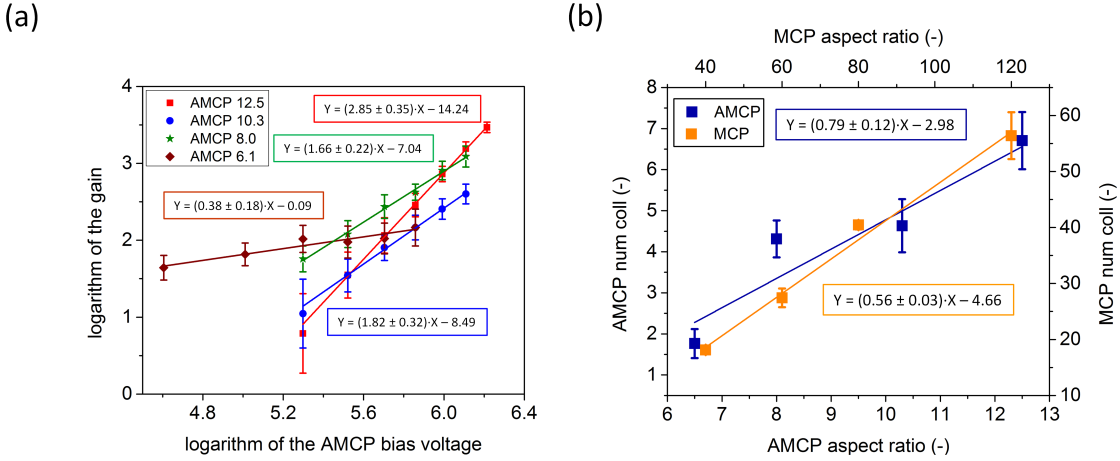


Figure 8.14: (a) *Logarithm of the gain versus the logarithm of the bias voltage for four AMCP aspect ratios, together with the linear regression curves.* (b) *Extrapolated number of collisions as a function of the aspect ratio for AMCPs and MCPs. Note the different sets of axis for the AMCP and MCP data.*

8.3.3 Effect of the long channel surface exposure to the impinging electrons

The measurements of electron multiplication, like the one presented in figure 8.12(a), were systematically followed by annealing steps. These were adopted because the AMCP gain was observed to be no longer reproducible after a certain number of multiplication phases (when the photocathode is biased). An example of gain measurement, after a cumulative time of multiplication phases of about 2 minutes, is shown in figure 8.15(a). The current growth at the beginning of the electron multiplication is less sharp, the current during the multiplication phase (highlighted in green) is not constant over time anymore and once the photocathode is grounded again, the leakage current on the anode does not go back to the initial value. Consequently, the gain calculation becomes complicated and its value is overestimated. Eventually, we found out that by annealing the AMCP to about 90 °C for 10–30 minutes, we could bring the AMCP back to the initial performance state.

After the measurement of figure 8.15(a) and the annealing at 90 °C for 15 minutes, we repeated the measurement of electron multiplication and we obtained the result of figure 8.15(b): At the beginning of the measurement, the leakage current on the anode was lower than at the end of the previous measurement, the current during multiplication still increased over time but less rapidly and after the multiplication phase, it came back almost to the initial level. The gain dropped from 34 as in figure 8.15(a) to 17 as in figure 8.15(b). With a longer annealing of about 30 minutes, the gain measurement became like those presented in figure 8.12(a).

The reason for this lack of repeatability is attributed to charge trapping in the a-Si:H localized states. This phenomenon is expected to take place near the channel surface, where the impinging electrons interact with a-Si:H and stimulated the emission of secondary electrons. Some of the impinging electron energy is also spent to promote electrons and holes to the a-Si:H extended states, where they drift due to the electric field. However, some of them

8.3. Quantification of the electron multiplication with the UV setup

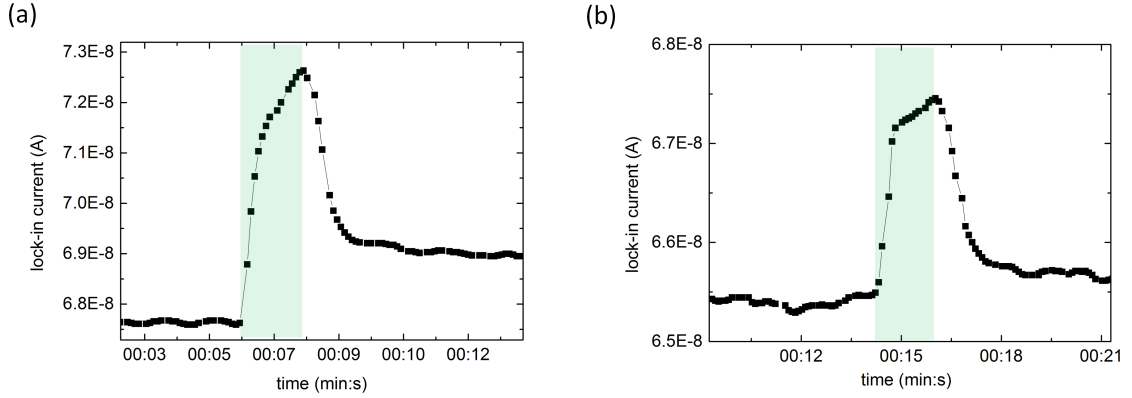


Figure 8.15: (a) Gain measurement with lock-in amplifier, after a cumulative time of multiplication phases of about 2 minutes. The current growth upon electron multiplication is less sharp than those of figure 8.12(a) and it does not stabilize. The calculated gain is 34 with an AMCP of 10.3:1, biased to 400 V and with $9 \times 10^9 \text{ cm}^{-2} \text{ s}^{-1}$ ($I_0 = 93 \text{ pA}$). (b) Same measurement as the left one, but after an annealing at 90°C for 15 minutes: gain drops to 17.

are trapped in the a-Si:H localized states (cf. Chapter 3) before being collected at either electrode. As long as the electron multiplication is sustained, these states become gradually filled. Macroscopically, this process of increasingly filled traps enables the new electron-hole pairs to drift for longer distances and to enhance the material conductivity near the surface. This, in turn, makes the leakage current grow during multiplication. This growth was observed not to saturate within a timeframe of 10 minutes. Measurements longer than 10 minutes were avoided because of the risk of thermal runaway. Indeed, the AMCP temperature was also measured to increase by a few degrees for such a long multiplication phase. This was measured by the Pt100 probe of the heating setup (glued on the copper element rather than on the AMCP itself) so that the actual AMCP temperature increase was likely to be larger than the measured one.

Once the electron multiplication was interrupted by grounding the photocathode, the leakage current went back to its original level with a dynamics similar to that observed in a-Si:H when charges are released from the localized states after conductivity probing [Street 90]. Our annealing simply accelerates this process due to the larger thermal energy available for the charge release.

The reason why this leakage current enhancement also affects the measurement of electron multiplication is attributed to the progressively weaker anode isolation (with respect to intermediate electrode) when progressively larger leakage current is evacuated. This mechanism is explained in Chapter 7 and it is based on the fact that due to the non-negligible $(n) \mu\text{c-SiO}_x$ intermediate electrode resistivity, the leakage current evacuation through this layer induces a voltage rise from the measured AMCP to the current extraction point (at the ground potential). Since the gain measurements with the UV setup were performed with many AMCPs connected together, this effect was particularly large due to the fact that some of the measured AMCPs are almost 1 cm away from the leakage current extraction point. Two examples of leakage current growth during electron multiplication—which also induced an increase in the leakage

current on the anode—are shown in figure 8.16. In figure 8.16(a), current on both intermediate electrode and anode is plotted versus time while photoelectrons are multiplied in the channels. Each sharp current increase corresponds to an increment in the AMCP bias voltage of 20 V. Additionally, for bias values above 140 V, the current starts to increase also between two voltage steps (highlighted in blue). The larger the bias, the steeper is the current increase over time because the multiplication is larger so that more electron-hole pairs are generated along the channel surface and the leakage current grows faster. This influences the leakage current on the anode, which shows a similar behavior.

For the same reason, in figure 8.17(b), current on both intermediate electrode and anode increases over time, for an AMCP biased at -300 V and it does not saturate after 11 minutes of electron multiplication.

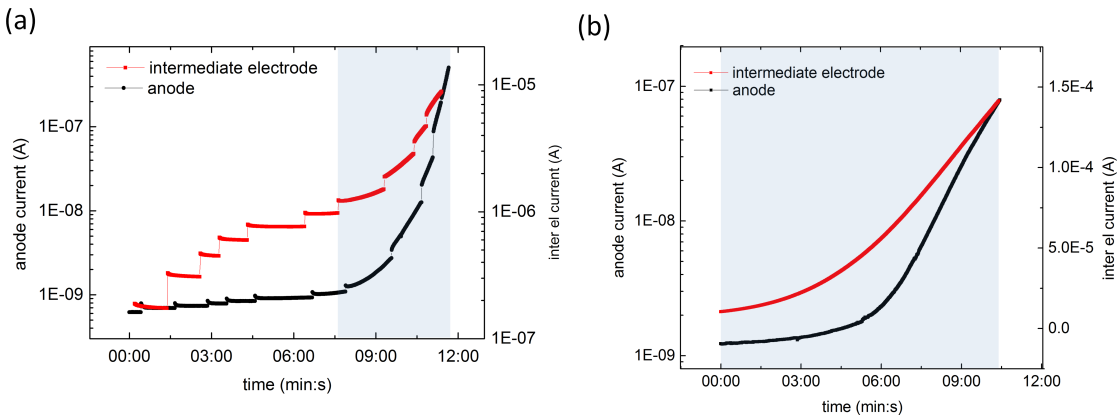


Figure 8.16: (a) Current on both the anode and the intermediate electrode for a progressively larger and larger AMCP bias, with steps of 20 V. The photocathode is also biased and provides a photoelectron flux of $9 \times 10^9 \text{ cm}^{-2} \text{ s}^{-1}$. The electron multiplication induces a growth over time of the leakage current between two voltage steps (in the region highlighted in blue), which, in turn, induces a similar increase on the residual leakage current on the anode. (b) Leakage current on the intermediate electrode and the anode for an AMCP of 10:1, biased to 300 V. The growth of the overall leakage current induces a similar effect also on the anode current.

To conclude, even though the leakage current on the anode must be minimized, for instance by the implementation of a more conductive material for the intermediate electrode and a more insulating material for the decoupling layer, this growing leakage current over time can be beneficial for the charge replenishment. However, it is important that the AMCP temperature is kept stable, for instance by providing some cooling. This was shown to effectively reduce the risk of thermal runaway when low-resistance lead-glass MCPs were fabricated for extending the dynamic range [Tremis 96a].

8.4 Quantification of the electron multiplication with the SEM

In the final part of this thesis, we used again the SEM beam to investigate the AMCP electron multiplication as a function of the parameters of the impinging electrons. The reason

for these additional measurements was that the UV setup had an intrinsic limitation when testing AMCPs, whose channels do not have a bias angle. As the photoelectrons follow the electric field lines, it was likely that some of them never collided inside the channels, whose axis was parallel to their movement. For the same reason, other photoelectrons probably experienced fewer collisions than the maximum achievable number. Therefore, the aim of the new measurements with the SEM was to simulate a channel bias angle, by tilting the sample holder (and the AMCP with it) with respect to the impinging electrons direction. The gain values were compared for two tilting angles corresponding to a channel portion exposed to the photoelectrons of 30% and 8%, respectively.

In the following sub-sections, we present the electron multiplication dynamics for the measurements with the SEM and, afterwards, the gain results as a function of both the AMCP design and the beam parameters.

8.4.1 Testing conditions with the electron beam

In Section 8.2.2, we explained that when the electron beam is focused inside only one channel, the large density of generated electron-hole pairs in a-Si:H adds a betaconductivity contribution to the output signal, which is larger than the contribution of the electron multiplication. Although the betaconductivity contribution is largely reduced by the introduction of the intermediate electrode (in 3rd-gen AMCPs) a too large leakage current can still interfere with the anode signal, according to the phenomenon presented in Section 8.3.3. Furthermore, if the electron beam is focused in one channel, the gain risks to be limited by an insufficient charge replenishment, due to the too large input flux. Therefore, we decided to sweep the beam across most of the AMCP surface, within an area of 3 mm², rather than keeping it focused inside one channel. Consequently, the electrons were injected into each channel for less than 10 μ s and with a repetition rate of 10 Hz. This rate was obtained by sweeping the frame with 484 horizontal lines of 0.21 ms each. The beam spot was also defocused from the standard 10-nm-wide spot to 4 μ m, so that 484 sweeps were enough to provide uniform electron intensity across the whole frame. With these parameters, the number of electrons inside each channel was limited to 3–7200 per frame, according to the selected beam current of 0.5–1200 pA.

The current collected at the anode was measured with the 6487 Keithley picoammeter. Then, this current was multiplied by the open area ratio (total channel area over frame area) to take into account that the measured current is constituted by an alternation of multiplication phases (when the beam is in correspondence of one channel) and inactive phases (when the beam is between two channels). The gain is calculated as this output current divided by the calibrated beam current (I_0).

Comparison with the testing conditions of the UV setup

In order to compare the results obtained with the SEM and the UV setup, we have to take care of being in similar testing conditions, especially in terms of input flux. This ranged within $3 \times 10^9 \text{ cm}^{-2} \text{ s}^{-1}$ – $5.5 \times 10^{12} \text{ cm}^{-2} \text{ s}^{-1}$ for the measurements with the SEM, whereas it

was within $1.4 \times 10^9 \text{ cm}^{-2} \text{ s}^{-1}$ – $9 \times 10^9 \text{ cm}^{-2} \text{ s}^{-1}$ for the measurements with the UV setup. The corresponding number of electrons injected in each channel per second ranged within 40–70000 for the measurements with the SEM and within 19–117 for that with the UV setup. In order to facilitate the comparison of the results obtained with the two setups, we have always reported the input electron flux.

The electron energy was set to 1 keV. This energy was chosen for having impinging electrons of about 500 eV at the first collisions, when the AMCP top electrode was biased to -500 V. In this way, we could compare the gain with that measured with the UV setup (where the photoelectrons have an energy of 500 eV).

The electron energy of 1 keV was kept also for lower AMCP bias voltages, with the approximation that the gain did not change significantly as a function of it. Indeed, the slightly larger SEE coefficient obtained by impinging electrons (at a grazing angle of incidence) more energetic than 500 eV at collision (up to 800 eV for an AMCP bias voltage of -200 V), had a smaller effect at a lower AMCP bias voltages, due to the smaller electron multiplication.

In conclusion, this approximation might have caused the gain curves presented in Section 8.4.3 to show a slight pronounced saturation behavior at the larger bias voltages.

8.4.2 Electron multiplication dynamics with the SEM electron beam

In this section, we present the evolution of the electron multiplication over time. During the same multiplication phase the gain is not constant during time, but it takes some time to reach the maximum value if the input flux is below $3.6 \times 10^{11} \text{ cm}^{-2} \text{ s}^{-1}$. Furthermore, it drops considerably, within a few seconds, after having reached the maximum value at input fluxes above $1.2 \times 10^{12} \text{ cm}^{-2} \text{ s}^{-1}$. Finally, it increases again for input fluxes above $1.5 \times 10^{12} \text{ cm}^{-2} \text{ s}^{-1}$. The explanation of these effects is presented below. For these measurements, the AMCP tilting angle was always within 14 – 18° , so that the first 30% of the channel length was exposed to the impinging electrons, according to the AMCP aspect ratio.

Gain stabilization at small input currents

At the beginning of a new measurement session, the gain is observed to slowly grow over time, before reaching its maximum value. The input flux is always $8 \times 10^{10} \text{ cm}^{-2} \text{ s}^{-1}$ ($I_0=17 \text{ pA}$) and the electrons inside each channel are about 1000 per frame. The gain evolution as a function of the multiplication and the waiting (between measurements) time is summarized in figure 8.17(a). The three measurements with the AMCP biased at -400 V show a gain that grows during each multiplication phase (highlighted in green in figure 8.17(b)-(c)-(d)). Additionally, this growth tends to stabilize as a function of the overall multiplication time, as evinced by a similar gain at the end of the multiplication phase in figure 8.17(c) and (d). Alternatively, the gain is observed to decrease of a certain amount between two consecutive measurements.

Qualitatively, this behavior suggests some sort of “activation”. We attribute it to the a-Si:H

8.4. Quantification of the electron multiplication with the SEM

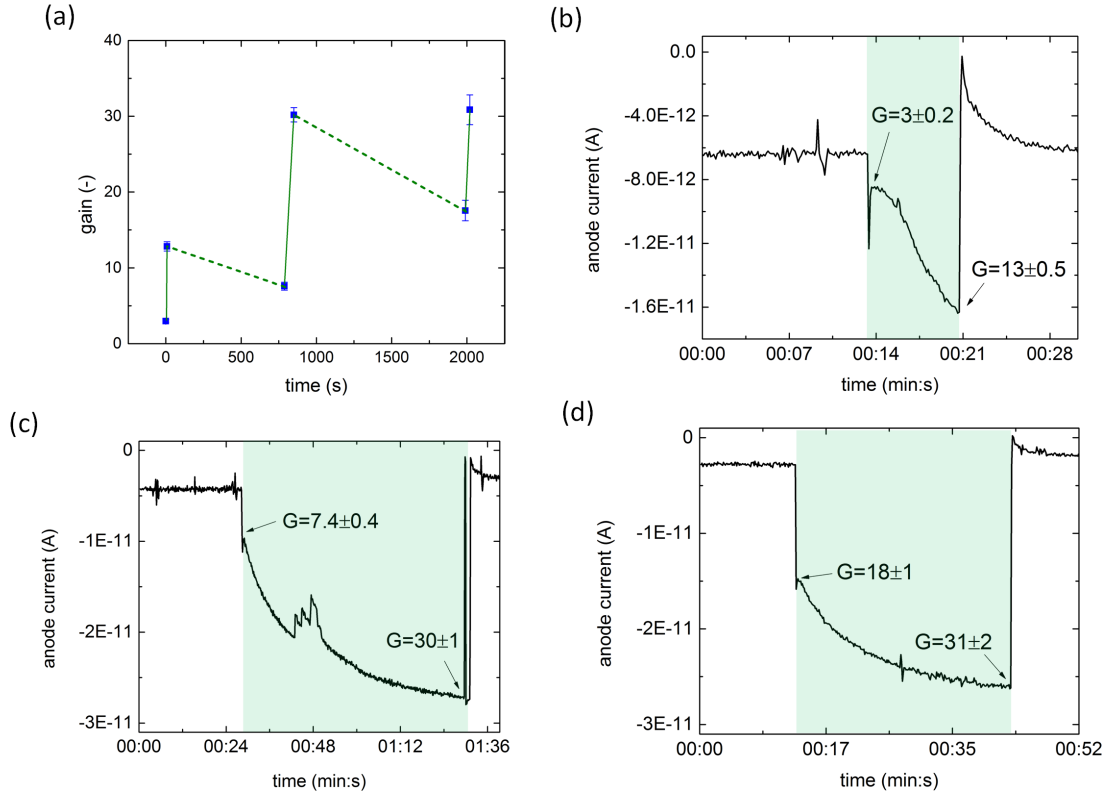


Figure 8.17: (a) Gain evolution as a function of time for a number of electron multiplication measurements. The full lines connect the gain values measured at the beginning and at the end of each multiplication phase, presented in graphs (b), (c) and (d) for an AMCP of 12:1 and biased at -400 V. The dashed lines evidence the gain drop between two consecutive measurements. In graphs (b), (c) and (d) the area highlighted in green corresponds to the multiplication phase. The input flux is $8 \times 10^{10} \text{ cm}^{-2} \text{ s}^{-1}$ ($I_0 = 17 \text{ pA}$).

temporal variations in the SE emission dynamics. This phenomenon has been observed for many SE emissive materials, but the dynamics are not fully clear to date.

We also observed that the gain stabilizes faster for both larger AMCP bias voltages and larger beam currents. These observations are compatible with an initial stabilization of the SEE process.

In conclusion, **once the gain stabilizes at its maximum value, it is reproducible at any input current**, at least before other phenomena come into play, as discussed in the next two subsections. This maximum gain value is the one that was used to investigate the dependencies on all the AMCP geometrical features and testing parameters, presented in Section 8.4.3.

Gain drop at medium and large input currents

Upon the initial gain stabilization to the maximum value, the gain is observed to drop over time during the same multiplication phase, as shown in figure 8.18. The measured AMCP has

an aspect ratio of 10.3:1 and it is biased at -400 V. The following observations are made:

1. the pace of the gain drop increases with I_0
2. the output signal drops even though the leakage current increases (shown by the red curves in figure 8.18(a)-(b)-(c)), which rules out any dependency of the anode signal on the leakage current (such as those presented in Section 8.2.1 and 8.3.3).

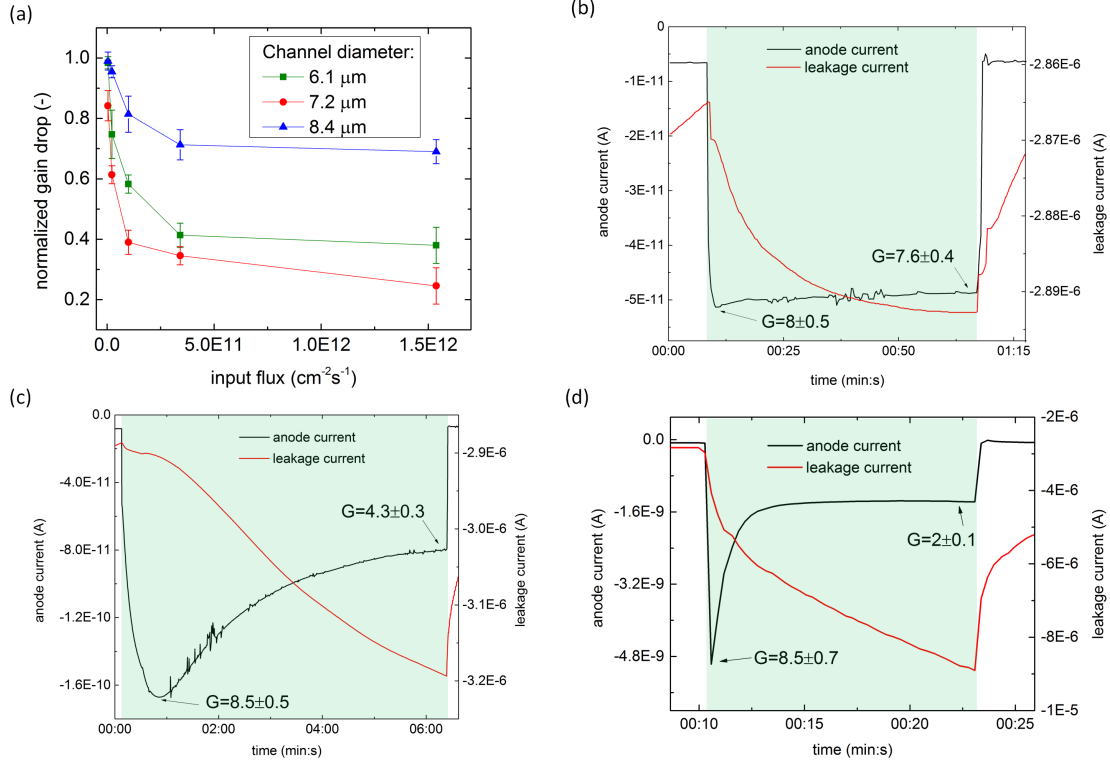


Figure 8.18: (a) Normalized gain drop, which was measured during the multiplication phase, as a function of the input flux and for three AMCPs of different channel diameters. (b)-(c)-(d) anode and leakage current before, during and after the electron multiplication phase (highlighted in green), for the AMCP of 10.3:1 with a channel diameter of 7.2 μm and biased to -400 V. (b) is obtained with an input flux of $4 \times 10^9 \text{ cm}^{-2}\text{s}^{-1}$, (c) with an input flux of $2 \times 10^{10} \text{ cm}^{-2}\text{s}^{-1}$, (d) with an input flux of $1.5 \times 10^{12} \text{ cm}^{-2}\text{s}^{-1}$.

This gain drop, during electron multiplication, cannot be attributed to the insufficient charge replenishment in the channel because the leakage current is a few orders of magnitude larger than output signal. Although the leakage current does not entirely flow near the channel surface, its increase during the multiplication phase is deemed to be localized near the channel surface, since it is induced by the electron multiplication (and interaction) with the channel surface.

Alternatively, this gain dynamics could be explained with a charging effect that occurs on the decoupling stack surface. Indeed, both the intermediate electrode and the anode are at a

8.4. Quantification of the electron multiplication with the SEM

nominal ground potential so that there is no charge replenishment in the decoupling stack. During the electron multiplication, this surface is progressively depleted of electrons until it attains a certain positively charged state. This modifies the electric field distribution in the bottom part of the channel, which could clog, to some extent, the electron multiplication. The larger the I_0 , the faster is the surface charging and the quicker the gain drops to its final stabilized value. This can be observed at the end of the exposure phase, for an input flux of $1.5 \times 10^{12} \text{ cm}^{-2} \text{ s}^{-1}$.

According to the proposed explanation, AMCPs with wider channels are expected to exhibit a smaller gain drop because for the same amount of surface charging, the electric field, in the channel center, is less affected. Two AMCPs, out of three measured, support this hypothesis because the one with the widest channels exhibits the smallest gain drop. This is shown in figure 8.18(d), where the normalized gain drop of the AMCP with 8.4- μm -wide channels (94 μm long, aspect ratio of 11:1) is smaller than that of the AMCP with 6.1- μm -wide channels (73 μm long, aspect ratio of 12:1). Also, the gain drops was slower over time for the AMCP with 8.4- μm -wide channels so that its variation was negligible within a few minutes, for the input flux of $1.6 \times 10^{10} \text{ cm}^{-2} \text{ s}^{-1}$.

However, the third AMCP with 7.2- μm -wide channels (75 μm long and aspect ratio of 10.3:1) shows the largest gain drop, in contradiction to our explanation. This mismatch could be explained in terms of channels that get narrower in correspondence of the decoupling layer, as the ones shown in figure 8.19.

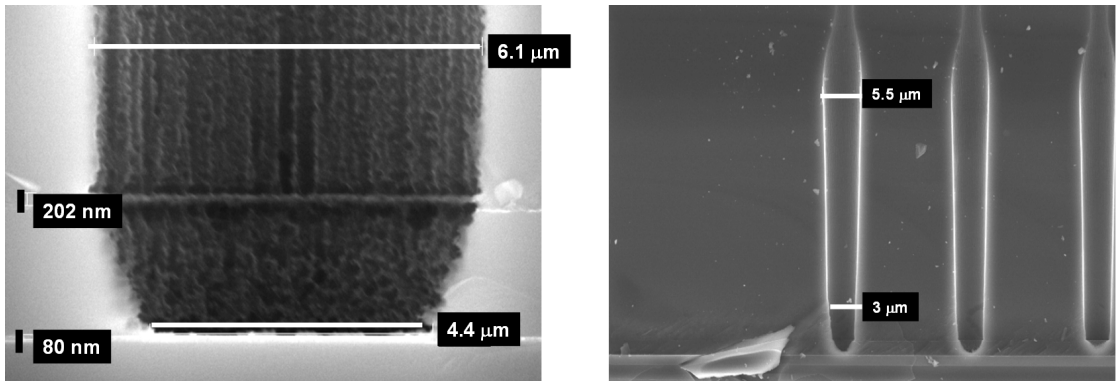


Figure 8.19: SEM images of AMCP cross sections showing that the channels are occasionally narrower at the bottom end.

These SEM images belong to the test structure that was next to this third tested AMCP. This channel narrowing mainly occurs for the test structures that are near the wafer edges, where the deposited thickness is slightly larger with the consequence that the DRIE process was occasionally not carried out long enough to get perfectly cylindrical channels.

The proposed explanation for the gain drop will need to be further investigated with other AMCPs because of the low statistics presented here. In the measurements with the UV setup, the input fluxes were too low to observe any significant gain drop, within the measurement time frame.

Gain increase at large input current

To conclude the description of the gain evolution during the multiplication phase, once the gain has stabilized to a value lower than the maximum one, it was observed to increase again (in a timeframe of 1 minute) if the input flux was large enough, i.e. above $2.5 \times 10^{11} \text{ cm}^{-2} \text{ s}^{-1}$. Two examples of this effect are presented in figure 8.20. We attribute this slow but steady increase over time to the voltage rise (progressively more negative with respect to the ground reference) across the intermediate electrode, caused by the leakage current evacuation. The voltage rise biases the decoupling stack so that some electrons, provided by the intermediate electrode, reach the decoupling stack and reduce the surface charging. Consequently, the electron multiplication could be less clogged, according to the hypothesis presented above.

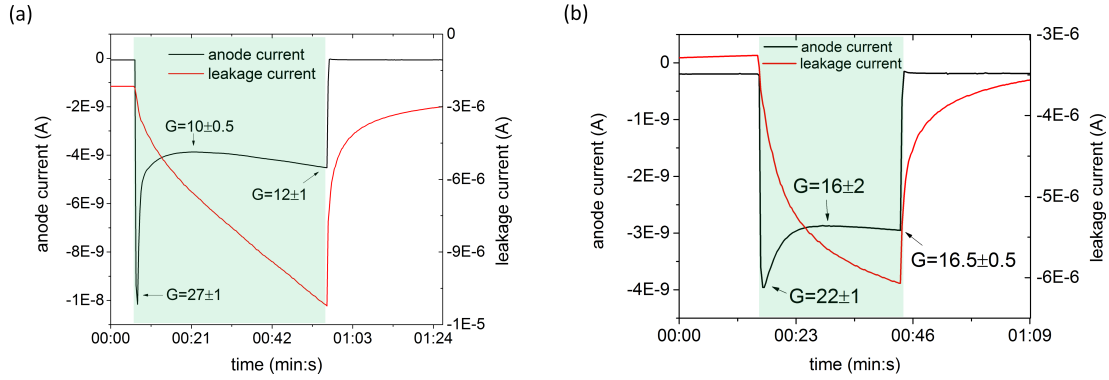


Figure 8.20: Anode and leakage current before, during and after the electron multiplication phase (highlighted in green). (a) measurement of the AMCP of 12:1 and channel diameter of $6.1 \mu\text{m}$, which is biased at -400 V . The input flux is $5.5 \times 10^{12} \text{ cm}^{-2} \text{ s}^{-1}$. (b) measurement of the AMCP biased at -500 V with aspect ratio of 11:1 and channel diameter of $8.4 \mu\text{m}$, input flux of $2.5 \times 10^{11} \text{ cm}^{-2} \text{ s}^{-1}$.

The polarization of the decoupling layer was also discussed in Section 8.3.3, but here the effect is smaller because only one AMCP is measured at a time and this is always the closest one to the extraction point of the leakage current, so that the voltage rise across the intermediate electrode is minimized.

8.4.3 AMCP gain results obtained with the SEM beam

In this section, we present the AMCP gain results as a function of the input current, the aspect ratio, the beam energy and the sample holder tilting angle. Finally, the gain enhancement when a SE emissive layer is deposited on the channel surface is discussed.

When not stated otherwise, the AMCP tilting angle was always within $14\text{--}18^\circ$ to guarantee that the first 30% of the channel length was exposed to the incoming electrons for all tested AMCP aspect ratio.

Gain curves for different input currents

The overview of the gain values as a function of AMCP bias voltage and input current is reported in figure 8.21, for the AMCP with aspect ratio of 12:1. The lowest flux of $1.5 \times 10^{10} \text{ cm}^{-2} \text{ s}^{-1}$ is the only one to provide a gain that is stable, during the multiplication phase of less than 1 minute, for all the tested bias voltages. For all the other larger fluxes, the gain drops because of the supposed charging of the channel surface in correspondence of the decoupling layer. Therefore, the gain curve at $1.5 \times 10^{10} \text{ cm}^{-2} \text{ s}^{-1}$ is the one that corresponds to the maximum gain achievable for that specific aspect ratio and bias voltage.

A couple of important observations are

1. When the gain curves are plotted in the semi-logarithmic scale, the gain increase is less than linear, which is normally attributed to the onset of saturation [Wiza 79]. This could also be partly attributed to the beam energy of 1 keV for all tested AMCP bias voltages (cf. Section 8.4.1).
2. Above 200 V, the gain drop as a function of the input flux, is larger between $8 \times 10^{10} \text{ cm}^{-2} \text{ s}^{-1}$ and $3.6 \times 10^{11} \text{ cm}^{-2} \text{ s}^{-1}$ than between $3.6 \times 10^{11} \text{ cm}^{-2} \text{ s}^{-1}$ and $3.8 \times 10^{12} \text{ cm}^{-2} \text{ s}^{-1}$. This confirms what was discussed in the Section 8.4.2, namely that the gain drop stabilizes once the decoupling layer surface cannot be charged any further.

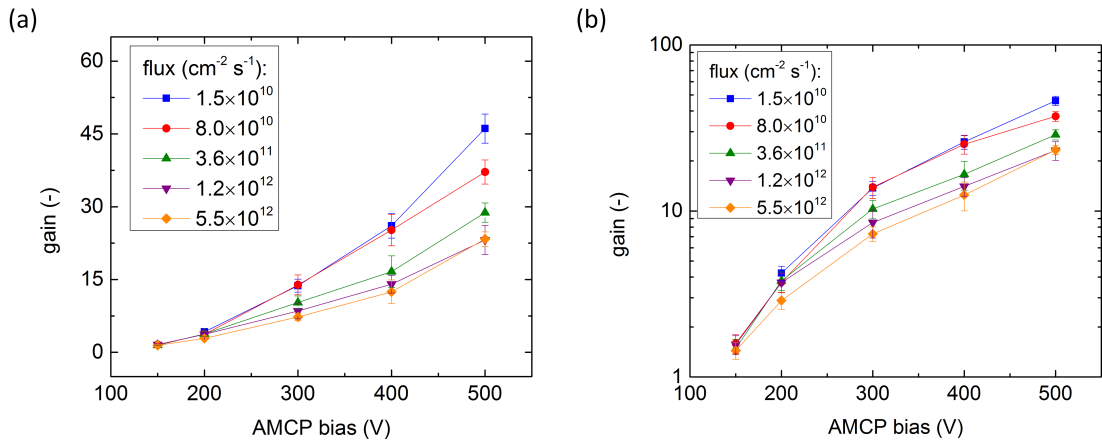


Figure 8.21: (a) AMCP gain versus bias voltage for different input fluxes. The smallest one of $1.5 \times 10^{10} \text{ cm}^{-2} \text{ s}^{-1}$ is the only one to yield a gain that does not drop over time for all the adopted bias voltages. (b) same data on a semi-logarithmic graph.

For all other results presented below, only the maximum achieved gain values are presented.

Gain curves for different aspect ratios

The electron multiplication was measured for the three aspect ratios of 12:1, 11:1 and 10:1. Different and newer AMCP test structures were tested, rather than those measured with the

UV setup, in order to confirm again the growing gain with the aspect ratio. The channel length is $74\text{ }\mu\text{m}$ for 12:1, $93\text{ }\mu\text{m}$ for 11:1 and $73\text{ }\mu\text{m}$ for 10:1. The channel diameter is $6.1\text{ }\mu\text{m}$ for 12:1, $7.2\text{ }\mu\text{m}$ for 10:1 and $8.4\text{ }\mu\text{m}$ for 11:1. This confirmation was successfully achieved as shown in figure 8.22, although the gain curves for the two largest aspect ratios are almost compatible within the error bars. Additionally, as observed in figure 8.22(b), the gain curve for the smallest aspect ratio of 10:1 is the one that saturates the most at large bias voltages. This agrees with the model of electron multiplication [Guest 71], for which the gain saturates more rapidly for smaller aspect ratio.

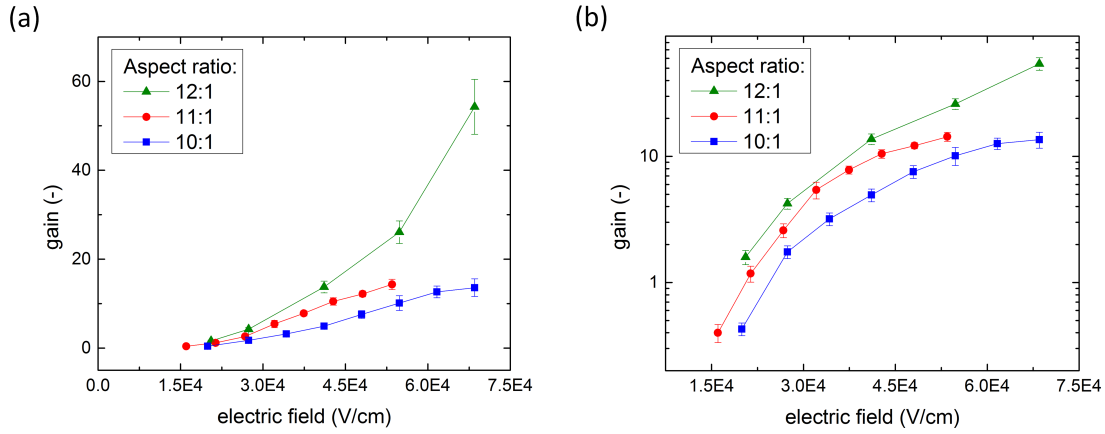


Figure 8.22: (a) Gain curves for a few aspect ratios of 12:1, 11:1 and 10:1. The electric field replaced the bias voltage here to correctly compare different channel lengths. The input flux was always $1.5 \times 10^{10}\text{ cm}^{-2}\text{ s}^{-1}$. (b) same data on a semi-logarithmic graph.

Comparison of gain measured with UV setup and SEM

The gain shown in figure 8.21 is slightly larger than that obtained with the UV setup (figure 8.13(b)). This is explained by the channel tilting with respect to the beam direction, which maximizes the number of collisions as well as the gain. In order to confirm the gain enhancement with the tilt of the AMCP, we repeated the measurements without tilt. The AMCP aspect ratio was 12:1 and the input flux was $9 \times 10^9\text{ cm}^{-2}\text{ s}^{-1}$ for the UV setup and $8 \times 10^{10}\text{ cm}^{-2}\text{ s}^{-1}$ for the SEM. This flux difference is small enough to have a negligible contribution on the gain. The results are shown in figure 8.23. As expected, the absence of a tilt yields gain values that are perfectly compatible with those measured with the UV setup.

8.4. Quantification of the electron multiplication with the SEM

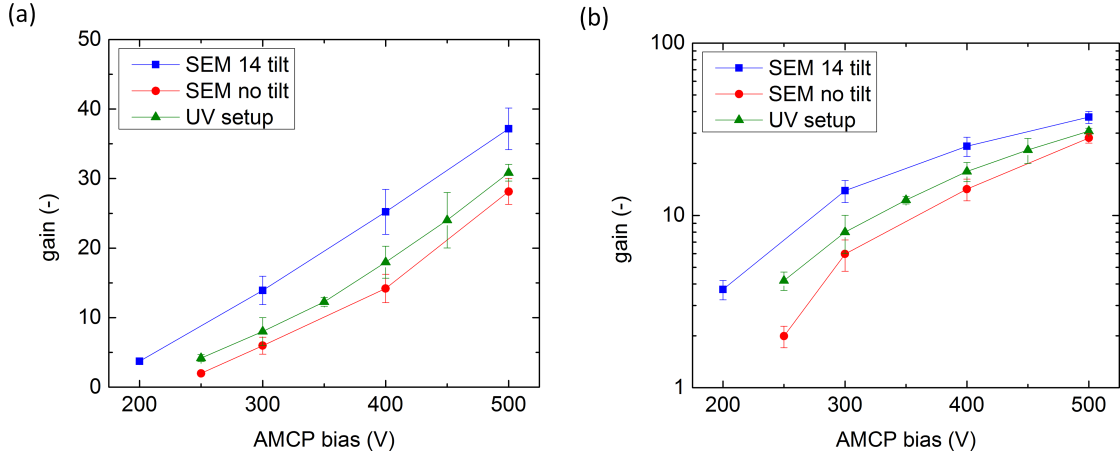


Figure 8.23: (a) Comparison of gain curve obtained with the UV setup and with the SEM, without tilt and with a tilt of 14° . (b) same data on a semi-logarithmic graph.

Gain dependence on the SEM beam energy and tilting angle

The measurements with the SEM beam enabled us to vary many parameters relevant to the impinging electrons so that the gain dependency on them was also investigated. Here, we present the gain results for different electron energies and two tilting angles. In this way, we modify the parameters relevant to the first collision inside of the channels.

First, we measured the gain for an electron energy that was varied within 1–20 keV. The input flux was $1.5 \times 10^{10} \text{ cm}^{-2} \text{ s}^{-1}$. The AMCP tilt was 14° (30% of channel length exposed to the electrons). The obtained gain curve as a function of the electron energy, shown in figure 8.24(a), for an AMCP of 12:1 and biased to 300 V, is similar to that of SEE coefficient versus the impinging electron energy. The latter has an asymmetric bell-shaped trend [Joy 95, Seiler 83, Mane 12], with a maximum at about 500 eV, for normal incidence. The reason for this similarity is explained by the strong dependency of the gain on the number of SEs emitted in the first collision. Additionally, it is important to note that

1. The gain dependency on the SEE coefficient at the first collision is amplified by the grazing impact angle of 14° . The maximum gain value of 52, attained at 7 keV, is more than three times that obtained at 1 keV.
2. The maximum of this curve is shifted to the larger energy of 7 keV, rather than 300 eV for normal incidence (according to [Seiler 83]).
3. The overall effect is reduced if the impinging angle is increased from 14° to 44° .

The explanation for the first two observations is related to the grazing angle of incidence. Indeed, this induces the interaction volume, between electrons and a-Si:H, to stay very close to the channel surface. Consequently, many secondary electrons (SEs) are produced at a

shallow depth so that they reach the surface and contribute to the electron multiplication. This explains why the gain varies so much with the electron energy and why the maximum is shifted to a larger energy than that of the empirical SEE curve, for normal incidence. For energies larger than 7 keV, the gain decreases again because, although even more SEs are produced overall, they are too deep into the material so that they cannot reach the surface anymore.

With respect to the third observation, if the tilting angle is increased to 44° , so that the exposed channel portion is decreased to 8%, the interaction volume goes deeper in a-Si:H and fewer secondary electrons reach the surface. Consequently, the gain enhancement is only double between 1 and 5 keV and the maximum shifts from 7 to 5 keV.

Figure 8.24(b) shows the gain curve as a function of the AMCP bias voltage, obtained with 1 keV electrons and the two tilting angles of 14° and 44° . Although the difference between the two gain curves is small, it confirms the results of figure 8.24(a) in terms of a larger gain for the smaller tilt, at least up to 350 V. The input flux was $1.5 \times 10^{10} \text{ cm}^{-2} \text{ s}^{-1}$.

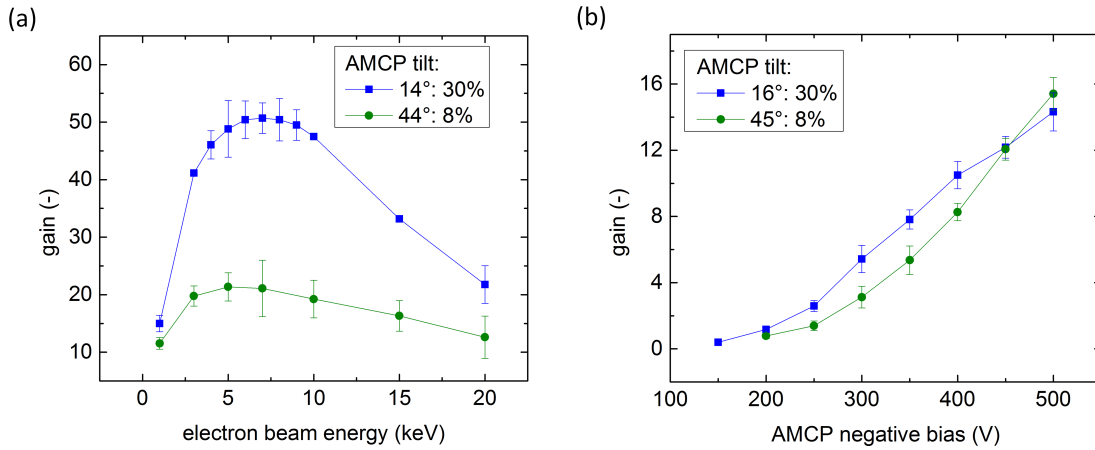


Figure 8.24: (a) Gain as a function of the electron beam energy for two impinging angles of the electrons on the channel surface. The measured AMCP has an aspect ratio of 12:1 and it is biased at 300 V. (b) Gain curves versus the AMCP bias voltage for two tilting angles. The AMCP aspect ratio is 11:1 and the beam energy is 1 keV.

Gain enhancement with a SE emissive layer on the channel surface

Hydrogenated amorphous silicon, similarly to c-Si, has a modest SEE coefficient. We investigated the possibility to enhance the electron multiplication by depositing a SE emissive layer. As discussed in Chapter 3, insulators have larger SEE coefficients because, despite the larger work function, the probability to re-absorb a SE before it reaches the surface is lower. The chosen emissive layer was aluminum oxide (Al_2O_3) because it was already proved to yield a gain enhancement in conventional MCPs [Mane 12]. In that work, it was mentioned that the parameters for the atomic layer deposition (ALD) have to be carefully optimized if a conformal coating of the whole channel surface has to be achieved. Nevertheless, the ALD performed at the Centre Multidisciplinaire (CMi) of EPFL was performed with the standard parameters to make a first investigation of its influence on the AMCP gain. The deposited thickness was 5 nm and it actually confirmed a remarkable effect on the gain, as shown in figure 8.25. For biases above 300 V, the gain almost doubled, which calls for future efforts to optimize the deposition of this SE emissive layer. Even more promising is the use of magnesium oxide (MgO) as SE emissive layer [Mane 12].

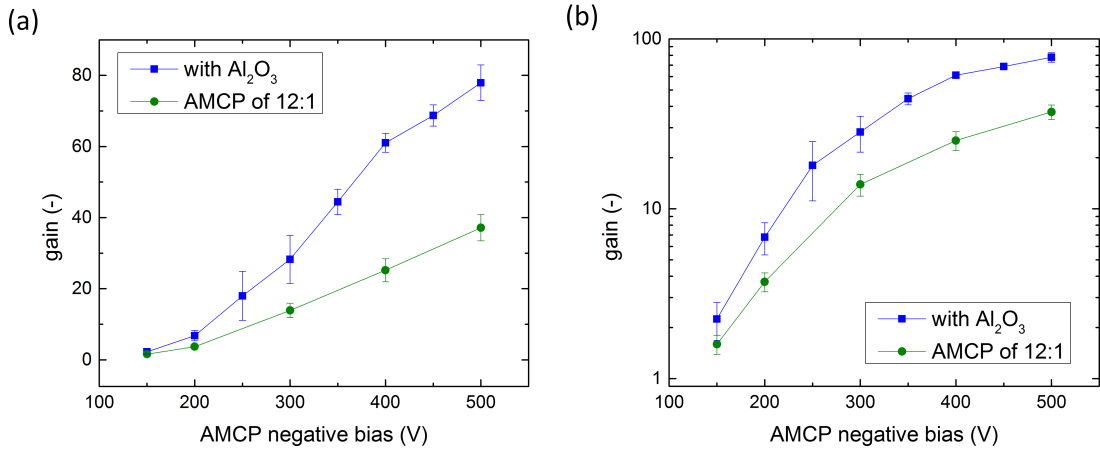


Figure 8.25: (a) Gain enhancement with the atomic layer deposition of aluminum oxide (Al_2O_3) on the channel surface. The AMCP, with an aspect ratio of 12:1, was exposed to an input flux of $1.5 \times 10^{10} \text{ cm}^{-2} \text{ s}^{-1}$ and energy of 1 keV. (b) same data on a semi-logarithmic graph.

8.5 Discussion and Outlook

8.5.1 Corrective actions for the gain variations over time

The evolution of the gain dynamics, presented in Section 8.4.2, must be tackled by a few corrective actions. First, the possible surface charging of the decoupling stack will be limited by a thinner and more resistive material, like a-Si:H with small quantities of carbon in it, to widen the bandgap (as already suggested in the outlook of Chapter 6).

Alternatively, the decoupling layer could be made of a sacrificial material, which is to be etched wider than the channel diameter, to prevent the multiplied electrons to collide against it, with its consequent charging. This sacrificial layer could be made of an organic compound, which can be partially etched by an oxygen plasma once that the channels have been machined.

Finally, the intermediate electrode could be made a bit thicker, or the number of channels could be reduced, so as to reduce the voltage rise (with respect to the ground potential), which is generated by the evacuation of the leakage current, and to limit the residual leakage current on the anode.

8.5.2 Estimation of the maximum gain with an AMCP aspect ratio of 12:1

In the previous section, we presented the possibility to increase the gain by a factor of two with the deposition of a SE emissive layer. The gain can also be increased by a factor of three by changing certain measurement parameters, such as the impinging electron energy. It is interesting to assess whether the gain could be increased sixfold, to about 270, when all these effects are put together, for an AMCP aspect ratio of 12:1. According to the gain drop presented in Section 8.4.2, the gain is still at 90% of its maximum value for an input flux of $8 \times 10^{10} \text{ cm}^{-2} \text{ s}^{-1}$ and a multiplication phase of about 1 minute (in the case of the AMCP with 8.4- μm -wide channels). Therefore, if the input flux is kept below $10^{10} \text{ cm}^{-2} \text{ s}^{-1}$ and the multiplication phase lasts 1 minute, gain values around 260 should be achievable. Since the final applications envisaged for AMCPs and overview in Section 8.5.3, entail much lower input currents, with the single-photon detection as ultimate goal, the condition of an input flux below $10^{10} \text{ cm}^{-2} \text{ s}^{-1}$ should be easily met.

8.5.3 Pulse testing mode

The two setups, employed for the characterization of the electron multiplication, enabled us to quantify only the gain, among the various multiplication parameters. Although the gain was of paramount importance for providing the AMCP proof of concept, the AMCP temporal resolution and the pulse height distribution, for instance, could not be investigated due to the lack of a fast readout electronics. Additionally, the characterization in pulsed mode should envisage relatively large fluxes because of the present moderate gain. A possible way to improve the input electron flux is to use a photocathode material with a quantum efficiency larger than that of gold, for instance caesium iodide (CsI) [Fraser 84, Siegmund 02]

and magnesium fluoride (MgF_2). Another possibility [Tremis 03] is to install a conventional MCP on top of the AMCP so as to provide a first multiplication of about 10^4 before the AMCP. The output signal (on the AMCP anode) can also be amplified by implementing a low-noise high-speed preamplifier.

In the last part of this thesis work, we actually upgraded the UV setup for testing in pulsed mode. We acquired a solid state neodymium-doped yttrium aluminum garnet (Nd:YAG) laser, tripled in frequency to 266 nm, with a pulse duration of 7 ns and a repetition rate of 1 kHz. In order to generate enough signal on the AMCP anode, the laser peak power was chosen to be 300 W. At this peak power, the number of photons per pulse is comparable to that obtained with the UV Pen-Ray lamp in one second. For the signal processing we have adopted a charge preamplifier connected to an oscilloscope. However, preliminary calibration tests revealed that the photoelectron intensity was much lower than expected (about three orders of magnitude). We attribute this lower intensity to a limitation of the gold quantum efficiency when too large photon fluxes are employed (the elliptical laser spot was only a few mm across). Therefore, future characterizations will have to take into account possible photocathode limitations when employing this laser. The installation of a conventional MCP on top of the AMCP, to increase the input intensity, should be envisaged.

8.5.4 AMCP possible applications

In this section, we provide a brief overview about the potential applications of AMCPs. As we proved the feasibility of the vertical integration on metallic anodes, AMCPs are planned to be implemented on application specific integrated circuits (ASICs), developed for high-energy physics (HEP) and medical applications. One of these could be Medipix2 [Llopart 02], a CMOS ASIC originally developed for x-ray imaging, which was already employed to readout the charge cloud of a MCP [Vallerga 08]. An AMCP that is vertically integrated on this ASIC will have the advantage that the spatial resolution is not degraded between the electron multiplier and the readout ASIC. Another imaging application with AMCPs vertically integrated on charge coupled devices (CCDs) could provide a variant of the electron-bombarded CCD [Cianfarani 94, Benussi 00] with an additional multiplication stage (provided by the AMCP), as already attempted with conventional MCPs [Vallerga 97].

The channel diameter smaller than $10\text{ }\mu\text{m}$, as well as the semiconducting bulk, are expected to be beneficial for the AMCP temporal resolution, thanks to the quicker dynamics of the electron multiplication and the improved charge replenishment. Possible applications could range from space science [McFadden 08], to life science [Michalet 07, Roy 08], chemistry [Jungmann 11] and mass spectroscopy [Hadjari 12].

The presence of a hydrogen content of 5–20% in the a-Si:H bulk makes the AMCP an interesting candidate also for the neutron detection [Beaulieu 09]. However, thicker a-Si:H layers should be adopted to increase the detection efficiency, by means of the neutron-proton recoil interaction (needed for the detection).

The ultimate goal is the single photon detection. A monolithic detector, made of an AMCP on

ASIC, with such sensitivity, could be an interesting candidate for the simultaneous positron emission tomography and magnetic resonance imaging [Judenhofer 08, Schlemmer 08], a main topic in today's medical diagnosis. To achieve the single photon detection, a conventional MCP with aspect ratio of about 40:1 is normally needed. We believe that an AMCP with aspect ratio above 25:1 should be feasible with our progresses in mastering the deposition of a-Si:H layers thicker than 100 μm . When micromachining the channels of such thick a-Si:H layers, the channel lateral widening (with respect to the nominal diameter) will have to be tackled. The possible missing gain for reaching the single photon detection could be compensated by future front-end electronic chips of very low noise.

8.6 Conclusion

In this chapter, we provided the experimental evidence of the electron multiplication taking place in AMCPs. We measured the electron multiplication with two setups. The former is called UV setup, it was built in this thesis and it features a vacuum vessel with optical window, a UV light and a photocathode. It is representative of the operation mode of an MCP in a sealed tube. With the UV setup, we tested the AMCPs in a quasi-continuous illumination mode, where all channels were contemporaneously exposed to photoelectrons. The other setup was a SEM, where each channel was periodically injected with electrons, by sweeping the beam across the AMCP. The output signal was measured mainly with a lock-in amplifier for the UV setup and with a picoammeter for the SEM. We confirmed the same gain values for similar testing conditions.

With 1st-gen and 2nd-gen AMCPs, we showed the large sensitivity of the electron multiplier to UV photons and electrons, due to a conductivity enhancement (produced by photoconductivity and betaconductivity).

We demonstrated a maximum gain above 45 for one of the largest channel aspect ratio of 12:1. This gain was obtained with an electric field in the channels of about $7 \times 10^4 \text{ V/cm}$ and an input flux of $1.5 \times 10^{10} \text{ cm}^{-2} \text{ s}^{-1}$. We confirmed that the gain increases as a function of the aspect ratio for two sets of AMCPs measured with either one or the other setup.

The results from one of these sets was analyzed with Eberhardt's model and we observed that the dependency of the number of collisions on the aspect ratio, in AMCPs, was similar to that of conventional MCPs. This analysis also permitted us to calculate the a-Si:H SEE coefficient of 1.7 for an impinging electron energy of 100 eV.

We reported the gain to drop for input fluxes larger than $1.5 \times 10^{10} \text{ cm}^{-2} \text{ s}^{-1}$ and a measurement timeframe of a few minutes. The percentage drop, with respect to the maximum gain, ranged within 30–75%. The proposed explanation was the channel surface charging in correspondence of the decoupling layer, where the charge replenishment cannot be provided.

We presented a threefold gain enhancement when the beam energy was increased from 1 to 7 keV, so as to maximize the emission of secondary electrons at the first collision. We also investigated how this trend changes with the impinging angle and we explained that a grazing angle is optimal for achieving the largest gain (due to a maximum in the extracted

secondary electrons). Finally, we obtained a twofold gain enhancement by coating the channel surface with a secondary electron emissive layer, namely 5 nm of alumina (Al_2O_3). This coating was performed by atomic layer deposition and could be an easy way to boost the AMCP performances, once this deposition process will be optimized.

Although the characterization was focused only on the quantification of the multiplication factor, it provides first evidences of the potential of this new promising fabrication process for MCPs, which has the unmatched advantage of enabling the vertical integration on readout electronics. This will open new frontiers for the exploitation of these vacuum-based electron multipliers. Additionally, AMCPs are expected to outperform conventional lead-glass MCPs in terms of dynamic range and count rate, thanks to their semiconducting bulk. Its resistivity can be tuned according to the deposition parameters so that the relevant charge replenishment can be optimized for each application. The photolithography and the DRIE process enable a high degree of customization regarding the channel geometry and possible funnel structures, at the channel entrance, to improve the open area ratio. The two main improvements that the next AMCP development will have to address are the enhancement of the aspect ratio and the implementation of a structural or electrostatic feature for promoting the first electron collision near the channel entrance. This second improvement is required to maximize the gain in the AMCP channels, which lack of a bias angle.

9 Conclusions and perspectives

In this thesis, we carried out research on two monolithic particle detectors, based on hydrogenated amorphous silicon (a-Si:H). The first one, a vacuum detector, was the amorphous-silicon-based microchannel plate (AMCP), whose fabrication method is completely different from the glass multifiber draw process of conventional microchannel plates (MCPs) and it exploits a-Si:H layers with thickness of up to $100\text{ }\mu\text{m}$ for the vertical integration on metallic anodes. The second one, a solid-state detector, was the thin-film-on-ASIC (TFA) particle detector, in which an a-Si:H diode, with a thickness between $5\text{--}20\text{ }\mu\text{m}$, is vertically integrated on an ASIC for the front-end readout processing.

The main motivation for developing AMCPs is the possibility to vertically integrate them onto a substrate like an application specific integrated circuit (ASIC). The AMCP vertical integration was demonstrated, in this thesis, on an oxidized wafer with metallic anodes. This substrate facilitated the AMCP development and closely simulates the upper surface of the future ASIC. The other key strength of AMCPs is a bulk material, i.e. a-Si:H, which is, on the one hand, resistive enough to withstand large bias voltages and, on the other hand, conductive enough to replenish the electrons dispensed during the multiplication. This is in line with other recent efforts to fabricate bulk-conductive MCPs [Sinor 00, Yi 08].

TFA detectors were already available at the beginning of this thesis. Our contribution consisted in the characterization of the signal modulation when tracking the beam of a scanning electron microscope (SEM) and in the assessment of the TFA spatial resolution when this particle detector is employed as beam hodoscope. The noticeable degradation of the a-Si:H electronic properties, observed in this study, motivated also a more fundamental investigation on the dynamic of defect creation induced by the electron beam and their quantification as a function of the absorbed dose.

In the following sections, we first summarize the key results of the thesis. Then, we discuss how these monolithic detectors could be further improved and the next steps required for completing their characterization. Finally, we outline some of their potential applications.

9.1 Summary of the key results

9.1.1 Fabrication of amorphous-silicon-based microchannel plates

AMCPs were patented shortly before this thesis. Although these first prototypes confirmed the feasibility of the vertical integration on metallic anodes, they suffered from several structural defects created during the fabrication process, which reduced the yield of functional devices. The first part of this thesis was spent in an intense engineering effort to remove these structural defects, as detailed in Chapter 6.

The main challenge consisted in the deposition of a-Si:H layers as thick as 100 μm . These thick layers were required for the successive realization of channels with an aspect ratio (channel length over diameter) large enough for being able to detect and characterize the electron multiplication. The deposition of a-Si:H was done by plasma-enhanced chemical vapor deposition (PE-CVD) with silane as the main gas precursor. In order to reach the targeted thickness, the deposition parameters were optimized for a deposition rate as high as 20 $\text{\AA}/\text{s}$, so as to deposit the 100 μm in about 14 hours. This rate induced the formation of powder in the plasma. However, we succeeded in limiting its embedding in the growing film by improving the uniformity of the gas precursors injection in the reactor chamber. The intrinsic stress, which occasionally lead to large delamination of the thick a-Si:H layer, was reduced by adapting the temperature profile during the a-Si:H deposition. We improved the adhesion to the substrate by two means: a short reactive ion etching treatment, to increase the surface roughness, and the implementation of SiO_x adhesion layers. We succeeded in preventing the formation of bubbles and local delamination by reducing the hydrogen content in the growing film. The hydrogen was indirectly proved, according to previous studies [Acco 96, Xu 09], to concentrate at the lower interface of the thick a-Si:H layer and to promote delamination.

The channel micromachining, which was performed by deep reactive ion etching (DRIE), was optimized by designing a new photolithographic mask with channels further apart, to tackle the inevitable channel widening during the DRIE process. We also improved the uniformity of the a-Si:H thickness across the wafer in order to guarantee that the channels always reached the anodes. The current limitation of this micromachining technique is that the channels do not have a bias angle, namely they are perpendicular to the electrode surface, contrary to conventional lead-glass MCPs.

The first AMCP prototypes were successfully upgraded by the implementation of an intermediate electrode, which was isolated from the anode by a 2- μm -thick a-Si:H layer. In this way, the anode signal was decoupled from the leakage current through the bulk, which was evacuated by the grounded intermediate electrode. Consequently, the accelerating electric field in the channels is set by the biased top electrode with respect to the grounded intermediate electrode, whereas the anode collects the multiplied electrons.

9.1.2 AMCP electrical characterization and electron multiplication

In Chapter 7, we showed that the implementation of the intermediate electrode enabled us to reduce the residual leakage current on the anode by about five orders of magnitude. Additionally, the AMCPs were biased up to -800 V, which evidences the a-Si:H capability to sustain electric fields of up to 10^5 V/cm, outperforming lead-glass MCPs that are rated to an electric field of 2×10^4 V/cm.

The AMCP electrical characterization evidenced a preferential conduction path along the channel surface, if the bias voltage was large enough. We suggested that this preferential path was activated by the thermal emission of trapped carriers from the a-Si:H localized states, which are present in a larger density near the channel surface.

Finally, we showed that the leakage current evacuation through the intermediate electrode, for an AMCP bias of -500 V, generates a voltage rise (with respect to the ground potential) of less than 1 V, but large enough to induce a residual leakage current of 1–10 pA on an anode of 4 mm^2 .

The electron multiplication in AMCPs was measured with two electron sources. The first one was the beam of a SEM. The second one consisted in a vacuum vessel, with optical window, and photocathode, which provided the full-field exposure of the AMCP to photoelectrons. This was realized in this thesis for providing a testing configuration more representative of the usual MCP operating conditions.

As presented in Chapter 8, the electron multiplication was confirmed by a multiplication gain that increases with the bias voltage and the channel aspect ratio. The gain dependency on the aspect ratio was analyzed with Eberhardt's model and we observed a fair match between our AMCPs and conventional lead-glass MCPs. We were also able to extract an average a-Si:H secondary electron emission coefficient of 1.7, for an impinging electron energy of about 100 eV.

When testing with the UV setup, which provides photoelectrons of about 500 eV, we measured a gain of about 30 for a bias voltage of -500 V and an aspect ratio of 12.5:1. Successively, we also tilted the AMCP channels with respect to the SEM beam, so as to promote the first collision near the channel entrance. By doing so, we measured a gain of about 45 for an AMCP bias of -500 V and an aspect ratio of 12:1. This gain was observed to drop, within a few minutes, by 30–75% for input electron fluxes larger than about $10^{10} \text{ cm}^{-2} \text{ s}^{-1}$. We attributed this drop to the surface charging of the decoupling stack, where the electron replenishment cannot be provided. The gain dependency on the beam parameters was also investigated and we obtained a threefold gain enhancement when the beam energy was increased from 1 to 7 keV. Finally, we proved that the gain can be doubled, from 40 to 80, by the atomic layer deposition of 5 nm of Al_2O_3 on the channel surface. Indeed, this material was shown to enhance the secondary electron emissive (SEE) coefficient [Mane 12]. This first attempt was motivated by the recent remarkable results of gain enhancement achieved with this deposition technique [Siegmond 13].

9.1.3 Evaluation of the TFA spatial resolution when tracking the SEM beam

TFA detectors had been previously tested with radioactive beta sources and a spatial resolution of a few micrometers had been demonstrated. This motivated our characterization of the TFA charge collection mechanism and the assessment of the spatial resolution when tracking the SEM beam. As presented in Chapter 4, the measurements were done with a number of pixels, whose metallization is patterned in a number of micrometric-sized strips. We showed that we were able to resolve each microstrip, for every patterning, even for the one with 0.6- μm -wide strips, spaced by 1.4 μm . This remarkable result, obtained with a 0.4- μm -wide interaction volume in a-Si:H and confirmed with three diode thicknesses of 5, 10 and 20 μm , is achieved thanks to the better charge collection in correspondence of each microstrip and the low charge diffusion of a-Si:H. The consequent charge loss between two strips is acceptable as long as the strips are spaced by no more than 30 μm , for a beam energy of 20 keV and a beam current of 350 pA.

The TFA signal modulation and spatial resolution was also investigated for an alternative a-Si:H diode configuration (with respect to the conventional n-i-p one), which lacks of the n-layer. This configuration, which reduces the pixel crosstalk, exhibits larger charge loss between strips that are spaced by more than 30 μm . This points out that the ultimate TFA configuration should be tailored according to the specific application.

9.1.4 a-Si:H degradation induced by the exposure to the SEM beam

The TFA spatial resolution study pointed out a large degradation of the a-Si:H electronic properties when exposed to the SEM beam. The electron-beam-induced current almost disappeared after a single beam sweep that produced an absorbed dose of 30 Gy. The width of the degraded zone corresponded to that of the interaction volume between the electrons and a-Si:H. We attributed the degradation to the formation of additional broken Si-Si bonds, known as dangling bonds or simply defects, which act as recombination centers and induce the signal to drop. In Chapter 5, we obtained two indications that the defects are also created by the ionizing energy released by the impinging electrons, in addition to the energy released upon charge recombination, as is the case for the light-induced degradation.

We also succeeded to confirm the reversibility of this degradation by annealing at 130 °C for 17 hours, which brought the defect density back to the initial level, as measured by FTPS measurements after an absorbed dose of 225–450 kGy.

Finally, simulations carried out with the ASA program enabled us to estimate that this absorbed dose of 225–450 kGy produced a defect density of about $3 \times 10^{17} \text{ cm}^{-3}$.

9.2 Perspectives

9.2.1 Future AMCP development

The results obtained in this thesis, about the fabrication and the electron multiplication of AMCPs, provide a crucial contribution for the future applications of this electron multiplier. However, there is still a large spectrum of activities that must be done to fully evaluate the potential of this novel fabrication process.

From the fabrication point of view, the deposition of thicker a-Si:H layers with the optimized deposition recipe developed during this thesis, should have the highest priority. Aspect ratios of 20:1 are within immediate reach and aspect ratio above 25:1 should be possible. An a-Si:H with ten times larger conductivity could be realized by adding a small quantity of doping species such as boron or phosphorous, or germanium, which narrows the material bandgap. Indeed, our AMCPs sustain ten times larger electrical fields than those adopted for conventional MCPs, without any electrical breakdown. The suspected charging of the decoupling stack surface should be solved by reducing its thickness and by increasing its resistivity. The atomic layer deposition of a SEE layer, such as alumina (Al_2O_3) or magnesium oxide (MgO), should be optimized. The AMCP active area, defined as the ratio between total channel and total AMCP surface, could be increased by engineering a funnel structure at the channel entrance by reactive ion etching.

Once that larger aspect ratio will be available, which is expected to increase the capability to characterize the multiplication process also in pulsed regime, other aspects of this fabrication process should be investigated. First, the influence of the channel surface roughness on the electron multiplication should be analyzed. The large hydrogen content in a-Si:H could desorb over time and its possible influence on the gain stability and the dark count rate should be investigated. Additionally, the gain should be measured for different input electron currents and count rates, in order to determine the portion of the total leakage current that contributes to the charge replenishment. Finally, simulations of the electrostatic field for various AMCP designs and semiconducting bulk properties should complement the experimental results. When the AMCPs will be implemented on an ASIC, among those developed for high-energy physics or medical applications, a few additional technological challenges will probably have to be solved.

Concerning the AMCP characterization, AMCPs will have to be tested in pulsed regime to get additional insights about the multiplication process, like the temporal resolution and the pulse height distribution of the gain. The recent upgrade of the UV setup with a pulsed laser at 266 nm should be the preferred testing platform for these measurements. If required, the input electron flux can be enhanced by the installation of a commercial MCP on top of the AMCP. Concerning the signal processing, a fast charge preamplifier, could be implemented between the AMCP anode and the oscilloscope.

9.2.2 Future AMCP applications

The AMCPs could be used in a number of applications, relevant to different domains: from chemistry, to biology, medicine, high-energy physics and space science.

- The compactness of the AMCP vertical integration, combined with the AMCP insensitivity to magnetic fields and the spatial resolution of a few micrometers, could be exploited for simultaneous magnetic resonance imaging and positron emission tomography [Schlemmer 08].
- The a-Si:H radiation hardness to displacement damages make the vertically integrated AMCP detector an interesting candidate as space plasma analyzer for the instruments used in space missions, such as the THESIS ESA [McFadden 08].
- The small channel diameter (less than $10\ \mu\text{m}$) is expected to provide a good temporal resolution due to an electron multiplication that rapidly propagates in the channels. This would be beneficial for a number of applications like the detection of fast fluorescence processes [Michalet 07, Roy 08] in life science and ion microscopy [Jungmann 11]. Additionally, the better charge replenishment performances expected by the a-Si:H semiconducting bulk could be exploited for applications requiring large count rates [Pearson 03].
- The variable atomic hydrogen content of 5–20% in a-Si:H could be exploited for the neutron detection, through the neutron-proton recoil reaction [Beaulieu 09]. Indeed, MCPs have recently been investigated for a number of neutron detection applications [Tremis 14].

9.2.3 Future TFA development and applications

As far as the TFA detectors are concerned, they had been extensively characterized for the detection of different type of particles prior to this thesis [Despeisse 08]. The possible applications had been also discussed. The most important one still consists in its use as a particle tracker in the big experiments at CERN, such as CMS and ATLAS, for the upcoming LHC luminosity upgrade to $10^{35}\ \text{cm}^{-2}\text{s}^{-1}$. Indeed, the large radiation hardness of the TFA detectors evidences its potential for surviving to the expected absorbed doses. This possible application motivated the evaluation of the TFA spatial resolution performed in this thesis, which demonstrated that features smaller than $1\ \mu\text{m}$ could be resolved when detecting an SEM beam. However, the adopted electron energy of a tens of keV corresponded to a large amount of deposited ionizing energy, which generated an induced signal easily measurable with the ASIC amplification. If similar resolution performances are to be attained for the typical energies of the LHC experiments, the flux will have to be large enough to compensate for the low stopping power in a-Si:H. In this way, enough electron-hole pairs will be generated in the a-Si:H diode to enable the detection. Additionally, if one aims at increasing the sensitivity of the TFA detectors,

Chapter 9. Conclusions and perspectives

thicker a-Si:H sensing diodes will be required to enhance the induced signal. These thicker diodes will require a larger polarization for their full depletion. Therefore, more effective blocking contacts, than those used so far, will have to be implemented, so as to maintain the diode leakage currents at a reasonable level.

Bibliography

- [Acco 96] S Acco, DL Williamson, PA Stolk, FW Saris, MJ Van den Boogaard, WC Sinke, WF Van der Weg, S Roorda & PC Zalm. *Hydrogen solubility and network stability in amorphous silicon*. Physical Review B, vol. 53, no. 8, pages 4415–4427, 1996.
- [Adams 66] J. Adams & B. W. Manley. *The Mechanism of Channel Electron Multiplication*. IEEE Transactions on Nuclear Science, vol. 13, pages 88–99, 1966.
- [Al-Dhafiri 02] AM Al-Dhafiri, HA El-Jammal, A Al-Shariah, HA Naseem & WD Brown. *Influence of nitrogen trifluoride and nitrogen plasma treatment on the formation of hillocks during aluminum induced crystallization of α -Si: H*. Thin solid films, vol. 422, no. 1, pages 14–19, 2002.
- [Albrecht 02] E. Albrecht, J. Baker, G. Barber, J. Bibby, M. Calvi, M. Charles, A. Duane, S. Easo, S. Eisenhardt, L. Eklund, M. French, V. Gibson, A. Halley, R. Halsall, N. Harnew, M.J.J. John, S.G. Katvars, J. Libby, F. Muheim, M. Paganoni, A. Petrolini, S. Playfer, D. Price, J. Rademacker, N. Smale, S. Topp-Jorgenson, D. Websdale, G. Wilkinson & S.A. Wotton. *Performance of a cluster of multi-anode photomultipliers equipped with lenses for use in a prototype RICH detector*. Nuclear Instruments and Methods in Physics Research, Section A: Accelerators, Spectrometers, Detectors and Associated Equipment, vol. 488, no. 1-2, pages 110–130, 2002. cited By (since 1996)20.
- [Anelli 99] G Anelli, M Campbell, M Delmastro, F Faccio, S Floria, A Giraldo, E Heijne, Pierre Jarron, K Kloukinas, A Marchioro *et al.* *Radiation tolerant VLSI circuits in standard deep submicron CMOS technologies for the LHC experiments: practical design aspects*. Nuclear Science, IEEE Transactions on, vol. 46, no. 6, pages 1690–1696, 1999.
- [Anelli 03] Giovanni Anelli, Kurt Borer, Luca Casagrande, Matthieu Despeisse, Pierre Jarron, Nicolas Pelloux & Shahyar Saramad. *A high-speed low-noise transimpedance amplifier in a 0.25 μ m CMOS technology*. Nuclear

- Instruments and Methods in Physics Research Section A: Accelerators, Spectrometers, Detectors and Associated Equipment, vol. 512, no. 1, pages 117–128, 2003.
- [Anelli 04] G. Anelli, S.C. Commichau, M. Despeisse, G. Dissertori, P. Jarron, C. Mi-azza, D. Moraes, A. Shah, G.M. Viertel & N. Wyrsh. *A new concept of monolithic silicon pixel detectors: hydrogenated amorphous silicon on ASIC*. Nuclear Instruments and Methods in Physics Research Section A, vol. 518, no. 1-2, pages 366 – 372, 2004.
- [Arch 92] JK Arch & SJ Fonash. *Origins of reverse bias leakage currents in hydro-genated amorphous silicon p-i-n detector structures*. Applied physics letters, vol. 60, no. 6, pages 757–759, 1992.
- [Ashie 05] Y Ashie, J Hosaka, K Ishihara, Y Itow, J Kameda, Y Koshio, A Minamino, C Mitsuda, M Miura, S Moriyama *et al.* *Measurement of atmospheric neutrino oscillation parameters by Super-Kamiokande I*. Physical Review D, vol. 71, no. 11, page 112005, 2005.
- [Austin 02] L Austin & H Starke. *Ueber die Reflexion der Kathodenstrahlen und eine damit verbundene neue Erscheinung secundärer Emission*. Annalen der Physik, vol. 314, no. 10, pages 271–292, 1902.
- [Bacci 91] C. Bacci, F. Evangelisti, P. Fiorini, C. Furetta, F. Meddi, A. Mittiga & M. Sebastiani. *Detection of strongly ionizing particles with a hydro-genated amorphous silicon detector*. Nuclear Instruments and Methods in Physics Research Section A, vol. 306, pages 182 – 186, 1991.
- [Barbier 09] Rémi Barbier, J Baudot, E Chabanat, P Depasse, W Dulinski, N Estre, CT Kaiser, N Laurent & M Winter. *Performance study of a MegaPixel single photon position sensitive photodetector EBCMOS*. Nuclear In-struments and Methods in Physics Research Section A: Accelerators, Spectrometers, Detectors and Associated Equipment, vol. 610, no. 1, pages 54–56, 2009.
- [Barnes IV 04] James H Barnes IV & Gary M Hieftje. *Recent advances in detector-array technology for mass spectrometry*. International Journal of Mass Spec-trometry, vol. 238, no. 1, pages 33–46, 2004.
- [Baroody 50] EM Baroody. *A theory of secondary electron emission from metals*. Physi-cal Review, vol. 78, no. 6, pages 780–787, 1950.
- [Beaulieu 09] D.R. Beaulieu, D. Gorelikov, H. Klotzsch, P. de Rouffignac, K. Saadat-mand, K. Stenton, N. Sullivan & A.S. Tremsin. *Novel fast neutron count-ing technology for efficient detection of special nuclear materials*. In IEEE Conference on Technologies for Homeland Security., pages 295–301, 2009.

- [Beaulieu 11] DR Beaulieu, D Gorelikov, H Klotzsch, P de Rouffignac, K Saadatmand, K Stenton, N Sullivan & AS Tremsin. *Plastic microchannel plates with nano-engineered films*. Nuclear Instruments and Methods in Physics Research Section A: Accelerators, Spectrometers, Detectors and Associated Equipment, vol. 633, pages 59–61, 2011.
- [Beetz 00] Charles P. Beetz, Robert Boerstler, John Steinbeck, Bryan Lemieux & David R. Winn. *Silicon-micromachined microchannel plates*. Nuclear Instruments and Methods in Physics Research Section A, vol. 442, pages 443 – 451, 2000.
- [Benussi 00] Luigi Benussi, V Fanti, D Frekers, A Frenkel, G Giannini, SV Golovkin, EN Kozarenko, IE Kreslo, B Liberti, G Martellottiet *al.* *A multichannel single-photon sensitive detector for high-energy physics: the megapixel EBCCD*. Nuclear Instruments and Methods in Physics Research Section A: Accelerators, Spectrometers, Detectors and Associated Equipment, vol. 442, no. 1, pages 154–158, 2000.
- [Beyer 12] W Beyer, W Hilgers, P Prunici & D Lennartz. *Voids in hydrogenated amorphous silicon materials*. Journal of Non-Crystalline Solids, vol. 358, no. 17, pages 2023–2026, 2012.
- [Bian 93] Bo Bian, Jian Yie, Boquan Li & Ziqin Wu. *Fractal formation in a-Si: H/Ag/a-Si: H films after annealing*. Journal of applied physics, vol. 73, no. 11, pages 7402–7406, 1993.
- [Bigas 06] M. Bigas, E. Cabruja, J. Forest & J. Salvi. *Review of CMOS image sensors*. Microelectronics Journal, vol. 37, pages 433 – 451, 2006.
- [Bingefors 93] N Bingefors, H Borner, R Boulter, M Caccia, V Chabaud, H Dijkstra, P Eerola, E Gross, R Horisberger, L Hubbelinget *al.* *The DELPHI microvertex detector*. Nuclear Instruments and Methods in Physics Research Section A: Accelerators, Spectrometers, Detectors and Associated Equipment, vol. 328, no. 3, pages 447–471, 1993.
- [Boccara 80] AC Boccara, Warren Jackson, Nabil M Amer & D Fournier. *Sensitive photothermal deflection technique for measuring absorption in optically thin media*. Optics letters, vol. 5, no. 9, pages 377–379, 1980.
- [Braem 02] André Braem, E Chesi, C Joram, Jacques Séguinot, Peter Weilhammer & Thomas Ypsilantis. *Development, fabrication and test of a highly segmented hybrid photodiode*. Nuclear Instruments and Methods in Physics Research Section A: Accelerators, Spectrometers, Detectors and Associated Equipment, vol. 478, no. 1, pages 400–403, 2002.

Bibliography

- [Brodsky 70] MH Brodsky, K Weiser, GD Pettit *et al.* *Structural, Optical, and Electrical Properties of Amorphous Silicon Films*. Physical Review B, vol. 1, no. 6, page 2632, 1970.
- [Bronshtein 68] IM Bronshtein & VA Dolinin. *The secondary electron emission–SEE–of solids at large angles of incidence of the primary beam*. Soviet Physics–Solid State, vol. 9, no. 9, pages 2133–2140, 1968.
- [Bruining 54] Hajo Bruining & H Bruining. Physics and applications of secondary electron emission, volume 391. Pergamon Press London, 1954.
- [Bustarret 91] Etienne Bustarret, Martin Brandt, Martin Stutzmann & Myriam Favre. *Explosive isothermal hydrogen exodiffusion in VHF-GD a-Si: H thick layers*. Journal of non-crystalline solids, vol. 137, pages 53–56, 1991.
- [Carlson 77] DE Carlson & CR Wronski. *Solar cells using discharge-produced amorphous silicon*. Journal of Electronic Materials, vol. 6, no. 2, pages 95–106, 1977.
- [Chabloz 96] P Chabloz, H Keppner, D Fischer, D Link & A Shah. *Amorphous silicon pin diodes, deposited by the VHF-GD process: new experimental results*. Journal of non-crystalline solids, vol. 198, pages 1159–1162, 1996.
- [Chae 07] Yongkee Chae, Tae K Won, Liwei Li, Shuran Sheng, Soo Young Choi, John White & Michel Frei. *Deposition of amorphous silicon/microcrystalline silicon for tandem solar cells using cluster PECVD tool on jumbo size substrates (Gen 8.5)*. In proceedings of the 22nd European photovoltaic solar energy conference, Milan, pages 1807–1809, 2007.
- [Charbon 14] E Charbon. *Single-photon imaging in complementary metal oxide semiconductor processes*. Philosophical Transactions of the Royal Society A: Mathematical, Physical and Engineering Sciences, vol. 372, no. 2012, page 20130100, 2014.
- [Chévrier 94] JB Chévrier & B Equer. *High electric-field amorphous silicon p-i-n diodes: Effect of the p-layer thickness*. Journal of applied physics, vol. 76, no. 11, pages 7415–7422, 1994.
- [Chi 77] Jim-Yong Chi & Harry C Gatos. *Nondestructive determination of the depth of planar pn junctions by scanning electron microscopy*. Electron Devices, IEEE Transactions on, vol. 24, no. 12, pages 1366–1368, 1977.
- [Cianfarani 94] C Cianfarani, A Duane, J-P Fabre, A Frenkel, SV Golovkin, AM Gorin, K Harrison, EN Kozarenko, AE Kushnirenko, EA Ladygin *et al.* *A high-resolution detector based on liquid-core scintillating fibres with readout via an electron-bombarded charge-coupled device*. Nuclear Instruments

- and Methods in Physics Research Section A: Accelerators, Spectrometers, Detectors and Associated Equipment, vol. 339, no. 3, pages 449–455, 1994.
- [Conneely 13] Thomas M Conneely, James S Milnes & Jon Howorth. *Extended lifetime MCP-PMTs: Characterisation and lifetime measurements of ALD coated microchannel plates, in a sealed photomultiplier tube*. Nuclear Instruments and Methods in Physics Research Section A: Accelerators, Spectrometers, Detectors and Associated Equipment, vol. 732, pages 388–391, 2013.
- [Cuony 12] Peter Cuony, Duncan TL Alexander, Ivan Perez-Wurfl, Matthieu Despeisse, Gregory Bugnon, Mathieu Boccard, Thomas Söderström, Aïcha Hessler-Wyser, Cécile Hébert & Christophe Ballif. *Silicon Filaments in Silicon Oxide for Next-Generation Photovoltaics*. Advanced Materials, vol. 24, no. 9, pages 1182–1186, 2012.
- [Dagamseh 10] AMK Dagamseh, B Vet, P Šutta & M Zeman. *Modelling and optimization of a-Si: H solar cells with ZnO: Al back reflector*. Solar Energy Materials and Solar Cells, vol. 94, no. 12, pages 2119–2123, 2010.
- [Danesh 02] P Danesh, B Pantchev, I Savatinova, E Liarokapis, S Kaschieva & AG Belov. *Electron irradiation of a-Si: H films prepared from hydrogen-diluted silane*. Vacuum, vol. 69, no. 1, pages 79–82, 2002.
- [de Boer 05] Bert de Boer, Afshin Hadipour, M Magdalena Mandoc, Teunis van Woudenberg & Paul WM Blom. *Tuning of Metal Work Functions with Self-Assembled Monolayers*. Advanced Materials, vol. 17, no. 5, pages 621–625, 2005.
- [De Ruijter 95] WJ De Ruijter. *Imaging properties and applications of slow-scan charge-coupled device cameras suitable for electron microscopy*. Micron, vol. 26, no. 3, pages 247–275, 1995.
- [Deenapanray 06] Prakash NK Deenapanray, CS Athukorala, Daniel Macdonald, WE Jellett, E Franklin, VE Everett, KJ Weber & AW Blakers. *Reactive ion etching of dielectrics and silicon for photovoltaic applications*. Progress in Photovoltaics: Research and Applications, vol. 14, no. 7, pages 603–614, 2006.
- [Despeisse 06a] M. Despeisse, S. Saramad, C. Ballif, S. Dunand, P. Jarron, J. Morse, I. Snigireva, C. Miazza, D. Moraes, G. Anelli, A. Shah & N. Wyrsh. *Characterization of a thick layer a-Si:H pixel detector with TFA technology using a scanning electron microscope*. Journal of Non-Crystalline Solids, vol. 352, pages 1832 – 1836, 2006.

Bibliography

- [Despeisse 06b] Matthieu Despeisse. *Etude et caractérisation d'un capteur en silicium amorphe hydrogéné déposé sur circuit intégré pour la détection de particules et de rayonnements*. PhD thesis, Institut National des Sciences Appliquées de Lyon, 2006.
- [Despeisse 08] M. Despeisse, G. Anelli, P. Jarron, J. Kaplon, D. Moraes, A. Nardulli, F. Powolny & N. Wyrsh. *Hydrogenated Amorphous Silicon Sensor Deposited on Integrated Circuit for Radiation Detection*. IEEE Transactions on Nuclear Science, vol. 55, pages 802–811, 2008.
- [Diehl 96] F. Diehl, W. Herbst, S. Bauer, B. Schröder & H. Oechsner. *Creation of metastable defects in a-Si:H by keV-electron irradiation at different temperatures*. Journal of Non-Crystalline Solids, vol. 198-200, pages 436–440, 1996.
- [Dorier 95] J-L Dorier, Ch Hollenstein & Alan A Howling. *Spatiotemporal powder formation and trapping in radio frequency silane plasmas using two-dimensional polarization-sensitive laser scattering*. Journal of Vacuum Science & Technology A, vol. 13, no. 3, pages 918–926, 1995.
- [Drouin 07] Dominique Drouin, Alexandre Réal Couture, Dany Joly, Xavier Tastet, Vincent Aimez & Raynald Gauvin. *CASINO V2. 42 A Fast and Easy-to-use Modeling Tool for Scanning Electron Microscopy and Microanalysis Users*. Scanning, vol. 29, no. 3, pages 92–101, 2007.
- [Dubeau 91] J. Dubeau, T. Pochet, L.-A. Hamel, B. Equer & A. Karar. *Response of amorphous silicon p-i-n detectors to ionizing particles*. Nuclear Instruments and Methods in Physics Research Section B, vol. 54, pages 458–471, 1991.
- [Eberhardt 79] Edward H Eberhardt. *Gain model for microchannel plates*. Applied Optics, vol. 18, no. 9, pages 1418–1423, 1979.
- [Eberhardt 81] EH Eberhardt. *An operational model for microchannel plate devices*. Nuclear Science, IEEE Transactions on, vol. 28, no. 1, pages 712–717, 1981.
- [Farrell 91] R Farrell, K Vanderpuye, G Entine & MR Squillante. *High resolution, low energy avalanche photodiode X-ray detectors*. Nuclear Science, IEEE Transactions on, vol. 38, no. 2, pages 144–147, 1991.
- [Franclova 05] J Franclova, Z Kucerovala & V Buršiková. *Electrical Properties of Plasma Deposited Thin Films*. WDS'05 Proceedings of Contributed Papers, vol. 1, pages 353–356, 2005.
- [Franco 12a] Andrea Franco, Yannick Riesen, Matthieu Despeisse, Nicolas Wyrsh & Christophe Ballif. *High Spatial Resolution of Thin-Film-on-ASIC Particle*

- Detectors*. Nuclear Science, IEEE Transactions on, vol. 59, no. 5, pages 2614–2621, 2012.
- [Franco 12b] Andrea Franco, Yannick Riesen, Nicolas Wyrsh, Sylvain Dunand, François Powolny, Pierre Jarron & Christophe Ballif. *Amorphous silicon-based microchannel plates*. Nuclear Instruments and Methods in Physics Research Section A: Accelerators, Spectrometers, Detectors and Associated Equipment, vol. 695, pages 74–77, 2012.
- [Franco 14] Andrea Franco, Jonas Geissbühler, Nicolas Wyrsh & Christophe Ballif. *Fabrication and characterization of monolithically integrated microchannel plates based on amorphous silicon*. Scientific reports, vol. 4, 2014.
- [Fraser 82] G.W. Fraser, M.A. Barstow, M.J. Whiteley & A. Wells. *Enhanced soft X-ray detection efficiencies for imaging microchannel plate detectors*. Nature, vol. 300, no. 5892, pages 509–511, 1982.
- [Fraser 84] GW Fraser, MA Barstow, JF Pearson, MJ Whiteley & M Lewis. *The soft x-ray detection efficiency of coated microchannel plates*. Nuclear Instruments and Methods in Physics Research, vol. 224, no. 1, pages 272–286, 1984.
- [Fraser 90] GW Fraser. *The gain, temporal resolution and magnetic-field immunity of microchannel plates*. Nuclear Instruments and Methods in Physics Research Section A: Accelerators, Spectrometers, Detectors and Associated Equipment, vol. 291, no. 3, pages 595–606, 1990.
- [Frenkel 38] J. Frenkel. *On pre-breakdown phenomena in insulators and electronic semi-conductors*. Physical Review, vol. 54, no. 8, pages 647–648, 1938.
- [Fridman 96] AA Fridman, L Boufendi, T Hbid, BV Potapkin & A Bouchoule. *Dusty plasma formation: Physics and critical phenomena. Theoretical approach*. Journal of applied physics, vol. 79, no. 3, pages 1303–1314, 1996.
- [Gorelikov 14] D. Gorelikov, N. Sullivan, P. De Rouffignac, H. Li, J. Narayanamoorthy & A.S. Tremsin. *Development of atomic layer deposition-activated microchannel plates for single particle detection at cryogenic temperatures*. Journal of Vacuum Science and Technology A: Vacuum, Surfaces and Films, vol. 32, no. 2, 2014.
- [Grosse-Knetter 06] Jörn Grosse-Knetter. *The ATLAS pixel detector*. Nuclear Instruments and Methods in Physics Research Section A, vol. 568, pages 252 – 257, 2006.

Bibliography

- [Gu 96] Qing Gu, EA Schiff, S Grebner, F Wang & R Schwarz. *Non-Gaussian transport measurements and the Einstein relation in amorphous silicon*. Physical review letters, vol. 76, no. 17, pages 3196–3199, 1996.
- [Guest 71] Guest. *Computer model of channel multiplier plate performance, (Un modele mathematique pour l'etude par ordinateur du fonctionnement d'une galette de microcanaux)*. Acta Electron, vol. 14, no. 1, pages 79–97, 1971.
- [Hadjar 12] Omar Hadjar, William K Fowler, Gottfried Kibelka & William C Schnute. *Preliminary demonstration of an IonCCD as an alternative pixelated anode for direct MCP readout in a compact MS-based detector*. Journal of The American Society for Mass Spectrometry, vol. 23, no. 2, pages 418–424, 2012.
- [Haque 94] M Shahidul Haque, HA Naseem & WD Brown. *Interaction of aluminum with hydrogenated amorphous silicon at low temperatures*. Journal of applied physics, vol. 75, no. 8, pages 3928–3935, 1994.
- [Haque 96] M Shahidul Haque, HA Naseem & WD Brown. *Aluminum-induced crystallization and counter-doping of phosphorous-doped hydrogenated amorphous silicon at low temperatures*. Journal of applied physics, vol. 79, no. 10, pages 7529–7536, 1996.
- [Hartmann 12] Frank Hartmann. *Silicon tracking detectors in high-energy physics*. Nuclear Instruments and Methods in Physics Research Section A: Accelerators, Spectrometers, Detectors and Associated Equipment, vol. 666, pages 25–46, 2012.
- [Hata 92] Nobuhiro Hata & Sigurd Wagner. *A comprehensive defect model for amorphous silicon*. Journal of applied physics, vol. 72, no. 7, pages 2857–2872, 1992.
- [Hecht 32] Karl Hecht. *Zum Mechanismus des lichtelektrischen Primaerstromes in isolierenden Kristallen*. Zeitschrift fuer Physik, vol. 77, no. 3-4, pages 235–245, 1932.
- [Hegedus 97] S.S. Hegedus. *Current-voltage analysis of a-Si and a-SiGe solar cells including voltage-dependent photocurrent collection*. Progress in Photovoltaics: Research and Applications, vol. 5, no. 3, pages 151–168, 1997.
- [Holman 12] Zachary C Holman, Antoine Descoeudres, Loris Barraud, F Zicarelli Fernandez, Johannes P Seif, Stefaan De Wolf & Christophe Ballif. *Current losses at the front of silicon heterojunction solar cells*. Photovoltaics, IEEE Journal of, vol. 2, no. 1, pages 7–15, 2012.

- [Holovský 12] J Holovský, M Schmid, M Stuckelberger, M Despeisse, C Ballif, A Poruba & M Vaněček. *Time evolution of surface defect states in hydrogenated amorphous silicon studied by photothermal and photocurrent spectroscopy and optical simulation*. Journal of Non-Crystalline Solids, vol. 358, no. 17, pages 2035–2038, 2012.
- [Hong 95] W.S. Hong, A. Mireshghi, J.S. Drewery, T. Jing, Y. Kitsuno, H. Lee, S.N. Kaplan & V. Perez-Mendez. *Charged particle detectors based on high quality amorphous silicon deposited with hydrogen or helium dilution of silane*. IEEE Transactions on Nuclear Science, vol. 42, pages 240–246, 1995.
- [Hordequin 01] C Hordequin, A Brambilla, P Bergonzo & F Foulon. *Nuclear radiation detectors using thick amorphous-silicon MIS devices*. Nuclear Instruments and Methods in Physics Research Section A: Accelerators, Spectrometers, Detectors and Associated Equipment, vol. 456, no. 3, pages 284–289, 2001.
- [Horton 90] Jerry R. Horton, G. William Tasker & John J. Fijol. *Characteristics and applications of advanced technology microchannel plates*. In Proceedings of SPIE - The International Society for Optical Engineering, volume 1306, page 169, 1990.
- [Hoshino 07] Masato Hoshino, Toyooki Ishino, Takashi Namiki, Norimitsu Yamada, Norio Watanabe & Sadao Aoki. *Application of a charge-coupled device photon-counting technique to three-dimensional element analysis of a plant seed (alfalfa) using a full-field x-ray fluorescence imaging microscope*. Review of Scientific Instruments, vol. 78, no. 7, page 073706, 2007.
- [Hultman 87] L Hultman, A Robertsson, HTG Hentzell, I Engström & PA Psaras. *Crystallization of amorphous silicon during thin-film gold reaction*. Journal of applied physics, vol. 62, no. 9, pages 3647–3655, 1987.
- [Iijima 11] Toru Iijima. *Status and perspectives of vacuum-based photon detectors*. Nuclear Instruments and Methods in Physics Research Section A: Accelerators, Spectrometers, Detectors and Associated Equipment, vol. 639, no. 1, pages 137–143, 2011.
- [Ilie 96] Adelina Ilie, B Equer & T Pochet. *Leakage current studies of thick a-Si:H detectors under high electric field conditions*. Nuclear Instruments and Methods in Physics Research Section A: Accelerators, Spectrometers, Detectors and Associated Equipment, vol. 380, no. 1, pages 18–22, 1996.

Bibliography

- [Ioannou 80] D. E. Ioannou. *A SEM-EBIC minority-carrier lifetime-measurement technique*. Journal of Physics D: Applied Physics, vol. 13, pages 611–616, 1980.
- [Jackson 82] Warren B Jackson & Nabil M Amer. *Direct measurement of gap-state absorption in hydrogenated amorphous silicon by photothermal deflection spectroscopy*. Physical Review B, vol. 25, no. 8, page 5559, 1982.
- [Jaeger 10] C Jaeger, M Bator, S Matich & M Stutzmann. *Two-step crystallization during the reverse aluminum-induced layer exchange process*. Journal of Applied Physics, vol. 108, no. 11, page 113513, 2010.
- [Janz 06] Stefan Janz. *Amorphous silicon carbide for photovoltaic applications*. PhD thesis, Fraunhofer Institut für Solare Energiesysteme, 2006.
- [Jarron 11] P. Jarron & N. Wyrsh. *Amorphous silicon based Microchannel plate and its manufacturing method*. no. EP patent 2,278,609, 2011.
- [Jelinsky 03] Patrick N Jelinsky, Patrick F Morrissey, James M Malloy, Sharon R Jelinsky, Oswald HW Siegmund, Christopher Martin, David Schiminovich, Karl Forster, Ted Wyder & Peter G Friedman. *Performance results of the GALEX cross delay line detectors*. In Astronomical Telescopes and Instrumentation, pages 233–240. International Society for Optics and Photonics, 2003.
- [Jingsheng 11] Pan Jingsheng, Lü Jingwen, Deng Tao *et al.* *Fabrication of a bulk conductive glass microchannel plate*. In SPIE, volume 8194, page 819407, 2011.
- [Joy 95] David C Joy. *A database on electron-solid interactions*. Scanning, vol. 17, no. 5, pages 270–275, 1995.
- [Judenhofer 08] Martin S Judenhofer, Hans F Wehrl, Danny F Newport, Ciprian Catana, Stefan B Siegel, Markus Becker, Axel Thielscher, Manfred Kneilling, Matthias P Lichy, Martin Eichner *et al.* *Simultaneous PET-MRI: a new approach for functional and morphological imaging*. Nature medicine, vol. 14, no. 4, pages 459–465, 2008.
- [Jungmann 11] Julia H Jungmann, Luke MacAleese, Jan Visser, Marc JJ Vrakking & Ron MA Heeren. *High dynamic range bio-molecular ion microscopy with the Timepix detector*. Analytical chemistry, vol. 83, no. 20, pages 7888–7894, 2011.
- [Kanaya 72] Kawakatsu Kanaya & H Kawakatsu. *Secondary electron emission due to primary and backscattered electrons*. Journal of Physics D: Applied Physics, vol. 5, no. 9, page 1727, 1972.

- [Kempenaars 08] M Kempenaars, JC Flanagan, L Giudicotti, MJ Walsh, M Beurskens, I Balboa & JET-EFDA Contributors. *Enhancement of the JET edge LI-DAR Thomson scattering diagnostic with ultrafast detectors*. Review of Scientific Instruments, vol. 79, no. 10, page 10E728, 2008.
- [Kishimoto 98] N. Kishimoto, H. Amekura, K. Kono & C. G. Lee. *Radiation resistance of amorphous silicon in optoelectric properties under proton bombardment*. Journal of Nuclear Materials, vol. 258-263, pages 1908 – 1913, 1998.
- [Kočka 91] J Kočka, CE Nebel & CD Abel. *Solution of the $\mu\tau$ problem in a-Si: H*. Philosophical Magazine B, vol. 63, no. 1, pages 221–246, 1991.
- [Kok 05] Angela Kok. *Signal formation and active edge studies of 3D silicon detector technology*. PhD thesis, Brunel University, Middlessex, West London, England, 2005.
- [Kosteski 98] Tome Kosteski, NP Kherani, F Gaspari, S Zukotynski & WT Shmayda. *Tritiated amorphous silicon films and devices*. Journal of Vacuum Science & Technology A, vol. 16, no. 2, pages 893–896, 1998.
- [Kroll 96] U Kroll, J Meier, A Shah, S Mikhailov & J Weber. *Hydrogen in amorphous and microcrystalline silicon films prepared by hydrogen dilution*. Journal of Applied Physics, vol. 80, no. 9, pages 4971–4975, 1996.
- [Kumaravelu 04] G Kumaravelu, MM Alkaisi, A Bittar, D Macdonald & J Zhao. *Damage studies in dry etched textured silicon surfaces*. Current Applied Physics, vol. 4, no. 2, pages 108–110, 2004.
- [Lampton 08] M Lampton & CW Carlson. *Low-distortion resistive anodes for two-dimensional position-sensitive MCP systems*. Review of Scientific Instruments, vol. 50, no. 9, pages 1093–1097, 2008.
- [Lapington 87] JS Lapington, AD Smith, DM Walton & HE Schwarz. *Microchannel plate pore size limited imaging with ultra-thin wedge and strip anodes*. Nuclear Science, IEEE Transactions on, vol. 34, no. 1, pages 431–433, 1987.
- [Lapington 02] JS Lapington, B Sanderson, LBC Worth & JA Tandy. *Imaging achievements with the Vernier readout*. Nuclear Instruments and Methods in Physics Research Section A: Accelerators, Spectrometers, Detectors and Associated Equipment, vol. 477, no. 1, pages 250–255, 2002.
- [Lapington 05] J.S. Lapington. *Developments in high count rate microchannel plate detectors*. In Proceedings of SPIE - The International Society for Optical Engineering, volume 5898, pages 1–10, 2005.

Bibliography

- [Lapington 09] JS Lapington, DP Thompson, PW May, NA Fox, J Howorth, J Milnes & V Taillandier. *Investigation of the secondary emission characteristics of CVD diamond films for electron amplification*. Nuclear Instruments and Methods in Physics Research Section A: Accelerators, Spectrometers, Detectors and Associated Equipment, vol. 610, no. 1, pages 253–257, 2009.
- [Lapington 13] J.S. Lapington, T.M. Conneely, S.A. Leach & L. Moore. *The capacitive division image readout: A novel imaging device for microchannel plate detectors*. In Proceedings of SPIE - The International Society for Optical Engineering, volume 8859, 2013.
- [Le Comber 70] P. G. Le Comber & W. E. Spear. *Electronic Transport in Amorphous Silicon Films*. Physics Review Letters, vol. 25, pages 509–511, 1970.
- [Le Comber 72] PG Le Comber, A Madan & WE Spear. *Electronic transport and state distribution in amorphous Si films*. Journal of Non-Crystalline Solids, vol. 11, no. 3, pages 219–234, 1972.
- [Leamy 82] H. J. Leamy. *Charge collection scanning electron microscopy*. Journal of Applied Physics, vol. 53, pages R51 –R80, 1982.
- [Llopart 02] Xavier Llopart, Michael Campbell, R Dinapoli, D San Segundo & E Pernigotti. *Medipix2: a 64-k pixel readout chip with 55- μ m square elements working in single photon counting mode*. IEEE Transactions on Nuclear Science, vol. 49, no. 5, pages 2279–2283, 2002.
- [Lule 99] T. Lule, B. Schneider & M. Bohm. *Design and fabrication of a high-dynamic-range image sensor in TFA technology*. IEEE Journal of Solid-State Circuits, vol. 34, no. 5, pages 704 –711, May 1999.
- [Lule 00] T. Lule, S. Benthien, H. Keller, F. Mutze, P. Rieve, K. Seibel, M. Sommer & M. Bohm. *Sensitivity of CMOS based imagers and scaling perspectives*. IEEE Transactions on Electron Devices, vol. 47, pages 2110 –2122, 2000.
- [Mackenzie 82] KD Mackenzie, PG Le Comber & WE Spear. *The density of states in amorphous silicon determined by space-charge-limited current measurements*. Philosophical Magazine B, vol. 46, no. 4, pages 377–389, 1982.
- [Maher 83] FJ Maher & CJ Rossouw. *Design and performance of an amplifier for EBIC imaging in a scanning electron microscope*. Journal of Physics E: Scientific Instruments, vol. 16, no. 12, pages 1238–1241, 1983.
- [Malamud 94] G Malamud, P Miné, D Vartsky, B Equer, A Breskin & R Chechik. *The photoyield of CsI, amorphous silicon and organometallic reflective photocathode materials*. Nuclear Instruments and Methods in Physics Re-

- search Section A: Accelerators, Spectrometers, Detectors and Associated Equipment, vol. 343, no. 1, pages 121–128, 1994.
- [Mane 12] Anil U Mane, Qing Peng, Jeffrey W Elam, Daniel C Bennis, Christopher A Craven, Michael A Detarando, John R Escolas, Henry J Frisch, Slade J Jokela, Jason McPhateet *et al.* *An atomic layer deposition method to fabricate economical and robust large area microchannel plates for photodetectors*. Physics Procedia, vol. 37, pages 722–732, 2012.
- [Martinelli 74] Ramon U Martinelli & DENNIS G Fisher. *The application of semiconductors with negative electron affinity surfaces to electron emission devices*. Proceedings of the IEEE, vol. 62, no. 10, pages 1339–1360, 1974.
- [Marty 05] Frédéric Marty, Lionel Rousseau, Bassam Saadany, Bruno Mercier, Olivier Français, Yoshio Mita & Tarik Bourouina. *Advanced etching of silicon based on deep reactive ion etching for silicon high aspect ratio microstructures and three-dimensional micro- and nanostructures*. Microelectronics journal, vol. 36, no. 7, pages 673–677, 2005.
- [Matsuda 04] Akihisa Matsuda. *Microcrystalline silicon.: Growth and device application*. Journal of Non-Crystalline Solids, vol. 338, pages 1–12, 2004.
- [McFadden 08] JP McFadden, CW Carlson, D Larson, M Ludlam, R Abiad, B Elliott, P Turin, M Marckwordt & V Angelopoulos. *The THEMIS ESA plasma instrument and in-flight calibration*. Space Science Reviews, vol. 141, no. 1-4, pages 277–302, 2008.
- [Melskens 08] J Melskens, G van Elzakker, Y Li & M Zeman. *Analysis of hydrogenated amorphous silicon thin films and solar cells by means of Fourier Transform Photocurrent Spectroscopy*. Thin Solid Films, vol. 516, no. 20, pages 6877–6881, 2008.
- [Miazza 06] Clement Miazza, N Wyrsh, G Choong, S Dunand, C Ballif, A Shah, Nicolas Blanc, R Kaufmann, F Lustenberger & D Moraes. *Image sensors based on thin-film on CMOS technology: Additional leakage currents due to vertical integration of the a-Si: H diodes*. In Materials Research Society Symposium Proceedings, volume 910, page 409, 2006.
- [Michalet 07] X Michalet, OHW Siegmund, JV Vallergera, P Jelinsky, JE Millaud & S Weiss. *Detectors for single-molecule fluorescence imaging and spectroscopy*. Journal of modern optics, vol. 54, no. 2-3, pages 239–281, 2007.
- [Mishima 88] Y Mishima & T Yagishita. *Investigation of the bubble formation mechanism in a-Si: H films by Fourier-transform infrared microspectroscopy*. Journal of applied physics, vol. 64, no. 8, pages 3972–3974, 1988.

Bibliography

- [Misiakos 88] K Misiakos & FA Lindholm. *Analytical and numerical modeling of amorphous silicon p-i-n solar cells*. Journal of applied physics, vol. 64, no. 1, pages 383–393, 1988.
- [Mulhollan 10] GA Mulhollan & JC Bierman. *Cesium and oxygen activated amorphous silicon germanium photocathodes for photoinjectors*. Journal of Vacuum Science & Technology B, vol. 28, no. 3, pages 495–499, 2010.
- [Nakamura 10] Kimitsugu Nakamura, Yasumasa Hamana, Yoshihiro Ishigami & Toshikazu Matsui. *Latest bialkali photocathode with ultra high sensitivity*. Nuclear Instruments and Methods in Physics Research Section A: Accelerators, Spectrometers, Detectors and Associated Equipment, vol. 623, no. 1, pages 276–278, 2010.
- [Navkhandewala 81] RV Navkhandewala, KL Narasimhan & S Guha. *Effect of electron irradiation on dark and photoconductivity of amorphous hydrogenated silicon*. Physical Review B, vol. 24, no. 12, page 7443, 1981.
- [Nicklaw 02] CJ Nicklaw, Zhong-Yi, DM Fleetwood, RD Schrimpf & ST Pantelides. *Structure, Properties, and Dynamics of Oxygen Vacancies in Amorphous SiO₂*. Physical review letters, vol. 89, no. 28, page 285505, 2002.
- [Nishida 09] Shohei Nishida, Ichiro Adachi, Rok Dolenec, Kohji Hara, Toru Iijima, Hirokazu Ikeda, Yoshikazu Ishii, Hideyuki Kawai, Samo Korpar, Peter Križanet *al.* *Study of an HAPD with 144 channels for the Aerogel RICH of the Belle upgrade*. Nuclear Instruments and Methods in Physics Research Section A: Accelerators, Spectrometers, Detectors and Associated Equipment, vol. 610, no. 1, pages 65–67, 2009.
- [Owens 12] Alan Owens. *Compound semiconductor radiation detectors*. CRC Press, 2012.
- [Pankove 84] Jacques I Pankove. *Semiconductors & semimetals*, volume 21. Academic Press, 1984.
- [Pearson 03] James F Pearson, George W Fraser, Chris H Whitford, Michele RF Siggel-King, Francis M Quinn & Geoff Thornton. *The development of a fast imaging electron detector based on the CODACON concept*. Nuclear Instruments and Methods in Physics Research Section A: Accelerators, Spectrometers, Detectors and Associated Equipment, vol. 513, no. 1, pages 183–186, 2003.
- [Peisert 92] A. Peisert. *Instrumentation in high energy physics*, volume Silicon Microstrip Detector. Singapore: World Scientific, 1992.
- [Pellegrini 08] G Pellegrini, M Lozano, M Ullan, R Bates, C Fleta & D Pennicard. *First double-sided 3-D detectors fabricated at CNM-IMB*. Nuclear Instruments

- and Methods in Physics Research Section A: Accelerators, Spectrometers, Detectors and Associated Equipment, vol. 592, no. 1, pages 38–43, 2008.
- [Perez-Mendez 86] V. Perez-Mendez, J. Morel, S.N. Kaplan & R.A. Street. *Detection of charged particles in amorphous silicon layers*. Nuclear Instruments and Methods in Physics Research Section A, vol. 252, pages 478 – 482, 1986.
- [Perez-Mendez 88] Victor Perez-Mendez, SN Kaplan, G Cho, I Fujieda, S Qureshi, W Ward & RA Street. *Hydrogenated amorphous silicon pixel detectors for minimum ionizing particles*. Nuclear Instruments and Methods in Physics Research Section A: Accelerators, Spectrometers, Detectors and Associated Equipment, vol. 273, no. 1, pages 127–134, 1988.
- [Perez-Mendez 91] V. Perez-Mendez, G. Cho, J. Drewery, T. Jing, S.N. Kaplan, S. Qureshi, D. Wildermuth, I. Fujieda & R.A. Street. *Amorphous silicon based radiation detectors*. Journal of Non-Crystalline Solids, vol. 137-138, pages 1291 – 1296, 1991.
- [Perreault 93] GC Perreault, SL Hyland & DG Ast. *High accelerating voltage electron beam induced current (EBIC) of thick and thin solar silicon specimens*. Solar energy materials and solar cells, vol. 30, no. 4, pages 309–326, 1993.
- [Ponpon 82] JP Ponpon & B Bourdon. *Oxidation of glow discharge a-Si:H*. Solid-State Electronics, vol. 25, no. 9, pages 875–876, 1982.
- [Puhlmann 91] N Puhlmann, G Oelgart, V Gottschalch & R Nemitz. *Minority carrier recombination and internal quantum yield in GaAs: Sn by means of EBIC and CL*. Semiconductor Science and Technology, vol. 6, no. 3, page 181, 1991.
- [Qureshi 89] S Qureshi, Victor Perez-Mendez, SN Kaplan, I Fujieda, G Cho & RA Street. *Signal generation in a hydrogenated amorphous silicon detector*. Nuclear Science, IEEE Transactions on, vol. 36, no. 1, pages 194–198, 1989.
- [Rangarajan 80] LM Rangarajan & GK Bhide. *Photoemission energy distribution studies of gold thin films under uv excitation by a photoelectron spectroscopic method*. Vacuum, vol. 30, no. 11, pages 515–522, 1980.
- [Rau 01] EI. Rau & S. Zhu. *A noncontact electron-probe method for measuring the diffusion length and the lifetime of minority charge carriers in semiconductors*. Semiconductors, vol. 35, no. 6, pages 718–722, 2001.
- [Renker 06] D Renker. *Geiger-mode avalanche photodiodes, history, properties and problems*. Nuclear Instruments and Methods in Physics Research Section A: Accelerators, Spectrometers, Detectors and Associated Equipment, vol. 567, no. 1, pages 48–56, 2006.

Bibliography

- [Repmann 07] T. Repmann, S. Wieder, S. Klein, H. Stiebig & B. Rech. *Production equipment for large area deposition of amorphous and microcrystalline silicon thin-film solar cells*. In 4th World Conference on Photovoltaic Energy Conversion, WCPEC-4, volume 2, pages 1724–1727, 2007.
- [Rossi 03] Leonardo Rossi. *Pixel detectors hybridisation*. Nuclear Instruments and Methods in Physics Research Section A: Accelerators, Spectrometers, Detectors and Associated Equipment, vol. 501, no. 1, pages 239–244, 2003.
- [Roy 08] Rahul Roy, Sungchul Hohng & Taekjip Ha. *A practical guide to single-molecule FRET*. Nature methods, vol. 5, no. 6, pages 507–516, 2008.
- [Schade 79] H Schade & JI Pankove. *Photoemission from cesiated hydrogenated amorphous silicon*. Surface Science, vol. 89, no. 1, pages 643–648, 1979.
- [Schlemmer 08] Heinz-Peter W Schlemmer, Bernd J Pichler, Matthias Schmand, Ziad Burbar, Christian Michel, Ralf Ladebeck, Kirstin Jattke, David Townsend, Claude Nahmias, Pradeep K Jacobet *al. Simultaneous MR/PET imaging of the human brain: feasibility study*. Radiology, vol. 248, no. 3, page 1028, 2008.
- [Schneider 87] Ulrich Schneider, Bernd Schröder & Friedhelm Finger. *The creation of metastable defects in a-Si:H films by high dose irradiation with keV-electrons*. Journal of Non-Crystalline Solids, vol. 97–98, pages 795–798, 1987. Amorphous and Liquid Semiconductors.
- [Schwarzenbach 96] W Schwarzenbach, AA Howling, M Fivaz, S Brunner & Ch Hollenstein. *Sheath impedance effects in very high frequency plasma experiments*. Journal of Vacuum Science & Technology A, vol. 14, no. 1, pages 132–138, 1996.
- [Seiler 83] H Seiler. *Secondary electron emission in the scanning electron microscope*. Journal of Applied Physics, vol. 54, no. 11, pages R1–R18, 1983.
- [Seitz 95] Peter Seitz, Kai Engelhardt, Thomas Spirig & Oliver Vietze. *Smart sensing using custom photo-application-specific integrated circuits and charge-coupled device technology*. Optical Engineering, vol. 34, no. 8, pages 2299–2308, 1995.
- [Sellin 06] P.J. Sellin & J. Vaitkus. *New materials for radiation hard semiconductor detectors*. Nuclear Instruments and Methods in Physics Research Section A, vol. 557, pages 479 – 489, 2006.
- [Shank 95] S. M. Shank, R. J. Soave, A. M. Then & G. W. Tasker. *Fabrication of high aspect ratio structures for microchannel plates*. Journal of Vacuum Science Technology B, vol. 13, pages 2736 –2740, 1995.

- [Shanks 81] HR Shanks & L Ley. *Formation of pin holes in hydrogenated amorphous silicon at high temperatures and the yield strength of a-Si: H*. Journal of Applied Physics, vol. 52, no. 2, pages 811–813, 1981.
- [Shih 97] A Shih, J Yater, C Hor & R Abrams. *Secondary electron emission studies*. Applied surface science, vol. 111, pages 251–258, 1997.
- [Shimizu 05] Satoshi Shimizu, Michio Kondo & Akihisa Matsuda. *A highly stabilized hydrogenated amorphous silicon film having very low hydrogen concentration and an improved Si bond network*. Journal of applied physics, vol. 97, no. 3, page 033522, 2005.
- [Siegmund 84] OHW Siegmund, RF Malina, K Coburn & D Werthimer. *Microchannel plate EUV detectors for the Extreme Ultraviolet Explorer*. IEEE Transactions on Nuclear Science, vol. 31, no. 1, pages 776–779, 1984.
- [Siegmund 01] Oswald HW Siegmund, Anton S Tremsin, John V Vallergera & Jeffrey Hull. *Cross strip imaging anodes for microchannel plate detectors*. Nuclear Science, IEEE Transactions on, vol. 48, no. 3, pages 430–434, 2001.
- [Siegmund 02] Oswald H. W. Siegmund. *Advances in microchannel plate detectors for UV/visible astronomy*. In Proceedings of SPIE - The International Society for Optical Engineering, volume 4854, pages 181–190, 2002.
- [Siegmund 06] O Siegmund, J Vallergera, J McPhate, J Malloy, A Tremsin, A Martin, M Ulmer & B Wessels. *Development of GaN photocathodes for UV detectors*. Nuclear Instruments and Methods in Physics Research Section A: Accelerators, Spectrometers, Detectors and Associated Equipment, vol. 567, no. 1, pages 89–92, 2006.
- [Siegmund 11] OHW Siegmund, JB McPhate, JV Vallergera, AS Tremsin, SR Jelinsky & HJ Frisch. *Novel large format sealed tube microchannel plate detectors for Cherenkov timing and imaging*. Nuclear Instruments and Methods in Physics Research Section A: Accelerators, Spectrometers, Detectors and Associated Equipment, vol. 639, no. 1, pages 165–168, 2011.
- [Siegmund 13] OHW Siegmund, JB McPhate, SR Jelinsky, JV Vallergera, AS Tremsin, R Hemphill, HJ Frisch, RG Wagner, J Elam & A Mane. *Large area microchannel plate imaging event counting detectors with sub-nanosecond timing*. Nuclear Science, IEEE Transactions on, vol. 60, no. 2, pages 923–931, 2013.
- [Simmons 71] JG Simmons. *Conduction in thin dielectric films*. Journal of Physics D: Applied Physics, vol. 4, no. 5, page 613, 1971.
- [Sinor 00] Timothy W Sinor, Edward J Bender, T Chau, Joseph P Estrera, A Giordana, John W Glesener, Mike J Iosue, PP Lin & S Rehg. *New frontiers*

- in 21st century microchannel plate (MCP) technology: bulk conductive MCP-based image intensifiers.* In International Society for Optics and Photonics, pages 5–13, 2000.
- [Smets 07] AHM Smets & MCM van de Sanden. *Relation of the Si—H stretching frequency to the nanostructural Si—H bulk environment.* Physical Review B, vol. 76, no. 7, page 073202, 2007.
- [Solomon 84] I Solomon, R Benferhat & H Tran Quoc. *Space-charge-limited conduction for the determination of the midgap density of states in amorphous silicon: Theory and experiment.* Physical Review B, vol. 30, no. 6, page 3422, 1984.
- [Spear 75] WE Spear & PG Le Comber. *Substitutional doping of amorphous silicon.* Solid State Communications, vol. 17, no. 9, pages 1193–1196, 1975.
- [Spear 76] WE Spear & PG Le Comber. *Electronic properties of substitutionally doped amorphous Si and Ge.* Philosophical Magazine, vol. 33, no. 6, pages 935–949, 1976.
- [Srour 98] JR Srour, GJ Vendura Jr, DH Lo, CMC Toporow, M Dooley, RP Nakano & EE King. *Damage mechanisms in radiation-tolerant amorphous silicon solar cells.* IEEE Transactions on Nuclear Science, vol. 45, no. 6, pages 2624–2631, 1998.
- [Staebler 77] D. L. Staebler & C. R. Wronski. *Reversible conductivity changes in discharge-produced amorphous Si.* Applied Physics Letters, vol. 31, pages 292–294, 1977.
- [Sterling 65] HF Sterling & RCG Swann. *Chemical vapour deposition promoted by rf discharge.* Solid-State Electronics, vol. 8, no. 8, pages 653–654, 1965.
- [Street 82] RA Street. *Doping and the Fermi energy in amorphous silicon.* Physical Review Letters, vol. 49, no. 16, pages 1187–1190, 1982.
- [Street 89] RA Street & K Winer. *Defect equilibria in undoped a-Si:H.* Physical Review B, vol. 40, no. 9, pages 6236–6249, 1989.
- [Street 90] RA Street. *Thermal generation currents in hydrogenated amorphous silicon p-i-n structures.* Applied physics letters, vol. 57, no. 13, pages 1334–1336, 1990.
- [Street 91] Robert A Street. Hydrogenated amorphous silicon. Cambridge University Press, 1991.
- [Stuckelberger 13] M Stuckelberger, M Despeisse, G Bugnon, J-W Schüttauf, F-J Haug & Christophe Ballif. *Comparison of amorphous silicon absorber materials:*

- Light-induced degradation and solar cell efficiency.* Journal of Applied Physics, vol. 114, no. 15, page 154509, 2013.
- [Stutzmann 84] M Stutzmann, WB Jackson & CC Tsai. *Kinetics of the Staebler–Wronski effect in hydrogenated amorphous silicon.* Applied Physics Letters, vol. 45, no. 10, pages 1075–1077, 1984.
- [Stutzmann 87] M Stutzmann, DK Biegelsen & RA Street. *Detailed investigation of doping in hydrogenated amorphous silicon and germanium.* Physical Review B, vol. 35, no. 11, pages 5666–5701, 1987.
- [Takada 87] J Takada & H Fritzsche. *Drift mobility of doped a-Si: H at high temperatures.* Physical Review B, vol. 36, no. 3, pages 1710–1714, 1987.
- [Tanielian 82] Minas Tanielian. *Adsorbate effects on the electrical conductance of a-Si: H.* Philosophical Magazine B, vol. 45, no. 4, pages 435–462, 1982.
- [Teyssieux 07] Damien Teyssieux, Laurent Thiery & Bernard Cretin. *Near-infrared thermography using a charge-coupled device camera: Application to microsystems.* Review of scientific instruments, vol. 78, no. 3, page 034902, 2007.
- [Tiedje 81] T Tiedje, JM Cebulka, DL Morel & B Abeles. *Evidence for exponential band tails in amorphous silicon hydride.* Physical Review Letters, vol. 46, pages 1425–1428, 1981.
- [Tremsin 96a] AS Tremsin, JF Pearson, GW Fraser, WB Feller & P White. *Microchannel plate operation at high count rates: new results.* Nuclear Instruments and Methods in Physics Research Section A: Accelerators, Spectrometers, Detectors and Associated Equipment, vol. 379, no. 1, pages 139–151, 1996.
- [Tremsin 96b] AS Tremsin, JF Pearson, JE Lees & GW Fraser. *The Microsphere Plate: a new type of electron multiplier.* Nuclear Instruments and Methods in Physics Research Section A: Accelerators, Spectrometers, Detectors and Associated Equipment, vol. 368, no. 3, pages 719–730, 1996.
- [Tremsin 03] Anton S Tremsin, John V Vallerga, Oswald HW Siegmund, Charles P Beetz & Robert W Boerstler. *The latest developments of high-gain Si microchannel plates.* In International Society for Optics and Photonics, pages 215–224, 2003.
- [Tremsin 06] Anton S Tremsin, Oswald HW Siegmund, Jeff S Hull, John V Vallerga, Jason B McPhate, Johan Soderstrom, Jau-Wern Chiou, Jinghua Guo & Zahid Hussain. *High resolution photon counting detection system for advanced inelastic X-ray scattering studies.* In Nuclear Science Symposium Conference Record, volume 2, pages 735–739. IEEE, 2006.

- [Tremisn 14] AS Tremisn, T Shinohara, T Kai, M Ooi, T Kamiyama, Y Kiyanagi, Y Shiota, JB McPhate, JV Vallerger, OHW Siegmund *et al.* *Neutron resonance transmission spectroscopy with high spatial and energy resolution at the J-PARC pulsed neutron source*. Nuclear Instruments and Methods in Physics Research Section A: Accelerators, Spectrometers, Detectors and Associated Equipment, vol. 746, pages 47–58, 2014.
- [Turala 05] M Turala. *Silicon tracking detectors—historical overview*. Nuclear Instruments and Methods in Physics Research Section A: Accelerators, Spectrometers, Detectors and Associated Equipment, vol. 541, no. 1, pages 1–14, 2005.
- [Turchetta 01] R Turchetta, JD Berst, B Casadei, G Claus, C Colledani, W Dulinski, Y Hu, D Husson, JP Le Normand, JL Riesterer *et al.* *A monolithic active pixel sensor for charged particle tracking and imaging using standard VLSI CMOS technology*. Nuclear Instruments and Methods in Physics Research Section A: Accelerators, Spectrometers, Detectors and Associated Equipment, vol. 458, no. 3, pages 677–689, 2001.
- [Vallerger 97] John V Vallerger, Oswald HW Siegmund, Josef Dalcomo & Patrick N Jelinsky. *High-resolution ($< 10\text{-}\mu\text{m}$) photon-counting intensified CCD*. In *Electronic Imaging'97*, pages 156–167. International Society for Optics and Photonics, 1997.
- [Vallerger 08] John Vallerger, Jason McPhate, Anton Tremisn & Oswald Siegmund. *Optically sensitive MCP image tube with a Medipix2 ASIC readout*. In *International Society for Optics and Photonics*, pages 702115–702115, 2008.
- [Van den Donker 06] MN Van den Donker, R Schmitz, W Appenzeller, B Rech, WMM Kessels & MCM Van de Sanden. *The role of plasma induced substrate heating during high rate deposition of microcrystalline silicon solar cells*. *Thin Solid Films*, vol. 511, pages 562–566, 2006.
- [van Swaaij 08] RACMM van Swaaij & A Klaver. *Comparison of amorphous silicon solar cell performance following light and high-energy electron-beam induced degradation*. *Journal of Non-Crystalline Solids*, vol. 354, no. 19, pages 2464–2467, 2008.
- [Vaněček 91] M Vaněček, J Kočka, E Šípek, A Tříska & RD Plättner. *Photocarrier collection efficiency in amorphous silicon down to liquid helium temperature*. *Solid state communications*, vol. 77, no. 6, pages 475–479, 1991.
- [Vaněček 95] M Vaněček, J Kočka, A Poruba & A Fejfar. *Direct measurement of the deep defect density in thin amorphous silicon films with the absolute constant*

- photocurrent method*. Journal of applied physics, vol. 78, no. 10, pages 6203–6210, 1995.
- [Vanecek 02] M Vanecek & A Poruba. *Fourier-transform photocurrent spectroscopy of microcrystalline silicon for solar cells*. Applied Physics Letters, vol. 80, no. 5, pages 719–721, 2002.
- [Watanabe 96] Yukio Watanabe, Masaharu Shiratani, Tsuyoshi Fukuzawa, Hiroharu Kawasaki, Yoshio Ueda, Sanjay Singh & Hiroshi Ohkura. *Contribution of short lifetime radicals to the growth of particles in SiH₄ high frequency discharges and the effects of particles on deposited films*. Journal of Vacuum Science & Technology A, vol. 14, no. 3, pages 995–1001, 1996.
- [Weisfield 83] RL Weisfield. *Space-charge-limited currents: Refinements in analysis and applications to a-Si_{1-x}Ge_x:H alloys*. Journal of applied physics, vol. 54, no. 11, pages 6401–6416, 1983.
- [Wermes 05] N. Wermes. *Pixel detectors for tracking and their spin-off in imaging applications*. Nuclear Instruments and Methods in Physics Research Section A, vol. 541, pages 150 – 165, 2005.
- [Willingale 98] R. Willingale, G. W. Fraser, A. N. Brunton & A. P. Martin. *Hard X-ray imaging with microchannel plate optics*. Experimental Astronomy, vol. 8, pages 281–296, 1998.
- [Winer 87] K Winer & L Ley. *Surface states and the exponential valence-band tail in a-Si: H*. Physical Review B, vol. 36, no. 11, pages 6072–6078, 1987.
- [Wiza 79] J. L. Wiza. *Microchannel plate detectors*. Nuclear Instrumentation and Method, vol. 162, pages 587–601, 1979.
- [Wooldridge 39] D Wooldridge. *Theory of secondary emission*. Physical Review, vol. 56, no. 6, pages 562–578, 1939.
- [Wronski 77] CR Wronski & DE Carlson. *Surface states and barrier heights of metal-amorphous silicon schottky barriers*. Solid State Communications, vol. 23, no. 7, pages 421–424, 1977.
- [Wronski 81] Christopher R Wronski & Ronald E Daniel. *Photoconductivity, trapping, and recombination in discharge-produced, hydrogenated amorphous silicon*. Physical Review B, vol. 23, no. 2, page 794, 1981.
- [Wronski 89] CR Wronski, S Lee, M Hicks & Satyendra Kumar. *Internal photoemission of holes and the mobility gap of hydrogenated amorphous silicon*. Physical review letters, vol. 63, no. 13, pages 1420–1423, 1989.

Bibliography

- [Wyrsh 91] N Wyrsh, F Finger, TJ McMahon & M Vanecek. *How to reach more precise interpretation of subgap absorption spectra in terms of deep defect density in a-Si: H*. Journal of non-crystalline solids, vol. 137, pages 347–350, 1991.
- [Wyrsh 95] N Wyrsh, N Beck, P Pipoz, M Goerlitzer, Haine Beck & A Shah. *Recent progress in the interpretation of a-Si: H transport properties: Lifetimes, mobilities and mobility-lifetime products*. Solid State Phenomena, vol. 44, pages 525–534, 1995.
- [Wyrsh 05] N. Wyrsh, C. Miazza, C. Ballif, A. Shah, N. Blanc, R. Kaufmann, F. Lustenberger & P. Jarron. *Vertical integration of hydrogenated amorphous silicon devices on CMOS circuits*. In Materials Research Society Symposium Proceedings, San Francisco, CA, volume 869, pages 3–14, 2005.
- [Wyrsh 06] N Wyrsh, C Miazza, S Dunand, C Ballif, A Shah, M Despeisse, D Moraes, F Powolny & P Jarron. *Radiation hardness of amorphous silicon particle sensors*. Journal of non-crystalline solids, vol. 352, no. 9, pages 1797–1800, 2006.
- [Wyrsh 08] N Wyrsh, G Choong, C Miazza & C Ballif. *Performance and Transient Behavior of Vertically Integrated Thin-film Silicon Sensors*. Sensors, vol. 8, pages 4656–4668, 2008.
- [Wyrsh 11] N Wyrsh, A Franco, Y Riesen, M Despeisse, S Dunand, F Powolny, P Jarron & C Ballif. *Amorphous silicon based particle detectors*. In Materials Research Society Symposium Proceedings, San Francisco, CA, volume 1321. Cambridge Univ Press, 2011.
- [Wyrsh 14] N Wyrsh, Y Riesen, A Franco, S Dunand, H Kind, S Schneider & C Ballif. *Amorphous silicon based betavoltaic devices*. In MRS Proceedings, volume 1536, pages 73–78. Cambridge Univ Press, 2014.
- [Xu 09] Yan Xu, Feng Fei, Zhang Jin & Wang Yuelin. *Smooth Surface Morphology of Hydrogenated Amorphous Silicon Film Prepared by Plasma Enhanced Chemical Vapor Deposition*. Plasma Science and Technology, vol. 11, no. 5, page 569, 2009.
- [Yacobi 84] BG Yacobi, TJ McMahon & A Madan. *Electron-beam-induced current microcharacterization of fabrication defects in hydrogenated amorphous silicon solar cells*. Solar cells, vol. 12, no. 3, pages 329–335, 1984.
- [Yi 08] JL Yi & Lihong Niu. *Making bulk-conductive glass microchannel plates*. In Integrated Optoelectronic Devices, pages 68900E–68900E. International Society for Optics and Photonics, 2008.

- [Zworykin 39] Vladimir Kosma Zworykin & JA Rajchman. *The electrostatic electron multiplier*. Proceedings of the IRE, vol. 27, no. 9, pages 558–566, 1939.

Andrea FRANCO

Rue Edmond-de-Reynier 22 21.08.1983
2000 Neuchâtel Italian, permit B
andrefranco57@gmail.com married



WORK EXPERIENCE

- | | |
|-------------|--|
| 2010 – 2014 | Research assistant at Photovoltaics and Thin-Film Electronics laboratory (PV-lab), EPFL.
Research about the development of the first microchannel plate based on amorphous silicon. |
| 2008 – 2009 | Young Graduate Trainee at the European Space Agency (ESA), ESTEC, The Netherlands. In the quality department, in charge of assessing the reliability of electronic components for space applications with radioactive sources. |
| 2007 – 2008 | Trainee at Thales Alenia Space, quality department, Italy. Support to activities for the qualification and standardization of Electrical, Electronic and Electromechanical (EEE) parts for space applications. |

EDUCATION

- | | |
|-------------|---|
| 2010 – 2014 | Ph.D. in Material Science at PV-Lab, EPFL, Neuchâtel, Switzerland.
<i>Monolithic particle detectors based on hydrogenated amorphous silicon.</i> |
| 2005 – 2007 | Msc. in Solid State Physics – University of Torino. Erasmus at University of Sophia Antipolis, Nice, France. Mark: 110/110 with honours.
Msc. thesis about the physical properties of high-temperature superconductors. |
| 2002 – 2005 | Bsc. in Physics – University of Torino. Mark: 106/110.
Bsc. thesis about the characterization of ultrasonic piezoelectric generators for biomedical applications, at the Italian Institute for Metrology Research (INRIM). |

AWARDS AND DIPLOMA

- Best Master Thesis in Physics of Advanced Technologies, year 2006-2007.
- Diploma of “Radiation Technician”, Level 5A, University of Delft, The Netherlands.

TECHNICAL AND IT SKILLS

- Realization of test systems, controlled by LabVIEW, to characterize photodetectors with visible and UV light (Ph.D.) and electronics components with sealed radioactive sources (ESA).
- Chemical and physical vapour deposition (CVD and PVD) of thin films, wet and dry etching (reactive ion etching, RIE), Scanning Electron Microscope (SEM) with related techniques (EDX, EBIC).
- Good knowledge of Office package and LabVIEW. Basic knowledge of programs for data analysis like Origin, Mathematica, Igor Pro.

LANGUAGE SKILLS

- | | |
|---------|--|
| Italian | Native language |
| English | C1. Studied for 8 years and professionally used for more than 6. |
| French | B2. Current working language. |

GENERAL INTERESTS

Running, focused on medium-distance mountain trails. Skiing.
Reading about current affairs and geopolitics.